Development and Commissioning of the Silicon Pixel GigaTracker for the NA62 Experiment at CERN

Bob Velghe

Université catholique de Louvain
Secteur des Sciences et Technologies
Institut de Recherche en Mathématique et Physique
Centre de Cosmologie, Physique des Particules
et Phénoménologie

Bruxelles, mars 2016

Thèse présentée en vue de l'obtention du grade de docteur en sciences.
Membres du jury:

Prof. Vincent Lemaitre	Président Université catholique de Louvain
Prof. Jean-Marc Gérard	Secrétaire Université catholique de Louvain
Prof. Eduardo Cortina Gil	Promoteur Université catholique de Louvain
Prof. Gilles De Lentdecker	Université libre de Bruxelles
Prof. John Fry	University of Liverpool
Prof. Flavio Marchetto	Istituto Nazionale Di Fisica Nucleare, Torino

Merci Ako, Claire, Julien, Pat, Pierre-Edouard, Rytis, Thibault, Vlasto.
Nos aventures m'ont permis de garder les pieds sur terre.

Merci Adeline, Adrien, Alban, Alex, Antoinette, Charlotte, Corentin,
Delphine, Eliane, François, Guillaume, Julie, Laurent,
Olivier, Thomas, Thérèse, Violette, Virginie.
Je n'oublierai pas vos encouragements.

Merci Benoît, Gauthier, Thomas. Les inclassables.

Merci Alessia, Arnaud, Claude, Olivier, membres de CP3.
Votre bienveillance est exemplaire.

Merci Carinne, Christine, Ginette, Jérôme, Luc, Pavel.
Les garants de l'esprit de CP3.

Grazie a tutti i membri della collaborazione NA62.
Voi avete reso i miei periodi al
CERN indimenticabili.

Merci Flavio, Jean-Marc, John, Gilles, Vincent.
Vos nombreux commentaires m'ont
été d'une aide précieuse.

Merci Adrien, Olivier, Laurent, Ludivine.
Toutes ces escapades tardives au Pantin
ont été plus que salutaires.

Merci Massimiliano, Mathieu, Matthew.
J'ai beaucoup appris à vos côtés.

Merci Elisa, Nicolas, Plamen, Sergey.
Votre contribution fut essentielle.

Merci Eduardo de m'avoir fait
confiance.

Merci Ella, Eric, Eva, MX.

Merci
Anaïs

This work has been partially supported by the *Fonds de la Recherche Scientifique* (FNRS) through a *Fonds pour la formation à la Recherche dans l'Industrie et dans l'Agriculture* (FRIA) fellowship.

Contents

Introduction

The standard model of particle physics (SM) describes the microscopic interactions of elementary particles with an unprecedented accuracy over a wide range of energies. However, observations such as the neutrino oscillations or the matter-antimatter asymmetry in the Universe do not fit with the current model. Furthermore, many authors consider the SM as a low energy effective theory valid up to an unknown scale $\Lambda \leq E_{\text{Plank}}$. In this framework, the bare Higgs boson mass square receives quantum corrections $\propto \Lambda^2$. However, the Higgs mass was measured around 125 GeV; such a huge cancellation between the quantum correction and the bare mass appear unnatural and suggests the existence of new physics at the TeV scale [1].

Many beyond the standard model (BSM) theories are proposed to overcome the SM limitations. The non-observation of new states during the 2009–2015 run of the Large Hadron Collider (LHC) suggests that the novel mechanisms involve energies above a few TeVs or interact weakly with the known particles. In a complementary manner to the direct searches, accurate measurements of rare processes could potentially reveal hints of BSM physics. The success of this program requires accurate theoretical predictions for observables; this is often complicated by the presence of non-perturbative hadronic effects.

High intensity particle beams are essential to perform studies of rare phenomena in a reasonable time. They bring new challenges in terms of detector time resolution, radiation hardness, material budget, and data processing capabilities. In addition, advanced trigger and data acquisition systems must be developed to absorb the stream of data. This dissertation focuses on the development and commissioning of a silicon pixel tracker with a hit time resolution below 150 ps for the NA62 experiment at CERN [2].

The motivations for this work are highlighted in the following sections; they will be detailed in the next two chapters. We close the introduction with the outline of the dissertation and a summary of my main contributions to the experiment.

Rare Kaon Decays

The study of the kaons and more generally of the *strange* particles has been an important source of inspiration in the construction of the SM. Indeed, they were central in the establishment key concepts like the flavour quantum number or the neutral meson states mixing. Furthermore, the CP violation was first observed in the kaon system [3, 4, 5].

An accurate measurement of the $K^+ \to \pi^+ \nu\overline{\nu}$ and $K_L \to \pi^0 \nu\overline{\nu}$ rare decays branching ratios is of considerable interest. To begin with, BSM mechanisms involving energy scales up to hundreds of TeV [6] could affect these branching ratios. Next, the measurement would constitute an additional test of the SM flavour structure. Indeed, it is possible to construct the Unitary Triangle (UT) from these branching ratios measurements [7]. This approach has the advantage to be complementary to the one based on the B meson system observables. Finally, the $K_L \to \pi^0 \nu\overline{\nu}$ decay is almost purely CP-violating. Any deviation from the SM predictions would indicate a new source of CP violation.

In the SM, the $K \to \pi\nu\overline{\nu}$ decays are induced by flavour-changing neutral currents (FCNC). They are described by Z-penguin and W-box Feynman diagrams. The internal top quark largely dominates the decay amplitude thanks to the GIM mechanism which suppresses the up and charm quarks contribution by a factor $\propto (m_q/m_W)^2$. Moreover, the decay amplitude is proportional to the CKM parameter V_{us} raised to the power of five. This additional $\propto 10^{-4}$ factor is specific to the kaon decays. The conjugation of the two effects explains the smallness of the branching ratio and its sensitivity to hypothetical BSM effects.

The present SM theoretical prediction are [8]:

$$\mathcal{B}\left(K^+ \to \pi^+ \nu\overline{\nu}\right) = (9.11 \pm 0.72) \times 10^{-11} \ ,$$
$$\mathcal{B}\left(K_L \to \pi^0 \nu\overline{\nu}\right) = (3.00 \pm 0.31) \times 10^{-11} \ .$$

Such an accuracy is possible because the hadronic matrix elements can be extracted from the $K^+ \to \pi^0 e^+ \nu_e$ branching ratio [9]. Moreover, the remaining long-distance effects are small. Nowadays, the main contributions to the uncertainties are the CKM parameters V_{cb} and γ. The remaining part is mostly due to the charm quark contributions to the loop which affects only the charged decay. As a result, the total theoretical uncertainties attached to the branching ratios are of the order of ten and eight percent for the neutral and charged decay respectively, which is remarkable for semileptonic meson decays.

The measurement of the branching ratios is complicated by the fact that both modes are largely suppressed in Nature. The current best experimental limits are [10, 11]:

$$\mathcal{B}\left(K^+ \to \pi^+ \nu\overline{\nu}\right) = \left(1.73^{+1.15}_{-1.05}\right) \times 10^{-10} \ ,$$
$$\mathcal{B}\left(K_L \to \pi^0 \nu\overline{\nu}\right) < 2.6 \times 10^{-8} \ .$$

The neutral mode branching ratio was measured by the E391a Collaboration

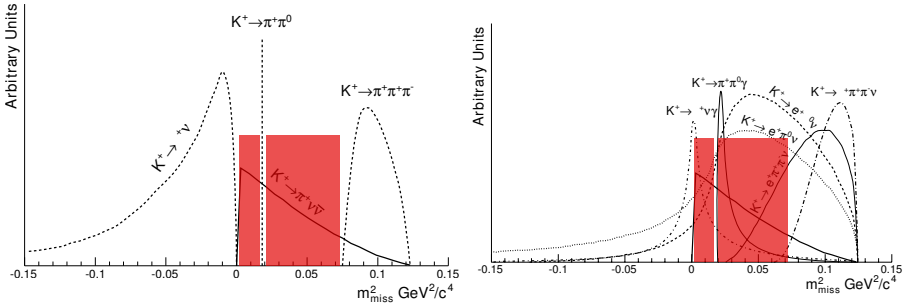

Figure 1: Squared missing mass distribution under the hypothesis that the charged track is a pion. The $K^+ \to \pi^+\nu\overline{\nu}$ signal region (in red) is split in two by the $K^+ \to \pi^+\pi^0$ peak and is bounded by the $K^+ \to \mu^+\nu_\mu$ and $K^+ \to \pi^+\pi^+\pi^-$ contributions. An accurate kinematic reconstruction of the decays is mandatory to maintain the ten percent signal acceptance. The figure on the left (right) shows the decay channels which are constrained (not constrained) by the reconstructed event kinematic.

at KEK while the charged mode branching ratio was measured by the E949 Collaboration at BNL.

A series of new experiments aimed to $K \to \pi\nu\overline{\nu}$ have be proposed in the 2000s. Two have been funded. The branching ratio of the neutral decay mode is being measured by the KOTO experiment in J-PARC [12], the collaboration plans to reach the SM sensitivity by 2020. Similarly, the NA62 collaboration at CERN will measure the charged decay mode.

NA62 Experiment

The NA62 collaboration aims to bridge the gap between the theory prediction and the measurement by collecting of the order of one hundred $K^+ \to \pi^+\nu\overline{\nu}$ decays during the 2016–2018 period. Contrary to all the previous experiments, that were based on the stopped kaons technique, NA62 will pioneer the decay-in-flight method. The setup is installed in the CERN North Area which is attached to the CERN SPS infrastructure. The experiment takes advantage of a 75 GeV/c, 750 MHz, mixed hadron secondary beam containing about six percent of kaons.

A rejection factor of the order of 10^{12} for the main kaon decay modes is essential to reach the 10:1 signal to background ratio target. A large fraction of the background signals can be identified on the base of their kinematic properties. As illustrated in Figure 1, the square missing mass

$$m^2_{\text{miss}} = (p_k - p_\pi)^2 \approx m^2_K \left(1 - \frac{|p_\pi|}{|p_K|}\right) + m^2_\pi \left(1 - \frac{|p_K|}{|p_\pi|}\right) - |p_\pi||p_K|\theta^2_{\pi K} \ , \quad (1)$$

gives a handle on 92 percent of the background signals [13]. As the signal

Table 1: NA62 particle tracking requirements. The material budget is given by station. The STRAW timing capabilities are seconded by a RICH detector ($\sigma_t \leq 100$ ps).

	GigaTracker	STRAW
σ_p/p	$\leq 0.2\%$	$\leq 1\%$
σ_θ	≤ 20 µrad	≤ 60 µrad
X/X_0	$< 0.5\%$	$< 0.5\%$
σ_t	≤ 200 ps	≤ 1 ns

regions lie on each side of the $K^+ \to \pi^+\pi^0$ peak, the squared missing mass resolution is a key element of the detector performance. The additional rejection power is provided by calorimetric measurements and particle identification.

The event kinematics is provided by particle trackers placed on either side of a fiducial volume. Upstream, the *GigaTracker* tracks the whole 750 MHz secondary beam while, downstream, the *STRAW* tracks all the charged decay products. A gap in STRAW let the secondary beam through therefore the hit rate in the active region of the detector is around 10 MHz. A detailed description of the NA62 setup is provided in Section 1.2.

The desired squared missing mass resolution drives the required momentum resolution, angular resolution and material budget of the tracking system; they are reported in Table 1. In addition, the track time resolution has to be below 200 ps to keep the decay products to parent particle matching efficiency well above 99 percent at 750 MHz. The STRAW timing capabilities are seconded by a large ring-imaging Čerenkov (RICH) detector.

The NA62 experiment was proposed in 2004 and approved in 2008; it is scheduled at least until the LHC "Long Shutdown 2" (LS2) in 2019. After a short technical run in 2012, commissioning runs took place in autumn 2014 and during the second half of 2015. The first physics run should start in the spring of 2016.

This dissertation focuses on data acquired in autumn 2014. At that time the state of the experiment was the following:

- The trigger and data acquisition system (TDAQ) could only absorb 20 to 50 percent of the nominal rate. This was caused in part by unexpected fluctuations in the beam intensity. Moreover, the level zero trigger was not fully commissioned and the level one and two triggers were not implemented.

- Some subdetectors were not installed or were partially commissioned. Notably, because of manufacturing issues with the GigaTracker carrier card, only ten percent of the pixels were readout. The muons rejection power was greatly reduced as two of the three muon vetoes were not fully operational.

- The GigaTracker and STRAW readout systems were running in standalone mode; their data streams were not synchronized with the common NA62 TDAQ infrastructure.

The situation was considerably improved in 2015. Particularly, all the installed detectors were included in the global DAQ, the muon veto detectors were all operational, the level zero trigger was fully commissioned and about two-thirds of the GigaTracker channels were readout.

Silicon Pixel GigaTracker

In view of the particle tracking requirements, a silicon pixel beam tracker was developed specifically for the NA62 experiment. The detector is composed of three independent stations operated in vacuum, they track the whole NA62 secondary beam.

The tracker specifications derive from the physics requirements for the $K^+ \to \pi^+ \nu\overline{\nu}$:

- The hit time resolution must be below 200 ps to keep the upstream-downstream track matching efficiency above 99 percent given that the average beam rate is 750 MHz.
- The material budget in the beam area must be kept under 0.5 percent of the radiation length (470 µm for the silicon) to ensure a good momentum resolution. Moreover, since GigaTracker is installed upstream of the fiducial volume, it is crucial to minimize the inelastic scatterings in the last station.
- The overall tracking efficiency must be above 99 percent to ensure a large $K^+ \to \pi^+ \nu\overline{\nu}$ signal acceptance.

To meet these specifications, a research and development program started in 2004. A 45 channels proof-of-concept prototype chip was fabricated and characterized in 2009–2010. As all the tests were conclusive, in autumn 2010 four prototype chips were bump-bonded to p-in-n type sensors and tested in beam at CERN. The full detector was installed and tested in beam for the first time in autumn 2014.

Two elements of the detector are especially innovative. First, the cooling is ensured by the circulation of C_6F_{14} in microchannels enclosed in a silicon plate. The system can maintain the sensor and readout chips close to -20 °C in the beamline vacuum. Eventually, the total thickness in the beam acceptance could by as little as 130 µm of silicon. This is the first application of such technology in high energy physics [14]. Second, each sensor is covered by ten custom readout ASIC named *TDCpix* [15]. This chip was developed specifically for the GigaTracker. It can handle particle rates up to 114 kHz/pixel while keeping the detection efficiency above 99 percent. The readout is "trigger-less", all the

hits are shipped off to an external readout board. The data throughput per ASIC can be as high as 12.8 Gbit/s.

Dissertation Outline

This dissertation focuses on the development and commissioning of the GigaTracker. The project is part of a larger research programme dedicated to the measurement of the rare $K^+ \to \pi^+ \nu\overline{\nu}$ decay branching ratio.

The text is organized as follow: in Chapter 1 we review the unique characteristics of the rare $K^+ \to \pi^+ \nu\overline{\nu}$ decay as well as the NA62 experimental setup. Silicon pixel detectors are discussed in Chapter 2; we collect the important formulae we need for the discussion. A special emphasis is put on radiation damage and on the time resolution of silicon sensors. The aspects of this work related to the GigaTracker development are grouped in Chapter 3. Finally, the Chapter 4 is mostly dedicated to the study of the GigaTracker performances. We close the text with a first exploration of the NA62 2014 pilot run data.

The author contributed to various aspects of the GigaTracker project. They will be detailed in the Chapter 3 and 4. The main outcomes are:

- The determination of the GigaTracker prototype hit time resolution [2].
- The characterisation of n-in-p silicon sensors [16].
- The implementation of a large part of the GigaTracker Monte Carlo simulation.
- The survey of the GigaTracker performances during the 2014 NA62 pilot run.

In addition, the author carried out a number of more technical projects. Resources that could be useful for further reference are collected in the appendices.

Chapter 1

NA62 Experiment

So far, only seven $K^+ \to \pi^+ \nu\overline{\nu}$ candidates have ever been observed. All were found in the BNL E787 and E949 combined dataset [10]. The measured branching ratio,

$$\mathcal{B}_{\text{Exp}}\left(K^+ \to \pi^+ \nu\overline{\nu}\right) = \left(1.73^{+1.15}_{-1.05}\right) \times 10^{-10} \ ,$$

is affected by large statistical uncertainties. The theoretical prediction is much more accurate [8]:

$$\mathcal{B}_{\text{SM}}\left(K^+ \to \pi^+ \nu\overline{\nu}\right) = (0.911 \pm 0.072) \times 10^{-10} \ .$$

Yet, the large experimental uncertainties prevent to draw any conclusion about BSM scenarios or to perform additional tests of the SM flavour structure.

To improve the experimental situation, the NA62 collaboration plans to collect about 100 $K^+ \to \pi^+ \nu\overline{\nu}$ decays in two years of data taking. The first physics run is due to start in April 2016. The experiment was designed to reach a total relative uncertainty of about ten percent on the branching ratio.

Next to the $K^+ \to \pi^+ \nu\overline{\nu}$ program, the experiment has a rich potential for the study of rare and forbidden kaon decays as well as exotic π^0 decays resulting from the $K^+ \to \pi^+\pi^0$ reaction. Among them, prospective Monte Carlo studies suggests that limits on the branching ratio of the lepton number violating (LNV) kaon decays $K^+ \to \pi^-\mu^+\mu^+$ could be improved [17]. Heavy neutrinos ($K^+ \to \mu^+ N$) and dark photons ($\pi^0 \to \gamma U$) searches could also benefit from the enhanced statistics and improved detectors performance.

In this chapter we first review the theoretical and experimental status of the $K \to \pi\nu\overline{\nu}$ decay. To start with, we highlight the connections between the branching ratios and the SM flavour structure. Then, we detail how selected BSM scenarios affects the branching ratio. In the second section, we present the guiding principles of the NA62 experiment.

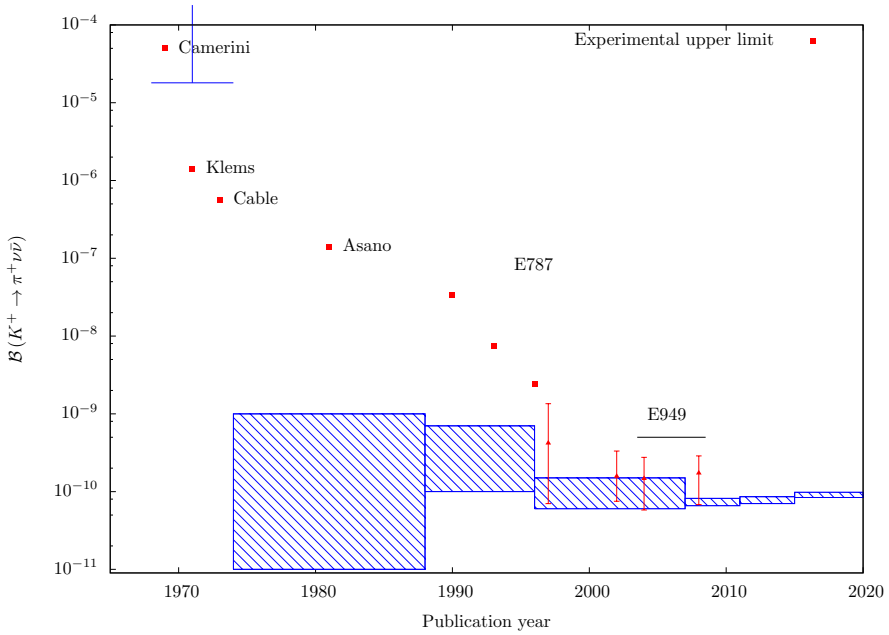

Figure 1.1: History of theoretical and experimental efforts directed towards the $K^+ \to \pi^+\nu\overline{\nu}$ decay. The blue hatched rectangles represent the theoretical uncertainties at different epochs, the first branching ratio prediction [18] didn't include uncertainties and is hence represented as a line. Only major progresses are represented, the sources are, from left to right, [18, 19, 20, 21, 9, 22, 8]. The last major improvement was the extraction of the decay matrix element from the $K^+ \to \pi^0 e^+ \nu_e$ decay by Mescia and Smith in 2007 [9]. The experimental values, in red, are extracted from [23] (Camerini), [24] (Klems), [25] (Cable), [26] (Asano), [27, 28, 29, 30, 31] (E787) and [32, 10] (E949). All the experiments used the stopped kaon technique.

1.1 $K^+ \to \pi^+\nu\overline{\nu}$ Decay

The measurement of $K^+ \to \pi^+\nu\overline{\nu}$ branching ratio has a long history which is summarized in Figure 1.1. The first limit on $\mathcal{B}(K^+ \to \pi^+\nu\overline{\nu})$ was reported in 1969. We had to wait until 1997 for the observation of a first candidate by the E787 experiment. Similarly, the theoretical prediction has been constantly improved to reach a relative total uncertainty of eight percent, which is remarkable. With NA62, for the first time, a measurement of the branching ratio with a comparable accuracy is within reach. In the next sections we will justify the previous points.

1.1.1 Weak Universality and Quark Mixing

The weak interaction is responsible for the decay of many unstable subatomic particles. It acts on all the fermions, including the neutrinos and it is the only interaction capable of changing the flavour of the quarks. Moreover, it violates the P, C and CP symmetries. This force is mediated by three massive gauge bosons, called the Z, the W^+ and the W^-, and hence acts only at short range.

We will now outline how the *flavour structure* of the SM was progressively discovered. We follow a phenomenological approach, a more detailed description can be found, for example, in ref [33, 34].

At first sight, the weak interaction is not universal; some decays are suppressed with respect to others while they look very similar:

$$\mathcal{B}\left(D^+ \to \pi^+ K^0\right) \approx 0.01 \ , \ \ \mathcal{B}\left(D^+ \to \pi^+ \pi^0\right) \approx 10^{-3} \ .$$

An explanation for the apparent difference of the weak coupling was proposed by Cabibbo in 1963 [35], before the advent of the quark model or the discovery of the D mesons. Let's assume that the weak interaction couples to u' and d' where the $'$ designs the weak eigenstates. Cabibbo postulated a relation between the weak and mass eigenstates:

$$d' = d\cos\theta + s\sin\theta \ ; \ u' = u \ , \tag{1.1}$$

where the Cabibbo angle, $\theta \approx 0.26$ rad, was obtained for instance by comparing the rate of $K^+ \to \mu^+\nu$ and $\pi^+ \to \mu^+\nu$. That is, the weak force eigenstates do not correspond to the strong force eigenstates and the $d \to u$ transitions are favoured over the $s \to u$. Put in another way, the weak interaction mixes quarks belonging to the first and second generation. The Cabibbo angle explained many other branching ratios which was a huge success.

The rotation restores the universality but it introduces a new issue: it allows the $K_L^0 \to \mu^+\mu^-$ decay that was not observed at that time. It turned out that $\mathcal{B}\left(K_L^0 \to \mu^+\mu^-\right) = (6.84 \pm 0.11) \times 10^{-9}$. More generally, such flavour-changing neutral currents (FCNC) are largely suppressed in Nature, for instance

$$\mathcal{B}\left(K^+ \to \pi^+ e^+ e^-\right) \approx 3 \times 10^{-7} \ , \ \ \mathcal{B}\left(K^+ \to \pi^0 e^+ \nu_e\right) \approx 0.05 \ .$$

The solution was proposed in 1970 by Glashow, Iliopoulos and Maiani (GIM) [36]. By adding a fourth quark to the model the FCNCs disappear at tree level and loop contributions are suppressed by a factor $\propto (m_q/m_W)^2$. Equation (1.1) transforms to

$$\begin{pmatrix} d' \\ s' \end{pmatrix} = \begin{pmatrix} \cos\theta & \sin\theta \\ -\sin\theta & \cos\theta \end{pmatrix} \begin{pmatrix} d \\ s \end{pmatrix} \ ; \ \begin{pmatrix} u' \\ c' \end{pmatrix} = \begin{pmatrix} u \\ c \end{pmatrix} \ . \tag{1.2}$$

And indeed, the existence of the charm quark was confirmed in 1974 with the observation of the J/Ψ. Going back to our example, the $D^+ \to \pi^+ K^0$ and $D^+ \to \pi^+ \pi^0$ decay involves $c \to d$ and $c \to s$ transition respectively.

Table 1.1: Quark mass entering the QCD Lagrangian in the $\overline{\text{MS}}$ renormalization scheme. The up, down, strange, charm and bottom running masses are obtained from lattice simulations or effective approaches. The top pole mass is extracted from direct observations.

Quark	Mass, $\mu = 2$ GeV (MeV/c^2)	Quark	Mass, $\mu = \overline{m}_q$ (GeV/c^2)
up	2.15 ± 0.15	charm	1.275 ± 0.025
down	4.70 ± 0.20	bottom	4.18 ± 0.03
strange	93.5 ± 2.5	top	173.5 ± 1.0

Kobayashi and Maskawa extended idea to a third generation of quarks [37]:

$$\begin{pmatrix} d' \\ s' \\ b' \end{pmatrix} = \underbrace{\begin{pmatrix} V_{ud} & V_{us} & V_{ub} \\ V_{cd} & V_{cs} & V_{cb} \\ V_{td} & V_{ts} & V_{tb} \end{pmatrix}}_{V_{\text{CKM}}} \begin{pmatrix} d \\ s \\ b \end{pmatrix} \; ; \; \begin{pmatrix} u' \\ c' \\ f' \end{pmatrix} = \begin{pmatrix} u \\ c \\ t \end{pmatrix} \; , \qquad (1.3)$$

where V_{CKM} is a 3×3 unitary matrix called the Cabibbo-Kobayashi-Maskawa (CKM) matrix. It can be parametrized by three angles and one phase which is the only source of CP violation in the electroweak sector.

As a side note, the neutrino oscillation is now a well-established fact; this implies that the neutrinos are massive. The SM does not account for that and there is no consensus on the underling mechanism. However, one can introduce the Pontecorvo-Maki-Nakagawa-Sakata (PMNS) matrix which plays a similar role as the CKM matrix but for the leptons.

On a more fundamental level, it is the *Yukawa* interaction between the Higgs and the fermions that is responsible for the quark mixing. The mass terms arise from the spontaneous breaking of the electroweak symmetry. The study of the CKM matrix is a central element in our understanding of the electroweak interaction. In the SM, the Yukawa sector is parametrized by V_{CKM} and the six quarks masses.

The CKM matrix elements have been extracted from various measurements [38], they are highly hierarchical. The magnitude of the elements governing the transitions within the same generation, between first and second generation, between first and third generation and between second and third generation are $\propto 1$, $\propto 10^{-1}$, $\propto 10^{-3}$ and $\propto 10^{-2}$ respectively. Similarly, the quark masses are not predicted by the model. Except for the top, all the quark masses have been determined using lattice QCD computation or effective approaches [38]. The masses are tabulated in Table 1.1.

The CP violation was first observed in $K \to \pi\pi$ decays; the magnitude the effect is usually quantified by two complex numbers, ε and ε'. Specifically, $\text{Re}\,(\varepsilon)$ is related to the *indirect* CP violation which is caused by the $K^0 - \overline{K^0}$ mixing whereas $\text{Re}\,(\varepsilon')$ is connected to the *direct* CP violation which involves the decay amplitudes. In the large N limit (N being the number of colors), the standard model prediction for $\text{Re}\,(\varepsilon)$ is quite compatible with its experimental

value and clearly favors a large value of $|V_{cb}|$, as extracted from inclusive decays [39]. In practice, it is more convenient to work with the ratio $\mathrm{Re}\,(\varepsilon'/\varepsilon) \approx \varepsilon'/\varepsilon$. See ref. [40] for a review of the topic.

The ratio was measured by NA48 and KTeV in the 90s:

$$\frac{\varepsilon'}{\varepsilon} = (16.6 \pm 2.3) \times 10^{-4} \ . \tag{1.4}$$

The non-zero value confirms the presence of direct CP violation in the kaon system. The theoretical prediction is complicated by the presence of non-perturbative QCD effects. Recently, progresses have been made and the standard model prediction in the large N limit reads now [41, 42]:

$$\frac{\varepsilon'}{\varepsilon} = (8.6 \pm 3.2) \times 10^{-4} \ . \tag{1.5}$$

We immediately notice a tension; this has not been solved so far. The correlation between ε'/ε and $K^+ \to \pi^+ \nu\overline{\nu}$ will be discussed in Section 1.1.3.

Thanks of the unitarity of V_{CKM} we can write the following equation:

$$V_{ud}V_{ub}^* + V_{cd}V_{cb}^* + V_{td}V_{tb}^* = 0 \ . \tag{1.6}$$

Five similar relations can be constructed; they all correspond to a triangle in a complex plane. The Equation (1.6) is called the $b \to d$ unitary triangle or simply the unitary triangle (UT). The UT is best visualized using the Wolfenstein approximate parametrization [43]:

$$V_{\mathrm{CKM}} = \begin{pmatrix} 1 - \frac{\lambda^2}{2} & \lambda & A\lambda^3 \left(\rho – i\eta\right) \\ -\lambda & 1 - \frac{\lambda^2}{2} & A\lambda^2 \\ A\lambda^3 \left(1 - \rho - i\eta\right) & -A\lambda^2 & 1 \end{pmatrix} + \mathcal{O}\left(\lambda^4\right) \ ,$$

where λ, A, ρ and η are real parameters that need to be measured. The CP violation is encoded by η.

The redefinition of the ρ and η parameters:

$$\overline{\rho} = \rho\left(1 - \frac{\lambda^2}{2}\right) \ , \ \overline{\eta} = \eta\left(1 - \frac{\lambda^2}{2}\right) \ , \tag{1.7}$$

allows to include terms of $\mathcal{O}\left(\lambda^5\right)$ in the expansion [7]. Using this parametrization, the Equation (1.6) can be represented as a triangle in the $(\overline{\rho}, \overline{\eta})$ plane. The unitary triangle (UT) extracted from the data is plotted in Figure 1.2; it is one of the most important test of the electroweak sector of the SM. A global fit including all available measurements gives [38]:

$$\lambda = |V_{us}| = 0.22537 \pm 0.00061 \ , \ \ A = 0.814^{+0.023}_{-0.024} \ , \tag{1.8}$$

$$\overline{\rho} = 0.117 \pm 0.021 \ , \ \ \overline{\eta} = 0.353 \pm 0.013 \ . \tag{1.9}$$

Note that they are unresolved tensions between the inclusive and exclusive measurement of $|V_{ub}|$ and especially $|V_{cb}|$. Nevertheless, both sources are included in the fit.

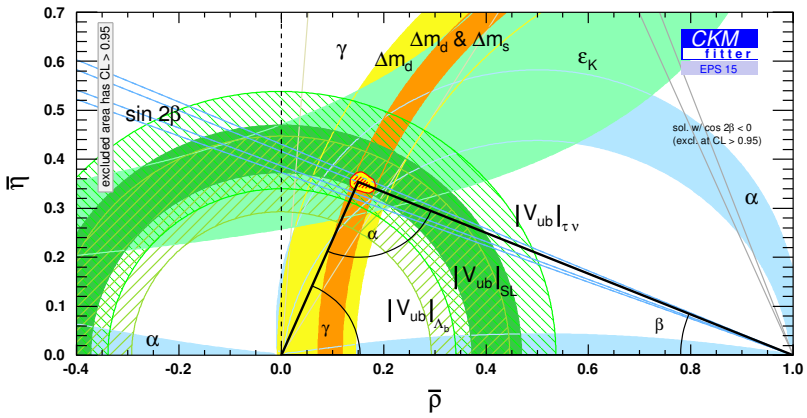

Figure 1.2: Constraints in the $(\overline{\rho}, \overline{\eta})$ plane [44], updated results and plots available at: `http://ckmfitter.in2p3.fr`. Testing the unitarity of the CKM matrix is an important constancy check of the SM.

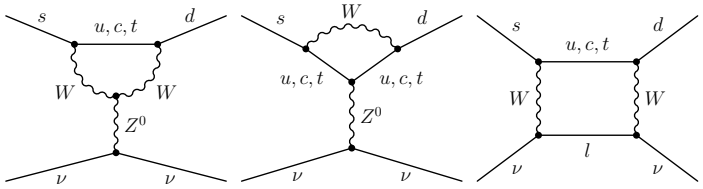

Figure 1.3: $K \to \pi\nu\overline{\nu}$ topologies in the SM.

The relation between the three CKM angles, α, β and γ, and $\overline{\rho}$ and $\overline{\eta}$ can be found in Ref. [7]. Any inconsistencies in the UT picture would be the sign of BSM physics.

So far no experimental measurements have been able to contradict this picture. Nevertheless, there are some tensions between observations and SM predictions. DØ observed an anomalous like-sign dimuon charge asymmetry in B^0 decays [45]. The discrepancy between the SM and the measurement was later reduced [46] but not completely eliminated. If confirmed, it could be the sign of anomalous CP violation in the mixing of neutral B-mesons. LHCb reported an anomaly in the angular analysis of the $B^0 \to K^{0*}\mu^+\mu^-$ decay [47]. However, a recent measurement by CMS is in good agreement with standard model predictions [48]. Finally, the measured values of the anomalous magnetic moment of the muon [49] and of the ε'/ε ratio are in slight disagreement with the SM predictions.

1.1.2 $K^+ \to \pi^+\nu\overline{\nu}$ Branching Ratio

The $K \to \pi\nu\overline{\nu}$ decays are represented by the "penguin" and "box" diagrams shown in Figure 1.3. The branching ratio, summing over the three neutrino

Table 1.2: Parameters entering in the $K^+ \to \pi^+ \nu\overline{\nu}$ branching ratio [8].

X_t	1.481 ± 0.009
P_c	0.365 ± 0.012
$\delta P_{c,u}$	0.04 ± 0.02
Δ_{EM}	-0.003
κ_+	See the Equation (1.11).

flavours reads [50]:

$$\mathcal{B}\left(K^+ \to \pi^+ \nu\overline{\nu}\right) = \kappa_+ \left(1 + \Delta_{\mathrm{EM}}\right) \left[\left(\frac{\mathrm{Im}\, \lambda_t}{\lambda^5} X_t\left(x_t\right) \right)^2 + \left(\frac{\mathrm{Re}\, \lambda_c}{\lambda} \left[P_c + \delta P_{c,u}\right] + \frac{\mathrm{Re}\, \lambda_t}{\lambda^5} X_t\left(x_t\right) \right)^2 \right] , \quad (1.10)$$

where $\lambda_i = V_{is}^* V_{id}$, $x_t = m_t^2 / M_W^2$. The parameter $\Delta_{\mathrm{EM}} \approx -0.3\%$ encodes the QED long distance radiative corrections [9].

$$\kappa_+ = (0.5173 \pm 0.0025) \times 10^{-10} \left(\frac{|V_{us}|}{0.225} \right)^8 , \quad (1.11)$$

summarises the long-distance contributions extracted from the $K^+ \to \pi^0 e^+ \nu_e$ decay [9].

The function X_t encodes the top quark contribution. It includes NLO QCD corrections [51] and NLO electroweak corrections [22]. Similarly, P_c and $\delta P_{c,u}$ summarise the short- and long-distance charm quark contributions respectively. They account for 30 percent of the decay amplitude. P_c contains NNLO QCD corrections [52] and NLO electroweak corrections [53]. The best estimation of the long-distance effect was provided by Isidori, Mescia and Smith [54]. The parameters are grouped in Table 1.2.

The Equation (1.11) highlights the connection between the $K^+ \to \pi\nu\overline{\nu}$ decay and the CKM matrix. The relation appear clearly using the Wolfenstein parametrization defined above. The factor $\lambda_c = V_{cs} V_{cd}$ is fully determined by λ which is known with a very good accuracy. On the other hand, $\lambda_t = V_{ts} V_{td}$ has a larger uncertainty. The problem can be reversed, by knowing the value of $\mathcal{B}\left(K^+ \to \pi^+ \nu\overline{\nu}\right)$ and λ, λ_t can be computed. Furthermore, the relation $|V_{ts}| \approx -|V_{cb}| = A\lambda^2$ can be used to extract the value of V_{td} from $\lambda_t = V_{ts} V_{td}$ assuming the value of A. Details and precise formulae can be found in ref. [50].

The CKM matrix can be completely determined from the branching ratios of the $K_L \to \pi^0 \nu\overline{\nu}$ and $K^+ \to \pi^+ \nu\overline{\nu}$ decays [21]. This is of prime interest since it would allow to test the constancy of CKM picture independently of the B meson system observables.

The Equation (1.11) can be parametrized in terms of the CKM parameters

Table 1.3: Error budget of the parameters entering in the $K \to \pi\nu\overline{\nu}$ branching ratio computation [8].

Quantity	Error budget (%)	Comment
$\lvert V_{cb}\rvert$	9.9	–
γ	6.7	–
P_c	1.8	Charm quark contribution [55]
$\delta P_{c,u}$	2.9	Long distance charm-quark contribution [54]
X_t	0.9	Top-quark contribution [22]
Other	0.5	–

[8]:

$$\mathcal{B}\left(K^+ \to \pi^+\nu\overline{\nu}\right) = (8.39 \pm 0.30) \times 10^{-11} \left[\frac{|V_{cb}|}{40.7 \times 10^{-3}}\right]^{2.8} \left[\frac{\gamma}{73.2^\circ}\right]^{0.74} . \tag{1.12}$$

This formulation highlights the $|V_{cb}|$ and γ dependence.

As highlighted in ref. [8] the CKM parameters entering in the amplitude can be determined in multiple ways. One can use tree-level observables which are likely not sensitive to hypothetical BSM effects but lead to less accurate predictions. Conversely, one can add constraints from loop level processes but then the SM prediction could be polluted by BSM contribution.

The theoretical error budget is summarized in Table 1.3. It is dominated by the CKM parameters. Any improvement on the determination of these values would have a direct impact on the branching ratio. To sum-up, the theoretical prediction of $K \to \pi\nu\overline{\nu}$ decay branching ratio reached a remarkable accuracy. A strong experimental effort is now needed to match the prediction.

1.1.3 Selected BSM Scenarios

As we already stressed, the $K \to \pi\nu\overline{\nu}$ decays are sensitive to BSM physics contributions. In this section, we will briefly review some recent studies, pointing to the original literature. The list of models presented is far from exhaustive.

Most of the SM extensions involve numerous new parameters. When looking for specific predictions, like branching ratios, it is often useful to impose a set of constraints to these models.

A common assumption is the minimal flavour violation (MFV) hypothesis. In this class of model, the CKM matrix is the only source of quark mixing and CP violation. One can also assume the existence of a new heavy gauge boson generically called the Z'. In general, this class of models allows for new sources of quark mixing and CP violation but one is free to add the MFV hypothesis. A good introduction to this type of model can be found in [56]. The phenomenology of $K \to \pi\nu\overline{\nu}$ in these models was recently extensively reviewed in [57]. Some fairly general scenarios predict the $K^+ \to \pi^+\nu\overline{\nu}$ decay branching

ratio to be above 20×10^{-11}. However, the allowed range for the branching ratio is greatly reduced if one adds simultaneously the MFV hypothesis and the constants from the $B_s \to \mu^+\mu^-$ decay and the ε'/ε ratio.

The $K \to \pi\nu\overline{\nu}$ branching ratio has also been computed for specific scenarios. We will briefly introduce three of them. First, the littlest Higgs models consider the Higgs as a pseudo-Goldstone boson of a spontaneously broken global symmetry [58, 59]. The $K \to \pi\nu\overline{\nu}$ decay was extensively reviewed in [60]. It appears that the branching ratio could be enhanced by a large factor.

Second, the minimal supersymmetric standard model (MSSM). In this model, fermions and bosons are related by a new symmetry. The $K \to \pi\nu\overline{\nu}$ decay could receive large contributions [61]. The branching ratio tends to be enhanced for light gluino masses but it can also be suppressed if the scale of the SUSY breaking is above 1 TeV.

Third, Randall and Sundrum (RS) model [62]. This model considers warped extra space-time dimension. Additional contributions from Kaluza-Klein modes on $K \to \pi\nu\overline{\nu}$ were investigated by [63]. A sizeable enhancements of the branching ratio is possible.

Finally, interesting correlations between the ε'/ε ratio and $K^+ \to \pi\nu\overline{\nu}$ in some models were pointed out [64]. Thanks to the recent progress in the theoretical prediction of the ratio, the combination of the ε'/ε and the $K^+ \to \pi^+\nu\overline{\nu}$ could allow to distinguish between difference BSM scenarios [57].

The Figure 1.4 sums-up the current situation. A precise measurement of both $\mathcal{B}(K^+ \to \pi^+\nu\overline{\nu})$ and $\mathcal{B}\left(K_L \to \pi^0\nu\overline{\nu}\right)$ branching ratio would be especially powerful to discover hints of new physics and eventually constraint the parameter space. It was pointed out that if we authorise general flavour-violating couplings, mechanism up to 1000 TeV could be probed [6].

1.1.4 Experimental Status

The study of the $K^+ \to \pi^+\nu\overline{\nu}$ decay is not new. The first experimental search for the decay took place in 1969 when experimentalists were looking for neutral currents. Camerini et al. looked at decays of kaons stopped in a bubble chamber filled with Freon and placed in a magnetic field [23]. The collaboration established the basic experimental techniques used in subsequent stopped kaon experiments. Three main criteria were used to disentangle the signal from the other backgrounds. First, a pion decaying at rest had to correspond to each stopped kaon. The pions were identified thanks to the $\pi^+ \to \mu^+ \to e^+$ chain reaction. Second, no detector activity compatible with photons could be seen. Third, the π^+ momentum, calculated by looking at its range, had to be away from the peaks corresponding to the $K^+ \to \mu^+\nu_\mu$ and $K^+ \to \pi^+\pi^0$ decays. The group reported $\mathcal{B}(K^+ \to \pi^+\nu\overline{\nu}) < 5 \times 10^{-5}$ with a 63 percent confidence level.

Two subsequent stopped kaon experiments were carried on at the Berkeley's Bevatron [24, 25], the advances of the electronics allowed them to record more

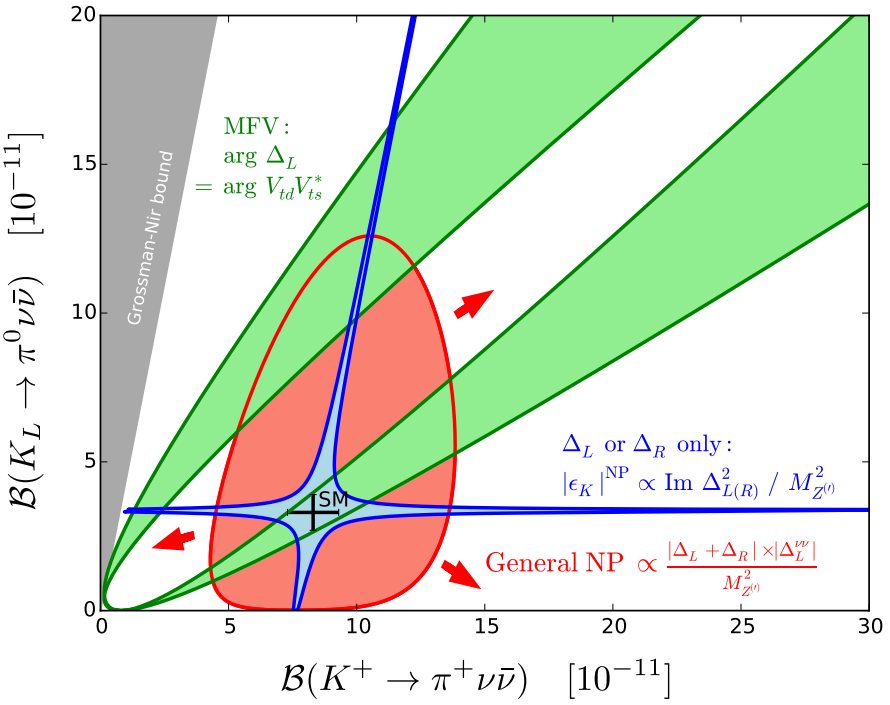

Figure 1.4: Correlations between the $K \to \pi\nu\bar{\nu}$ decays. Δ represent new flavour violating couplings. Reprinted from [57].

kaon decays. The incoming particles were stopped in scintillation counters surrounded on one side by spark chambers and on the other side by lead glass Čerenkov counters. A stack of scintillation counters placed on top of the spark chambers was used to determine the range of the produced pion. A Čerenkov detector identified the pions and the kaons in the beam. The groups used the same criteria as the experiment of Camerini et al. to select the signal. They lowered the upper limit to 5.6×10^{-7} with a 90 percent confidence level.

A similar geometry was used by Asano et al. at KEK [26]. The spark chambers were replaced by multi-wire proportional chambers otherwise the analysis technique was similar as the three previous experiments. The group set the upper limit for the branching ratio at 1.4×10^{-7} with a 90 percent confidence level.

The E787 experiment and its successor, E949, moved to a "4π" solid angle coverage [65] by equipping both detector hemispheres with drift chambers and stacks of scintillators. The whole apparatus was placed inside a uniform 1 T magnetic field directed along the beam axis. The experiment benefited from a 790-710 MeV/c beam composed of 75 percent of kaons. Kaons were stopped in an active segmented target build with scintillating fibres. The photon rejection was assured by electromagnetic calorimeters placed between the target and the drift chambers. The particle momentum was extracted from the bending radius and from the number of triggered scintillator layers. A Čerenkov detector identified and tagged the beam particles. Combining their datasets, E787 and E949 reported the observation of seven $K^+ \to \pi^+\nu\overline{\nu}$ candidates and established the current best branching ratio measurement [66]:

$$\mathcal{B}\left(K^+ \to \pi^+\nu\overline{\nu}\right) = \left(1.73^{+1.15}_{-1.05}\right) \times 10^{-10} \ .$$

A good review of the analysis techniques used by the E787 and E949 collaborations can be found in [67].

1.2 NA62 Experiment

The previous stopped kaon experiments were mainly limited by the $K^+ \to \pi^+\nu\overline{\nu}$ signal acceptance and by the number of kaons stopping in the target. As an illustration, the E949 collaboration reached a total acceptance equal to $(1.37 \pm 0.14) \times 10^{-3}$ and about one-quarter of the beam kaons were stopped by the target.

NA62 is the first decay-in-flight experiment dedicated to the study of the $K^+ \to \pi^+\nu\overline{\nu}$ decay. The experiment is hosted in the CERN North Area where it takes advantage of the high intensity SPS proton beam.

The setup layout was optimized to achieve a rejection factor of the order of 10^{12} for the main kaon decay modes while keeping the $K^+ \to \pi^+\nu\overline{\nu}$ acceptance around ten percent. The technique is based on four basic principles. First, an accurate kinematic reconstruction of the decays as it gives a strong handle on the background signals through the squared missing mass (m^2_{miss}) variable.

Table 1.4: Nominal beam characteristics at the third GigaTracker station position. The muon halo refers to the muons travelling outside of the hadron beam envelope.

Characteristic	Value
Instantaneous hadron rate	750 MHz
Instantaneous muon rate	5 MHz
Instantaneous muon halo rate	2.5 MHz
Divergence (X-axis/Y-axis)	0.09 mrad / 0.10 mrad
Spot size	27.5 mm $\times$ 11.4 mm

Second, the photon and muon rejection over a large range of angles by means of calorimetry measurements and particle identification. Third, a high level of redundancy; it is fundamental to achieve the required background rejection power. Finally, the accurate time tagging of the kaons and their decay products is mandatory to reconstruct the events and identify any accidental activity in the detector.

At the time of writing the performances of many subdetectors were still under study. In the following sections, if there are no published figures available, we report first conservative estimates. The reader is invited to refer to [13] for a complete description of the subdetectors and of the trigger and data acquisition system.

1.2.1 Beam and Vacuum

The primary 400 GeV/c proton extracted from the SPS are first directed to the T4 target, a 300 mm long beryllium plate. About 50 percent of the primary protons cross the target, however, the beam is spread out because of the multiple scattering in the plate. The remaining protons are guided towards a pair of motorized collimators capable of absorbing the full beam (Target Attenuator eXperimental area, TAX). They control the amount of protons transmitted to the T10 target, a 400 mm long beryllium cylinder, via the *P42* beam line. The infrastructure was dimensioned to sustain an instantaneous rate of 1.1×10^{12} protons per second (pps) on T10. Assuming a 0.8 transmission factor for TAXs in front of P42 beam line, 1.1×10^{12} protons on T10 requires 2.75×10^{12} protons on T4.

The target marks the beginning of the *K12* line that is under the control of the experiment, two TAXs are placed immediately after it. They can be moved to control the secondary beam intensity. After the TAXs, a series of magnets and collimators form a well-defined +75 GeV/c $\pm$ 1% mixed hadron beam. The nominal beam composition is 71 percent pions, 23 percent protons and 6 percent kaons, tungsten absorbers reduce the positron component to a negligible level. During the 2014 run, the SPS supercycle was 30 to 42 seconds long with two 5 seconds cycles allocated to NA62. The main characteristics of

the beam are tabulated in Table 1.4.

The right-handed Cartesian coordinate system of the experiment is defined as follow: the origin of the reference frame is the centre of the production target (T10), the X-axis points to the Jura mountains, the Y-axis is oriented towards the zenith and the Z-axis follows a straight line from the centre of the T10 target to the centre of the downstream end of the *LKr* beam pipe.

Forty centimetres before the last GigaTracker station, a small magnet (TRIM-5) deflect the beam by an angle of 1.2 mrad in the X-axis direction. Between the two first and two last *STRAW* chambers a 3.2 m aperture dipole magnet (MNP-33) provides a -270 MeV/c momentum kick in the X-axis direction. Finally, the beam is deflected by an angle of -13.6 mrad in the X-axis direction by 2 m long dipole magnet (MBPL-TP) to keep the beam particles out of the *SAC* acceptance. A complete description of the secondary beam line can be found in [13].

The NA62 vacuum is divided in seven sectors, from the T10 target to the beam dump. The GigaTracker, the *CHANTI*, the STRAW and part of the *LAV*s are operated inside the vacuum. A complex setup of turbopumps and cryopumps keep the pressure in the fiducial volume around 10^{-6} mbar.

1.2.2 Detectors

The NA62 setup (see Figure 1.5) is divided into three parts: first, the *upstream region*, in which the secondary beam is tracked and the kaons are tagged; second, the 60-meter-long evacuated *fiducial volume*, which defines the decay acceptance region; and third, the *downstream region*, in which the properties of the decay products are tracked and identified. The beam particles fly through the last region inside a beam pipe, without interacting with the detectors. We will now describe the different subdetectors.

Particle Identification

The KTAG identifies and accurately time tags the kaons present in the secondary beam with an efficiency higher than 95 percent. The Čerenkov differential counter is the first detector encountered by the beam. An adjustable diaphragm can be configured to only let through the Čerenkov light emitted by 75 GeV/c kaons; this reduces the hit rate from 750 MHz to a more manageable 50 MHz. The hit time resolution is of the order of 100 ps.

A large ring-imaging Čerenkov detector (RICH) detector installed after the STRAW spectrometer helps to separate the pions from the muons in 15 GeV/c and 35 GeV/c momentum range. Moreover, it accurately time tags the charged tracks and, therefore, plays a key role in the kaon-pion track matching. The hit time resolution is better than 100 ps.

The *LKr* electromagnetic calorimeter and the *MUV1* and *MUV2* hadronic calorimeters complement the particle identification.

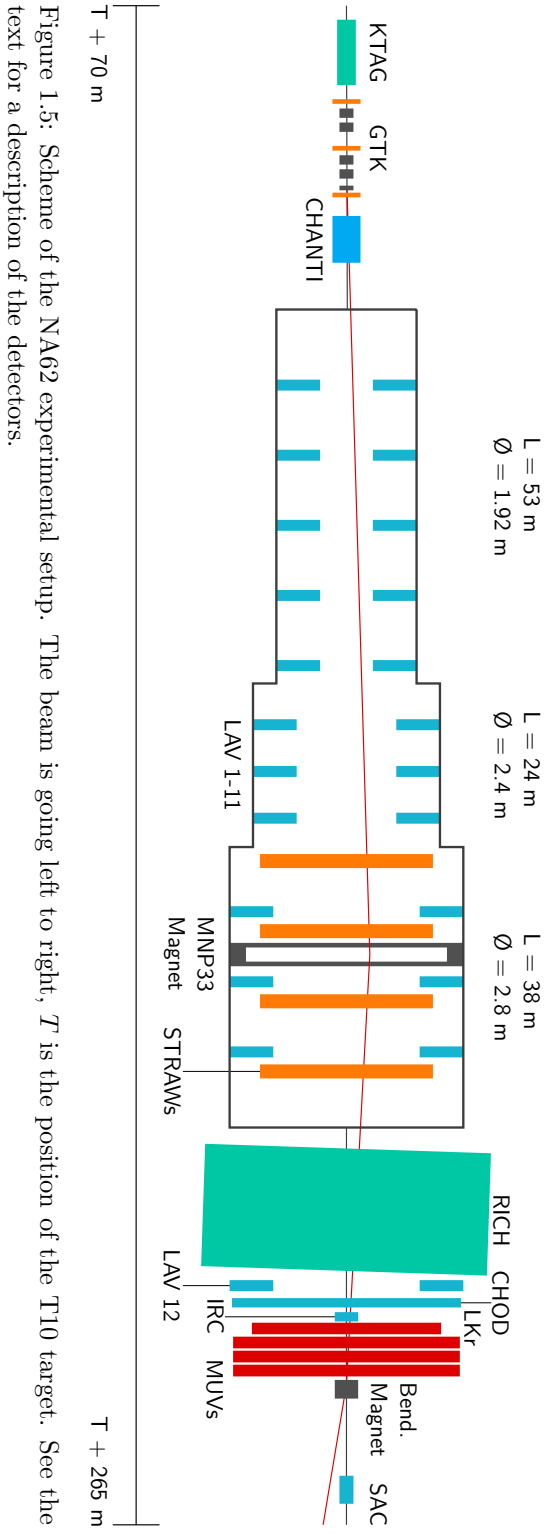

Figure 1.5: Scheme of the NA62 experimental setup. The beam is going left to right, T is the position of the T10 target. See the text for a description of the detectors.

Photon Rejection

The 35 GeV/c upper momentum cut on the reconstructed pion tracks (see above) guarantee that the π^0s originating from the $K^+ \to \pi^+\pi^0$ decays have a momentum above 40 GeV/c. The detection inefficiency must be below 10^{-8} for the corresponding photons.

Twelve large angle veto (LAV1-12) calorimeters cover the 8.5–50 mrad range around the beam axis. The stations are made of stacked rings of lead glass counters. Eleven vetoes are disposed around the fiducial volume; the twelfth station is placed after the RICH. The LAVs hit time resolution is of the order of 1 ns.

Similarly, the liquid krypton (LKr) electromagnetic calorimeter covers the 1–8.5 mrad range. Thanks to the excellent uniformity of the medium and to the fine granularity electrodes the detector has an excellent energy and position resolution [68]:

$$\frac{\sigma\left(E\right)}{E} = \frac{3.5\%}{\sqrt{E}} \oplus \frac{40\ \text{MeV}}{E} \oplus 0.5\% \ ,$$

$$\sigma_x = \left(\frac{4.2}{\sqrt{E\ (\text{GeV})}} \oplus 0.6\right)\ \text{mm} \ , \quad \sigma_y = \left(\frac{4.3}{\sqrt{E\ (\text{GeV})}} \oplus 0.6\right)\ \text{mm} \ .$$

Its time resolution is below 500 ps. The LKr is already very well understood as it was previously part of the NA48 setup.

Finally, two smaller sampling calorimeters covers the < 1 mrad region. The intermediate ring calorimeter (IRC) is placed immediately before the LKr and, to complete the coverage, the small angle calorimeter (SAC) is installed after the MBPL-TP magnet. The SAC is centred on the non-deviated beam axis, therefore, it is not affected by the charged beam particles but sensitive to the photons travelling inside the beam pipe. The SAC and the IRC time resolution is below 2 ns.

Muon Rejection

A series of calorimeters complement the muon rejection power provided by the RICH and the LKr. The muons are identified based on the amount of energy deposed and on the showers shape.

The muon veto system is composed of three independent subdetectors called the muon veto 1, 2 and 3 (MUV1, MUV2, and MUV3); they are all installed behind the LKr. MUV1 and MUV2 are standard sampling calorimeters formed by iron plates interleaved with scintillator strips. MUV3 is composed of scintillator tiles disposed behind an 80 cm thick iron wall. The muon vetoes have a time resolution below 1 ns.

Particle Tracking

As we saw in the introduction, 90 percent of the kaon decays can be constrained using the squared missing mass; it is a powerful handle to discriminate many of the background signals. It is defined as

$$m^2_{\text{miss}} = (p_K - p_\pi)^2 \tag{1.13}$$

$$\approx m_K^2 \left(1 - \frac{|p_\pi|}{|p_K|}\right) + m_\pi^2 \left(1 - \frac{|p_K|}{|p_\pi|}\right) - |p_\pi||p_K|\theta^2_{\pi K} \ , \tag{1.14}$$

where $\theta_{\pi K}$ is the angle between the reconstructed kaon track and the reconstructed pion track. To reach a sufficient resolution the tracking of the beam is mandatory.

The secondary beam particles momentum and direction are measured by the GigaTracker (GTK) that is installed just upstream of the fiducial volume. The detector is described in more details in Section 3.1.

The kaon decay products momentum and direction are measured by the STRAW tracker. The spectrometer is composed of four independent chambers, two on each side of the MNP-33 magnet. The chambers are made of four stacked *views*, each rotated by 45° with respect to the others. One view is composed by four staggered layers of 112 parallel *straws*. The straws are 9.8 mm diameter, 210 cm long and 36 µm thick PET tubes coated with two thin layers of Cu and Au and filled with a mixture of Ar (30 percent) and CO_2 (70 percent). A gold-plated tungsten wire runs in the middle of the tubes and serves as anode. The material budget of a single chamber is below $X/X_0 < 0.5\%$.

Accidental Events Rejection

Three subdetectors are dedicated to the detection of the interactions between the secondary beam and the subdetectors, the beam pipe, the residual gas, etc.

The charged ANTI (CHANTI), placed downstream of the GigaTracker, detects the charged particles resulting from inelastic interactions in the last GigaTracker station. It is composed of six groups of scintillator bars arranged to form a hollow rectangular shape with a central gap of 90 mm by 50 mm.

The charged hodoscope (CHOD) help to flag the inelastic interactions that can happen in the RICH mirrors. It is installed between the RICH and the LKr. The CHOD was partially recycled from the NA48 setup, it is made of two layers of scintillator strips. It will be complemented by an assembly of scintillator tiles that will be installed before for 2016 run. The CHODs have a time resolution of the order of 1 ns.

1.2.3 Data Acquisition and Trigger

The architecture of the trigger and data acquisition system is summarized in Figure 1.6.

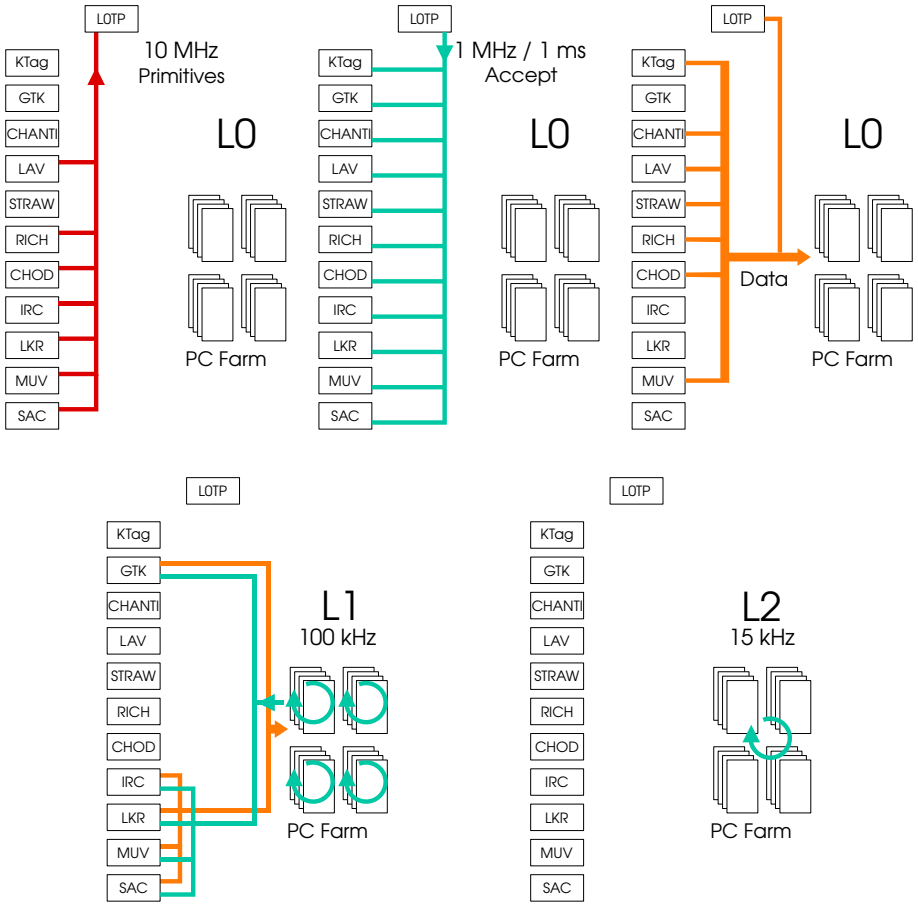

Figure 1.6: Schematic representation of the trigger decisions chain. The sequence is going from left to right and from top to bottom. The detectors participating to the level zero (L0) trigger decisions send *primitives* to a level zero trigger processor (L0TP). If some pre-programmed condition is matched, the L0TP propagates back a L0 trigger accept signal to the detectors. Upon reception of the signal the data are transfered to the PC farm where level one (L1) and level two (L2) algorithms are running. The L1 algorithms can use all the data coming from a single subdetector to take a decision. Notice that the GigaTracker and the LKr buffer locally the data while waiting for a L1 decision. The L2 trigger algorithms have access to the whole events, in case of a positive decision, the data are stored on disk.

Table 1.5: Design parameters of the trigger system.

	Level zero	Level one	Level two
Input rate	10 MHz	–	–
Output rate	1 MHz	100 kHz	15 kHz
Input latency	50–100 µs	–	–
Output latency	1 ms	Burst duration	Inter-burst duration

KTAG, CHANTI, the LAVs, STRAW, RICH, CHOD and MUV3 are read out by a unified system build around *TEL62* motherboards. Depending on the requirements, up to four daughter boards can be plugged in. Each *TDCB* daughter board interfaces four HPTDC chip [69]. The TEL62 memory buffers store the hits while waiting for a L0 trigger accept signal. The IRC, the SAC, the LKr, the MUV1 and the MUV2 are read out by *CREAM* boards [70]. Each module provides 32 channels connected to 14-bit 40 Msamples/s ADCs. The boards buffers the data while waiting for a L1 trigger decision. In parallel, it provides energy sums for triggering purposes. GigaTracker uses its own readout chain that will be detailed in Section 3.1.6.

The interesting events are selected by a three-level fully digital trigger. The first level (level zero or L0) is implemented on FPGAs. The LAVs, the STRAW, the RICH, the CHOD, the LKr and the MUV3 TEL62s are programmed to generate and send simple *primitives* to the level zero trigger processor (L0TP). A primitive is the digital equivalent of an analogue trigger signal; when a given set of conditions are met, a 32-bit word is built and immediately transmitted. The conditions are programmable; for instance, it can be hit multiplicities or coincidences between channels. The readout boards can assert a chock/error line if needed; however this feature has not been tested during the 2014 run. The TEL62s apply subdetector-dependent time offset to the primitives it generates to ensure that they are all time aligned.

The L0TP stores the primitives from each subdetector in a RAM at the address defined by the trigger time. Next, it combines them and it looks for matching conditions. For each match (or *event*), the L0TP sends a L0 trigger accept signal to all the subdetectors after a fixed latency of 1 ms. A 32-bit timestamp is assigned to the event using the time attached to the primitive coming from the reference detector. In response to the trigger accept signals, all the subdetectors except LKr must send the corresponding hits to a PC farm for further evaluation. The LKr readout stores the data waiting for a L1 trigger decision.

The level one (L1) and level two (L2) trigger algorithms run on an off-the-shelf PC farm. The L1 routines have access to the complete data stream of individual subdetectors and can reconstruct higher level objects like tracks or clusters. Finally, the L2 algorithms combines the information from all the subdetectors to make the final decision on whether to store the event or discard it. A summary of the rates and the latencies is provided in Table 1.5.

During the 2014 pilot run, only a partial version of the L0 was commissioned. Instead of primitives, traditional NIM signals were feed to the L0TP. If programmable coincidence (or anti-coincidence) conditions were met, the L0 trigger accept signal was sent. An artificial dead time of 1.6 µs between two consecutive triggers had to be introduced to avoid TEL62 crashes. Moreover, the beam rate had to be limited to 10 to 20 percent of the nominal intensity. The L0 primitive generation and matching, and the L1 and L2 algorithms were commissioned during the summer of 2015.

1.3 Summary and Discussion

The $K^+ \to \pi^+\nu\overline{\nu}$ decay is forbidden at tree level in the standard model (SM). The amplitude is further suppressed by the CKM elements at play. As a result, the decay branching ratio is of the order of 10^{-10}. Thanks to the GIM mechanism, the process is dominated by short-distance contributions. Furthermore, the matrix element can be extracted from the $K^+ \to \pi^0 e^+ \nu_e$ decay. As as consequence, the theoretical control on the amplitude is outstanding.

The theoretical cleanness and the tiny branching ratio make of the $K^+ \to \pi^+\nu\overline{\nu}$ decay an ideal channel to look for beyond the standard model (BSM) effects. Indeed, large enhancement of the branching ratio with respect to the SM are predicted by some scenarios. Moreover, a competitive value of the CKM parameter $|V_{td}|$ could be extracted from the branching ratio if the relative uncertainty is kept below ten percent. Remarkably, a measurement of the complementary $K_L \to \pi^0\nu\overline{\nu}$ decay branching ratio would allow to check the consistency of the CKM matrix unitarity in an independent way of the B meson system. It would also considerably reduce the parameter space available to the BSM scenarios.

The main motivation for the NA62 experiment is the search of beyond the standard model effects in the $K^+ \to \pi^+\nu\overline{\nu}$ decay. For that purpose, NA62 aims to collect about 10^{13} kaon decays in two years. This will be achieved with the help of a high intensity 75 GeV/c mixed hadron beam decaying in flight. The experiment was designed to keep a ten percent $K^+ \to \pi^+\nu\overline{\nu}$ signal acceptance while achieving 10^{12} rejection factor for the main kaon decays.

Both the initial and the final states particles are characterized. The excellent time resolution of the detectors is essential to disentangle the events within a bunch of particle. Finally, dedicated photons and muons vetoes detectors helps to control the backgrounds. The events kinematic reconstruction plays a key role in the background rejection. Full beam tracking capability is needed to guarantee a sufficient squared missing mass resolution. This role is fulfilled by the silicon pixel GigaTracker.

Pilot runs were conduced in autumn 2014 and during the second half of 2015. The first physics run will likely starts in April 2016.

Chapter 2

Silicon Pixel Detectors

Silicon pixel detectors have several advantages for particle tracking. To begin with, the sensor segmentation ensures a good hit position resolution. Furthermore, the large charge carrier mobility allows the detector to sustain substantial hit rates. Finally, the silicon ionization energy is very low compared to other detector technologies. This fact coupled with the high density of the medium guarantee a high signal to noise ratio.

Nonetheless silicon pixel detectors have drawbacks that need to be addressed. First, most silicon pixel sensors have no internal amplification and hence require advanced front-end electronics. In addition, because of their high channel count the pixel detectors are in general more demanding for the readout system. Second, the system integration is challenging; complex arrangements and interconnections are required to cover large surfaces since the sensor size is limited. Lastly, the thermomechanical integration is challenging, the readout chip power dissipation, the large number of signal and power lines, and the mechanical fragility of the detector assemblies must be taken into account.

In the first section of this chapter we gather important results related to the silicon pixel detectors operation and performances. Next, we detail the effects of radiation damage on the sensor; we use some of the results in the radiation hardness study of the GigaTracker sensors. Finally, we highlight the different contributions to the hit time resolution of a typical silicon pixel detector.

For the reader interested in silicon pixel detector good starting points are the books by Spieler [71] and Rossi, Fischer, Rohe and Wermes [72]. For a more complete treatment of the underling physics, the reader can refer to books by Kittel [73] and Sze [74].

2.1 Detector Operation

Nowadays, the pixel silicon detector can be divided into two main families: the *hybrid* detectors where the sensor and the readout electronics are implemented on distinct wafers and the *monolithic* detectors where the sensor and readout electronics are placed on the same wafer. The hybrid approach allows for high density electronics and therefore smart readout chips. Furthermore, the sensor-readout chip assembly, typically realized by flip chip bonding, is expensive. The monolithic detectors can be made extremely thin, for instance the Belle II PDX material budget is 0.21% of X_0 [75]. In addition, the pixels can be made very small since there is need for sensor-readout chip bonding. The readout electronics complexity is however limited.

In this section, we will focus on hybrid detectors. To begin with, we briefly introduce essential points related to the sensor operation: the bulk doping, the charge carrier generation and recombination, the leakage current, the depletion region and the pixel capacitance. Next, following a bottom-up approach, we outline how the energy loss in the sensor is turned in a usable analogue signal. When appropriate, we will illustrate the formulae with examples inspired from the GigaTracker.

2.1.1 Sensor Operation

Most of the sensor are made from Float-Zone grown silicon crystals. This process produces wafers with a very low level of impurities and therefore a high resistivity (> 1 kΩ cm). To form sensors, a controlled amount of dopant, typically electron acceptors like boron (p-type bulk) or electron donors like phosphorus (n-type bulk), is added to the crystal during the fabrication stages. p- or n-type implants are added later to complete the junctions. When working with sensors, it is convenient to define the *effective doping concentration*, N_{eff}, as the donor concentrations minus the acceptors concentration in the sensor bulk.

When two regions of same crystal are doped differently electrons diffuse from the n-type material to the p-type and vice versa for the holes. The ionized dopant atoms are fixed in the lattice; they induce an electric field that opposes to the diffusion. As some point a dynamic equilibrium is reached and a region free of charge carriers is established at the interface between the n-type and the p-type material.

Without any external field, the depletion region extends over a few micrometres. This region can be widened by applying a reverse bias to the device. i.e. positive voltage on n-type side or a negative voltage on p-type side. Neglecting the junction built-in voltage (0.3 – 0.6 V at 300 K for silicon), the voltage required to deplete a thickness w of silicon is

$$V_{\text{dep}} \approx \frac{w^2}{2\epsilon\mu\rho} \ , \tag{2.1}$$

where ρ is the silicon resistivity (Ω cm), $\epsilon = \epsilon_0 \epsilon_{\mathrm{Si}} = 1.054$ pF cm^{-1} is the silicon permittivity, μ is the mobility of the electrons (n-type bulk) or holes (for p-type bulk). Using

$$\rho = \frac{1}{N_{\mathrm{eff}} q \mu} \ , \tag{2.2}$$

where q is the elementary charge we can rewrite the Equation (2.1) as

$$w \approx \sqrt{\frac{2\epsilon}{e N_{\mathrm{eff}}} V_{\mathrm{dep}}} \ . \tag{2.3}$$

This last formula is useful, as it gives a relation between the thickness of the depleted region, the effective doping concentration and the bias voltage.

In semiconductors charge carriers are constantly created and annihilated in the bulk, this mechanism is partially responsible of the sensor leakage current and it affects the charge collection efficiency. Surfaces and interfaces also act as charge generation and recombination centres but their role is less important in the sensor performance. In silicon and for doping concentration up to $\approx 10^{18}$ cm^{-3} the Shockley-Read-Hall (SRH) recombination dominates. It involves indirect band transitions via recombination centres (*traps*) such as impurities and crystal defects. This effect is of primary importance for silicon detectors, indeed radiation damage can greatly increase the trap density and therefore significantly reduce the carrier's lifetime. A good review of generation and recombination in semiconductors can be found in ref. [76]. Typically, the recombination lifetime is of the order of 100 µs [77], much bigger than the usual charge collection time in silicon sensors which is of the order of nanoseconds up to tens of nanoseconds depending on the bias voltage.

The overall sensor leakage current has multiple sources: we have to distinguish the bulk current and the surface current. The surface current is caused by the chipping of the sensor edges, scratches on the silicon surface or simply contamination of the surfaces. It is independent of the temperature. The bulk current is induced by the charge carrier generation in the depleted region and by the diffusion of electrons and holes through the junction. The first component is proportional to the depleted volume and to the intrinsic charge carrier concentration and inversely proportional to the charge carrier lifetime. The bulk current strongly depends on the temperature (see below) and is proportional to the square root of the applied bias voltage.

It is often useful to scale the measured current from a temperature T_A to a temperature T_B (in Kelvin) [78] (p. 531):

$$I\left(T_B\right) = I\left(T_A\right) \left(\frac{T_B}{T_A}\right)^2 \exp\left\{-E_g \Big/ \left[2k_B \left(\frac{1}{T_B} - \frac{1}{T_A}\right)\right]\right\} \ , \tag{2.4}$$

where $k = 8.617 \times 10^{-5}$ eV K^{-1} is the Boltzmann constant and $E_g = 1.12$ eV is the silicon band gap energy. Typical values for non-irradiated silicon sensors varies from a few nA/cm^2 to a few µA/cm^2. These figures are strongly dependent on the device and on the operating conditions.

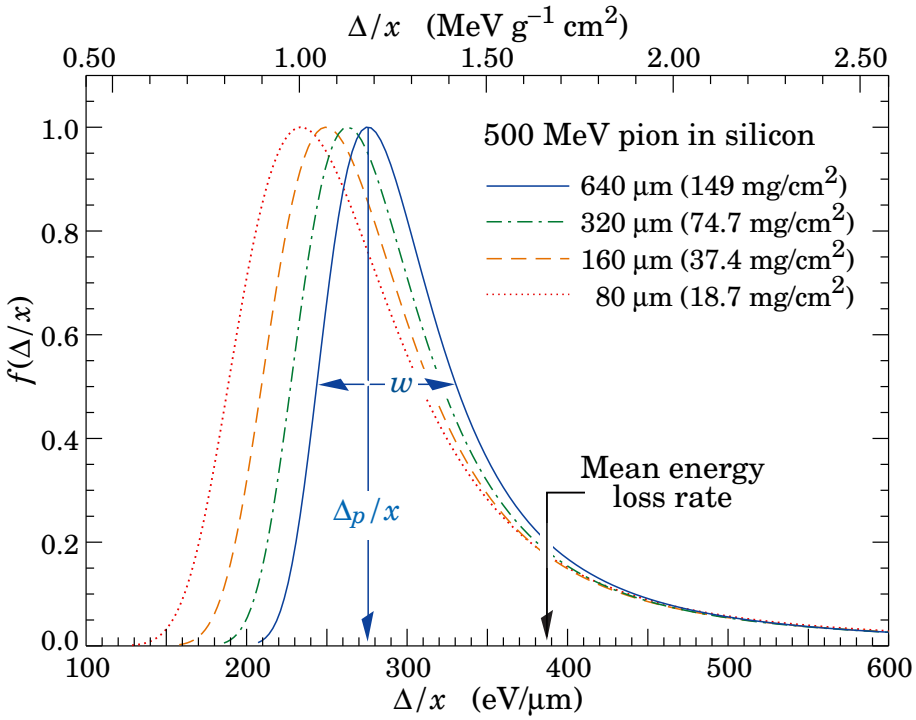

Figure 2.1: Straggling function normalized to unity at the most probable value (MPV) Δ_p/x. w corresponds to the full width at half maximum. Reprinted with permission from [38]. The MPV depends on the medium thickness; the distribution has a long tail due to rare but hard collisions.

As we will see, the pixel capacitance plays an important role in the noise characteristics of the detector and in the amount of signal crosstalk between adjacent pixels. It can be computed in good approximation using parallel plates with surface area A

$$C = \epsilon \frac{A}{w} \ , \tag{2.5}$$

and using Equation (2.3) we have

$$C \propto \begin{cases} \sqrt{\epsilon e N_{\text{eff}}/2V} \ , & V < V_{\text{dep}} \ , \\ \epsilon/d \ , & V > V_{\text{dep}} \ , \end{cases} \tag{2.6}$$

where d is the sensor thickness and V the bias voltage. The full depletion voltage can be extracted from the C-V curve, indeed, the capacitance C depends on the bias voltage only if for $V < V_{\text{dep}}$. For silicon pixel detectors with relatively large pixels (300 µm by 300 µm), the typical capacitance is a few hundreds fF.

2.1.2 Energy Loss in Silicon

We will focus on the energy loss of fast ($\beta > 0.25$) heavy charged particles in thin mediums (thickness $t < 3$ mm). We use the standard notations, all the variables are defined in ref. [38].

This class of particles predominantly losses energy via electromagnetic interactions. The mean energy loss is given by the Bethe formula; it is defined in ref. [38].

The amount of energy released by a single particle is subjected to large statistical fluctuations. The distribution, shown in Figure 2.1, has a long tail caused by rare hard high energy δ-rays; this phenomenon is called the *energy straggling*. As a consequence, the most probable energy loss is lower than the mean energy loss. The distribution depends on the detector thickness and on the particle velocity; it is especially relevant for thin silicon detectors.

The energy loss probability density function is often approximated by a Landau distribution. The most probable value is

$$\Delta_p = \xi \left[\ln \frac{2m_e c^2 \beta^2 \gamma^2}{I} + \ln \frac{\xi}{I} + j - \beta^2 - \delta \right] , \tag{2.7}$$

where $\xi = (K/2) \langle Z/A \rangle \left(x/\beta^2\right)$ MeV is the Laudau parameter, x is the absorber thickness in g cm^{-2} and $j = 0.200$ [79]. The width at half maximum w is roughly equal to 4ξ. In general, the Landau distribution overestimates the most probable energy loss and underestimates the width of the distribution. A more accurate energy-loss straggling function for thin medium which includes shell binding energies was derived by Bichsel [79].

Fast secondary electrons (δ-rays) can create clusters of hits in silicon pixel detector. Their energy spectrum is [80]:

$$\frac{\mathrm{d}^2 N}{\mathrm{d}T \mathrm{d}x} = \frac{1}{2} K z^2 \frac{Z}{A} \frac{1}{\beta^2} \frac{F(T)}{T^2} , \tag{2.8}$$

with, for spin-0 incident particles,

$$F(T_\delta) = 1 - \frac{\beta^2 T}{T_{\max}} . \tag{2.9}$$

This formula is valid for $T \gg I$ (mean excitation value, 173 eV for silicon). The average number of δ-rays with an energy between $T_{\min}$ and $T_{\max}$ is calculated by integrating the Equation (2.8) from $E = T_{\min}$ to $E = T_{\max}$ and from $x = 0$ to $x = \rho L$. We have

$$\langle n_\delta \rangle = \frac{1}{2} K z^2 \frac{Z}{A} \frac{\rho L}{\beta^2} \left[\frac{1}{T_{\min}} - \frac{1}{T_{\max}} \left(1 + \beta^2 \log \frac{T_{\max}}{T_{\min}} \right) \right] . \tag{2.10}$$

For a 75 GeV/c kaon traversing 200 µm of silicon, setting $T_{\min}$ to 22.5 keV, an average of 0.158 δ-rays are produced. Most of the δ-rays are low energy and are therefore emitted perpendicularly to the incident particle.

Table 2.1: Values of the parameters entering the Equation (2.13) at 300 K, fitted from data. Reproduced from [86].

	Electrons	Holes	Units
v_s	1.05×10^7	8.10×10^6	cm s^{-1}
E_C	7240	18000	V cm^{-1}
β	1.30	1.21	–

Simulation have shown that the δ-rays adds about 60 ps to the GigaTracker time resolution when the detector is biased at 300 V [81].

Charged particles traveling through the matter are scattered by Coulomb interactions with the nuclei. The total deflection angle is distributed as a Gaussian for small angle values. If we project the distribution on a plane, its width is parametrized by [38]:

$$\theta_{\mathrm{MS}} = \frac{13.6 \text{ MeV}}{\beta cp} z \sqrt{x/X_0} \left[1 - 0.038 \ln \left(x/X_0\right)\right] \ , \tag{2.11}$$

where z is the charge number of the incident particle, x is the material thickness in g/cm^2 and X_0 the radiation length of the material. The above formula is accurate to 11 percent or better for $10^{-3} < x/X_0 < 100$ [38]. For 75 GeV/c kaons crossing the GigaTracker detector the width of the distribution is about 10 µrad.

2.1.3 Signal Formation

The energy deposited by a particle in the sensor bulk creates electron-hole pairs. In silicon, the ionization energy is 3.6 eV [82].

The signal measured on the sensor electrodes is induced by the drift of the generated charge carriers in the sensitive volume. The instantaneous current can be computed using the Shockley-Ramo theorem [83, 84] that states that the current induced by a charge q moving at a velocity v on a given reading electrode is

$$i\left(t\right) = qE_v\left(\vec{x}\right) v\left(t\right) \ , \tag{2.12}$$

where E_v is the *weighting field* parallel to the **v** direction. The weighting field corresponds to the electrical field computed under simple boundary conditions, namely, the potential of the electrode of interest is set to unity while all the other conductors are grounded. As a corollary, charge carriers drifting in the high field regions contribute more to the current pulse.

The theorem was generalized to cases were electrodes are interconnected by a network of idealized electrical component connected perfectly conducting wires [85].

The charge carrier drift velocity as a function of the electric field parallel to $\langle 111 \rangle$ direction can be modelled with the following phenomenological expression

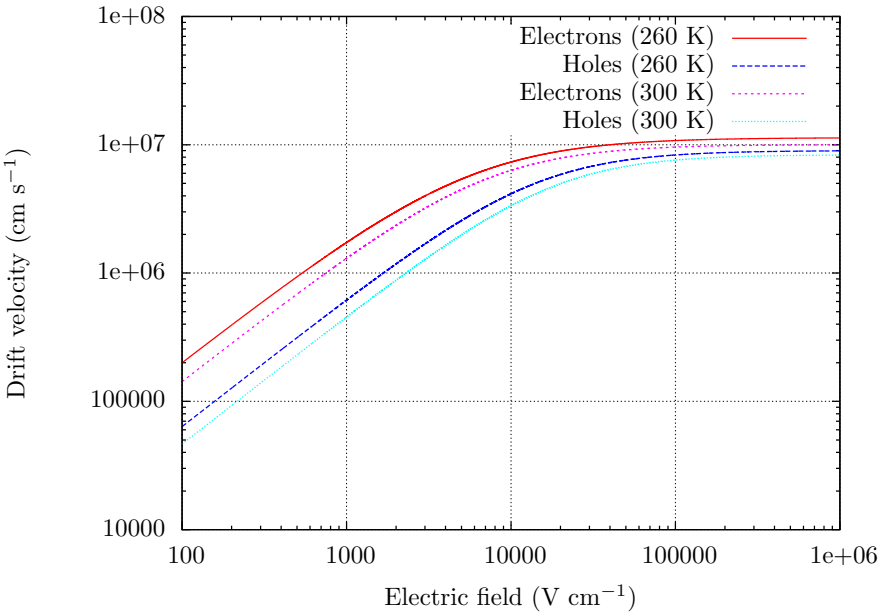

Figure 2.2: Charge carrier drift velocity in silicon at 300 K and 260 K.

[86]:

$$v_d = v_s \frac{E/E_C}{\left[1 + (E/E_C)^{\beta}\right]^{1/\beta}} \ . \tag{2.13}$$

The parameters entering the equation are extracted from measurement, they are assembled in Table 2.1. The drift velocity depends on the temperature; the full expression can be found in ref. [86]. The function is plotted in Figure 2.2.

2.1.4 Readout Electronics

The detailed implementation and performances of the front-end readout depend on the underlying technology. A complete description is out of the scope of this work nevertheless the idealized model presented in Figure 2.3 allow to understand the basic features.

A typical pixel front-end is divided into three stages: first, a *preamplifier*, second, a *pulse shaper* and finally a *comparator* (also called a *discriminator*). For each of these stages, many technical implementations are possible. We will now briefly detail each section of the circuit, when numerical values are given, they correspond to 75 GeV/c kaon crossing a 200 µm thick sensor operated at 300 V.

As we saw in section above, the energy deposited by a particle in the sensor bulk generates free charge carriers in the depletion region. Under the action of

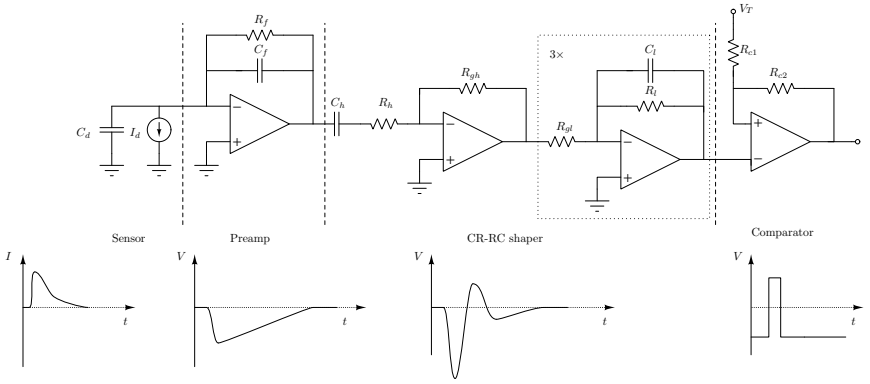

Figure 2.3: Idealized schematic of a typical analog pixel front-end. A sketch of the output signal is depicted below each stage. The charge release in the bulk is model by the I_d current source.

the electric field the carriers drift towards the pixel electrodes. This movement induce a short current pulse (few µA during a few ns) on top of the constant leakage current (a few hundreds nanoamperes). To sense this current, the pixel, represented by the C_d capacitor, is coupled to a charge sensitive preamplifier (preamp). A discharge resistor R_f avoids the preamp saturation by discharging the feedback capacitor C_f and absorbing the constant leakage current. Typical values for C_d, C_f and R_f are of the order of hundreds fF, tens fF and hundreds kΩ respectively. An important feature of charge sensitive preamplifier is that the gain is independent of the detector capacitance C_d. Indeed, the detector capacitance depends on the bias voltage and is influenced by the radiation damage. The Miller effect ensures that for the input signal C_f appears much bigger than C_d. This condition ensures a good charge collection efficiency and reduce the charge sharing among pixels.

The signal is further amplified and shaped in a narrower peak by a succession of active high pass and low pass filters. In this case a high pass active CR filter is followed by three low pass RC filters. Short peaking time is beneficial for the time resolution but it generally requires more current to drive the electronics. Note that the peaking time should be larger or equal to the charge drift time otherwise the charge collection efficiency is reduced. Finally, the last stage of the circuit is an inverting Schmitt trigger, the voltage V_T sets the detection threshold. The circuit hysteresis helps to avoid spurious triggering that could be caused by small signal variation (noise).

2.1.5 Electronic Noise

The equivalent noise charge (ENC) is a common figure of merit for silicon detectors. It is the input charge for which the signal to noise ratio is equal to one. Typical silicon pixel detectors have a very high signal to noise ratio,

indeed, ENC of the order of a few hundreds e^- can be achieved without too many difficulties.

Three types of noise are considered for pixel analogue front-end. First, the thermal noise (or voltage noise) due to the random thermal velocity of charge carriers, it is modelled by a voltage source. Second, the shot noise (or current noise), caused by variation of the number of charge carriers, is it modelled by a current source. Third, the flicker noise which is technology and frequency dependent.

Specializing the developments from Rossi [72] p. 182 Equation (3.54), to a preamp followed by CR-RC3 filter we found

$$\mathrm{ENC}^2 = \frac{4}{3}\frac{\mathrm{e}^6}{\mathrm{q}^2}\left(\frac{15}{8}\tau\frac{I_0}{2\pi} + \frac{1}{\tau}\frac{V_0}{2\pi}C_{\mathrm{in}}^2 + 2V_{-1}C_{\mathrm{in}}^2\right) , \tag{2.14}$$

where e is the Euler's number and q the elementary charge. I_0, V_0 and V_{-1} model, respectively the thermal noise, the shot noise and the flicker noise. Typically, the following trends are applicable

$$\begin{aligned} I_0 &\propto I_{\mathrm{leak}} , \\ V_0 &\propto T , \\ V_{-1} &\propto \mathrm{Cst.} . \end{aligned}$$

The input capacitance (C_{in}) and the shaper peaking time (τ) explicitly enters the Equation (2.14): the lower the input capacitance is, the lower is the noise, similarly, for each configuration, an optimal peaking time can be found. In practice many parameters are interdependent (for instance, for shorter peaking times we need more current, which can then generate more noise, etc.) and their optimization is a complicated business that depends greatly of the underlying technology. Numerical simulations are therefore used in practical cases [87].

2.2 Radiation Damage

Silicon sensor are altered by the particles passing across them. Due to their different nature, the damage are often divided into surface damage, involving the interfaces and the metal and silicon oxide layers, and bulk damage, affecting the silicon lattice. We will focus the on bulk damage since they are the most relevant to the detector performance.

This section covers the material needed for the following chapters, for an in-depth review the reader can refer to the work of the RD48 [88] and RD50 [89] collaboration and, more specifically, to refs. [90, 91, 92].

2.2.1 Bulk Damage

Particles can impart enough energy to the silicon to create lattice defects [93]. The minimum energy needed to knock off an atom from its lattice position,

the *displacement energy*, E_d, is about 25 eV in silicon. Below a couple of keV damage are localized, above clusters of defects are formed by the recoil of the fragments of the knocked off atom. If the displaced atom moves to an interstitial position, creating a vacancy at its original position, the damage is called a *Frenkel defect*. Damage are not static, because of the thermal motion the lattice defects evolve in time causing *annealing* and *reverse annealing* effects.

Overall, the lattice defects act as charge *traps*. The traps have well defined energy levels and act as generation and recombination centres. Moreover, the damage modifies the effective doping concentration, N_{eff}. Three effects are important for particle sensors: the increase of the leakage current, the reduction of the charge collection efficiency and the bulk material type inversion, from n to p.

To assess the amount of damage we can either measure the leakage current or determine the full depletion voltage of the device. Indeed, there is a linear relation between the leakage current and the particle fluence. The second technique takes advantage of the effective doping concentration dependence of the depletion voltage (see Equation (2.3)), we can extract the depletion voltage from a simple C-V measurement.

2.2.2 NIEL Scaling Hypothesis

It has been observed that the bulk damage is proportional to the non-ionizing energy loss (NIEL) for a large range of energy and heavy charged particles [93, 94, 95]. The NIEL is defined as the energy dissipated by the displacement of atoms of the lattice or absorbed directly by the lattice. Differences between proton and neutron induced damage have been observed [91] and electrons cause less damage [96] because of the absence of nuclear interactions. There is no precise microscopic understanding of why the damage scale with the NIEL.

The amount of damage depends on the particle fluence, type and energy. That is, 75 GeV kaons are not equivalent to 50 MeV protons. To ease the comparisons, it is customary to report the fluence in 1 MeV equivalent neutron (1 MeV eq. n). The relation

$$\Phi_{\text{eq}} = \int_{E_{\min}} \frac{D\left(E\right)}{D_n\left(1\text{ MeV}\right)} \phi\left(E\right) \mathrm{d}E \ , \tag{2.15}$$

allow to convert a general spectral-fluence, $\phi\left(E\right)$, to 1 MeV equivalent neutron fluence. $E_{\min}$ is the neutron displacement damage threshold energy, about 10 keV, D is the *damage function*, by convention, the displacement damage function for 1 MeV neutrons is $D\left(1\text{ MeV}\right) = 95$ MeV mb [97]. A complete expression for D can be found in section 4.2.1 of [78]. Through this text we will use the shorthand Φ_{eq} to indicate 1 MeV equivalent neutron fluences.

In practice Equation (2.15) is difficult to compute, for mono-energetic beams we can use tabulated *hardness parameter*, κ, to do the conversion

$$\Phi_{\text{eq}} = \kappa\Phi \ , \tag{2.16}$$

κ depends on the energy and type of beam. The literature on the topic is abundant, Vasilescu et al. did a literature survey for protons [98]. Classic references for protons includes [99, 100, 101, 102], the curve for the proton was obtained by extrapolating data from pion measurements, therefore holds only if the NIEL scaling is valid.

2.2.3 Leakage Current

The additional generation centres increase the reverse current inside the bulk. Since the quantity of defects appears to directly proportional to the fluence, we have

$$\Delta I_{\text{leak}} = \alpha \Phi_{\text{eq}} \ , \tag{2.17}$$

where ΔI_{leak} is the excess leakage current and α the *current damage parameter*. Experimental studies have confirmed the linear relationship, for silicon $\alpha = 8.0 \times 10^{-17}$ A cm^{-1} at 20 °C and without annealing [96].

The leakage current can be substantially reduced by cooling the detector.

2.2.4 Charge Trapping

The additional recombination centres raise the trapping probability of the charges carrier and, therefore reduce the signal amplitude. For the same reasons as above the charge trapping probability seems to scales linearly with the fluence:

$$\frac{1}{\Delta \tau_{\text{eff}_{e,h}}} = \beta_{e,h}\left(t, T\right) \Phi_{\text{eq}} \ , \tag{2.18}$$

where β depends on the temperature and annealing time. The value of β was measured for different type of particles [103]. For instance, for silicon at -10 °C exposed to a beam of pion and left 10 days at room temperature for annealing

$$\beta_e = (5.7 \pm 0.2) \times 10^{-16} \text{ cm}^2 \text{ ns}^{-1} \ , \beta_h = (7.7 \pm 0.2) \times 10^{-16} \text{ cm}^2 \text{ ns}^{-1} \ .$$

The values are very similar for protons but 22 - 28 percent less for a NIEL equivalent fluence of neutrons [103].

2.2.5 Type inversion

The irradiation of silicon leads to the removal of donor states and the creation of acceptor states in the bulk hence after a fluence of typically 2×10^{12} 1 MeV eq. n cm^{-2} [96] the buck changes from n-type to p-type. The p-in-n sensors are not affected by this effect.

2.2.6 Damage Evolution

The clusters of defects are not stable at room temperature. “Annealing” and “reverse annealing” effects occur. In general, the rate constant (k) of the

damage evolution is given by the Arrhenius relation:

$$k = k_0 \exp\left(-\frac{E_A}{k_B T}\right) , \tag{2.19}$$

where $E_A = 1.09 \pm 0.14$ eV [104] is activation energy. The evolution is considerably reduced below -5 °C. The time evolution of the effective doping concentration, N_{eff} is reproduced by Hamburg Model [90].

2.3 Time Resolution

Generally, the time resolution of a silicon pixel detector can be written as [87]:

$$\sigma_t \propto \frac{\text{ENC} \cdot \tau}{Q_{\text{in}}} , \tag{2.20}$$

where ENC is the total equivalent noise charge of the charge amplifier, Q_{in} the input charge and τ the peaking time. In other words, one wants to maximise the signal slope ($\mathrm{d}V/\mathrm{d}t$) while keeping the noise level to the minimum. To achieve that, the peaking time should be large enough to collect most of the charges (large $\mathrm{d}V$) but not more (short $\mathrm{d}t$). As we saw before, the noise depends on the technology and on the pixel size, smaller is better. Many parameters are interdependent therefore detailed simulation of the device are used to find the optimums.

Let's decompose the time resolution into three independent contributions. First, the readout electronics. On top of the unavoidable jitter, the analogue signal digitisation adds a quantization error. If the input signal is much larger than the least significant bit (LSB) (or TDC bin) on can consider that the error is uniformly distributed over the bin. Therefore, the error is simply the width of the LSB divided by $\sqrt{12}$. When running at the nominal frequency (320 MHz) the GigaTracker TDC least significant bit (LSB) corresponds to 97.7 ps. In total, the GigaTracker analogue front-end and the TDC adds 40 ps to the time resolution [15].

Next, the energy straggling. As illustrated on Figure 2.4 the time lapse between the particle crossing the detector and the shaped signal crossing the discriminator threshold depends on the energy released in the sensor. This time interval is called the *time walk*. It can reach several nanoseconds; time walk compensation is therefore crucial to achieve a good hit time resolution. The time walk can be compensated at the electronics level by using a constant fraction discriminator. Alternatively, if the readout electronics is based on a time-over-threshold discriminator offline corrections are required. The GigaTracker uses the latter, the corrections will be covered in Section 3.2.4. Simulations indicate that, after the time walk correction, the straggling adds around 60 ps to the time resolution [105].

And finally, the pixel geometry. The shape of current pulse depends on hit position. To illustrate this, we simulated the current pulses generated by a

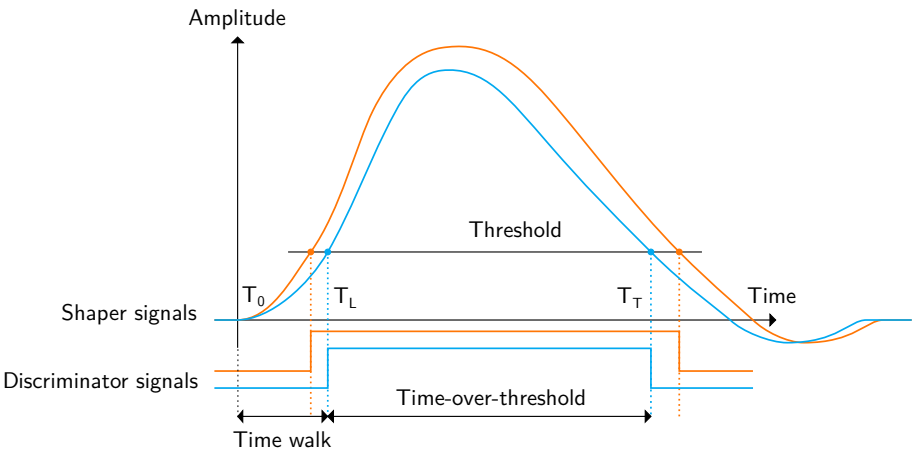

Figure 2.4: Illustration of the relation between the time walk and the time-over-threshold. Higher amplitude signals lead to bigger time-over-threshold and vice versa.

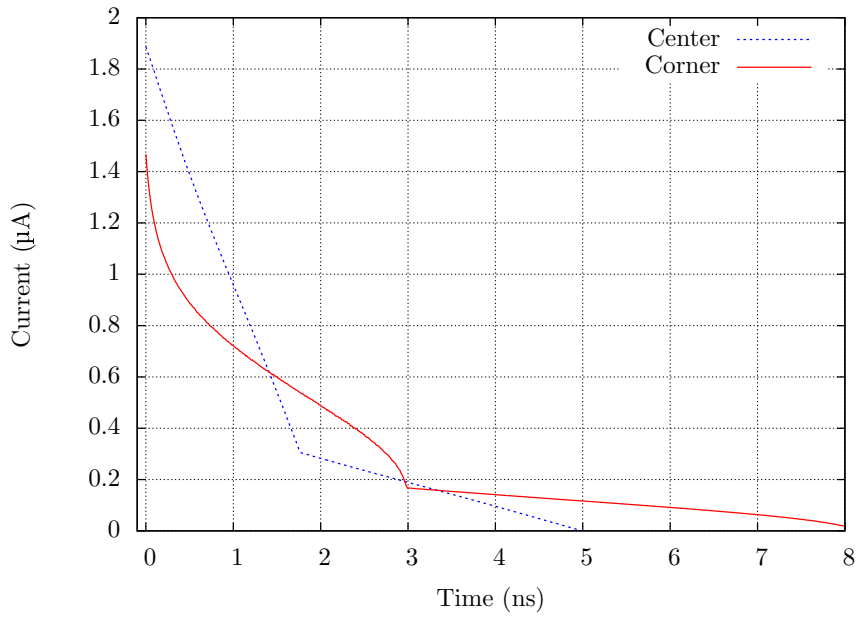

Figure 2.5: Simulated signal shape for a bias voltage of 300 V. The electrons (fast) and holes (slow) components are summed. The hit position on the sensor significantly alters the signal shape, it is caused by the electric field non-uniformity inside the pixel.

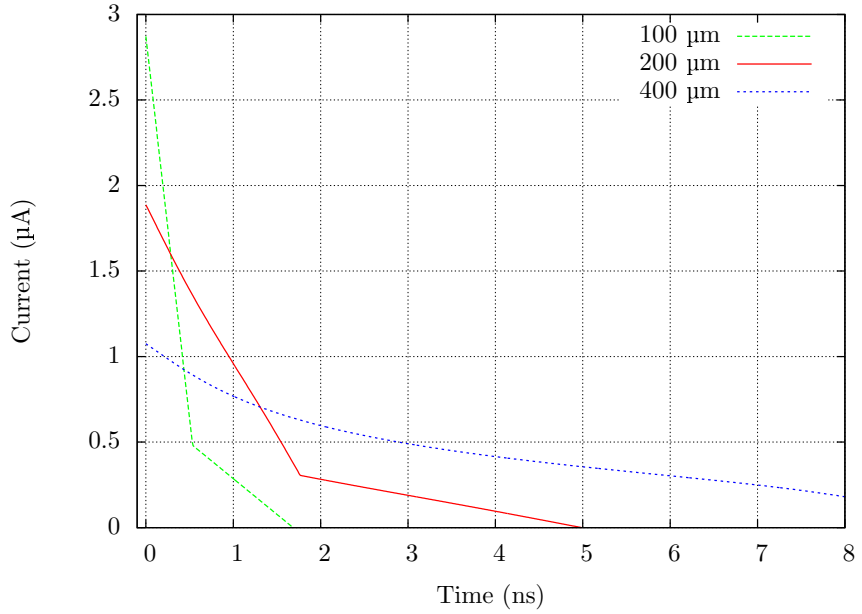

Figure 2.6: Simulated signal shapes for a bias voltage of 300 V. The electrons (fast) and holes (slow) components are summed. At fixed bias voltage the average strength of the electric field is lower in thick detector and therefore the current pulse is smaller. In addition, the charge collection takes more time.

particle crossing the centre ($x = y = 0$) and close to the corner of the pixel ($x = y = 125$ µm), the results are shown in Figure 2.5. This effect is caused by the non-uniformity of the electric field inside the pixel. Laser tests performed on the GigaTracker prototype have shown that the pixel geometry adds roughly 70 ps to hit time resolution when the detector is biased at 300 V [106]. Moreover, as we can see in Figure 2.6, the sensor thickness has also a significant impact on the signal shape and therefore on the time resolution. Since it is a fixed parameter it can be viewed as a constant term. Thin sensors produce shorter pulses, which is an advantage for timing application.

To sum up, multiple phenomena contribute to the hit time resolution, when measured separately and in ideal condition the readout chip, the energy straggling and the pixel geometry adds about 40, 60, and 70 ps to the resolution respectively. The time walk compensation also contributes. This is to compare with the 150 ps measured with the GigaTracker prototype during a test beam [2].

2.4 Summary and Discussion

Silicon pixel detectors are part of the standard experimental physicist toolbox and a key element of many physics studies since more than 20 years. The development of the Superconducting Super Collider (SSC) and of the Large Hadron Collider (LHC) in the 1980s drove the need for detectors able to track the secondary particles close to the interaction point. That location put strong constraints on the radiation hardness, the material budget, the spatial resolution and the readout electronics. After decades of development, silicon pixel detectors are ideal for beam tracking application in high rate environment.

The hit time resolution and the data throughput are the most important figures of merit for the GigaTracker. The rapid progress of the silicon-based semiconductor technologies have dramatically increased the readout throughputs. One the other hand, the energy straggling, the charge carrier drift velocity, the sensor geometry, the front-end electronics and the signal digitalisation all contribute to the detector time resolution. The GigaTracker is biased to values where charge carrier drift velocity is close to saturation. Similarly, adequate time walk compensation reduces the impact of the energy straggling on the hit time resolution. The effects due to the pixel geometry are harder to compensate. At the end, the front-end electronics accounts only for about one-third of the hit time resolution.

The radiation damage on the sensor increases of the leakage current and reduces of the charge collection efficiency. As the leakage current is strongly influenced by the sensor temperature, it is beneficial to cool the sensor. The charge collection efficiency can be partially compensated by increasing the bias voltage. This issue is less critical for the GigaTracker as the detector will be swapped regularly. Nevertheless, the long term effects of the total ionizing dose on the GigaTracker readout chip (TDCpix) are still largely unknown.

Chapter 3

Silicon Pixel GigaTracker

The NA62 experimental technique rests on the accurate kinematic reconstruction of the kaon decays. As we saw in the introduction, the desired physics performances set the beam tracker time and spatial resolution requirements. Specifically, the track candidate time resolution, angular resolution and relative momentum resolution must be below 200 ps, 20 µrad and 1% respectively. The overall tracking efficiency must be well above 99 percent.

The three main technology challenges in the tracker construction were the thermomechanical integration, the readout system and the radiation hardness. First, to minimize the beam interaction with matter the detector has to be operated in vacuum and the material in the beam path has to be kept minimum. These two facts put serious constraints on the detector cooling solution. Second, the readout system has to cope with the 750 MHz beam which translates to an average data throughput of 7.6 Gbit/s per ASIC at the centre of the detector. Moreover, to keep the hit time resolution below 200 ps complex front-end and time to digital conversion electronics were needed. Finally, since the sensor and the readout chips are placed in the beam acceptance the whole detector has to be radiation hard. Protection against single event upset (SEU) is included in the chip design. The detectors will be exchanged regularly to cope with the permanent sensor damage; tests show that it should sustains at least 100 days of operation at nominal beam intensity.

The existing solutions could not meet the specifications therefore the NA62 collaboration started a research and development program. Before building the full scale detector, two demonstrator ASICs were designed, fabricated and characterized. Next to the hardware development, significant software developments had to be done. Specifically, the code for the Monte Carlo simulation of the detector, the track candidate reconstruction, the detector operation and calibration, and the data unpacking had to be written.

This chapter covers the developments that led from the prototype to the full scale GigaTracker detector. GigaTracker is described in the first section, both the full scale detector and the demonstrator are covered. In the second section,

Table 3.1: Parameters of the magnets installed close to the GigaTracker.

Name	Type	Active length (m)	Bending power (Tm)	Aperture (mm)	$I_{\max}$ (A)
MCBV	dipole	2.5	4.5	80×160	880
MDXH	dipole	0.4	0.523	100×80	250
XCMV	muon scraper	5	–	80×80	200

we detail the detector status in 2014 and 2015. Finally, the author main contributions to the development of the full scale GigaTracker are presented: the Monte Carlo and reconstruction code, the detector time and spatial alignment procedures, and the characterisation of the n-in-p sensor.

3.1 Detector Description

The GigaTracker (GTK) measures the momentum, the direction and the time of passage of all the NA62 secondary beam particles. Two constraints are immediately apparent: the detector has to cope with the high intensity hadron beam and the amount of matter in the beam path must be minimal to reduce the elastic and inelastic scatterings.

Given the challenges in terms of time resolution and data throughput, two architectures were investigated and tested before designing the full scale ASIC. Similarly, because of the limited material budget and vacuum operation, a microchannel cooling plate and a gas cooling assembly were studied. After reviewing the options, the collaboration opted for the so-called TDCpix readout ASIC and a microchannel cooling plate for the final detector.

GigaTracker is a new milestone in the hybrid silicon pixel detector landscape. The custom readout ASIC (TDCpix) has an unprecedented hit rate and timing capabilities. Moreover, it is the first application of microchannel cooling in High Energy Physics. The full detector was installed and tested in beam for the first time in autumn 2014.

In the next sections we go through the different elements that compose a single GigaTracker station. We follow a bottom-up approach, starting with a description of sensors and finishing with mechanical integration. Finally, in the last section we detail the specificities of the GigaTracker demonstrator.

3.1.1 GigaTracker Layout

As illustrated in Figure 3.1, GigaTracker is composed of three independent stations. The two first are enclosed in individual vessels while the third is installed in the CHANTI enclosure. The first and second station are separated by 13.2 m while the second and the third are 9.6 m apart. A long lever arm helps to measure accurately the direction of the particles. The middle station is placed between two achromatic magnet pairs and displaced by -60 mm along the Y-axis. The vertical offset matches the 75 GeV/c beam momentum and the

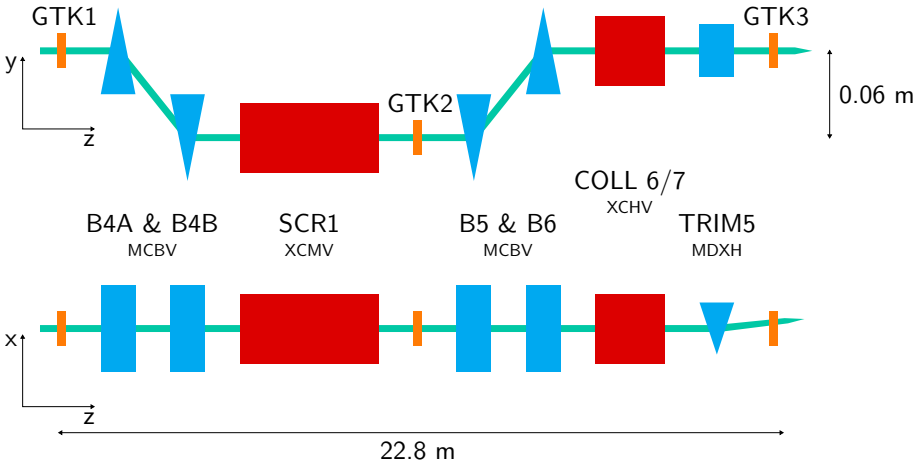

Figure 3.1: Scheme of the beam line in GigaTracker region. The magnets B4A, B4B, B5 and B6 are standard dipoles. The SCR1 (scraper) is a toroidally-magnetized motorized collimator that absorbs the neutral particles and the muons with having a momentum < 55 GeV/c. The COLL6/7 is a 1 m long four-jaw motorized collimator. The TRIM5 is short dipole magnet. See the Section 1.2.1 for more details on the beam line.

field strength of the magnets. The magnets parameters are detailed in Table 3.1. A full description can be found in ref. [107].

The influence of the detector geometry on the momentum and angular resolution is detailed in Appendix A.

Each GigaTracker station houses a *detector*. They are completely interchangeable, a detector can be installed in any of the three stations as the mechanical interface is identical. All the detectors are operated inside the secondary beam vacuum (10^{-6} mbar). The detector itself is made of successive assemblies mounted together. A 3D model is presented in Figure 3.2. The dif-

Table 3.2: Material budget of a GigaTracker station. All thicknesses are given in "silicon equivalent". We approximate the bump-bonds to 14 µm radius SnPb spheres ($\rho = 8.46$ g/cm^3). The glue density is 1.3 g/cm^3.

Element	Design (µm)	2014–2015 (µm)
Sensor	200	–
Bump-bonds	0.002	–
Readout chip	100	100–450
Glue layer	0.084	–
Cooling plate	130	275
Total	430.086	580.086–930.086

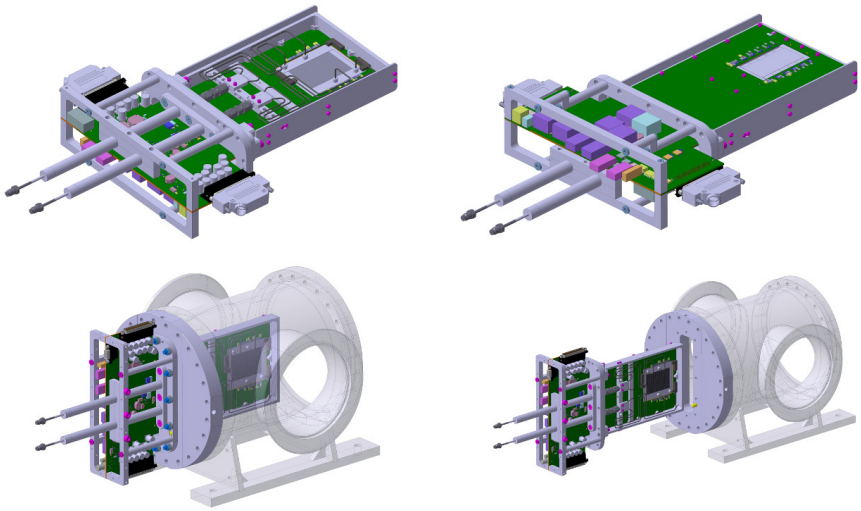

Figure 3.2: 3D views of a GigaTracker station. Courtesy of Jordan Degrange (CERN).

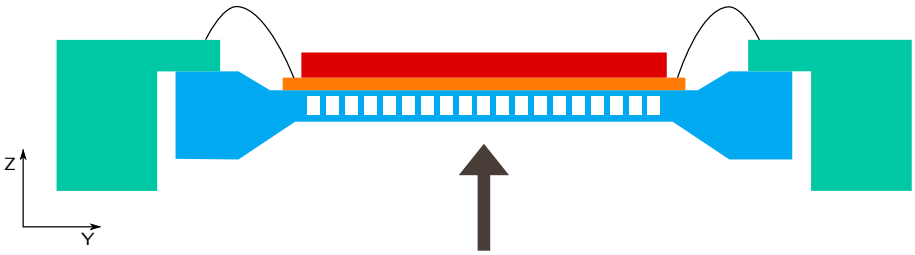

Figure 3.3: Cross section (Z-X) of the central region of a GigaTracker station. The sensor is in red, the readout chips in orange, the cooling plate in blue and the carrier card in turquoise. The bump-bonds, the glue and the thermal interfaces are not represented. The beam is going from bottom to top. This schema is not on scale.

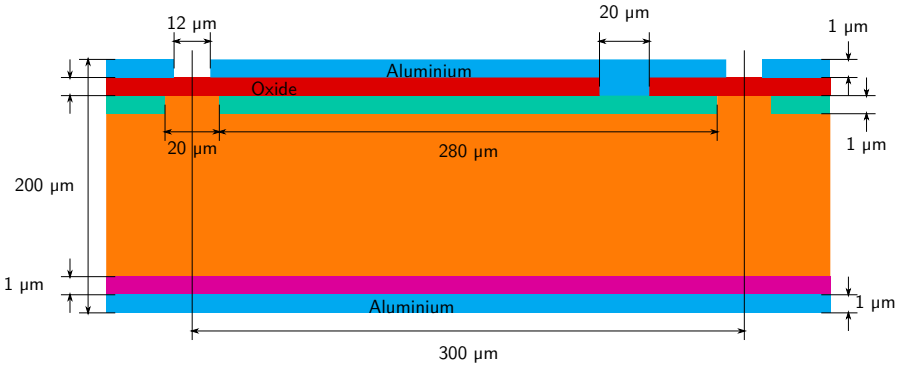

Figure 3.4: Cross-section of the GigaTracker sensor. One pixel implant and its corresponding aluminium contact is represented. On the backside, highly doped layer ensures an ohmic contact between the aluminium layer and the bulk.

ferent pieces are (a) the sensor assembly which is a sensor *flip chip* bonded to ten readout chips. (b) The cooling assembly which consists of a sensor assembly glued on a cooling plate. (c) The carrier card assembly, which is a cooling assembly clamped to carrier card. (d) Finally, a complete detector is a carrier card mounted on a mechanical frame. The material budget is summarised in Table 3.2. A sketch of the detector is presented in Figure 3.3.

GigaTracker is a new milestone in the hybrid silicon pixel detector landscape. The readout ASIC (TDCpix) has unprecedented timing capabilities: the hit time resolution is about 40 ps without a sensor and below 150 ps with a sensor attached for a bias voltage of 300 V. It can process up to 210 MHits/s spread over the 1800 channels. GigaTracker is the first detector which is equipped with a microchannel cooling plate; the total thickness in the beam acceptance is equivalent to less than 0.5 mm of silicon.

3.1.2 Silicon Sensor

The GigaTracker silicon sensor measures 27.0 mm by 60.8 mm and is 200 µm thick. The most probable charge released by a 75 GeV/c charged hadron in such sensors is about 2.4 fC.

The sensor is segmented into 300 µm by 300 µm pixels except in the inter-chip regions where they are enlarged to 400 µm by 300 µm. To improve the electric field uniformity in the active area, an aluminium field plate go over the edge of the implant. The sensor is biased using the punch-through technique. Twelve guard rings prevents the surface leakage currents to extend from the sensor to the pixels. The outermost ring is 300 µm wide and biased to 0 V while the twelve to sixteen others are 25 µm wide and left floating to harmonise the voltage drop.

A sketch of the sensor cross-section is shown in Figure 3.4. Since the stan-

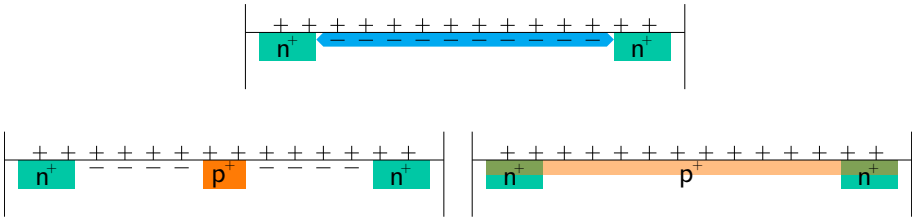

Figure 3.5: Sketch of an n-in-p type sensor. Positive charges tends to accumulate at the silicon oxide-silicon interface. If nothing is done, an electron layer just below the silicon oxide creates a low resistivity path between adjacent pixel implants (top). Two common techniques to circumvent to problem are the p-stop (bottom left) and the p-spray (bottom right) implantation.

dard implants size (280 µm) is large compared to the gap between the pixel (20 µm), in very good approximation, the depletion voltage can be calculated using Equation (2.1). For the typical dopant concentration of 10^{12} cm^{-3}, about 30 V are needed to completely deplete the sensor. Nevertheless, GigaTracker will be operated between 300 V and 600 V to optimize the charge drift velocities.

The readout ASIC is specified to be compatible with p-in-n and n-in-p type sensors. Both type have been manufactured. The p-type bulk is slightly more radiation hard than the n-type as it does not suffer from type inversion and as it "collects" electrons which are less sensitive to trapping. The GigaTracker detectors installed in 2014–2015 were equipped with p-in-n sensors.

p-in-n Type Sensors

The p-in-n type sensors were manufactured by the Fondazione Bruno Kessler (FBK) and CiS Forschungsinstitut für Mikrosensorik GmbH (CiS) on Float Zone (FZ) wafers. The bulk is doped with phosphorus. The resistivity is required to be above 3 kΩ/cm which corresponds to a dopant concentration around $10^{12}/\text{cm}^3$.

This kind of sensors is standard, easy to fabricate, and relatively low cost. However, at high irradiation dose the bulk type tends to change from n-type to p-type ("type inversion") [96].

n-in-p Type Sensors

The n-in-p type sensors were manufactured by FBK on FZ wafers. The bulk is doped with boron. At the same impurities concentration, the bulk resistivity is about three times lower than for the p-type; 3 kΩ/cm corresponds to a dopant concentration of the order of $4 \times 10^{12}/\text{cm}^3$.

During the operation of this kind of sensors positive charges tend to accumulate at the oxide interface. As a consequence, electrons gather at the interface and create a low resistivity path between adjacent pixels which increases

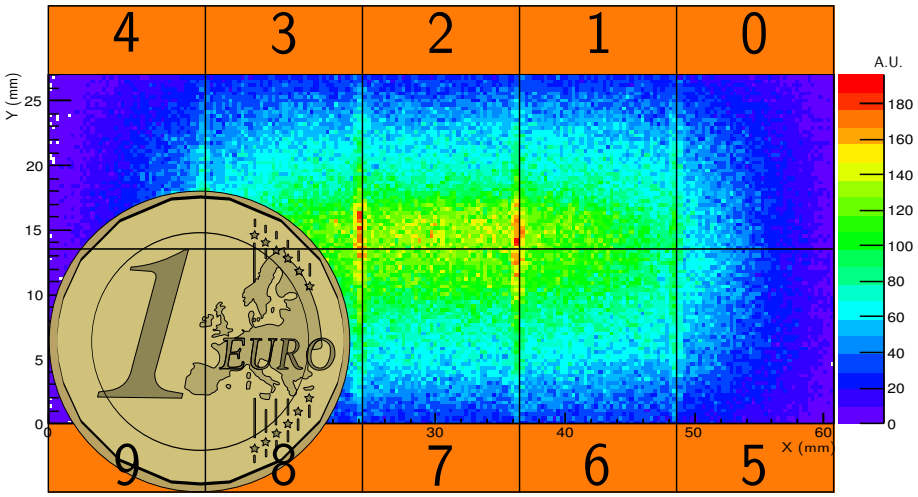

Figure 3.6: GigaTracker readout ASIC numbering scheme superimposed on the simulated illumination of the sensor. The orange areas represent the "end of column" regions of the readout chips where most of the TDCpix digital logic is implanted. The higher rates in the inter-chip regions is due to the larger pixel size.

the crosstalk. This must be avoided to ensure a good spatial resolution. As illustrated in Figure 3.5, two techniques have been developed to restore the inter-pixel isolation, they can be combined. First, the *p-stop* [108, 109] approach: a high concentration (typically of the order of 10^{14} cm^3) and well localized p-type implant is added around the n-type regions, hence interrupting the electron layer. The layout of the implant has to include a small gap or channel to allow the punch-through biasing. This method requires one additional photolithographic mask. Second, the *p-spray* [110] technique: medium concentration (about 10^{12} cm^3) and uniform implant are added on the whole surface, overlapping the n-type regions. This approach does not require an additional photolithographic mask. The most appropriate method depends on individual detector specification like the maximum operating voltage, the allowed leakage current, the inter-pixel gap or the foreseen radiation hardness. For the GigaTracker sensors, both technique have been combined. A precise description of this topic is outside the scope of this work.

3.1.3 Readout Electronics

The sensor is bump-bonded to ten 12 mm by 20.37 mm, 100 µm, custom readout ASICs. Each readout covers 1800 pixels arranged in a 45 by 40 matrix. All the power and signal connection are placed at the bottom of the readout chips, outside of the beam area. The chip layout is shown in Figure 3.6.

Before discussing the technical implementation, we will outline the general

Table 3.3: Main readout chip specifications.

Max. chip hit rate	210 MHz
Max. channel hit rate	114 kHz
Input signal dynamic range	0.8-9.6 fC
Hit time resolution	$\leq$ 200 ps RMS
Channels	40 by 45 pixels
Power dissipation	< 2 W/cm^2
Radiation dose	6×10^4 Gy
Max. leakage current / pixel	1 µA
Surface	12 mm by 20 mm
Thickness	100 µm

readout ASIC requirements focusing on the input signal characteristics and on the system and environmental constraints.

The average hit rate for a pixel placed at the centre of the sensor was estimated to 114 kHz at nominal intensity. For the central chip, this rate corresponds to an average of 58 kHz/channel or 105 MHz/chip. In addition, provisions must be made for inevitable beam fluctuations.

The readout chip is "trigger-less", all the hits are processed and shipped off to external FPGA based readout cards. For that reason and in view of the hit rates the chip has to support substantial data throughput. At full beam intensity, assuming that the hit words are 48 bits wide, *8b10b* encoded (20 percent overhead) and adding a 30 percent contingency, a chip would output up to 7.6 Gbit/s

The specified input dynamic range is 0.8 – 9.6 fC, the most probable value being 2.4 fC. A time walk compensation mechanism is mandatory to achieve the desired hit time resolution. This subject is detailed in Section 3.2.4.

Since the detector is operating in vacuum the electronics power dissipation is a major issue. The maximal acceptable flux was set to 2 W/cm^2 averaged over the whole surface. This is substantial for a silicon pixel detector.

A significant part of the ASIC is crossed by the secondary beam therefore key digital logic elements have to be protected against single event upset (SEU). Finally, for practical reasons, the ASIC had to be manufactured with the IBM 130 nm CMOS technology. The main chip specifications are summarised in Table 3.3.

Two ASIC prototypes were developed, implementing different time measurement mechanisms. One is based on a constant fraction discriminator (CFD) coupled to a time to amplitude converter (TAC). The other one is built around on a time-over-threshold discriminator (ToT) and a delay locked loop (DLL). Both solutions were evaluated in a test beam and after an external review the time-over-threshold architecture was selected for the final detector. A brief overview of the architectures is given in the following sections. A more detailed description can be found in ref. [13].

Constant Fraction Discriminator (P-TDC)

The P-TDC ASIC pixel matrix is divided into columns of 45 pixels. Current pulses are amplified and shaped before being fed to Constant Fraction Discriminator (CFD). The CFD takes care of the time walk compensation, removing the need for an offline correction. The analogue signal digitisation is carried out in the pixel cell. For that reason, a 320 MHz digital clock signal is propagated to the pixel matrix.

When the pixel is fired the value present on the digital clock bus is latched into a local register. Simultaneously, a Time to Amplitude converter (TAC) generates a voltage proportional to the time interval between the hit and the next digital clock edge, giving the fine time. Analogue fine time and digital coarse time are buffered separately.

Each column is readout by a dedicated controller implanted in the end of column region of the chip. A busy line is asserted when data is available in at least one of column's pixels. Upon reception, the analogue fine time is digitalized and transferred together with the coarse time and the pixel address in an output buffer. The hits are then sorted and dressed with header and trailer words by a merger circuit. Eventually the data are serialized and shipped off chip.

Since a significant part of digital electronics is directly in the beam acceptance the registers are encoded using a Hamming code to protect them from single event upset (SEU).

The P-TDC approach has the advantage that no offline time walk compensation is needed. In addition, since the hit are derandomized at the pixel level, the end of column electronics can be relatively simple. However, one has to mitigate the risk of noise being induced by digital clock. SEU could also be an issue in the NA62 radiation environment.

Time-over-Threshold (TDCpix)

The "end of column" (EoC) architecture was selected to equip the full scale GigaTracker detector; the resulting ASIC was named the TDCpix [15]. A simplified bloc diagram of the chip is presented in Figure 3.7.

The ASIC is composed of four identical *QuarterChip* organized in ten columns of 45 pixels. The pixel cell consists of a charge sensitive preamp, a shaper, a time-over-threshold discriminator and a line driver. Analogue signals are propagated through the pixel matrix via transfer lines.

In the end of column region, five pixel cells are connected to a single *hit arbiter* that masks the signals from the others four pixels during the analogue and digital processing of a hit. Each hit arbiter is in turn connected to a TDC. At the arrival of a signal, the value of two 32-bit coarse counters and the state of a 32 elements delay-locked line (DLL) are latched onto registers, and the address of the hit pixel is recorded. If driven at the nominal 320

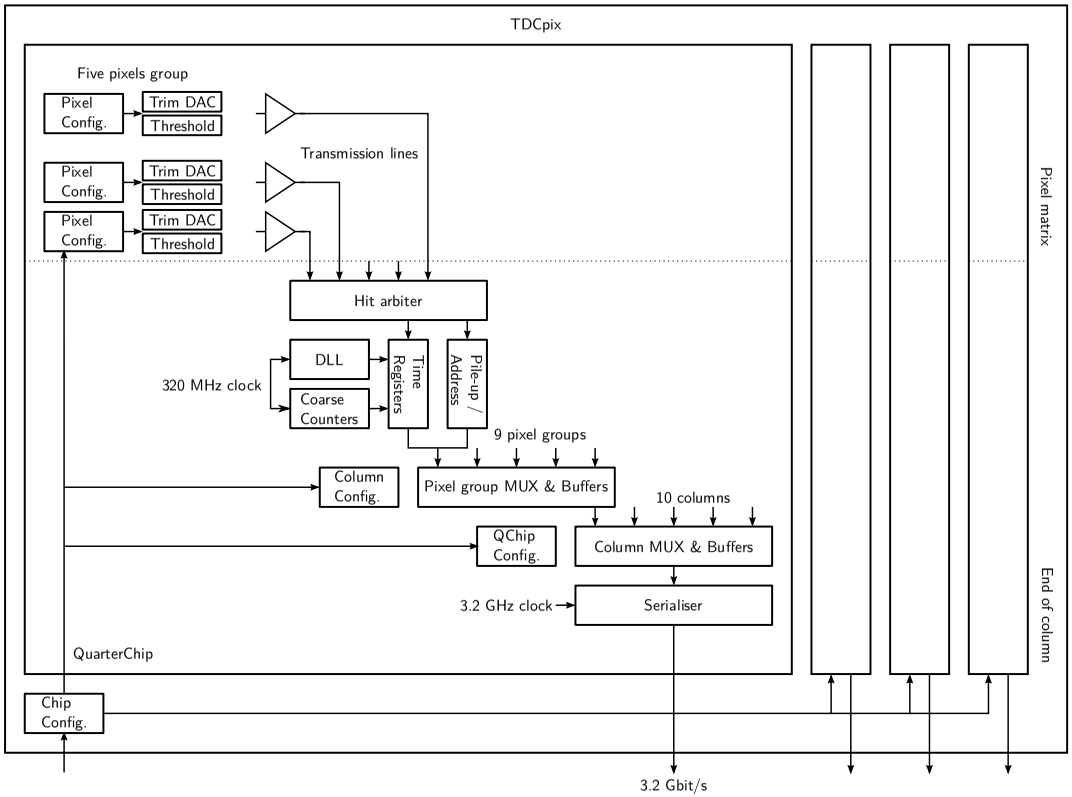

Figure 3.7: TDCpix dataflow. The chip is divided into four identical QuarterChip (QChip). There is no clock running in the pixel matrix except while reading or writing into the pixel configuration registers. Most of the digital electronics is situated in the end of column region, out of the beam acceptance.

MHz, the TDC fine time bin is 97.7 ps. The digital values stored into the TDC registers are then transferred to buffers and dressed with a header and a trailer. Eventually the data is serialised and asynchronously sent off-chip via a 3.2 Gbit/s serial link. There is one 3.2 Gbit/s serialiser per QuarterChip hence the total bandwidth is well above the required 7.6 Gbit/s.

A series of configuration blocks allow to set the chip up. Parameters of special importance are the trim DAC values (see below), the threshold levels and the serialiser operating mode. Despite being less exposed because situated in the end of column region of the chip, key registers are triplicated for SEU protection.

The discriminator threshold is adjusted by the pixel trim DAC and the column threshold DAC. Since each pixel cell has different characteristics it is critical to equalize the pixel thresholds to have a good response uniformity.

The equalization of the thresholds is done by injecting a fixed charge in a given pixel N times (with N of the order of $10^4 - 10^5$). For each set of injections the threshold is swept through a large range. The result is a sigmoid: at low thresholds all the N injections are detected while for large thresholds none of the injections are going through the discriminator. The width of the sigmoid, defined from 10 to 90 percent of N, is directly connected to the baseline jitter and known as equivalent noise charge (ENC). The thresholds can be adjusted in groups by column and finally individual trim DAC are set to ensure that for the same charge 50 percent of the injections are counted in output.

To verify the consistency of the calibration, the pixels are exposed to a well-known radiation source. Simultaneously, the thresholds are varied and for each level the hit count is logged. A good set of calibration parameters gives a smooth function of number of hits through the active area.

Since all the digital processing is done in the end of column region no clock signals have to be distributed in the pixel matrix except for reading or loading pixel configuration register. This limits the risk of electronic noise that could be caused by digital clock signals propagating in the chip. Nevertheless, the time walk has to be corrected offline.

3.1.4 Electrical Integration

The electrical integration of the cooling assemblies with the outside world is done through a carrier card which also provides mechanical support for the cooling assembly. It is a complex multi-layers T-shaped PCB carrying the signal lines and the power lines from the readout chips through the vacuum-atmosphere interface. A gap to host the cooling assembly is machined in the vacuum end of the card. A stair structure supports the assembly on the top and bottom edges.

More specifically, the accessible signals are: one general digital clock; one clock for the delay-locked loops; one test pulse signal; one reset coarse frame counter signal; ten 320 Mbit/s serial configuration link; ten 320 Mbit/s serial

configuration status link and forty 3.2 Gbit/s serial data links. The electrical connection between the readout chips and the carrier is provided by wire bonds. The signal lines are connected to optical transceivers installed on the carrier and eventually transmitted to the GigaTracker readout boards.

The detector is powered by ten 1.2 V "analogue" lines and ten 1.2 V "digital" lines; two lines for each of the ten chips. Furthermore, 2.5 V, 3.3 V and 5 V lines are needed for the carrier card. All these channels are interlocked with the readout chips temperature sensors. A 5.3 V non-interlocked line supplies the temperature interlock logic.

The low voltages power supplies (CAEN A3009) are installed in the cavern, next to the detector. High voltage power supplies (CAEN A1821) are sitting in surface for easy access.

3.1.5 Thermomechanical Integration

As before described, the detector is operated in vacuum and the available material budget is very limited. This puts serious constraints on the possible cooling solution. The requirements were the following: the radiation length in the active beam area plus a 10 mm buffer zone have to be inferior to 0.5% of X_0, the temperature gradient across the sensor must be less than 5 K while keeping the sensor below 5 °C and finally the system must be able to dissipate at least 32 W per station. The typical power densities are 0.4 W/cm^2 in the active area and 3.2 W/cm^2 in the end-of-column region.

A microchannel silicon plate heat exchanger and nitrogen gas cooling were investigated. After review the microchannel plate was chosen for the final GigaTracker detector. Nevertheless, we will briefly describe both techniques starting with the gas cooling.

The gas cooling solution consists of an enclosure made of two concentric cylindrical thin Kapton walls supported by an aluminium structure placed outside of the beam acceptance. The sensor assembly is sandwiched between the two hemispheres of the gas vessel which is fixed to the carrier card. To cool the detector a constant flow of cold nitrogen is circulated inside the enclosure.

The microchannel plate is fabricated by etching 200 µm by 70 µm, 40 mm long, channels and two distribution manifolds in a silicon wafer. The wafer is then covered by a second one; both are joined using the *direct bonding* technique. In 2014, the assembly was finally thinned to 275 µm in the beam area. The thickness will be reduced to about 205 µm for 2016 batch of plates. The plate is thicker in the outer region to ensure good mechanical properties. A 300 W cooling plant installed next to the detectors cools C_6F_{14} in liquid phase which is circulated in the channels to evacuate the heat. A very detailed description of the microchannel cooling plate can be found in ref. [111].

The collaboration receives the sensor assemblies from the Fraunhofer-Institut für Zuverlässigkeit und Mikrointegration (IZM); the rest of the assembly is done at CERN. We will briefly describe the procedure. First, the sensor assembly

is glued to a microchannel cooling plate with 3M™ double-sided adhesive film; it forms a cooling assembly. The cooling plate fabrication and assembly is detailed in [111]. Next, the cooling assembly is fixed to the carrier card with three carbon fibre clamps and the readout chips pads are wire bonded to it. The carrier card is attached to a light aluminum frame which is in turn bolted to a flange. Finally, the cooling plate inlets and outlets are connected to stainless steel tubes folded in a particular way to absorb the mechanical stresses.

The first and second detectors are installed in barrel-shaped stainless steel vessels; the last detector is inserted in the CHANTI enclosure. See the Figure 3.2 for a 3D view of the assembled detector.

The detectors were designed to be easily replaceable. Indeed, to guarantee excellent time resolution and because of the radiation damage, the initial plan is to exchange the detector every 100 days of operation at nominal intensity. The status of the sensor will be monitored through leakage current measurement.

To exchange a detector, one has to disconnect the cooling fluid inlet and outlet, two power connectors and eight optical fibre cables. The flange can then be unbolted and the detector quickly replaced.

3.1.6 Data Acquisition System

Each TDCpix ASIC is connected via the carrier card and optical fibres to a custom FPGA based 6U VME module ("GTK-RO"). The card receives and buffers the data sent over the four 3.2 Gbit/s ASIC's serial lines. Upon level zero trigger reception the board transmits the relevant hits to an off-the-shelf PC for further processing. In addition, the board configures the ASIC and interfaces with the TTC system [112] which provide timing and synchronisation signals. Ten boards are needed for each detector so thirty board are required to readout the full GigaTracker. They are all installed in the counting room, in surface, and therefore always accessible.

3.1.7 GigaTracker Demonstrator

The demonstrator played an important as it proved the feasibility of the readout technique. Moreover, it established the reference for timing resolution in silicon sensors [2]. In this section we focus on the differences between the prototype and final TDCpix chip which is described in the previous section.

The GigaTracker demonstrator (or *single assembly*) is the assembly of a small 1.8 mm by 3.0 mm 45 pixels sensor and of a TDCpix ASIC prototype. The single assembly was wire bonded to a custom made carrier PCB who was in turn connected to an off-detector readout card. The carrier provided the biases for the chip and the sensor as well as the clock signals.

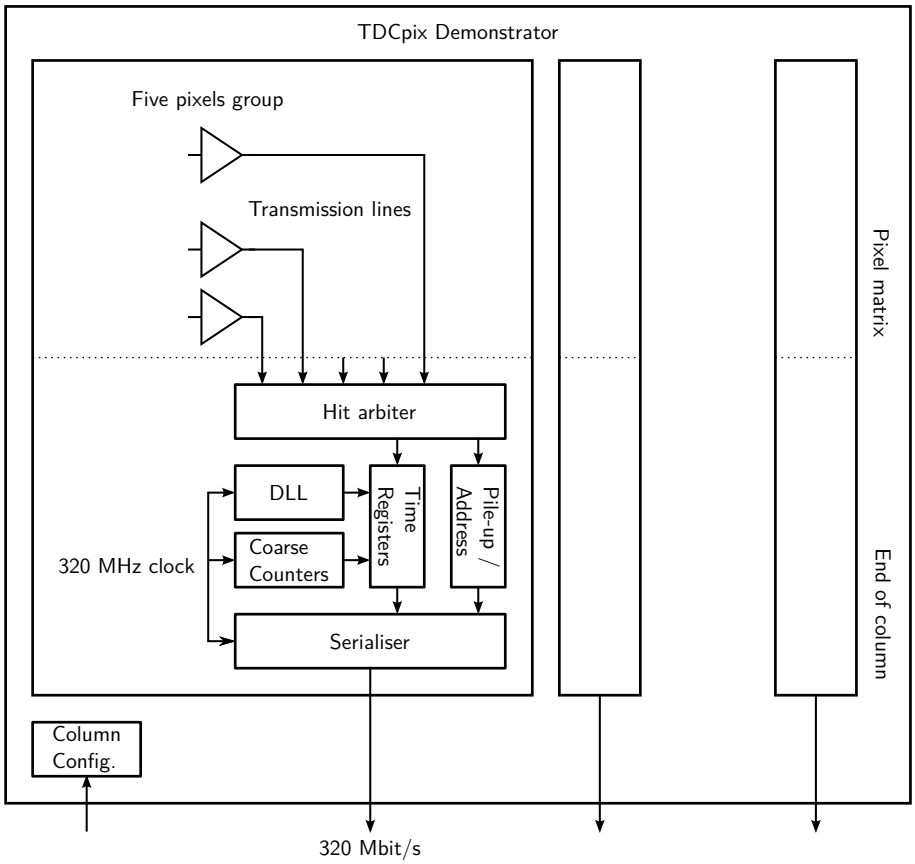

Figure 3.8: Simplified block diagram of a five pixels group, the demonstrator ASIC is made of nine of them.

Sensor

The GigaTracker demonstrator uses a 1.8 mm by 3.0 mm, 200 µm thick, p-in-n sensor divided in six columns and ten rows of 300 µm by 300 µm pixels, one row and one column were not connected to the readout chip and are therefore inactive. The sensor active area was surrounded by twelve guard rings to reduce the surface leakage current through the pixels. It was manufactured by FBK on 4 inches float zone wafers. The pixel structure is the same as the one of the full size sensor, the details were presented in the section 3.1.2.

Readout ASIC

The ASIC implements a single 45 pixels column structure which is folded to form a six by ten matrix. The main differences with respect to the final design are the use of one 320 Mbit/s serialiser for each of the five pixels group instead of four 3.2 Gbit/s serialiser per chip, the absence of in-pixel threshold trimming

possibilities and the use of a dual coarse counter for hit time disambiguation while the final design uses parity bits. The GigaTracker demonstrator chip was fabricated with the 130 nm CMOS IBM technology.

A simplified block diagram of a pixel group is shown at Figure 3.8. At each clock cycle two 32 bit binary counters are incremented, one on the leading edge and the other one on the trailing edge of the signal. They are used for coarse time measurement. When a pixel is fired, the hit arbiter masks the four other pixels belonging to the group. Simultaneously, the state of a 32 element delay line, the value of the two coarse counters and the pixel address are latched in registers. The values stored in the registers are then buffered, serialised and asynchronously pushed off-chip. This pixel group structure was replicated nine times to constitute the demonstrator ASIC.

The demonstrator ASIC is affected by a hardware bug: if a pixel is hit twice in a row in a five pixels group a constant delay is added to the timestamps. This happens irrespective of the activity in the other groups. The hits affected (about 20 percent) by the bug are flagged and not used to compute the stations time resolution. They are however used for the efficiency computation.

3.2 GigaTracker Development

As it has been described is the previous sections the GigaTracker involves complex heat exchangers, advanced microelectronics, delicate mechanical integration, elaborate software, etc.

The project was carried out by a team of engineers and physicists, it took about ten years from inception to completion. The readout ASIC and microchannel cooling plate developments were driven by the CERN Electronics Systems for Experiments (ESE) and Detector Technologies (DT) groups with the help of INFN Ferrara, INFN Torino and UCLouvain.

The author main contributions to the project are the characterisation of the FBK n-in-p sensor radiation hardness; the implementation of most of the detector Monte Carlo simulation; the study of the accidental background caused by the last GigaTracker station and the development of spatial and time alignment algorithms. These contributions are detailed in this section.

Beside this, two other projects are worth mentioning. The author contributed to the first assessment of the flip chip bonding yield. The results are grouped in Appendix H. In addition, the author wrote an interface to the NA62 condition database; this very technical project is detailed in a separate note [113]. They are outside of the scope of the dissertation but provided useful inputs to the GigaTracker working group.

3.2.1 Sensor Characterisation

The whole secondary beam crosses the GigaTracker stations, therefore, the silicon sensors are exposed to an uneven particle flux, going from about 134 MHz/cm^2 at the centre to roughly 89 kHz/cm^2 at the corners for nominal beam intensity. Supposing that particles are delivered to the experiment 100 days per year with a duty cycle of 0.2, the above fluxes lead to 2.3×10^{14} part. cm^{-2} yr^{-1} on the central region of the sensor.

The previous fluxes can be converted to 1 MeV equivalent neutron (1 MeV eq. n) fluences using the appropriate *hardness parameter* κ (see Section 2.2 for a more detailed explanation). Given the NA62 beam composition (19 percent protons, 74 percent pions and 7 percent kaons) and momentum (75 GeV/c) we chose $\kappa \approx 0.42$ [102]. Using this factor, the expected yearly fluence at the centre of the sensor is

$$\Phi \approx 9.8 \times 10^{13} \text{ 1 MeV eq. } n \text{ cm}^{-2} \text{ yr}^{-1} \ .$$

For comparison, the innermost layer of the CMS tracker, anticipated yearly fluence of 3×10^{14} 1 MeV eq. n cm^{-2} yr^{-1} at full LHC luminosity [114]. Radiation damage are detrimental to time resolution and to the efficiency which are key parameters for GigaTracker. The spatial resolution of the detector is less affected.

To have a better view of the potential GigaTracker sensor lifetime, a test campaign to assess the radiation hardness of the FBK n-in-p sensors was carried out. They were fabricated on high resistivity Float Zone (FZ) wafers thinned to 200 µm (see section 3.1.2). The leakage current and full depletion voltages after proton irradiation was measured for test structures implemented on three different sensor wafers. A full assessment of the p-in-n FBK sensors radiation hardness has been conducted by the NA62 collaboration prior to this work [115].

Test Structures

The test devices (diodes) were implemented on the same wafers as the sensors. Each one occupies a surface of 4.72 mm by 4.72 mm on the wafer. A 2 mm circular opening of the metalization on the front side allow to illuminate the diode bulk with a laser. The 3 mm by 3 mm active area is surrounded by twelve guard rings. A cross section of the device is shown in Figure 3.9.

Twelve diodes from three wafers, named W1, W8 and W12, were diced and used for this study. Depending on the wafer, the p-spray and p-stop doping concentration varies, see Table 3.4.

Irradiation Campaign

The irradiations took place at the Cyclotron Resource Centre (CRC) in Louvain-la-Neuve. The high intensity T2 line with a 50 MeV, 0.1 µA proton beam was

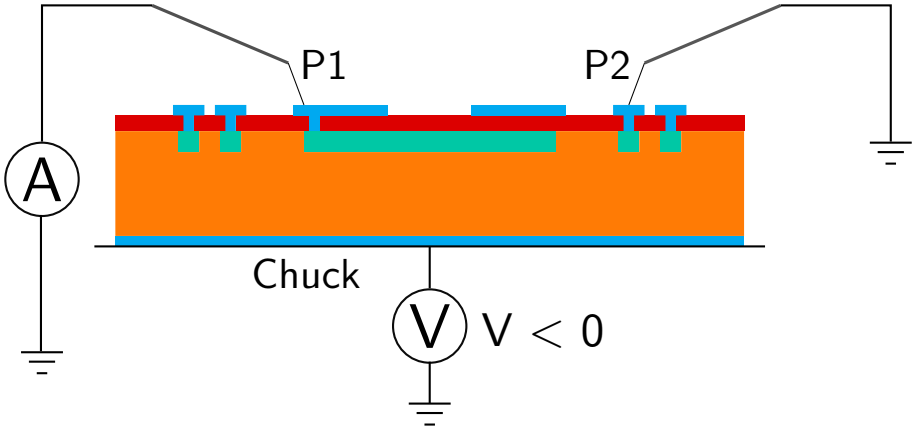

Figure 3.9: Schematic cross section of the test diodes we characterized. A sketch of the electrical connections is superimposed. The large central opening in the metallisation allows for the laser illumination of the diode bulk. The drawing is not to scale and only two out of the twelve guard rings are represented.

Table 3.4: Doping densities of the inter-pixel isolation structures.

Wafer	*p*-spray (10^{12} cm^{-2})	*p*-stop
1	0.5	4
8	1	2
12	1	4

Figure 3.10: Photograph of the T2 beam line. The sample supports are slided between two copper plates inside the last vacuum chamber of the line. After the insertion, the chamber is closed and evacuated. The beam is going from the top right to the bottom left.

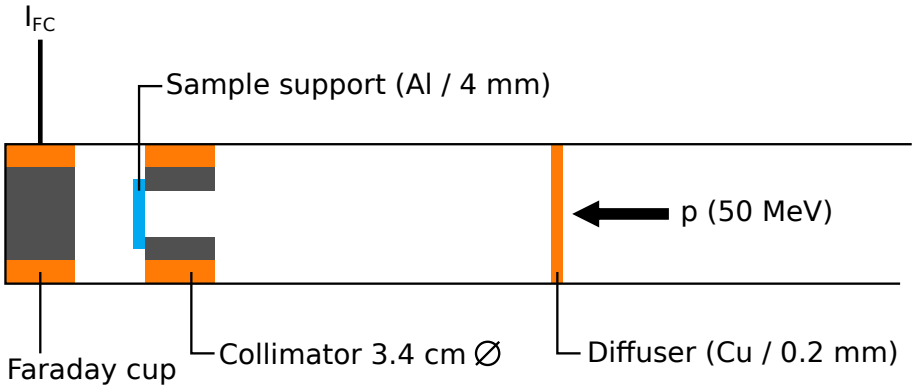

Figure 3.11: Schema of the T2 beam line. The proton beam is uniform within ± 10% after the collimator. The I_{FC} current corresponds to the Faraday cup reading.

Table 3.5: Devices and target fluence.

Diode	Target Fluence (1 MeV eq. n cm^{-2}) W1	W8	W12
D1	Damaged	5.0×10^{13}	3.8×10^{13}
D2	1×10^{14}	1.0×10^{14}	8.4×10^{13}
D3	1×10^{14}	1.0×10^{14}	8.4×10^{13}
D4	2×10^{14}	2.0×10^{14}	1.8×10^{14}
D5	2×10^{14}	N/A	1.8×10^{14}
D6	5×10^{13}	1.0×10^{13}	8.4×10^{13}
D7	1×10^{14}	5.0×10^{13}	1.8×10^{14}
D8	1×10^{14}	8.4×10^{13}	2.7×10^{14}
D9	2×10^{14}	1.8×10^{14}	4.7×10^{14}
D10	2×10^{14}	2.0×10^{14}	N/A
D11	2×10^{14}	2.7×10^{14}	1.8×10^{14}
D12	3×10^{14}	3.0×10^{14}	2.7×10^{14}

used for this test. The work area is shown in Figure 3.10. The test diodes were placed on custom 4 mm thick aluminium supports that can host up to 20 test structures. As illustrated in Figure 3.11 before reaching the samples, the protons cross a 2 µm thick copper sheet and a 3.4 cm diameter graphite collimator. The mean proton energy at the samples position was estimated to be 48.5 MeV.

The delivered fluence was continuously monitored by a Faraday cup placed at the end of the beam line. An automated control program stopped the beam when a predetermined fluence was reached.

To check beam uniformity and the absolute delivered dose alanine pellets were inserted in the test supports. According to the manufacturer the pellets saturate at around 100 kGy. The reading device was calibrated for a ^{60}Co gamma ray source, depending on the actual particle type and energy one has to apply an efficiency correction. For 48.5 MeV proton this factor is close to one [116].

The delivered dose to the pellets was converted into a proton fluence with the following formula:

$$\Phi\left(\mathrm{cm}^{-2}\right) \approx D\,(\mathrm{Gy})\,\frac{6.24 \times 10^{9}}{\mathrm{d}E/\mathrm{d}x}\ , \tag{3.1}$$

where $\mathrm{d}E/\mathrm{d}x = 12.72$ MeV g/cm^{-2} for 48.5 MeV proton in alanine [116]. The delivered dose on the top and on the bottom of the illuminated area agrees within ten percent, however the absolute values are increasingly inconsistent for doses superior to 10 kGy, likely because of the saturation of the alanine.

The irradiation plan is detailed in Table 3.5. Through the text we always refer to 1 MeV eq. n cm^{-2} fluence, the 48.5 MeV proton fluence was converted by applying a hardness factor of 1.822 [99, 100]. Immediately after each irra-

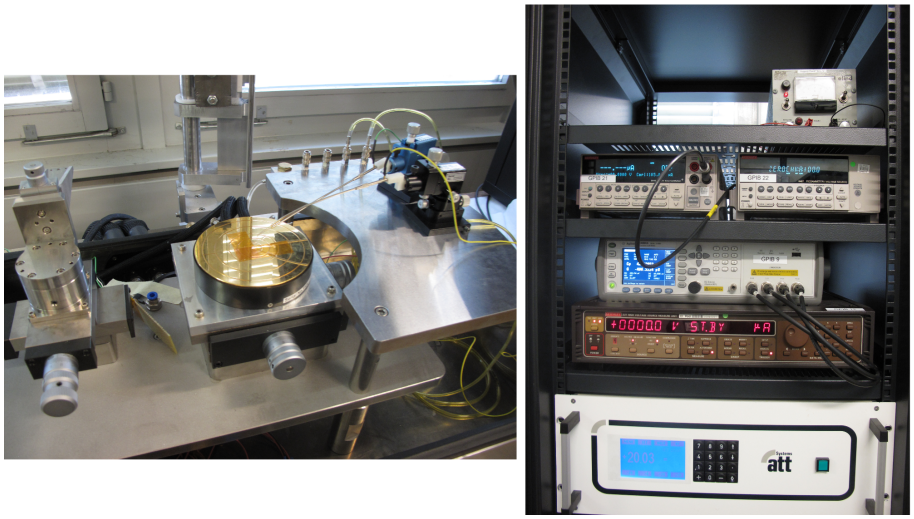

Figure 3.12: Photograph of the probe station (left) and of the lab equipment (right). The probe needles are placed manually on the sample, the chuck temperature is regulated.

diation cycle the test diodes were stored in a cold box with carbon ice; after a few hours they were moved for permanent storage in a freezer at −18 °C.

Measurements

The measurements were carried out in the Silicon Sensor R&D lab at CERN with the setup shown in Figure 3.12. The test setup principle scheme is displayed in Figure 3.9, probe needles are placed on the central pad (P1) and on the innermost guarding of the diode (P2). The chuck provides the electrical connection to the backside of the device. For each test structure a I-V and a C-V curves were successively measured. Currents were measured with a Keithley 6487 current meter. In the 0 – 200 µA range the relative accuracy of the instrument is ± 0.1%. The bias voltage was provided by a Keithley 2410 voltage source. In the 0 – 1000 V range relative accuracy of the device is ± 0.02%. Finally, the capacitance was measured with an Agilent E4980A LCR meter. The setup was let warm up for 20 minutes before the first measurement.

To froze defect clusters, the test diodes were keep at low temperature during their transfer to CERN and were immediately put in the Silicon Sensor R&D lab freezer upon reception. Therefore, for all the comparison with the literature we suppose that no annealing took place. The probe station we used was equipped with a thermally regulated chuck, all the measurements were performed at 20 °C. All the results are grouped in Appendix C, in the following only examples and summary plots are presented.

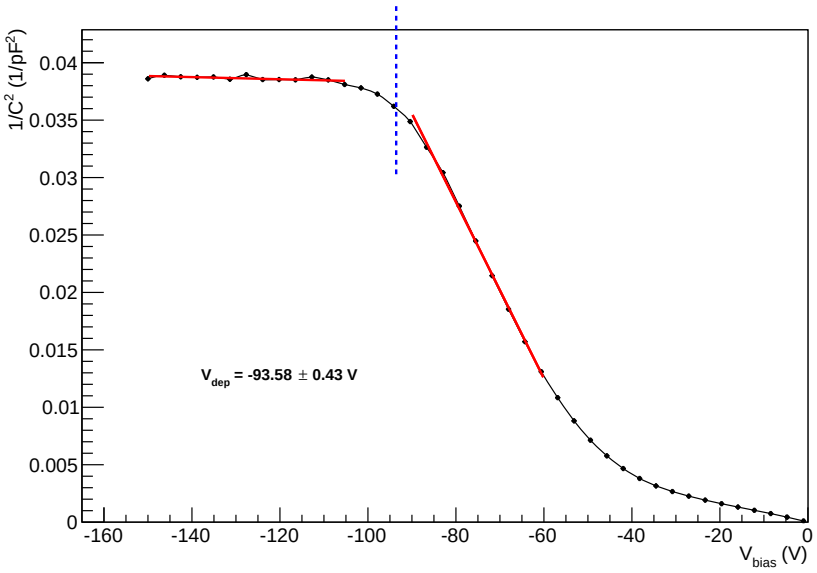

Figure 3.13: Typical $1/C^2$-V curve. The full depletion voltage is determined by the intersection of the two fitted curves. This particular curve is for the diode 2 diced from the wafer 1; it was exposed to 10^{14} 1 MeV eq. n cm^{-2}.

Depletion Voltage Measurements The full depletion voltage can be extracted from the C-V curve, indeed, the capacitance C of the diode

$$C\left(V\right) \propto \begin{cases} 1/\sqrt{V} & , \quad V < V_{\text{dep}} \\ \text{cst.} & , \quad V > V_{\text{dep}} \end{cases} , \tag{3.2}$$

depends on the bias voltage as long as it is lower than the full depletion voltage.

The baseline LCR settings were 500 mV signal at 10 kHz. Four diodes (W1D2,W1D3,W1D7 and W1D8) were also measured at 455 Hz, indeed, for irradiated devices the C-V the curve displays a test signal frequency dependence. The relationship between the capacitance and the bias voltage is less pronounced at high frequencies [117]. The magnitude of the effect increases with the delivered fluence. The effect is visible in Figures C.5 and Figure C.6 (in Appendix C).

The full depletion voltage is obtained by plotting $1/C^2$ against the bias voltage and fitting two straight lines, one in the constant region and one in the descending part, the intersection point of the two lines gives the full depletion voltage. A typical example is shown in Figure 3.13. The figure 3.14 summarises the results.

As one expects, the full depletion voltage is proportional to the delivered fluence. The required bias voltage grows from about 30 V for non-irradiated sensor to around 125 V for typical yearly fluence (1×10^{14} 1 MeV eq. n cm^{-2}).

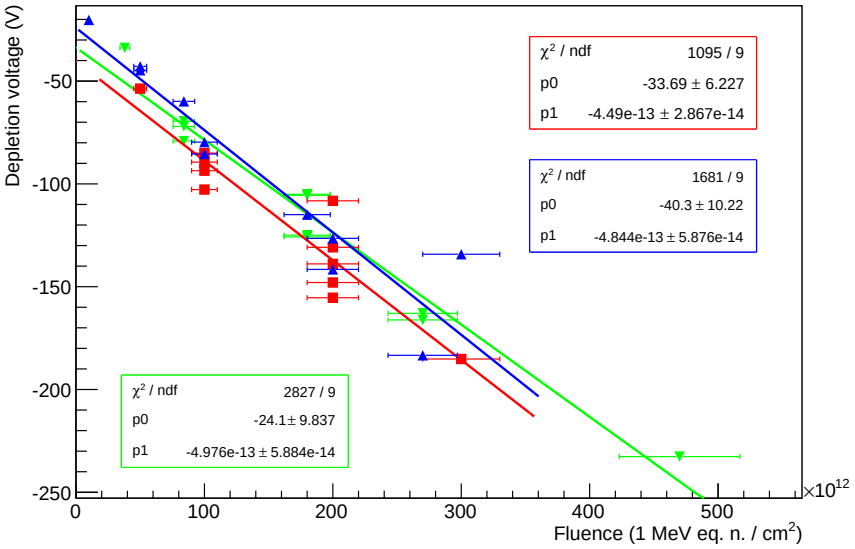

Figure 3.14: Summary plot, the points corresponding to diodes diced from the wafer 1, 8 and 12 are, respectively, colored in red, blue and green.

This effect can be compensated by increasing the sensor bias voltage.

Leakage Current Measurements The I-V measurements allow to extract the leakage current. It is directly proportional to the received fluence:

$$J \propto \alpha\Phi \ , \tag{3.3}$$

where, according to the literature [91] the *damage constant* α, is independent of the silicon material and of the fluence on a large range. In contrast, α depends on the annealing duration and on the temperature [104]. At 20 °C and with no annealing we have $\alpha = 8.0 \times 10^{-14} \pm 4\%$ mA/cm [96] (p. 105).

The power supply compliance was set to 100 µA, we swept the voltage from 1 V to 1000 V by step of 20 V, the current was measured at each step.

The Figure 3.15 summarises the results normalized to the diode active volume. Fitting a straight line to the data point belonging to each wafer separately we find $\alpha = 8.0 \times 10^{-14}$ mA/cm , $\alpha = 8.5 \times 10^{-14}$ mA/cm and $\alpha = 8.2 \times 10^{-14}$ mA/cm for the wafers W1, W8 and W12 respectively. The slope is in good agreement with the literature.

Scaling the leakage current to the full scale sensor leads to 3 mA/cm^3 at 20 °C and 200 V. This is one order of magnitude above the typical values for the bulk current. The reasons for these relatively high currents were not identified with certainty. Multiple effects probably contribute: the measurements were not carried out in a clean environment, the aluminium support surface was not

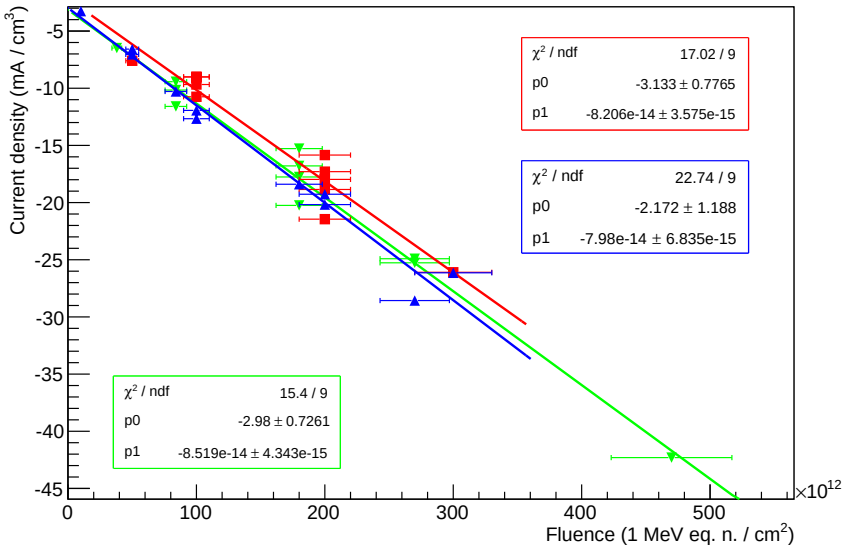

Figure 3.15: Summary plot, the leakage currents correspond to a bias voltage of 200 V and are normalized to the active volume of the diode. The points corresponding to diodes diced from the wafer 1, 8 and 12 are, respectively, colored in red, blue and green.

Table 3.6: Leakage current of selected diodes scaled to full scale sensor. All the diodes were biased at 200 V. The uncertainties on the measured current are negligible however all the diodes behave slightly differently.

Diode	Fluence (1 MeV eq. n cm^{-2} ± 10%)	Operation days (at nominal intensiy)	Leakage Current (µA) 20 °C	5 °C	−10 °C	−20 °C
W8D6	1×10^{13}	10	1070	286	88	43
W8D1	5×10^{13}	50	2160	576	178	87
W1D3	1×10^{14}	100	2957	789	244	119
W1D11	2×10^{14}	200	6190	1652	510	250

smooth and the test devices were clamped to the support with an aluminium grid. Scratches and surface contamination greatly increase the surface leakage current. Currents for different fluences and operating temperatures are reported in Table 3.6.

Results and Conclusions

The results obtained show that the doping concentration of the p-stop and p-spray does not affect significantly the radiation hardness of the test diodes. Independently of the received fluence, the measured currents were relatively high. This is likely linked to surface contamination or scratches. More importantly, the sensor response to the fluence agrees well with the literature. From this point of view, the detectors should be able to run at the required performance level for at least one year at nominal beam intensity. We can conclude that the FBK n-in-p sensors radiation hardness is adequate for the GigaTracker radiation environment. The detailed results are reported in Table C.1, Table C.2 and Table C.3 (in Appendix C).

3.2.2 Monte Carlo Simulation

The NA62 Monte Carlo (MC) simulation, `NA62MC`, models the full experimental chain: the particle generation, the transport, the decays and the energy deposition in the matter. During R&D phases the MC gave useful inputs for the detector design and allowed physics sensitivity studies. At later stages, the MC is an invaluable tool to understand non-trivial effects in the data.

The NA62 detector layout is modelled using the `Geant4` toolkit [118]. It simulates propagation of particles through matter and magnetic fields, including complex physical processes involved in the energy transfers to the medium. *NA62MC* uses the standard `FTFP_BERT` *physics list* to model the interactions. Particles are propagated through the secondary beam line by the TURTLE routine [119]. Kaon decays are parametrized by custom FORTRAN routines inherited from the NA48 experiment. The interested reader is referred to the source code [120] for the list of simulated decays. Pions and muons decays are directly handled by Geant4, thus, only the $\pi \to \mu\nu$ decay is simulated.

A detailed GigaTracker geometry, including the material composition, is implemented in `NA62MC`. In addition to the sensor, bump-bonds, chips and collimator that were already simulated, over the four last years, the microchannel cooling plate, the carrier card, the carrier support frame, the cooling plate connectors and related tubing, and the achromatic magnets were added. Moreover, the existing code has been made more modular. A snapshot of the GigaTracker "responsibility region" is presented in Figure 3.16. The implemented GigaTracker geometry is shown in Figure 3.17 and 3.18.

During the detector development phase, we used the MC to assess the carrier support frame design. Two configurations were under consideration, a standard aluminium frame (Figure 3.19) or a lighter but closer to the beam

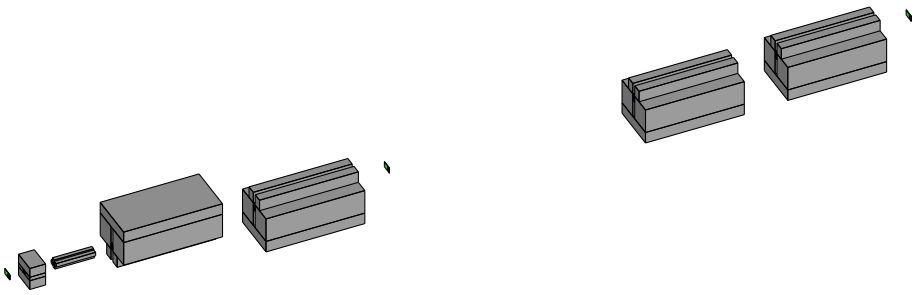

Figure 3.16: GigaTracker responsibility region, following the notation introduced in the section 3.1, from right to left, we have the station *GTK1*, the magnet *B4A*, the magnet *B4B*, the station *GTK2*, the magnet *B5*, the magnet *B6*, the *COLL 6/7*, *TRIM5* and *GTK3*. The *SCR1* scrapper, installed before GTK2, is not yet simulated.

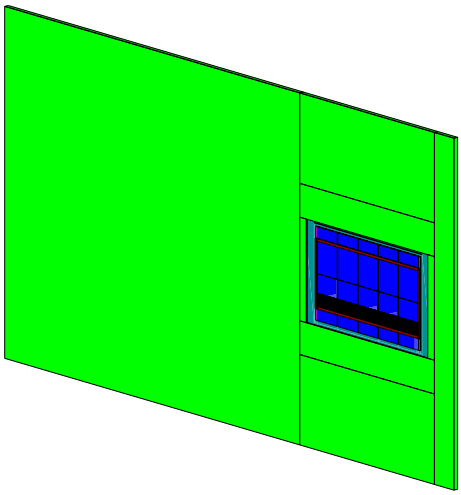

Figure 3.17: Downstream view, the pixels (black) are partially represented to show the underling readout chips (blue).

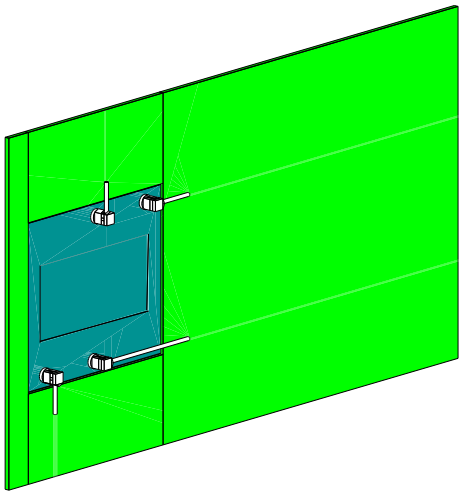

Figure 3.18: Upstream view, without mechanical frame. The cooling plate is colored in cyan while the PCB is painted in green.

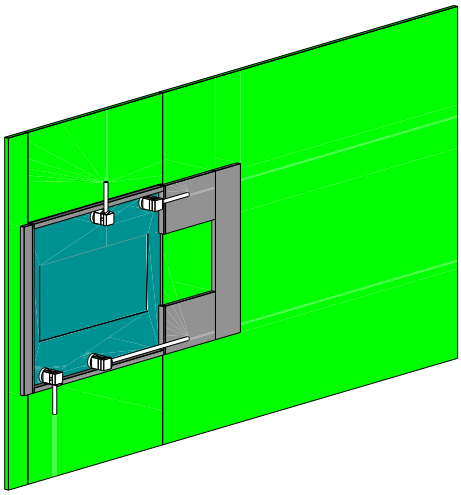

Figure 3.19: Downstream view, aluminum frame (gray).

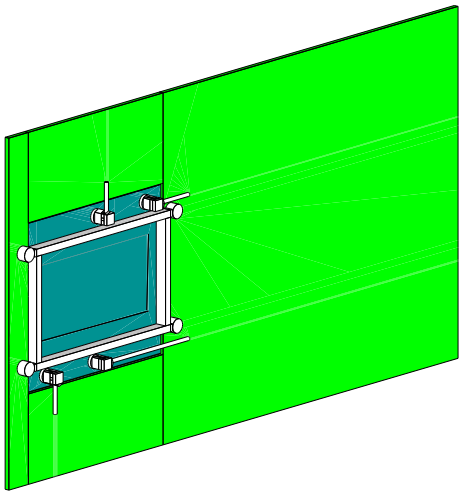

Figure 3.20: Upstream view, carbon frame (white).

area carbon frame (Figure 3.20). The aluminium and carbon frame effects on terms of secondary particle production proved to be indistinguishable. Finally, the material budget was further reduced by replacing the carbon frame by three carbon clamps.

3.2.3 Accidental Background

The hadron-nucleus interactions in the GigaTracker stations produce a variety of secondaries particles. The products of the inelastic interactions occurring in the two first stations are not transmitted thanks to the achromatic magnetics and to the collimator placed immediately before the last station. However, interactions taking place in the last station are more problematic. If not identified, they could mimic the $K^+ \to \pi^+ \nu\overline{\nu}$ signal. The CHANTI subdetector is installed just after the GigaTracker to reject this type of events. It covers the angular region between 50 mrad and 1.16 rad with respect to the beam axis.

In this section, the contribution of such reactions on the backgrounds to the $K^+ \to \pi^+ \nu\overline{\nu}$ signal is estimated. For that purpose, we developed a simplified Monte Carlo of the NA62 setup. Indeed, it was necessary to optimize the computation time and some subdetectors were not yet implemented in `NA62MC`. As one could have anticipated, Monte Carlo studies cannot give a definitive answer because of the lack of precise knowledge of the underlying processes. However, we identified interesting tools for rejecting part of the induced background.

Table 3.7: Cross sections for K^+p, π^+p and pp interactions (p = 70 GeV/c) [121]. The average numbers of charged particles resulting from one inelastic interaction, $\langle n_{\rm ch}\rangle$, are derived from [122, 123].

	$\sigma_{\rm el}$ (mb)	$\sigma_{\rm tot}$ (mb)	$\sigma_{\rm inel}$ (mb)	$< n_{\rm ch} >$
K^+p	2.30 ± 0.10	18.36 ± 0.09	16.06 ± 0.14	5.43
π^+p	3.35 ± 0.12	23.16 ± 0.12	19.81 ± 0.17	5.59
pp	7.41 ± 0.31	38.24 ± 0.19	30.83 ± 0.37	5.89

Interaction Cross Sections

Before starting the simulation, let's look at the order of magnitude of the phenomena. Some relevant hadron-proton cross sections are tabulated in Table 3.7. In general, the interaction probabilities depend on the nature and energy of the hadron, however, the total cross sections are essentially flat over the 10–100 GeV range. Computing the hadron-nucleon cross sections from the hadron-nucleus is not easy, values for various media have been calculated using the Glauber model [38]. Specifically, for high energy hadron on silicon the nuclear and pion collision length are 70.2 g cm^{-2} and 96.2 g cm^{-2} respectively. In other words, the probability of nuclear interaction in 500 µm of silicon is 1.7×10^{-3} for protons and neutrons and 1.2×10^{-3} for pions. That means that the rate of inelastic events is close to 1 MHz at nominal NA62 beam intensity.

The charged particle multiplicities distributions were measured in the 1970s for hadron-nucleon interactions [122, 123], the dispersion $D = \sqrt{\langle n_{\rm ch}^2\rangle - \langle n_{\rm ch}\rangle^2}$ grows linearly with $\langle n_{\rm ch}\rangle$.

The less probable charge-exchange processes could also contribute to the backgrounds. For instance, the reaction $K^+n \to K^0p$, changes a K^+ into a K^0 that can then decay into $\pi^+ l \nu_l$. Since the K_L^0 is relatively long lived, this process features displaced vertices and is therefore harder to control. The total cross section of the charge exchange was studied for relatively low hadron momentum ($3 < P < 12$ GeV/c) [124], extrapolating to 75 GeV/c we found 1.3 µb. This effect is much less probable than the inelastic interaction.

Monte Carlo Simulation

We chose the quark-gluon string (QGS) `Geant4` model to simulate the nuclear interactions. This model is valid in 50 GeV – 50 TeV range. For efficiency reasons, we only implemented the complete geometry of two last stations of the GigaTracker. The CHANTI, the STRAW chambers and the CHOD were active mock-ups; only their simplified shape and sensitive volumes were implemented in the simulation. We rely on geometrical acceptance criteria to simulate the RICH, the LAV stations and the MUV3. We used a broad definition of inelastic event: more than one charged or neutral tracks must cross a 3.5 cm diameter

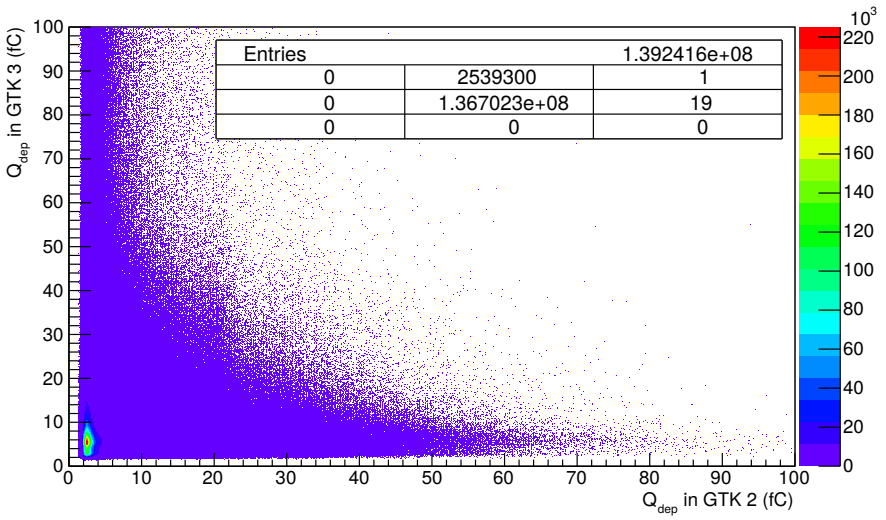

Figure 3.21: Inelastic events in the third GigaTracker station before the preselection.

imaginary sphere centred on the last GigaTracker station. Kaon decays were also filtered out. In total, we generated ten billion charged kaons and ninety thousand $K^+ \to \pi^+ \nu\overline{\nu}$ decays. Only events with an inelastic interaction in the last GigaTracker station were stored on disk for later analysis.

Inelastic Events Rejection

A simple level zero trigger simulation was implemented, the requirements were at least one charged track in CHOD and no hits in the MUV3 acceptance. A preselection was then applied to select single track events: exactly one K^+ in GigaTracker, one π^+ in RICH, and one charged particle with a momentum between 15 GeV/c and 35 GeV/c in the STRAW station. The momentum cut ensures that the pion and muon tracks with the RICH can be separated efficiently.

Four additional cuts were applied to reject the inelastic events, namely, no hits in CHANTI and in the LAV stations, the reconstructed square missing mass of the event must be between 0 and 0.01 $\mathrm{GeV}^2/\mathrm{c}^4$ or between 0.026 and 0.068 $\mathrm{GeV}^2/\mathrm{c}^4$ and, finally, the reconstructed decay vertex must be at least 49 cm after the last GigaTracker station.

The GigaTracker stations are purposely mounted with the sensor on the downstream side of the detector. The time-over-threshold, which is proportional to the deposited energy, can be used to reject inelastic events occurring the cooling plate or in the readout chips. To test this feature, we cut the hits that have a time-over-threshold greater than 22 ns, which corresponds to

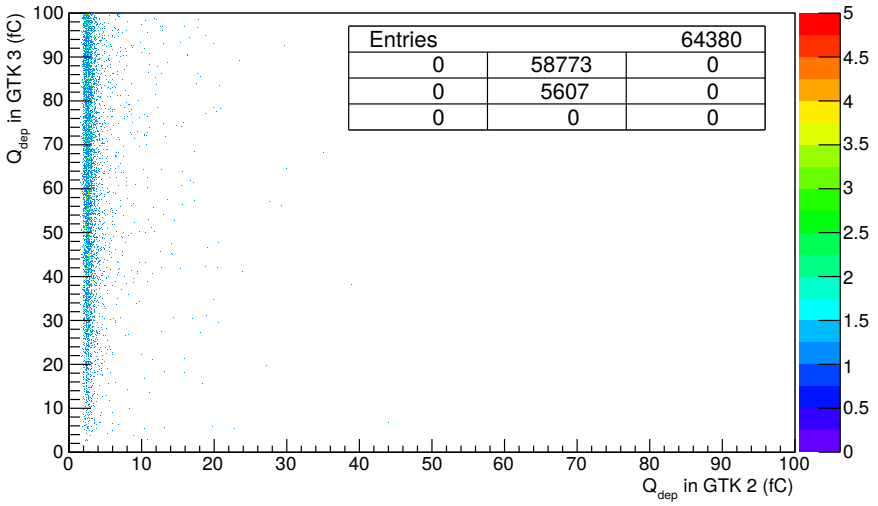

Figure 3.22: Inelastic events in the third GigaTracker station after the preselection. Applying the cut on the time-over-threshold on third station hits is equivalent to rejecting all the event with $Q_{\text{dep}} > 18$ fC. It allows to reject a significant fraction of the remaining events.

18 fC in the digitisation. As illustrated in Figure 3.21 and in Figure 3.22, the cut removes a significant fraction of all the inelastic events that pass the preselection.

Results and Conclusions

Out of 10^{10} generated K^+ decays only two events passed all the cuts. The study does not allow to draw strong conclusions about the background rejection factor however interesting variables were identified. Specifically, a cut on the GigaTracker hits time-over-threshold cut allow to gain almost one order of magnitude in the rejection power without degrading the signal acceptance. The combination of a good vertex reconstruction, the CHANTI veto and the time-over-threshold cut is especially powerful. The numerical results are summarised in Table 3.8.

3.2.4 Time Alignment and Time Walk Correction

All NA62 detectors use the same synchronised clock but the cables lengths, the particles time of flight and others delays introduce constant time offsets between them. The offsets can only be corrected offline. In doing so all the hits belonging to an event are centred around the trigger time. Every GigaTracker pixel has its own time offset, they have to be accounted for individually. This step is essential in the timing analysis.

Table 3.8: Fraction of the signal that passes the cuts. The numbers in parentheses are without the constraint on the time-over-threshold in the last GigaTracker station.

Cut	Signal	Background
Pre-selection	0.325	2.13×10^{-8} (6.44×10^{-6})
On the pre-selection set		
CHANTI	1	0.277 (0.020)
LAV	1	0.211 (0.261)
m_{miss}	0.565	0.394 (0.353)
Vertex	0.998	0.437 (0.013)
Total	0.183	2×10^{-10} (1.2×10^{-9})

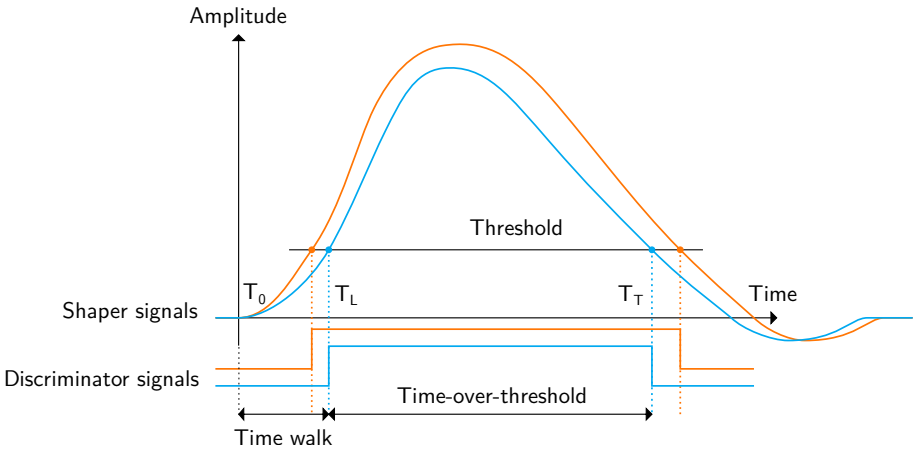

Figure 3.23: Illustration of the relation between the time walk and the time-over-threshold. Higher amplitude signals lead to bigger time-over-threshold and vice versa.

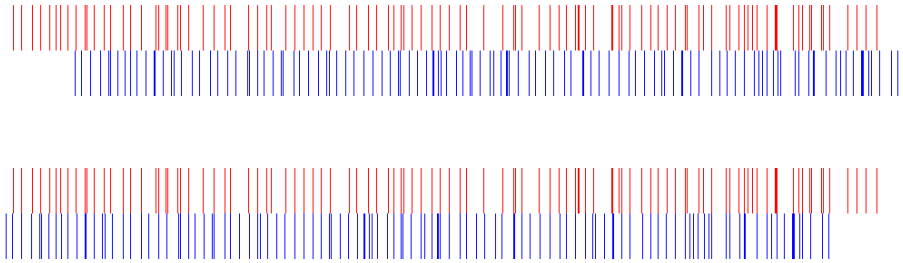

Figure 3.24: Representation of the simulated data used to develop the global time alignment algorithm before (top) and after (bottom) the procedure. The blue and red bars symbolise the hit arrival time measured on two successive fictive detectors. The two time series are derived from an unique master but noise, detection inefficiencies and time resolution effects are added. Furthermore, a known global time offset is introduced between the two series. The global time alignment algorithm finds the time offset for which the overlap between the two time series is the maximum.

The GigaTracker front-end is based on a *time-over-threshold* discriminator which requires an offline time walk compensation. As we will see, calibration curves are extracted from the data. Given that each pixel front-end is unique, a specific correction curve is needed for each pixel; the correction also depends on the detector operating conditions. Moreover, the aging of the sensor will affect the charge collection properties. For the reason stated above, the correction curve has to be recomputed regularly.

We will deal with the global time alignment of the detector before describing the time walk correction methods.

Global Time Alignment

All stations share the same clock but because of the time of flight and of various constant electronic delays, depending on the station, the hits corresponding to a same particle are shifted by a constant time amount. The first step in any reconstruction is to compensate for this effect.

The standard method consists of computing all the possible time differences between the hits belonging to a pair of stations. The corresponding distribution peaks at the time offset between the stations. In addition, the width of the peak gives the convoluted raw time resolution of the both GigaTracker stations. The time complexity of the algorithm is $\mathcal{O}(nm)$ where n and m are the number hits on the stations belonging to the pair.

We proposed another method based on Fast Fourier Transforms (FFT). The procedure is illustrated in Figure 3.24. It can be shown that the time offset T_{off} between two time series f and g is the argument of the maximum of the

series cross-correlation:

$$T_{\text{off}} = \arg\max_{t} (f \star g)(t) \ , \tag{3.4}$$

where $\arg\max_{t} H(t)$ (argument of the maximum) is the value of t for which the function H is maximal. More intuitively, we are computing the time offset which maximise the overlap of the two series.

We can take advantage of the FFT algorithm to compute the cross-correlation:

$$\mathcal{F}\{f \star g\} = (\mathcal{F}\{f\})^* \cdot \mathcal{F}\{g\} \ , \tag{3.5}$$

where $\mathcal{F}$ denotes the Fourier transform. The time complexity of the algorithm is $\mathcal{O}((n+m)\log(n+m))$ where n and m are the length of the time series. Since the typical values of n and m are large this technique is significantly faster than the standard method ($\mathcal{O}(nm)$). We used the proven FFTW3 library to compute the FFTs [125].

Time Walk and Pixel Time Offsets

To reach the best hit time resolution we need to correct the time walk and the individual pixels time offsets. Two methods will be presented to compute the individual pixel time offsets; one uses an external time reference, while the other one rely only on the GigaTracker assemblies.

Let's begin with the time walk correction. The idea behind the correction method is presented in Figure 3.23. Two timestamps are recorded when a shaped pulse crosses a predefined threshold, the first on the signal rising edge (T_L) and the second on the signal falling edge (T_T). The time-over-threshold ($T_T - T_L$) is proportional to pulse height and therefore indirectly to the amount of energy deposited in the pixel. Bigger time-over-threshold leads to smaller time walk and vice versa, one can use this relation to compensate for the time walk. The relation is fairly linear for medium energy deposits but non-linear behaviours appears for low and high energy depositions [126].

The correction curve for a given pixel is extracted by first fitting a Gaussian to the distribution of the hit time differences between the time reference and the pixel for a particular time-over-threshold bin. The procedure is repeated to cover the time-over-threshold range. Second, the means of the Gaussians are fitted to a correction curve. We compared two types of corrections: linear, as illustrated in Figure 3.25, and polynomial of fourth order. The polynomial correction did not significantly improve the time resolution. As an example, the correction factors (constant term and slope) obtained with the GigaTracker prototype are summarised in Figure 3.26. One immediately sees the large variability of the factors. The technique gives both the individual pixel time offset and the time walk correction.

A new method based on the Dijkstra algorithm for computing the pixel time offsets using only the GigaTracker detectors was developed. This tool was originally implemented for the 2014 pilot run but it has also been tested

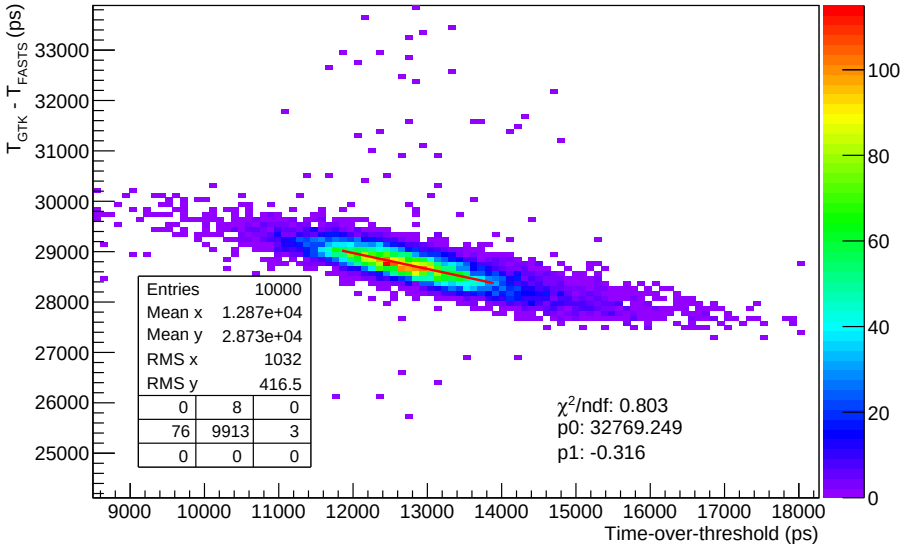

Figure 3.25: Typical linear ($\mathrm{TW_{corr}} = p_0 + p_1 \cdot \mathrm{ToT}$) time walk correction curve. This particular one is for the pixel 44 of the GTK2 demonstrator at a bias voltage of 300 V. The *FASTS* detector provided an accurate time reference. The color scale indicates the number of entries per 97.7 ps × 97.7 ps bin. The results obtained with the GigaTracker demonstrator are described in Section 4.1.

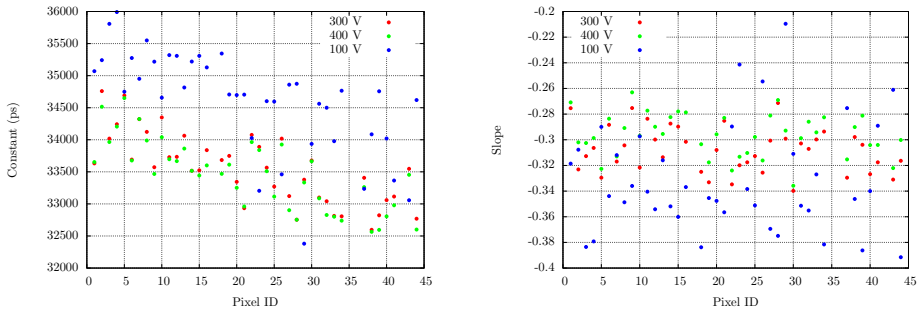

Figure 3.26: Illustration of the variation of the time walk correction factors. We see that the correction has to be computed separately for every pixel and every bias voltage. These correction factors were computed for the GTK2 demonstrator using data collected during a test beam; refer to Section 4.1 for more details.

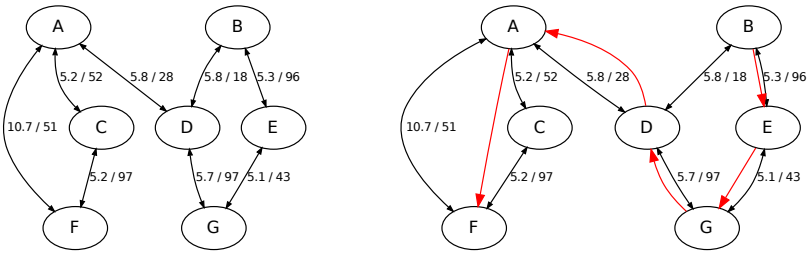

Figure 3.27: Illustration of the application of the graph algorithm on a simple example. The pixels are represented by the graph vertices. The edge labels are indicating the time offset and the number of tracks used to compute it. The red arrows on the right graph indicates the optimal path.

on GigaTracker demonstrator data. It has the advantage of not requiring a calibrated and aligned external time reference and was therefore useful during the full scale GigaTracker commissioning phase.

The time offset compensation can be included in the time walk correction. Nevertheless, in situations where the amount of data is limited or where an external time reference is not available one could be tempted to compute only the time offsets.

Let's use a digraph to represent the time offsets between the pixels. The vertices of the graph represent the pixels. The edges of the graph represent a collection of N *tracks* connecting a given pair of pixels. In this context, a track is simply defined by a time coincidence between two pixels. For this particular application, we used a 10 ns coincidence window. At this stage, with have a directed graph, each edge is labelled with the average time offset between the nodes it connects and the number of tracks used to compute the average. The situation is illustrated in Figure 3.27.

The goal is now to find an optimal path between a reference pixel (source) and all the others pixels (destinations). We define the optimal path as the route that maximises the number of tracks used to compute the time offsets. Indeed, doing so we reduce the statistical uncertainty attached to the offsets. More precisely, we used the Dijkstra Algorithm to find the path that minimise the distance

$$D_{ij} = 1/N_{ij} \ , \tag{3.6}$$

where N_{ij} is the number of tracks connecting the pixel i and the pixel j. The edge connecting i and j is noted k. The procedure is repeated for all the destinations.

We assign a *score* to each route:

$$S = \sum_k D_k = \sum_k \frac{1}{N_k} \ , \tag{3.7}$$

Table 3.9: Root node B. Lower scores are better.

Target node	Time offset	Score
A	-1.1	0.08
C	4.1	0.1
D	4.7	0.04
E	5.3	0.01
F	9.6	0.1
G	10.4	0.03

where D_k is the *length* of the edge k. The lower the score, the lower the statistical uncertainty. If a pixel cannot be reached, its score is $+\infty$. The statistical error attached to a time offset is then simply

$$\sigma_{\text{off}} = \sigma_t \sqrt{S} \ , \tag{3.8}$$

where σ_t is the pixel time resolution. The results corresponding to the example presented in Figure 3.27 are reported in Table 3.9.

The *Graph* method is indirect: it is not a substitute for the classical method. However, it is fast and require no external information. It is ideal when the statistics are limited or to make cross-checks. We applied the method to test beam data for comparison. The results of both methods are presented in Figure 3.28. The differences are smaller than the intrinsic pixel time resolution.

3.2.5 Spatial Alignment

The spatial alignment of GigaTracker is relatively straightforward, the stations are mechanically very well constrained by the vessel and the only relevant degrees of freedom are in XY plane. As explained in Section 3.1.5, the sensor assembly is glued to the cooling assembly which is clamped to the carrier card. The latter is glued and bolted to the aluminium mechanical frame which is in turn bolted to the vessel. Finally, the vessels were aligned by surveyors. Nevertheless, small offsets can be introduced during the assembly of all the components hence the alignment must be carefully checked.

While investigating the different track reconstruction methods we implemented a simple Kalman filter. With only three tracking stations and no magnetic field this approaches brings no real benefits over a standard linear regression. Nevertheless, the algorithm is very flexible. Instead of trying to determine the track momentum knowing the detector geometry we can extract the detector geometry knowing the track momentum.

We used a simplified model for the track propagation where the multiple scatterings were not included. In addition, the direction of all the incoming particles was considered to be normal to the first station sensor surface. Under these assumptions and using the first station as the reference position, we can

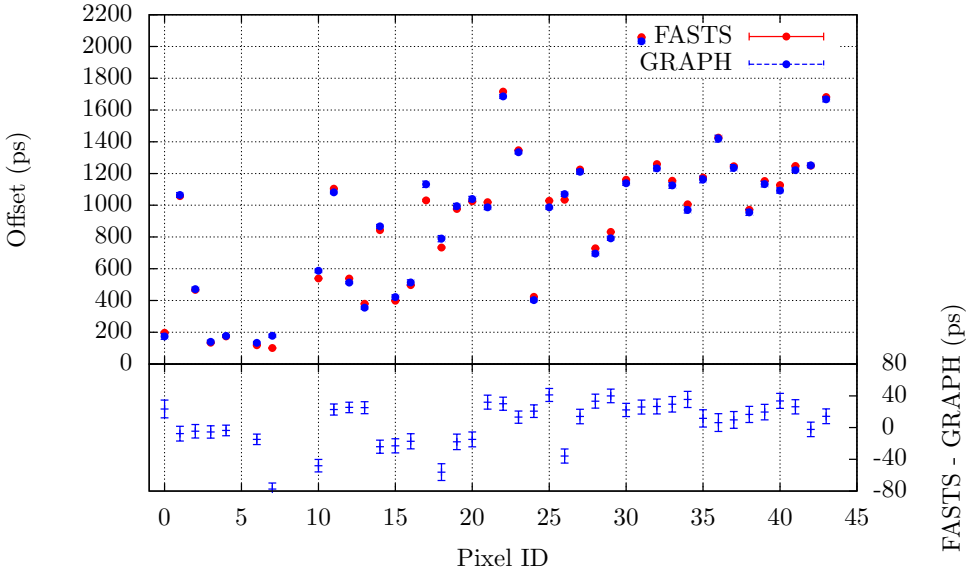

Figure 3.28: Comparison of the two methods used to compute the pixel time offsets. The *Graph* technique uses only information from the GigaTracker assemblies.

write down a simple model for the track propagation:

$$x_2 = x_1 + x_2^{\text{off}} \ , \tag{3.9}$$

$$y_2 = y_1 + \frac{\beta}{p_z} + y_3^{\text{off}} \ , \tag{3.10}$$

and

$$x_3 = x_1 + \frac{\alpha}{p_z} + x_3^{\text{off}} \ , \tag{3.11}$$

$$y_3 = y_1 + y_3^{\text{off}} \ , \tag{3.12}$$

where x_i and y_i are the position of the hit on the station one, two and three, and x_i^{off} and y_i^{off} are the unknown offsets of the station two and three with respect to the first station. The parameters

$$\alpha = 585 \times 300.2 \times 0.299892458 \ \text{MeV}^{-1} \ \text{c mm} \ , \tag{3.13}$$

$$\beta = 3600 \times 4169.5 \times 0.299892458 \ \text{MeV}^{-1} \ \text{c mm} \ , \tag{3.14}$$

encode the geometry and the magnet bending power for the TRIM5 and the bending magnets respectively. The magnets bending power as a function of the current can be found in [107]. See Section 3.1.1 for a description of the detector geometry and of the magnets installed in the GigaTracker region.

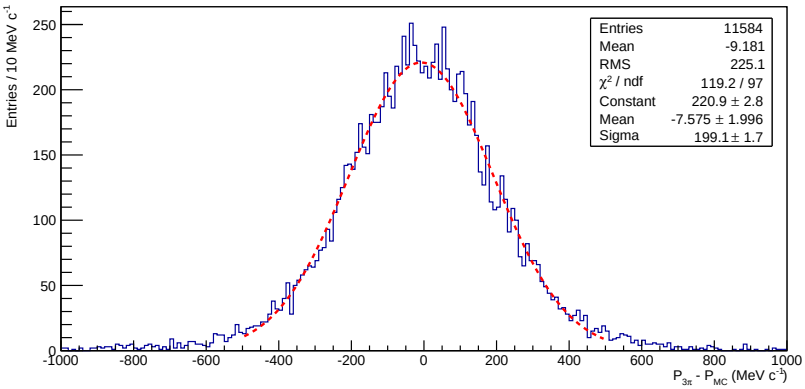

Figure 3.29: Kaon momentum reconstructed from simulated $K \to \pi^+\pi^+\pi^-$ decays.

As an input, the algorithm takes the hit positions x and y on the three stations and the track momentum. An initial state vector is constructed using the hit position on the reference station. After the two steps, it holds the updated values of x^{off} and y^{off}.

Since we assume that the GigaTracker is misaligned, we need to extract the track momentum from another source, we investigated three options. First, we can simply use the nominal beam momentum since it is well defined ($\sigma = 750$ MeV/c) by the beam line configuration. Second, we can select $K^+ \to \pi^+\pi^+\pi^-$ decays and reconstruct the kaon momentum. A simple selection using Monte Carlo data is shown in Figure 3.29 ($\sigma = 200$ MeV/c). This method assumes that the STRAW tracker is itself well calibrated. Finally, we can turn off the TRIM5 magnet and steer a low intensity muon beam into the STRAW tracker acceptance. The last technique could also be useful for the global alignment of the NA62 particle tracking system.

Results and Conclusions

The algorithm was tested for different offsets combination using a sample of ten thousand Monte Carlo generated tracks. At the nominal trigger rate, they could be collected in about ten seconds of beam. The results are shown in Figure 3.30.

The algorithm is very linear but depending on the situation a small systematic bias is present. If one station is misaligned along one axis the bias is less than 1 µm while when all the stations are misaligned on both X and Y axis it increses to 20 µm. Furthermore, the results are very sensitive to variations of the magnetic field.

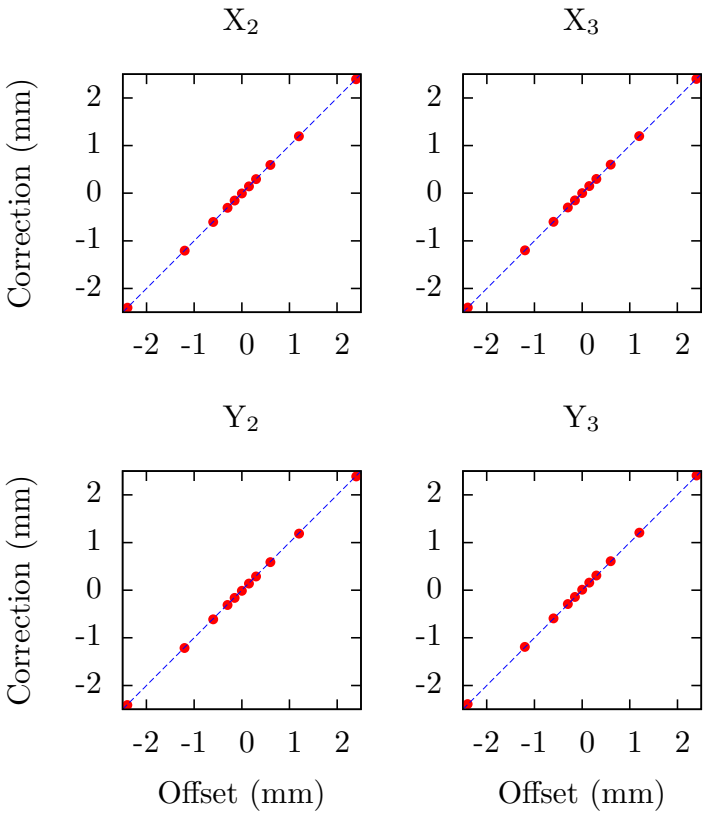

Figure 3.30: Performance of the alignment algorithm. The red dots indicate the algorithm output for a given offset. The blue dashed line represents a perfect correction. In this case we assume the beam momentum to be 75 GeV/c.

Table 3.10: Configuration of the detectors used during the 2014–2015 run. The *station* column refers to station in which the detector is installed. GTK_2 was affected by temperature interlock problem on chip #0 when it was first installed the 25th Nov. 2014. The issue was caused by bad contact between the chip and the cooling plate; it was fixed and the detector was reinstalled 9th Dec. 2014. The GTK_1 cooling plate broke the 18th June 2015 because of an over pressure caused by a misconfiguration of the cooling plant; the detector was replaced with GTK_2.

Detector	Station	Chip thickness (µm)	Cooling plate	Carrier	Installation
GTK_1	3	450	CEA Leti Batch 1	ELTOS Batch 2	6th Nov. 2014
GTK_2	1	450	CEA Leti Batch 1	ELTOS Batch 2	9th Dec. 2014
GTK_3	2	100	CEA Leti Batch 1	ELTOS Batch 3	11th Dec. 2014
GTK_1	1	–	–	–	17th Jun. 2015
GTK_2	1	–	–	–	1st Jul. 2015
GTK_3	3	–	–	–	29th Jul. 2015
GTK_4	2	100	CEA Leti Batch 1	ELTOS Batch 3	5th Aug. 2015

3.3 2014–2015 Operation Summary

The GigaTracker detectors have been named GTK_X, where X is the serial number. An overview of the detectors is presented in Table 3.10. A photograph of a detector before installation is shown Figure 3.31.

In 2014, NA62 received beam from 6th October 2014 at 8 am to 15th December 2014 at 8 am. The run was mostly dedicated to the commissioning of the subdetectors and of the trigger and data acquisition systems.

The TDCpix chip were untested before being diced from the wafer and bonded to the sensor. In addition, because of fabrication issues with the carrier card, only one chip on GTK_1 and GTK_2 and two chips on GTK_3 were operational and fully characterized. All sensors where p-in-n type manufactured by FBK. The first batch of cooling plates were 275 µm thick instead of the nominal 130 µm.

The first GigaTracker detector (GTK_1) was installed in the third vessel the 6th November 2014. The commissioning of the cooling plant and the power supplies took place during the following days. Initially, the communication with the DAQ was prevented by inverted optical fibre adapters. Moreover, an excessive voltage drop across the low voltage supply cables tripped the low voltage power supplies (PSUs) when the TDCpix phase-locked loops (PLLs) were powered on: the PSUs were not able to react in time to the sudden current draw. The issue was temporally solved by doubling the cables. The first beam data were acquired on 28th November 2014.

To test the tracking capabilities of the detector at least three chips need to be aligned in the beam. Indeed, as the beam divergence at the third GigaTracker station is about 100 µrad, the beam particles are crossing the same regions of the sensor on each detector. To assure the alignment, GTK_3 was installed in the second station with the sensor upstream. In other to mount it,

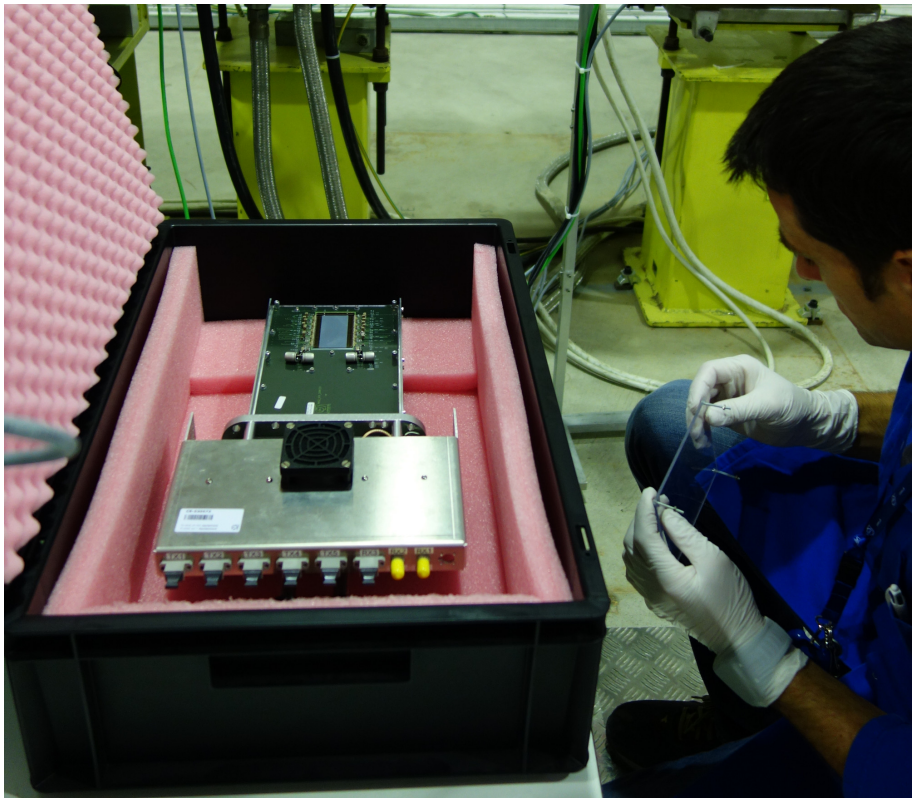

Figure 3.31: Photograph of a GigaTracker detector still inside its transport box. The sensor is the gray patch close to the picture centre. The oval flange marks the air-vacuum interface.

the vessel vacuum flange had to be inverted. The flange rotation displaced the centre of the sensor by +20 mm along the Y-axis and by +15 mm along the Z-axis. In order words, most of the beam was passing below the active area of the second station. This was not immediately recognised.

The sensor bias voltage was set to 200 V. Two 100 kΩ resistors placed in series with the sensor as current limiter decreased the effective bias voltage to about 170 V. Under these conditions, the sensors draw about 135 µA which is considered rather high. Part of the current was probably caused by enhanced surface effects because of chipping during the sensor dicing, the problem is investigated by IZM which produces the sensor assemblies.

The cooling plant chiller was not turned on during the commissioning phase therefore the cooling plates temperatures were close to the cavern ambient temperature, about 20 °C. The operating pressure was 3.2 bar for a coolant flow of 2.1 g/s for each detector.

The readout system was running in standalone trigger-less mode. That is, it was not synchronized with the global NA62 trigger and data acquisition system. The raw data were directly stored on dedicated off-the-shelf PC.

To sum up, the TDCpix chip was never tested in beam before the 2014 run. Despite the small hiccups during the installation the chip performed very well.

In 2015, NA62 received beam from 15th June at 8 am to 16th November at 8 am. Many of the 2014 issues were resolved, namely, the low voltage drop caused at the PLL startup was solved by adding decoupling capacitors to the carrier card; thanks to improvements to carrier card six, eight and six chips were readout on GTK_2, GTK_4 and GTK_3 respectively; the cooling plant operating temperature was set to −20 °C; the readout system was integrated in the global NA62 data acquisition system and the second station offsets were corrected. However, new issues appeared. First, the 18th June, the cooling plate of GTK_1 broke because of an over pressure caused by a misconfiguration of the cooling plant. This was immediately corrected. Second, the new integrated data acquisition starts to lose packets when the beam intensity reach about 40 percent of the nominal intensity. This is currently addressed. Finally, an abnormal number pixels are noisy. In addition, the phenomenon is burst dependent, the noisy pixel seems to appears and disappears randomly. This is not yet understood and it is probably the most pressing concern.

3.4 Summary and Discussion

GigaTracker measures the momentum, the direction and time of passage of all the secondary beam particles. It is made of three identical and independent silicon pixel detectors operated in vacuum. The TDCpix readout ASIC was specially developed for the GigaTracker. It can process 210 million of hits per second while keeping the detection efficiency above 99 percent and the hit time resolution below 200 ps.

Significant research and development efforts have been directed towards the thermomechanical integration. To keep the material budget minimal, the final detector is cooled by a silicon microchannel cooling plate. It is the first application of this technology in high energy physics. During the 2014–2015 period the total thickness of the GigaTracker in the area crossed by the beam was between 605 and 805 µm. This figure will be reduced to 535 µm with next batch of detectors which will be installed in 2016.

The detectors will be regularly exchanged to ensure that the hit time resolution and the detection efficiency stays optimal. The replacement frequency will depend on the beam conditions during the runs.

The irradiation and characterisation of n-in-p diodes diced from FBK sensor wafers indicates that sensors radiation hardness is adequate for the NA62 experiment. The damage constant measured agrees well with the literature however the leakage current was higher than expected, independently of the delivered fluence. The indications, confirmed by IZM which is dicing the sensors are that it is due to surface damage. Nevertheless, the sensor should sustain at least 100 days of operation at nominal intensity.

We studied the accidental background caused by last GigaTracker station using an early Monte Carlo model of NA62 experiment. We pointed that the hit time-over-threshold allow to identify the inelastic events in a complementary way to the standard cuts. The background caused by inelastic events in the last GigaTracker should be evaluated directly from the data.

Finally, we created time and spatial alignment tools for the GigaTracker. Time walk correction was thoroughly explored, we demonstrated that a linear correction per pixel is sufficient to reach the required time resolution. The correction curve strongly depends on the bias voltage.

Confronted to the low statistics and lack of synchronization between the GigaTracker and NA62 DAQ during the 2014 pilot run, we devised two algorithms to extract the detector and pixel time offsets. Notably, a technique based on the graph theory was used to extract the pixel time offset using only the GigaTracker data. It is fast and reasonably accurate even if it was not designed as a substitute to the more traditional methods which rely on an external time reference. Finally, we proposed a simple solution to align in space the three GigaTracker detectors. It is based on the independent measurement of the kaon momentum from the $K^+ \to \pi^+\pi^+\pi^-$ decay.

In the next chapter, we will study the performances of the prototype and of the full scale GigaTracker detector in real conditions.

Chapter 4

GigaTracker and NA62 Commissioning

The NA62 experiment was officially approved by the CERN in July 2007. The preparation phase lasted until June 2015. The first beams were delivered in autumn 2014 to allow the commissioning of the experiment.

The GigaTracker was partially installed in the NA62 cavern in November 2014. As it has been reported in the Section 3.3, the detector was not fully commissioned. Notably, only 10 percent of the channels were readout and the data acquisition system was running independently of the global NA62 system. Nevertheless, it was a moment of truth as only a 45 pixels demonstrator had ever been tested in beam.

Moreover, the pilot run gave us a first opportunity to study the general performance of the NA62 experimental setup. Like the GigaTracker, many subdetectors were not fully commissioned. Especially, the muon vetoes were not operational, the STRAW tracker data were not included in the global NA62 data stream and the trigger system was based on simple NIM logic. Despite this, the collaboration was able to show very encouraging results.

This chapter starts with the determination of the hit time resolution and hit detection efficiency of the GigaTracker prototype. The results obtained sets the bar for the full scale detector. Furthermore, we used the data collected during that campaign to establish the best time walk correction methods.

Next, we explored the data collected with full scale GigaTracker detector during the 2014 pilot run. We began with an overview of the secondary beam properties and of general behaviour of the detector. Then, we applied the techniques developed with the test beam data to do a first estimate of the hit time resolution of the full scale detector. The state of the detector in 2014 prevented us to evaluate the tracking performance of the detector.

Moving on to the NA62 data, an unexpected *beam component* was spotted in the downstream detectors. That is, a 75 GeV/c beam like component hit

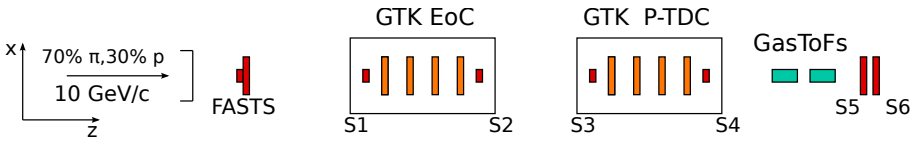

Figure 4.1: Schema of test beam experimental setup viewed from the top. Only the FASTS and the GTK *EoC* detectors were used in the present analysis. The beam is going from left to right.

directly the STRAW tracker; it should not happen. We tried to reproduce this effect with the Monte Carlo simulation of the detector. Finally, we did a preliminary $K^+ \to \pi^+\pi^+\pi^-$ decay selection. As a benchmark, we compared the shape of the reconstructed kaon mass distribution with the one predicted by the Monte Carlo.

4.1 GigaTracker Demonstrator

The results presented in this section are the outcomes of a re-analysis of datasets collected during a test beam in 2010. It was motivated by a better understanding of the readout chip and of the time walk compensation technique. Moreover, compared with the previous analysis the clock drift has been more carefully compensated. The main objectives were to measure the hit time resolution, the detection efficiency, the charge sharing effects.

The GigaTracker demonstrator is described in Section 3.1.7, here we will focus on the study of the prototype performances. To begin with, the experimental setup and the analysis workflow will be described. Then, we will explain in details how the time resolution, the detection efficiency and the charge sharing effects have been determined for different bias voltages.

4.1.1 Test Facility and Experimental Setup

The test beam was carried out at the CERN PS T9 secondary beam line from 16th Sept. to 7th Oct. 2010.

The beam was composed of 70 percent of pions and 30 percent of protons with a selected momentum of 10 GeV/c $\pm$ 0.7%. Two spills of 0.4 s each per PS super cycle ($\approx$ 47 s) were allocated for this test. The beam intensity was not logged but was estimated to be around 2×10^5 particles / spill.

Three orthogonal axes were defined to form a right-handed coordinate system: the Z-axis follows the beam direction while the Y-axis points towards the zenith.

Following the scheme presented in Figure 4.1, after exiting the secondary beam line vacuum, the particles crossed a pair of scintillator bars placed in a cross shape, perpendicular to the particle axis. The bars were equipped with

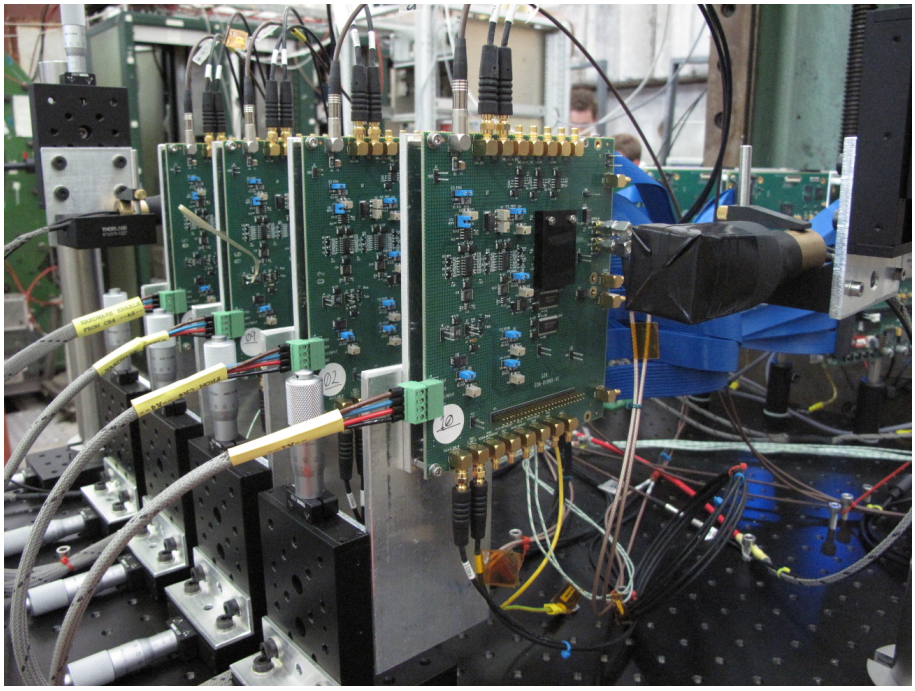

Figure 4.2: The detectors were installed in the CERN PS East Area T9 beam line. The four GigaTracker demonstrators are surrounded by two small plastic scintillators, the beam is going from right to left. The sensors and the readout chip are attached at the centre of the carrier card and protected by black plastic covers.

Table 4.1: Naming convention and position of the GTK assemblies. The chip ID refers to a unique identifier present in the raw GTK data stream. The positions are relative to the table edge.

Chip ID	Position along the Z axis (mm)	Assembly
10	207.1	GTK10
2	308.4	GTK2
9	408.0	GTK9
5	508.4	GTK5

one photomultiplier tube (PMT) at each end. We will use the shorthand *F12* and *F23* to refer to the horizontal bar and vertical bar respectively. Collectively, the bars are treated as a single *FASTS* detector. The assembly provided an external time reference to the GigaTracker demonstrators. Two small 3.8 mm by 5 mm, 5 mm thick, plastic scintillators, S1 and S2, were placed before and after the described setup. Their main purpose was to trigger the readout of the system.

Subsequently, four GigaTracker *EoC* demonstrators were placed on a moving table. In the following we will use the shorthand *GTK assembly* for the GigaTracker *EoC* demonstrator. The GTK assembly is a 1.8 mm by 3.0 mm 45 pixels sensor bump-bounded to a TDCpix ASIC prototype, see Section 3.1.7 for a description. The beam was impinging normally on the sensors. Following the beam direction, they were named GTK10, GTK2, GTK9 and GTK5.

The four GigaTracker *P-TDC* demonstrators [13] and the two GasToF [127] placed next were not part of our data acquisition system and are not used for this analysis.

Before the test beam all the detectors were aligned by surveyors with an accuracy of 150 µm. A photograph of the four GigaTracker stations as they intercepted the beam during test beam is presented in Figure 4.2. The positions of the GTK assemblies relative to table edge are tabulated in Table 4.1.

4.1.2 Data Acquisition Systems

The demonstrator ASIC transmits the data over nine high speed serial links. They were handled by a single readout board built around a FPGA. The formatted data were then sent via a Gigabit Ethernet interface to an off the shelf PC. We named this system the GTK DAQ.

The FASTS and the plastic scintillators were read out by a second DAQ built around VME CFD and a CAEN V1290N TDC. A high precision external clock generator was distributing a 40 MHz clock to the TDC. To reduce the rate, the signal from F1, F2, F3 and F4 were gated with S1 in coincidence with S2. The TDC was configured in *Trigger Matching* mode: the device looks for hits in a time window which is open each time it receives an external trigger signal. For our application a window length of 51 µs was set. The trigger signals

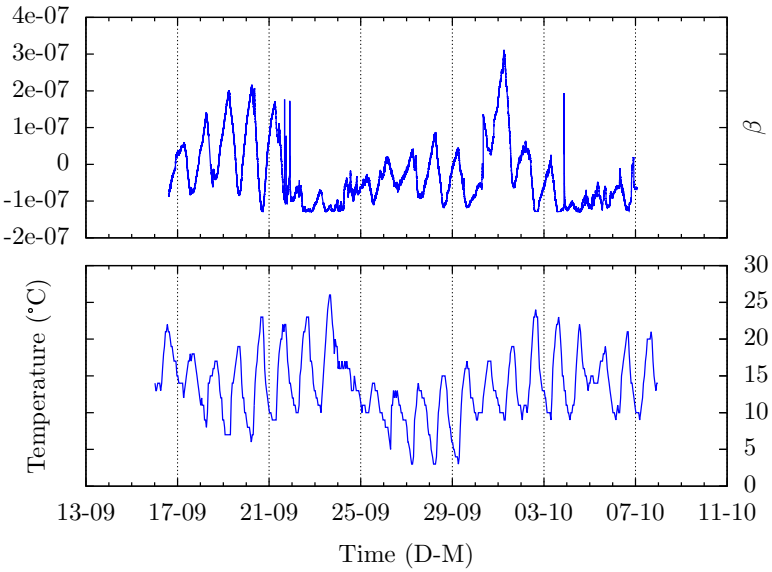

Figure 4.3: Deviation from a perfect time conversion, $\beta = (1 - b)$, where b is the slope of curve (see the text for an explanation) and temperature at the Geneva International Airport. The weather station is situated at 4.15 km from the CERN.

were generated by a pulse generator at 20 kHz in order to have a small overlap between the windows. To cover the whole PS spill length, we exploited the *Extended Trigger Time Tag* feature of the V1290N, when enabled, the trigger signals are time tagged. Knowing the trigger time and the hit time inside the corresponding window, we can place the hit on a time line without ambiguity. The data were read out on an off-the-shelf PC via an USB-VME bridge. We named this system the SDAQ.

A signal generator sending a train of 6000 pulse at 10 kHz to the TDC was used for calibration and cross-checks. The measured signal leading times were compared to a calibrated 10 kHz source; we plotted the leading edge arrival time measured by the TDC on one axis while on the other axis we assume a perfect 10 kHz source. We looked at the linearity and at the slope of the curve. If the conversion is perfect one expects a unitary slope. We found a small slope variation over time as shown on Figure 4.3. It was most probably caused by the variation of the ambient temperature (more than ten degrees between day and night). This drift was accounted for in the data analysis. Note that this issue is irrelevant for the full scale GigaTracker detector as its temperature will be strictly controlled.

The time synchronization of the two DAQs relied on the *spill warning* signal sent by the PS a couple of seconds before the delivery of a spill. This signal was

Table 4.2: Definition of the subsets used for the present analysis.

Subset	Number of spills	Spill IDs	Assemblies	Bias voltage (V)
A	8866	31675 – 41190	2, 5, 9, 10	300
B	2953	13990 – 17262	10 2, 5, 9	350 400
C	2155	17296 – 19989	2, 10 5, 9	100 200

delayed by one second and sent to one channel of the CAEN TDC; the trailing edge of the pulse gave the global time reference for the detector connected to the scintillators DAQ. Similarly, the signal triggered a reset of the GigaTracker assembly's coarse counters. In addition, to synchronize the software part of the scintillators DAQ, an Ethernet packet containing a unique spill ID was distributed over the network upon reception of the *spill warning*.

4.1.3 Data Preparation and Analysis

The data preparation pipeline was made of three independent stages. First, the raw data from the two DAQs were decoded and grouped by spill ID. Depending on the source of the data different quality checks were done. The SDAQ data had to contain 6000 leading edges on the TDC channel 15 for each spill and no error flags could be set. This helped to ensure that all the signal edges were recorded. Likewise, GTK DAQ data had to have a valid cyclic redundancy check (CRC) and no pile-up flag set. About 4.6 percent of the spills were rejected at this stage.

Second, all the detectors were aligned in time spill-by-spill. Indeed, the time offsets of the two datasets were not constant. The values were stored in a database for later use. This step will be covered in more details in the next sections.

Finally, hits of all the selected detectors were grouped to form events. The events were defined as a group of hits falling in a 10 ns time window. Given the estimated beam rate (500 kHz) and size (480 mm^2), the probability that more than one particle hits the sensor within the time window is around 4×10^{-5}. For this particular analysis, an event was defined by a coincidence between F1 and one of the GigaTracker assemblies.

Datasets

We grouped the spills coming from the both DAQs into unified datasets indexed by spill ID. The definition of the datasets is reported in Table 4.2. The sets were defined to ensure stable conditions of the DAQs and of all the detectors. The spill IDs are not unique because a 16-bit counter rolled over during the

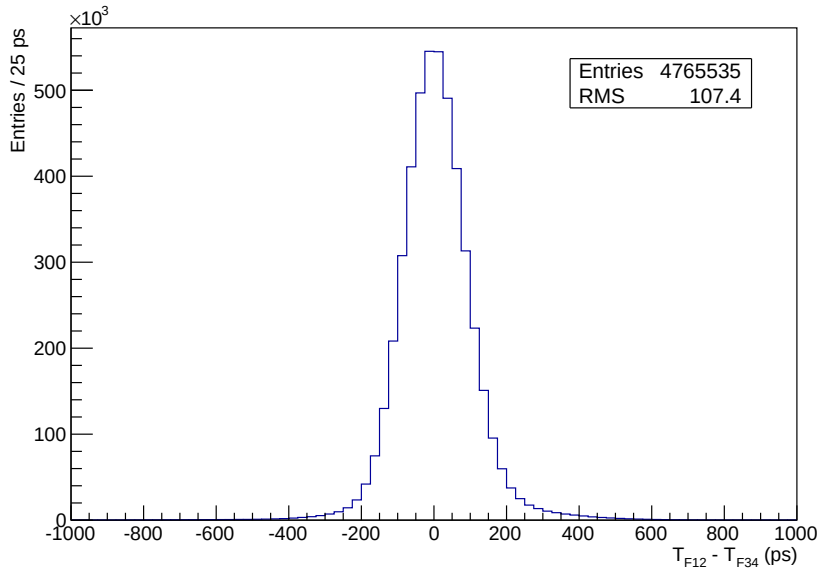

Figure 4.4: Distribution of the time differences between the two scintillators bars (F12 and F34) using the data from the subset A. The distribution displays non Gaussian tails, therefore, we decided to quote RMS/$\sqrt{2}$ as the time resolution for the FASTS.

test beam. However, they are strictly monotone for a given dataset.

Time Reference Detector

The reference time for a given event is defined as the average of the hit arrival times on the scintillators bars F12 and F34. Since the two bars are identical we assume that they have the same intrinsic hit time resolution.

The FASTS time resolution corresponds to the width of the distribution of the time differences between the two scintillators bars divided by $\sqrt{2}$. Indeed, we assume that the two bars are identical and that their errors are uncorrelated. The distribution is plotted in Figure 4.4. We deduce that the FASTS has a stable time resolution of about 76 ps.

Pixel Masking

If the number of hits in a pixel is less than the half of the assembly average, then the pixel is declared *dead*. These pixels, listed in Table 4.3, are excluded of the detection efficiency computation.

Table 4.3: Pixels excluded of the detection efficiency computation.

Station	Dead pixels
GTK10	8, 9 and 44
GTK2	0 and 17
GTK9	None
GTK5	8, 26, 27 and 44

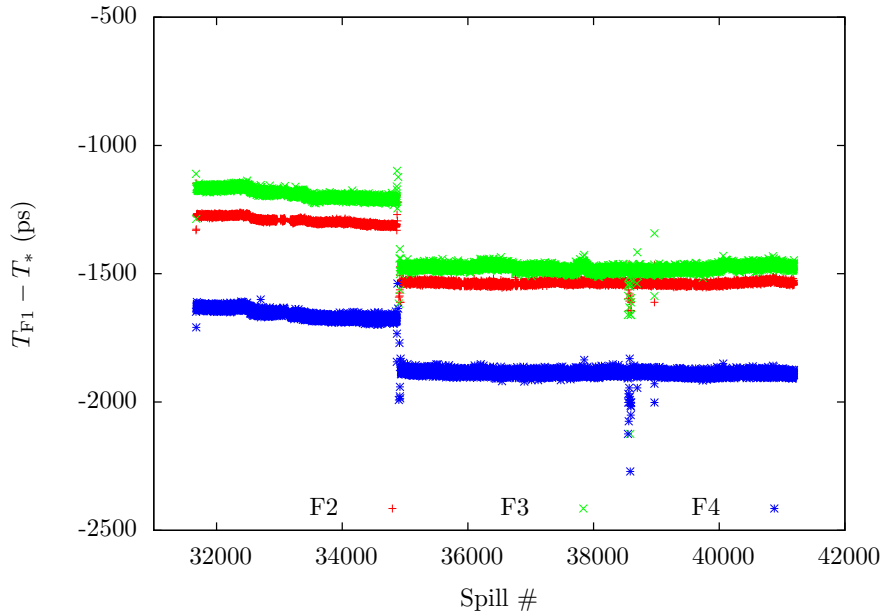

Figure 4.5: Time offsets with respect to F1 for the data subset A. The step was caused by a cable exchange.

Time Alignment

A good time alignment of the different detectors is mandatory to extract the time resolution. We have to account for two effects, the fixed offsets between the detectors and the drift due to the environmental conditions variation. To achieve the best results, a spill-by-spill alignment is required. We have chosen the leading edge of F1 as a common reference. Note that the results quoted below correspond to averages over a whole spill. At this stage, the single hit time resolution is much worse.

Except for a jump caused by a cable exchange, the time offsets between F1 and F2, F1 and F3, and F1 and F4 are very stable, with a standard deviation of less than 10 ps. The discontinuity is visible in Figure 4.5.

Similarly, the time offsets between the GigaTracker demonstrators are very

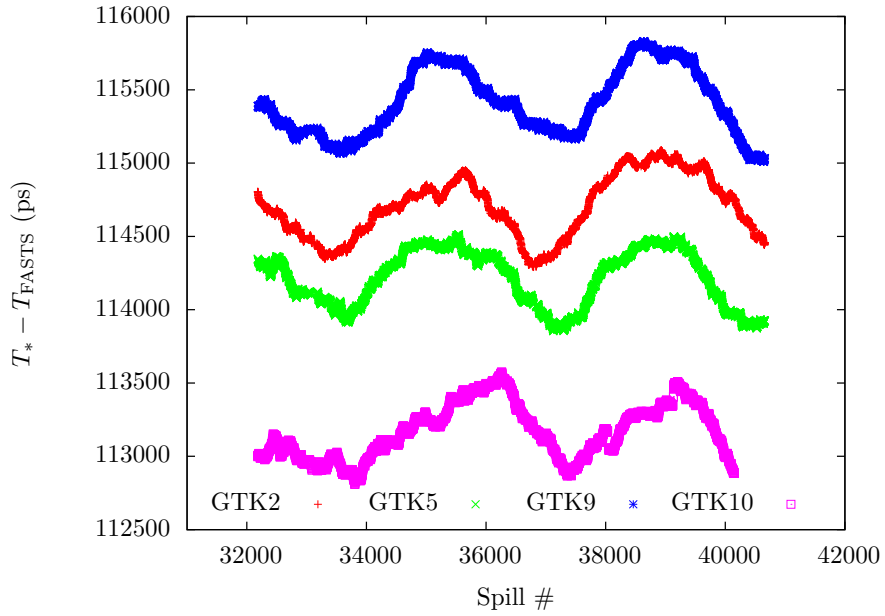

Figure 4.6: The time offset is defined as the average time difference between F1 and the GigaTracker assemblies. The values are for the data subset A.

stable, with a standard deviation of about 90 ps. This large dispersion can be explained by the fact that at this stage all pixels are included and no time walk correction or pixel time offsets compensation are performed.

As shown in Figure 4.6, unlike the two previous situation, the offsets between the FASTS and the GigaTracker assemblies varies with the time. The standard deviation is around 187 ps; this can be explained by the fact that the two DAQs were using separate clocks. Indeed, we showed above that at least the SDAQ clock was affected by a measurable drift.

Hits Clustering

A particle crossing the detector can fire more than one pixel. In the case of the GigaTracker demonstrators, since the beam direction is normal to the sensor surface, it is caused by the charge sharing between pixels and the delta-rays. Hits clusters are defined as contiguous groups of pixels hit within a 10 ns window. For each cluster the position and leading time are defined as the mean of the values of the individual pixels weighted by their respective time-over-thresholds. All hits are treated as clusters; i.e. single hits appear as clusters containing one pixel.

Table 4.4: Spatial misalignment extracted from the data. The assemblies were manually realigned during the test beam.

	Offsets (µm)					
	GTK 2		GTK 9		GTK 5	
Subset	X	Y	X	Y	X	Y
A	-4 ± 12	0 ± 14	-205 ± 20	198 ± 24	-178 ± 28	265 ± 36
B	0 ± 12	29 ± 13	3 ± 19	36 ± 23	-6 ± 28	16 ± 33
C	2 ± 12	26 ± 13	9 ± 20	32 ± 23	0 ± 29	12 ± 34

Stations Spatial Alignment

To achieve the best spatial alignment a simple but sufficient alignment algorithm was used. Two small plastic scintillators were placed immediately before and after the four GigaTracker demonstrators. They were used to check the beam alignment, hence, we can safely assume that the beam was perpendicular to the assemblies. Then, using the first assembly as a reference, the differences between the expected positions were measured for the X and Y axis. Averaging the differences gives the misalignment. These offsets are taken into account when we compute the detection efficiency of the demonstrator. The results of the alignment procedure are reported in Table 4.4.

Track Reconstruction

Tracks have been reconstructed by considering all the possible triplets of points belonging to an event. One station is left out of the procedure to allow the computation of the detection efficiency. The quality of the tracks is characterized by a χ^2 value:

$$\chi^2 = \sum_{i=1}^{3} \left(\frac{x_m - x_p}{\sigma_x} \right)^2 + \sum_{i=1}^{3} \left(\frac{y_m - y_p}{\sigma_y} \right)^2 , \tag{4.1}$$

where i indicates one of the three stations included in the fit. The variable x_m and y_m stand for the measured point. One the other hand, x_p and y_p are the projected points from the fitted track parameters. The variable $\sigma_x = \sigma_y$ are set equal to $300/\sqrt{12}$ µm. The χ^2 distribution is shown in Figure 4.7, all the tracks with $\chi^2 \leq 2.5$ were kept for the analysis.

4.1.4 Demonstrator Performance

In this section we present the results of the study: the detector time resolution, the detection efficiency and the magnitude of the charge sharing effects. For these three performance figures we examined the influence of the pixel thresholds and of the bias voltage.

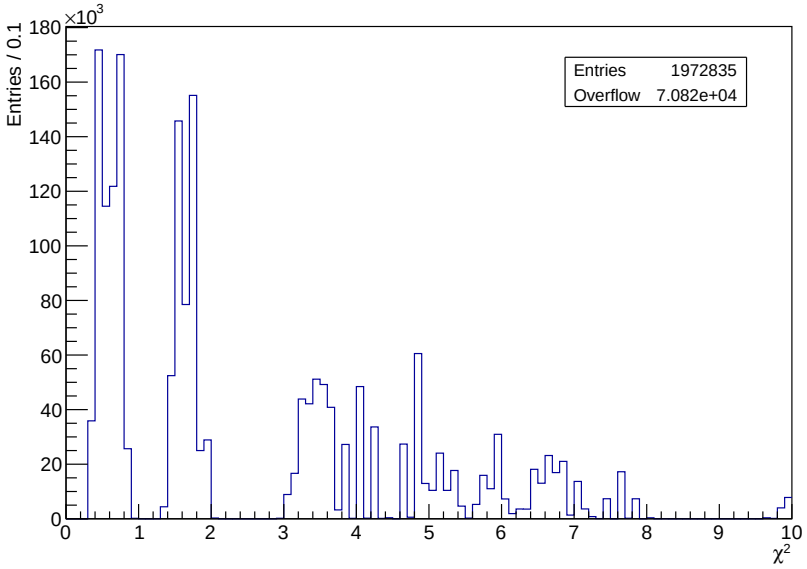

Figure 4.7: χ^2 distribution for the tracks reconstructed with the subset A. We kept all the tracks with $\chi^2 \leq 2.5$ for the analysis. The regular structure reflects the discrete nature of hit spatial coordinates. The time of the hits were not used to compute the χ^2.

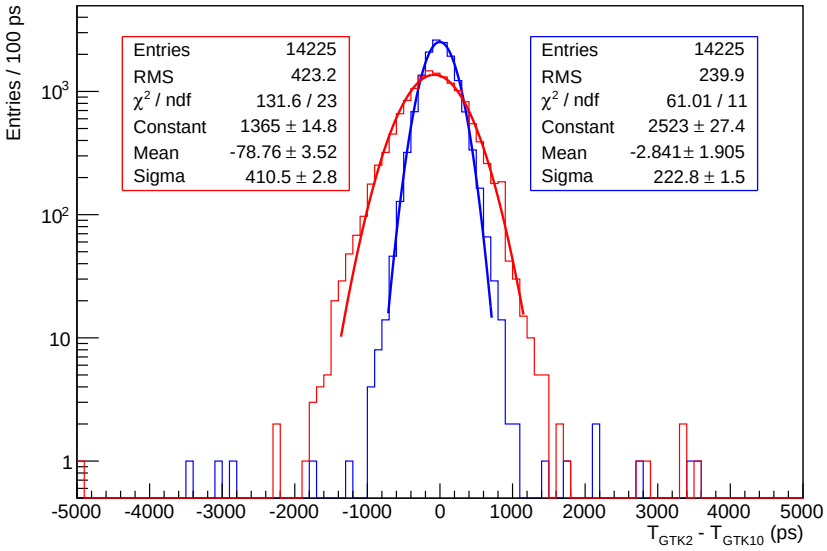

Figure 4.8: Distribution of the time differences between the pixel 11 on GTK2 and GTK9 at a bias voltage of 300 V. The red and blue curves are, respectively, before and after the time-walk correction.

Time Resolution

The hit time resolution of the pixels was computed using only the GigaTracker stations (the standalone method) and using the FASTS as an external time reference.

When using GigaTracker only, we applied the time walk corrections (see Section 3.2.4) and we looked at the time difference between two given pixels. If we make the reasonable assumption that the timing errors on the two stations are not correlated and that they have the same time resolution, then, the hit time resolution is the width of the time difference distribution divided by $\sqrt{2}$. A typical distribution before and after the time walk correction is displayed in Figure 4.8.

When using the FASTS, an additional step is needed, indeed the time offsets between the GigaTracker pixels and the FASTS varies in time. In the Section 4.1.3, we computed one global time offset correction per station, we now need to apply a pixel-by-pixel fine time offset. To do so, for each pixel the data sample was divided in slices of 1000 events. Then, a Gaussian was fitted to time difference between the given GigaTracker and the FASTS and the mean of the distribution was extracted for each slice. A representative example of the procedure is shown in Figure 4.9.

If one assumes that the timing errors on the GigaTracker station and on the

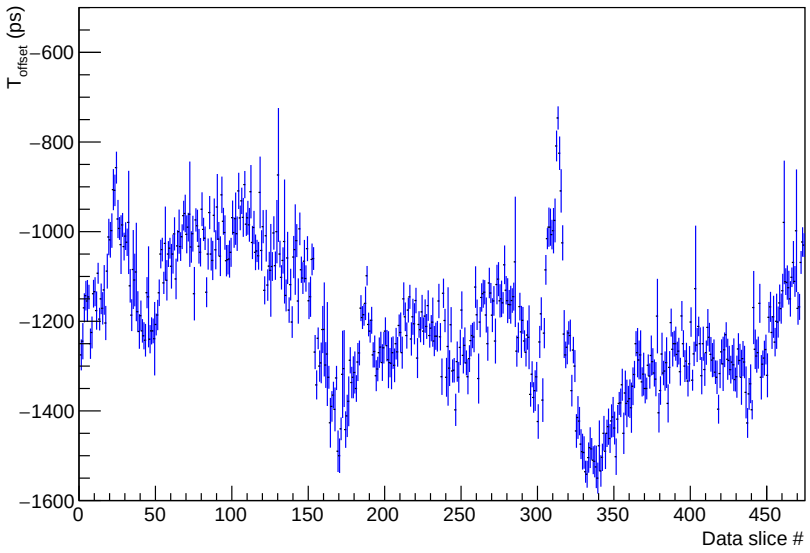

Figure 4.9: Fine time offset between the pixel 3 of GTK9 and the FASTS as a function of the time, from the data subset A. The error bars correspond to one standard deviation of the fitted Gaussian.

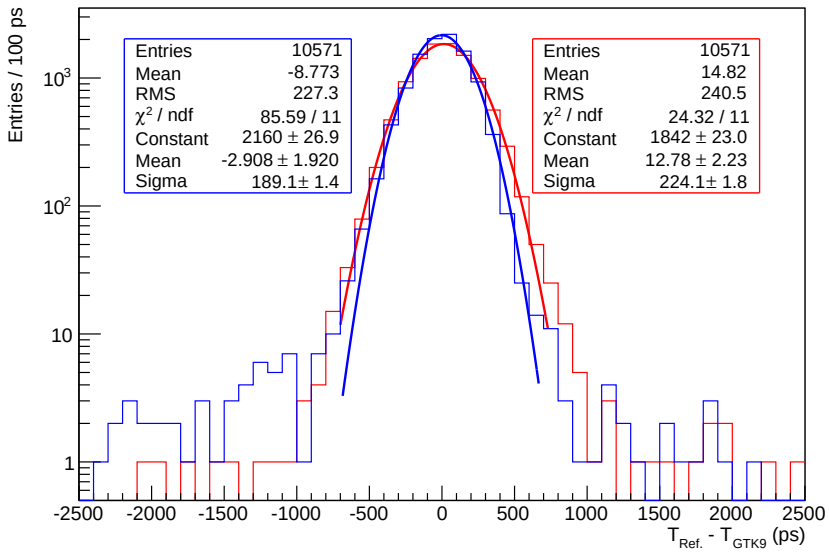

Figure 4.10: Distribution of the time differences between the pixel 1 on GTK9 and the FASTS (blue) and between the pixel 1 on GTK9 and the pixel 1 on GTK9, data subset A.

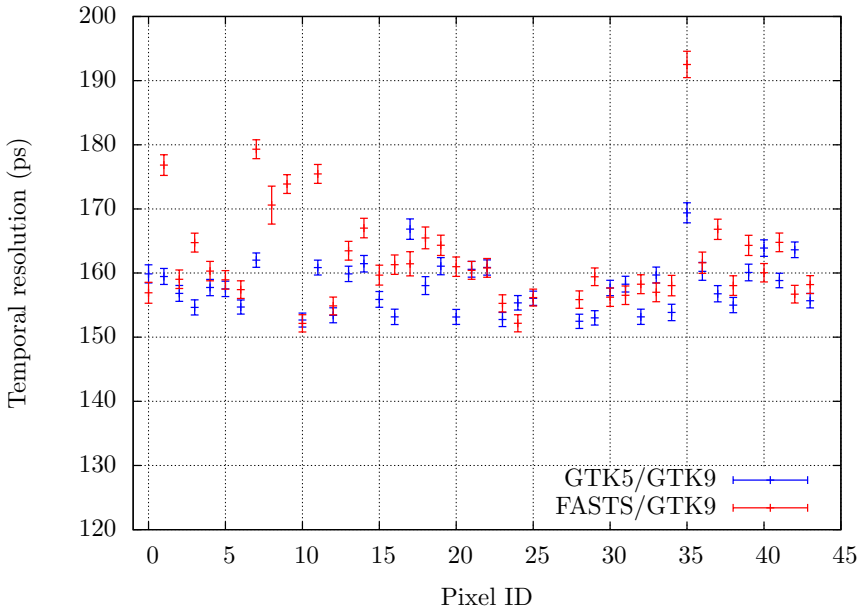

Figure 4.11: Time resolution of the individual pixels at 300 V bias voltage, data subset A. The error bars are scaled (see text) one-standard-deviation of the fitted Gaussian.

FASTS are not correlated, we can use the FASTS time resolution calculated in Section 4.1.3 to compute the pixel time resolution. A typical distribution of the time differences is plotted in Figure 4.10.

As illustrated in Figure 4.11, the two methods are in good agreement, however the second method suffers from the variation of the time offsets between the FASTS and the GigaTracker stations. The procedure was repeated for four bias voltages. The results are summarized in Table 4.5 and Figure 4.12. In Figure 4.11, the uncertainty attached to the hit time resolution was computed using simple error propagation formulas: $\sigma_T = \sigma_\Delta/\sqrt{2}$ and $\sigma_T = (\Delta/T)\,\sigma_\Delta$ for the standalone and the external reference methods respectively. In the previous expression, σ_Δ corresponds to the one standard-deviation error returned by the

Table 4.5: Averaged hit time resolution. The errors correspond to one standard deviation of the mean time resolution of all the pixels.

V_{bias} (V)	GTK σ_t (ps)	FASTS σ_t (ps)
100	313 ± 14	325 ± 14
200	194 ± 13	199 ± 10
300	160 ± 12	165 ± 17
400	139 ± 12	144 ± 7

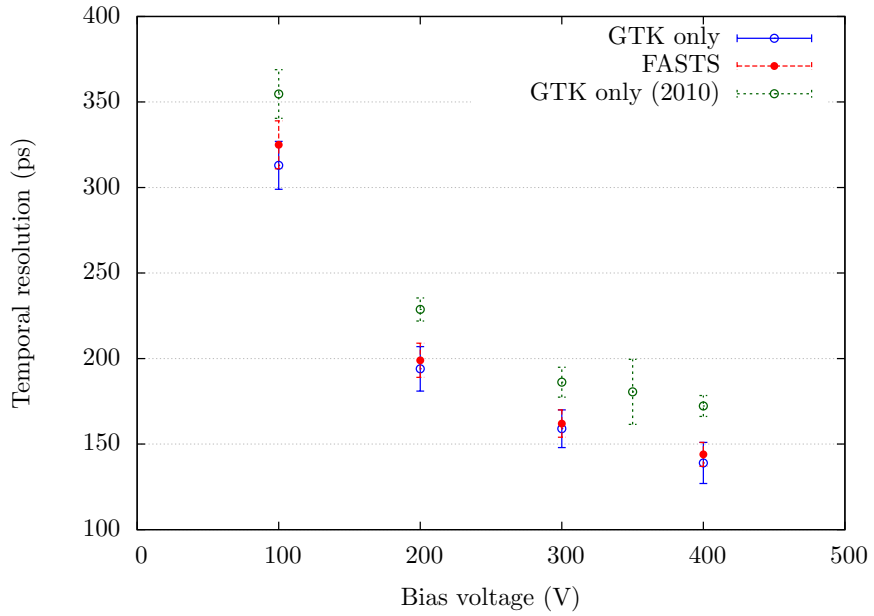

Figure 4.12: The quoted value is the mean time resolution of all the pixels of one station. The influence of the charge carrier drift velocity is clearly visible. The error bars are one-standard-deviation of the mean.

Table 4.6: Pixel threshold distribution of the four GigaTracker stations.

Chip ID	Column setting (fC)	Pixels mean (fC)	Pixels - RMS (fC)
10	0.7	0.7154	0.1511
2	0.35	0.7098	0.1752
9	0.77	0.7154	0.1511
5	0.49	0.7665	0.1741

fit, Δ is the width of the time differences distribution and T the GigaTracker hit time resolution.

The demonstrator architecture did not allow to individually trim the pixel thresholds. However, a global value for the whole column could be set. Depending on individual pixel properties the column setting translates into an effective value that can be read back. The column setting for each chip are reported in Table 4.6. A typical pixel threshold distribution is shown at Figure 4.13. The final TDCpix ASIC allows to individually trim the pixel threshold.

As shown in Figure 4.14, the time resolution is strongly affected by the pixel threshold level. This effect is easy to understand if we consider the shape of the signal. Indeed, the slope of the rising edge of the signal is smaller at low and high threshold and a smaller slope leads to a lower time resolution.

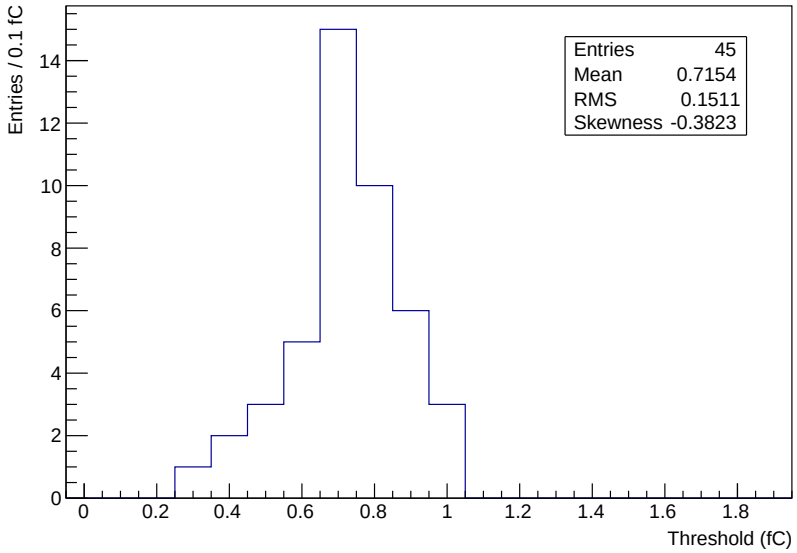

Figure 4.13: Pixel threshold distribution of GTK10.

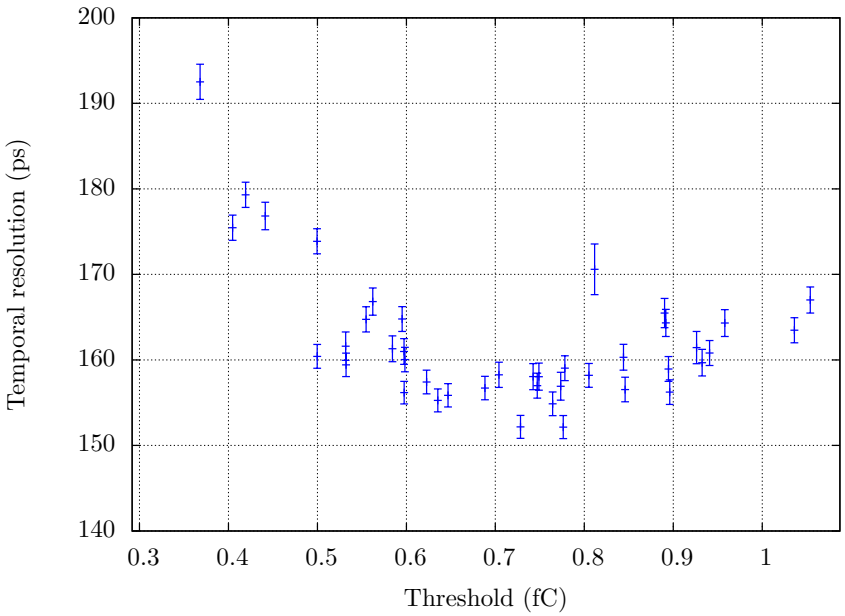

Figure 4.14: Hit time resolution of GTK9, run 345/8. The FASTS are used as time reference.

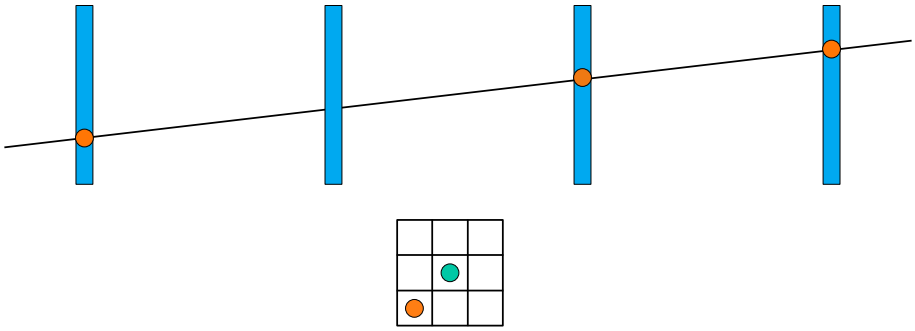

Figure 4.15: Sketch of the method used to compute the detection efficiency. The blue rectangles represent the GigaTracker stations while the 3×3 grid is a zoom on the station not used for the track reconstruction. The green circle points to extrapolated position of pixel, the orange circles indicate presence of a hit.

Detection Efficiency

The method used to compute the detection efficiency is illustrated in Figure 4.15. A set of tracks is reconstructed with the information from three out of the four stations. Then, using the track parameter the hit position can be extrapolated on the station that was not used for the fit. Since the pointing capabilities of the tracker were rather poor we looked for a hit in the extrapolated pixel or in its eight neighbours. To not bias the detection efficiency, it was computed only for pixel with eight good neighbours; the borders and all the pixels around the dead ones (the pixels 0, 8, 9, 17, 26, 27 and 44) were excluded. A typical example is presented in Figure 4.16. In general, the detection efficiency is above 99 percent.

Finally, the bias voltage has no significant influence on the detection efficiency. Indeed, the depletion voltage of 200 µm silicon sensor is around 30 V. Likewise, the pixel thresholds variation has no measurable effects on the detection efficiency.

Charge Sharing Effects

The distribution of the cluster size is presented in Figure 4.17, about 96 percent of them contain only one pixel. As expected, the fraction of clusters with more than one pixels diminishes when the bias voltage increases. Indeed, as the charge carrier drift velocity increases the transversal diffusion decreases. This is clearly visible in Figure 4.18.

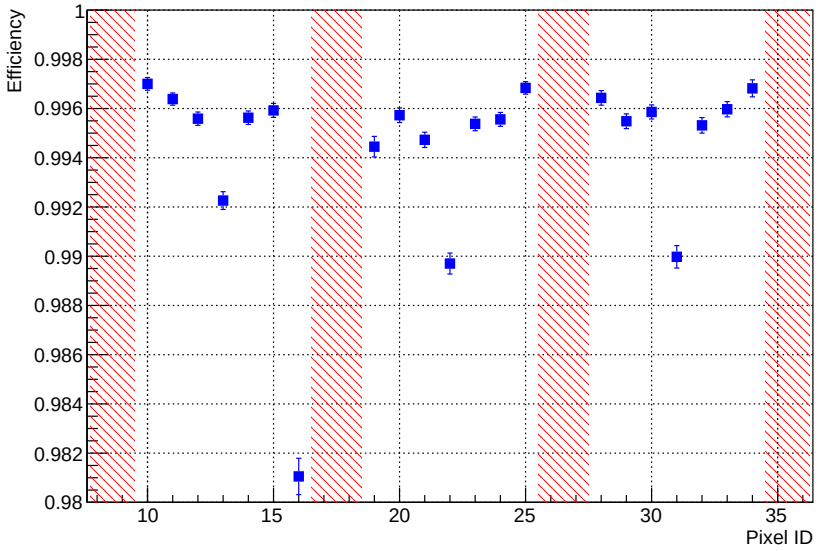

Figure 4.16: Detection efficiency of GTK2, data subset A. The red hashed zones indicates the excluded pixels. The uncertainties corresponds to the 68 percent confidence interval.

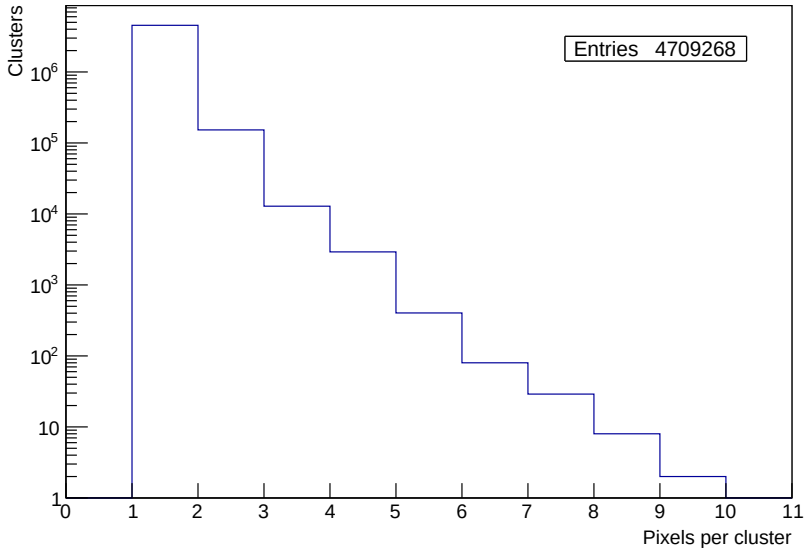

Figure 4.17: Distribution of the cluster size for a bias voltage of 300 V.

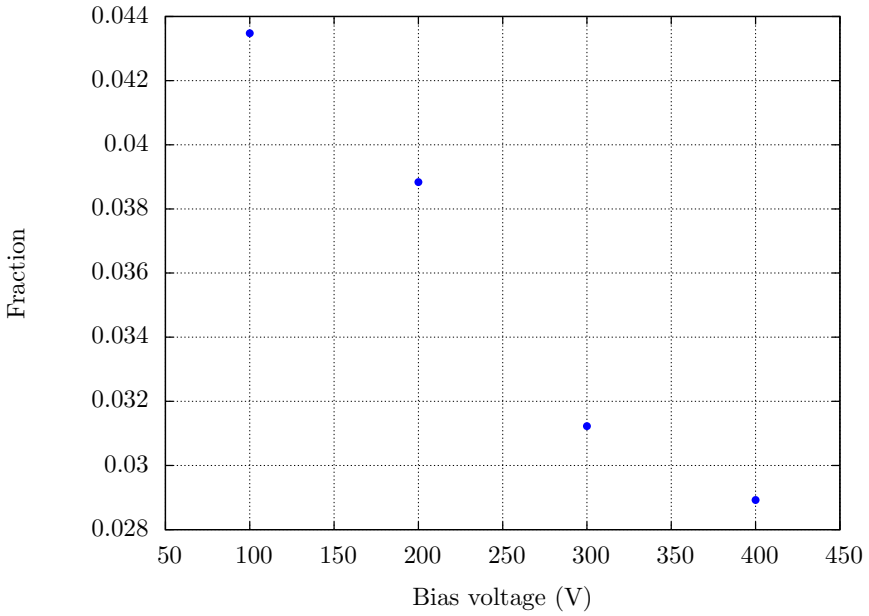

Figure 4.18: Fraction of clusters with more than one pixels as a function of the bias voltage.

4.1.5 Summary

The GigaTracker prototype was tested with a 10 GeV/c mixed hadron beam. With the data collected we demonstrated that:

- Hit time resolution below 150 ps at 300 V can be achieved; the results are summarised in Table 4.5.
- The detection efficiency is above 99 percent, see Figure 4.16.
- The charge sharing effects are negligible in first approximation, see Figure 4.18.

Furthermore, the analysis helped to understand how to account for the time walk and the pixel time offsets in an efficient way. The techniques developed for the prototype have been applied with success to the full scale GigaTracker detector. We believe that this analysis constitutes the state of the art for timing measurement with silicon pixel detectors. The results presented in this section have been published in [2].

4.2 GigaTracker Pilot Run

In 2014, NA62 received beam from Monday 6th October at 8 am to Monday 15th December at 8 am. The run was mostly dedicated to the commissioning of the subdetectors and of the trigger and data acquisition (DAQ) systems. The GigaTracker was only partially operational: the DAQ was running independently of the global NA62 system and only ten percent of the channels (one chip per detector), were usable for analysis. The detector status during the pilot run is detailed in the Section 3.3.

Since we are dealing with single chips, we will work with a Cartesian right-handed coordinate system were the X-axis and the Y-axis correspond to the pixel *columns* and the *rows* respectively. We will use the notation (column,row) to refer to a particular pixel. The beam is going in the direction opposite to the Z-axis. That is, the beam is going into the page. Notice that this coordinate system does not corresponds to the NA62 one.

We follow the nomenclature introduced in the Section 3.3: the *detectors* are named GTK_X, where X is the serial number. The *station* refers to the position in the beam. The station one is the first encountered by the beam and so on. In 2014, GTK_1, GTK_2 and GTK_3 were installed the third, first, and second station respectively.

We begin this section with the study of the secondary beam time structure It was among the first observation made with the GigaTracker. Next, we detail the procedure we followed to evaluate the detector hit time resolution.

4.2.1 Beam Properties

The beam hit rate profiles were among the first control plots we produced. They provide a first hint of the correct behaviour of complete readout chain. In addition, as we will see, the excellent time resolution of GigaTracker allows to study the beam dynamics.

Burst Profile

The burst hit rate profiles, or simply burst profiles, were among the first proof of the proper functioning of the detector. The involved time scales require no correction or calibration. In addition to the beam monitoring, these profiles were a key element in understanding the general DAQ issues NA62 experienced in 2014. Indeed, the observed huge hit rate variations were not anticipated.

A representative burst profile is presented in Figure 4.20; a periodic pattern can clearly be seen when we zoom in. Some bursts also display a sharp intensity peak when the first particles are delivered.

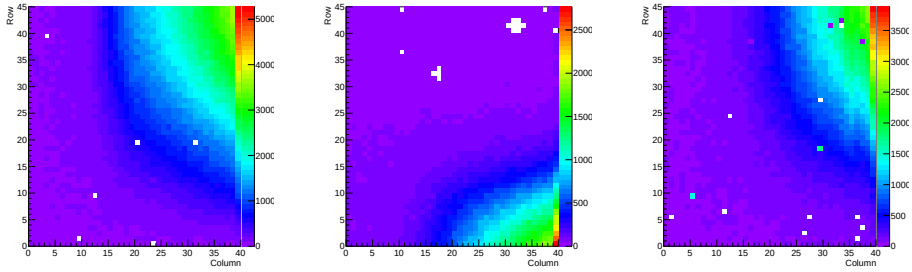

Figure 4.19: Illumination of the three good chips. GTK_2 (first station) is on the left, GTK_3 (second station) is at the centre, GTK_1 (third station) is on the right. The second station was displaced by +20 mm along the Y-axis, as a consequence most of the beam was passing below the sensor.

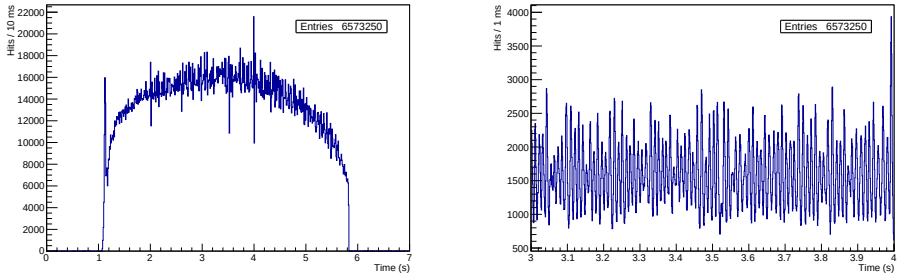

Figure 4.20: Typical burst profile in 2014 (left), a periodic pattern is apparent when we zoom in (right). Burst 1418476262, GTK_2, Dec. 13, 2014, 14:11 UTC.

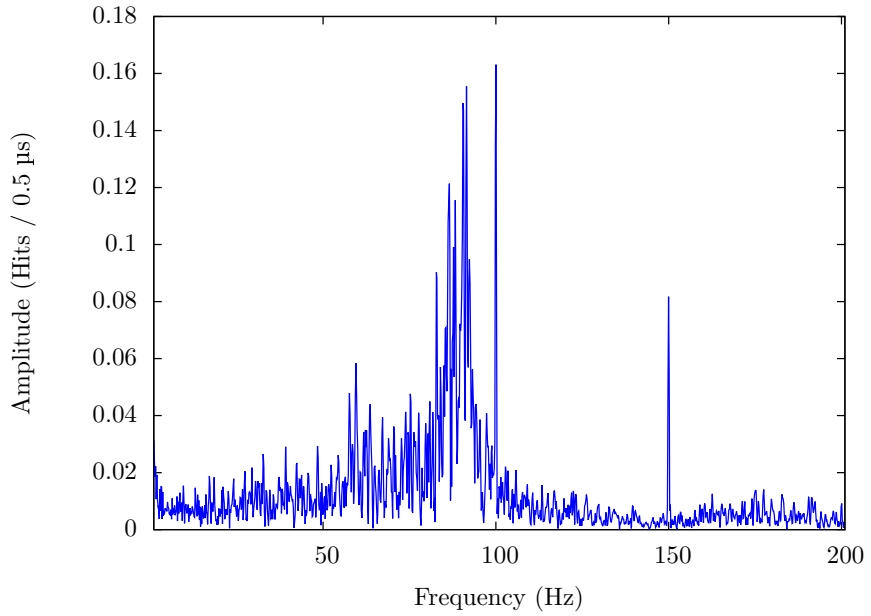

Figure 4.21: Low frequency components spectrum of burst 14184766262. In addition to the 100 Hz component, harmonics of mains frequency (50 Hz) are visible.

Frequency Analysis

We computed the discrete Fourier transform (FFT) of burst profiles to characterize the periodic components of the beam rate. A Hann window have been applied to the sampled data before computing the FFT. Compared with a rectangular window it slightly degrades the frequency resolution but it also reduces the frequency leakages. The window is defined by

$$w(n) = \frac{1}{2}\left(1 - \cos\left(\frac{2\pi n}{N}\right)\right), \; n \in \mathcal{Z} \; , \tag{4.2}$$

where n is the index of the time bin.

The routine returns an unnormalised frequency spectrum. To get back the original time series when the inverse transformation is applied the amplitudes must be multiplied by $2/N$. Furthermore, the Hann window reduces the average amplitude by a factor

$$F_w = \frac{1}{N}\sum_{n=0}^{N} w(n) = \frac{1}{2} \; , \tag{4.3}$$

hence the amplitudes have to be multiplied by an additional factor 2.

We ran the algorithm on the burst presented in Figure 4.20. A zoom on the 0–200 Hz region is shown in 4.21. We recognize the 100 Hz component visible

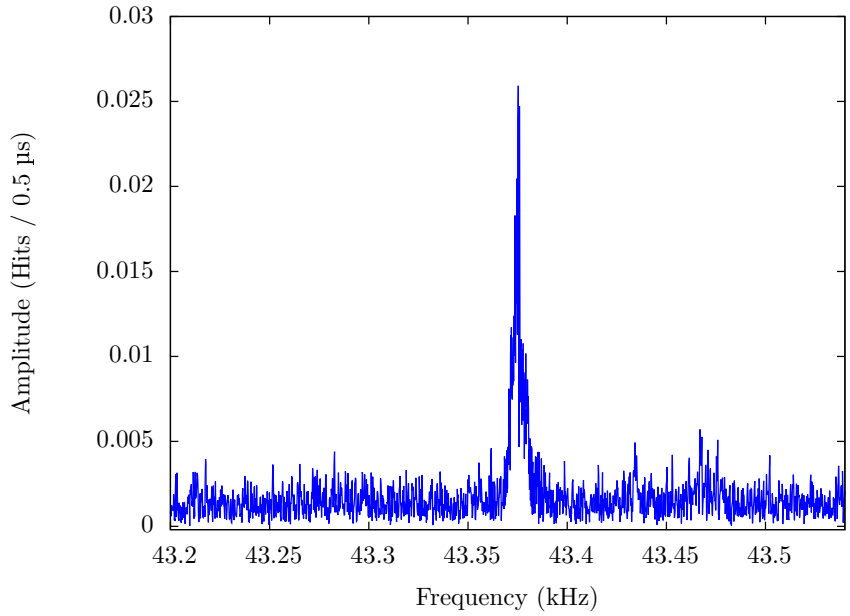

Figure 4.22: First harmonic of the 43.37 kHz component.

in the burst profile zoom. It is a remnant of the mains frequency (50 Hz) and its harmonics. The broad peak around 75 Hz is known from the SPS experts [128].

Another interesting peak is located at 43.37 kHz (see Figure 4.22). Indeed, for 400 GeV/c protons, that frequency corresponds to a revolution length of 6911.463 ± 0.634 m, which is close to the documented SPS circumference (6911.503 m [129]).

4.2.2 Data Preparation and Analysis

In the next sections we will explore more in deep the data collected during the 2014 pilot run. We follow a similar path as the one used for the GigaTracker demonstrator: time alignment, time walk correction and finally the hit time resolution. Because of the status of detector in 2014, we were not able to compute the detection efficiency and the tracking performance of the detector.

To abstract ourselves from the absolute time calibration, most of the computations were done using *Least Significant Bit Units* (LSBU). One LSBU corresponds to the least significant bit (LSB) of the fine time counter of the TDCpix. In 2014, the NA62 global clock was running at 961.883 MHz / 24 [130]. This frequency is multiplied by eight (320.628 MHz) and distributed to the TDCpix chips. Finally, the TDC based on a DLL further divide the period into 32, which corresponds to 97.47 ps.

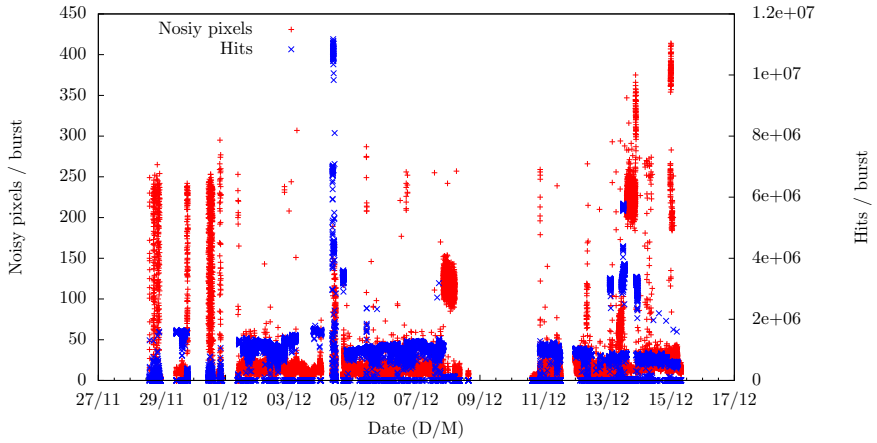

Figure 4.23: The number of noisy pixels varies greatly and returns to the baseline when the DAQ is reset. This behaviour is surprising at the first sight. The data are from the detector GTK_1.

The data format of the 2014 GigaTracker data is not compatible with the NA62 raw data format; it is detailed in Appendix E.

Datasets

To begin with, we observed the behavior of five basic metrics across the whole run: the pixel hit rates, the time-over-threshold overflows, the number of noisy pixel and the number of illegal pixel addresses.

The pixel hit rates and the number of time-over-threshold overflows correspond to the expectations. Conversely, the number of noisy pixels reveal surprising variations (Figure 4.23). During the 2014 run, the single event upset protection (SEU) logic of the TDCpix was configured to report the anomalies and to not automatically reset the affected registers. This mode is useful to study the rate of SEUs.

Finally, we looked at the number of illegal pixel addresses. As we saw in Section 3.1.3 when a pixel is activated the four others pixels belonging to the group are temporally masked by the hit arbiter. However, if two pixel connected to the same group are hit almost at the same time the hit arbiter has no time to mask the pixels and returns an illegal hit address. The rate of hits having an illegal address is directly proportional to the beam rate (see Figure 4.24). However, as it can be seen in Figure 4.25, some hit arbiters return more illegal addresses for the same input hit rate. This feature is not yet understood.

For most of the studies, we selected five periods during which the conditions were relatively stable (see Table 4.7 and Figure 4.26).

Table 4.7: Definition of the datasets used in this work. All the times are in UTC.

Dataset	From	To	# Burst	Comment
P1	10th Dec. 22:19	11th Dec. 12:17	1398	Two stations were operational.
P2	13th Dec. 23:05	14th Dec. 09:48	2073	One station was operational, overlap with NA62 run 1520.
P3	14th Dec. 18:09	14th Dec. 20:29	466	Three stations were operational.
P4	13th Dec. 10:57	13th Dec. 11:57	201	Three stations were operational, high intensity run.
P5	12th Dec. 00:57	12th Dec. 06:17	1060	Two stations were operational.

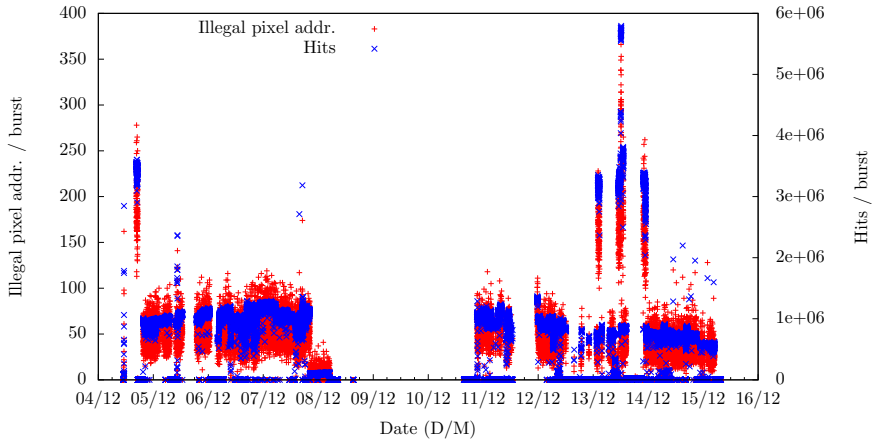

Figure 4.24: The number of hits having an illegal pixel address is proportional to the beam intensity. The data are from the detector GTK_1.

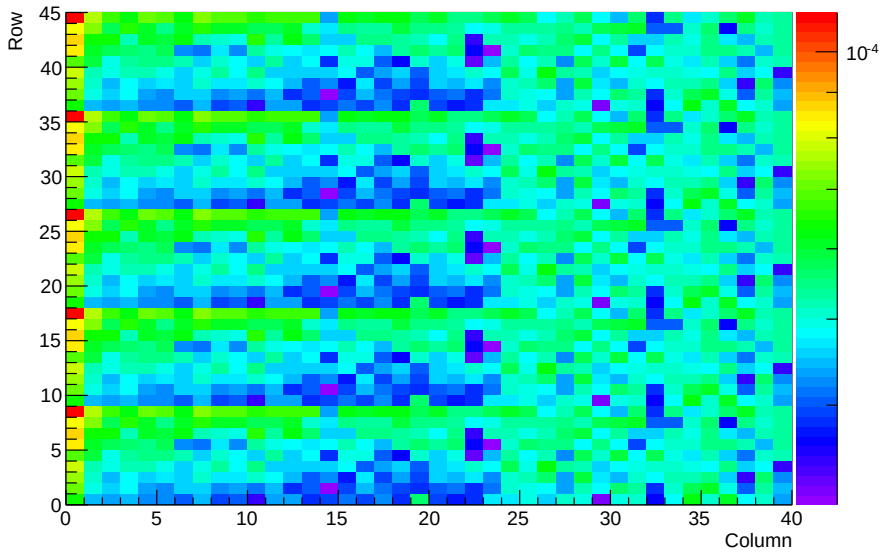

Figure 4.25: Ratio of the number of illegal pixel addresses over the total number of hits for GTK_3. The five pixel group structure is clearly visible.

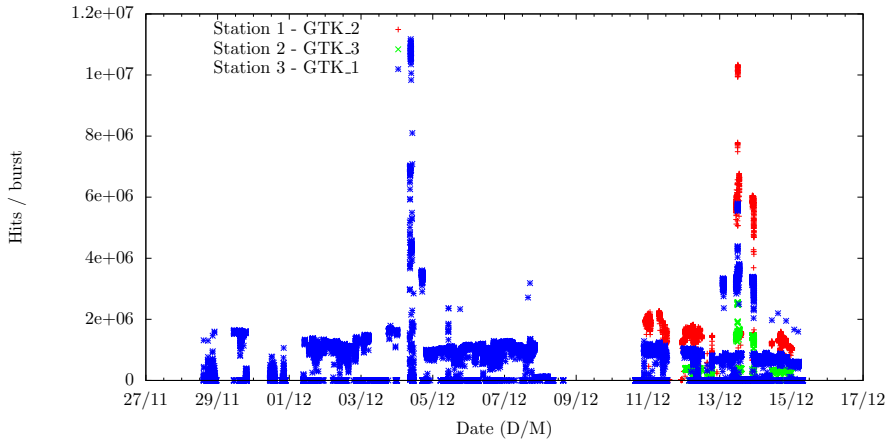

Figure 4.26: Number of hits per burst. The noisy pixels were filtered out. The short high intensity test runs are clearly visible.

Pixel Masking

A small fraction of the pixels had a hit rate, R, significantly lower or higher than their neighbours. They can be either noisy, i.e. counting fake hits, or dead, i.e. not responding when a particle hits. We can take advantage of the beam shape, which is approximately Gaussian, to tag them. For each pixel we compute the average, μ_N, and the variance, σ_N, of the hit rate of its eight neighbours. For any pixel, the hit rate should be close to the mean, therefore we tag pixel for further analysis if $|R - \mu_N| > \sqrt{\mu_N \sigma_N}$.

As stated above, the pixel masking has to be done burst-by-burst as the noisy pixels tend to appears and disappears randomly.

Table 4.8: Time offsets between the GigaTracker stations. The dataset P1 and P4 correspond to periods where only one station was operational. Similarly, the dataset P3 corresponds to the only period were all the stations were taking data.

Dataset	Station 1 – 2 (LSBU)	Stations 1 – 3 (LSBU)
P1	–	-798 ± 8
P2	–	–
P3	-900 ± 2	-767 ± 9
P4	–	–
P5	–	-767 ± 9

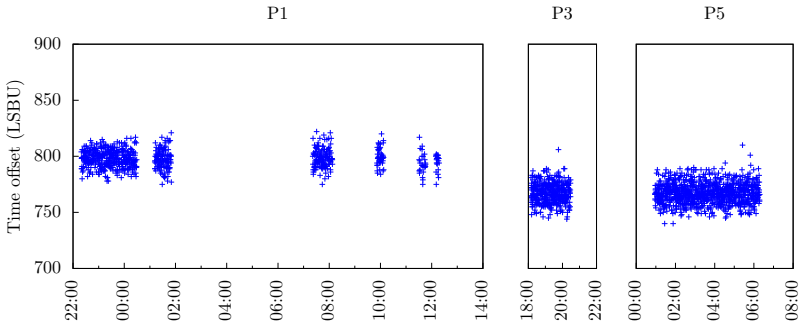

Figure 4.27: The time offsets between the first and the third GigaTracker station as a function of the time.

Time Alignment

The time alignment procedures are described in Section 3.2.4. The time offset we obtained using the FFT algorithm are tabulated in Table 4.8. The stability of the offsets is presented on Figure 4.27. There is a jump of about 30 LSBU (3.02 ns) between the dataset P1 and P2, we were not able to identify the exact cause it as the configuration of the detector was rapidly evolving at that time.

In addition, we computed the pixel time offset using the graph method. We selected the pixel (36,43) on GTK_3 (first station) as the reference; all the time offset are given with respect to that pixel. The score attached to each pixel is detailed in Figure 4.28. The results are summarized in Figure 4.29.

Once that the stations are aligned in time, one can start to look for coincidences between the stations. For each hit in given station, we look for one or more hits in the others stations within a defined time window. The size of the window is a compromise between the efficiency, if the window is too small

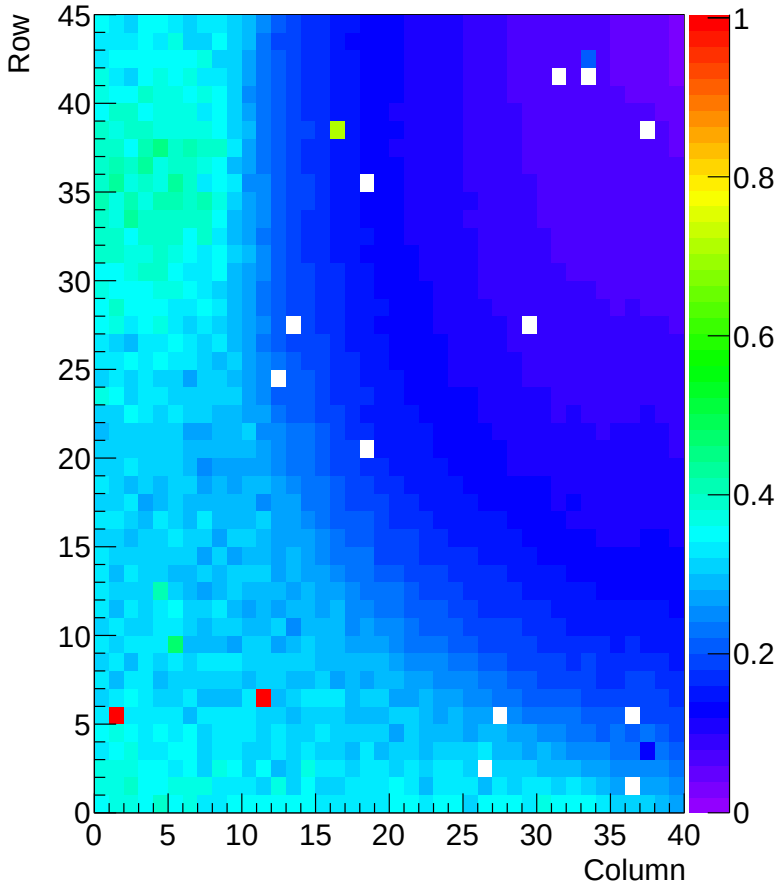

Figure 4.28: Score attached to the pixel of GTK_1 (third station) for dataset P1. The reference pixel is (36,43) on GTK_3 (first station). Smaller is better, since the beam divergence is small (about 100 µrad) less hops are needed to reach the GTK_1 pixel situated in the same area as the pixel (36,43) on GTK_3.

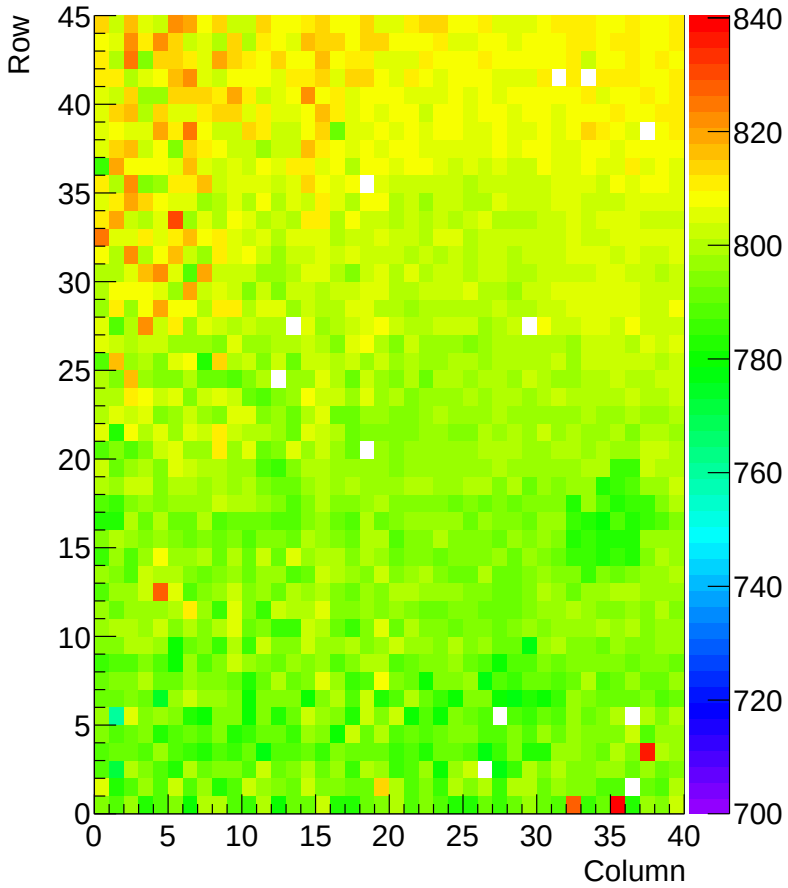

Figure 4.29: Time offsets (LSBU) between the pixel (36,43) on GTK_3 (first station) and all the pixel on GTK_1 (third station) for the dataset P1. The row structure clearly appears (see also the Figure 4.38).

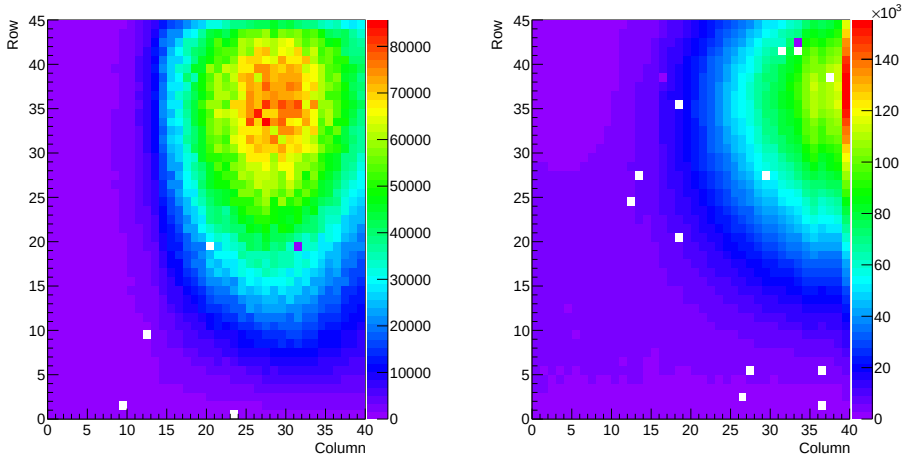

Figure 4.30: Hit maps of the coincidences between the first and third stations, dataset P5. The pixels of the column 0 and 39 are larger (400 µm instead of 300 µm). The color scale indicates the number of coincidence between a particular pixel of a station and all the others pixels of the other station. GTK_2 (first station) is on the left and GTK_1 (third station) is on the right. We see the focusing effect of the magnetic field on the beam.

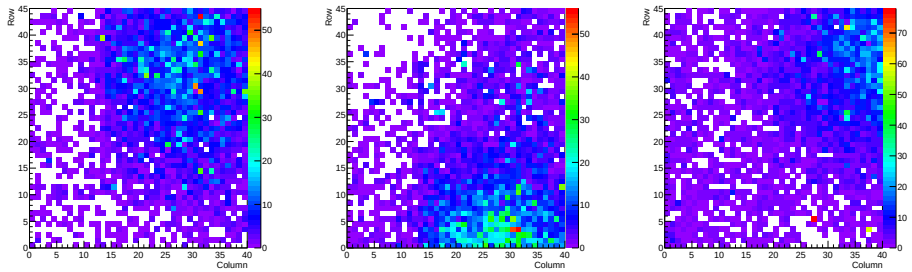

Figure 4.31: Hit maps of the coincidences between the three stations, dataset P3. The pixels of the column 0 and 39 are larger (400 µm instead of 300 µm). The color scale indicates the number of coincidence between a particular pixel of a station and any pairs of pixels of the two other station. GTK_2 (first station) is on the left, GTK_3 (second station) is in the centre and GTK_1 (third station) is on the right.

Table 4.9: Summary of early attempts to align the GigaTracker with the NA62 global DAQ. The NA62 runs were selected based on the NA62 log book entries. We found time coincidences with two NA62 runs, 1406 and 1433. The following runs were affected by "bit flips": many trigger timestamps were corrupted. This problems was corrected to some extent for the run 1520.

NA62 run	# GTK Stations	Trigger	Reconstruction	Comment
1406	1	Pass	Pass	$(T_{\mathrm{KTAG}} - T_{\mathrm{GTK\_1}}) \approx 500$ ns
1433	1	Pass	Pass	$(T_{\mathrm{KTAG}} - T_{\mathrm{GTK\_1}}) \approx 500$ ns
1482	2	–	–	No RAW files on the storage
1483	2	Fail	Pass	–
1487	1	Fail	–	–
1495	1	Fail (flipped bits)	Pass	Bit flip correction failed
1509	3	Fail (flipped bits)	–	GTK stations are noisy
1520	1	Fail (flipped bits)	Pass	"Golden" run
1542	–	–	–	KTAG vessel was empty
1543	–	–	–	KTAG vessel was empty

we will reject good pairs of hits, and the quality, if the window is too large we will select a lot of fake pairs of hits. For this first study we decided to use a 100 LSBU window which corresponds approximately to 10 ns. The window covers the Gaussian peak of the hit time differences between two stations. The map of the coincidences between the first and the third station are illustrated in Figure 4.30. The same exercise was repeated with three stations, see Figure 4.31. There is much less coincidences with the second GigaTracker station as it was offset by +20 mm on the Y-axis with respect to the nominal position. Most of the beam was passing below the sensor.

Finally, we selected a particular pixel on the first GigaTracker station and looked at where the coincidences appear on the third station. Naively, we expect a circular shape caused by the natural divergence of the beam. As we can see in Figure 4.32, we observe instead an ovoid shape caused by the focusing action of the beam line magnets. The beam is slightly smaller at the last GigaTracker station. The effect is well reproduced by the `TURTLE` simulation of the beam.

4.2.3 GigaTracker Performance

Using the 2014 pilot run data, we extracted the hit time resolution for a bias voltage of 170 V. Due to the low statistics, a pixel-by-pixel time walk correction could not been performed. Two techniques were tried: a "standalone" method using only the GigaTracker station and the "traditional" method using KTAG as an external time reference. Because of the configuration of the detector, it was not possible to study the tracking performances and the detection efficiency.

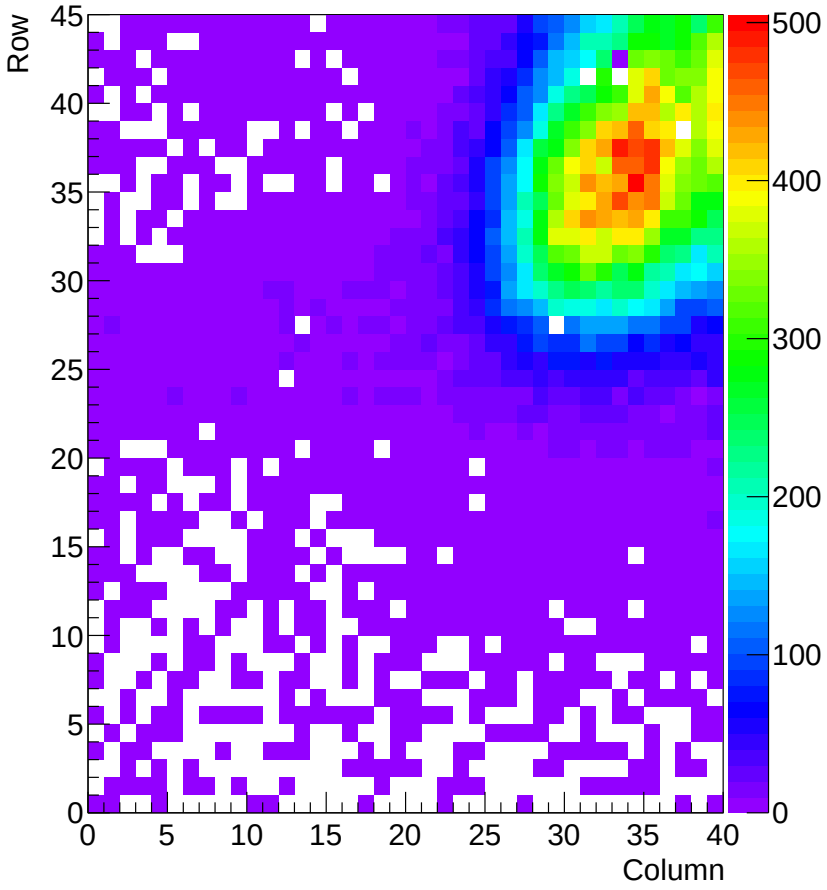

Figure 4.32: Hit maps of the coincidences between the pixel (28,25) of the first station and all pixels of the third station, dataset P5. The color scale indicates the number of coincidence between a particular pixel of a station and all the others pixels of the other station.

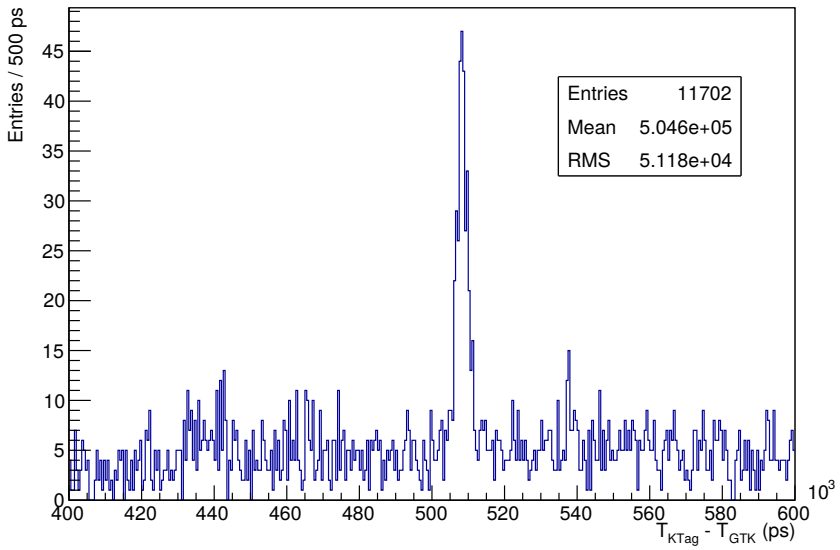

Figure 4.33: The first coincidences found between GigaTracker and KTAG. NA62 run 1406, burst 36. GigaTracker burst 1417789418.

Time Resolution

As we briefly covered in the introduction, the GigaTracker DAQ and the NA62 global DAQ were asynchronous. However, both used the same clock source and received synchronized SPS signals (*start of burst*, etc.). The NA62 data are organized in *runs* during which the detector conditions are kept more or less stable. Each run has a unique ID and is composed of a variable number of SPS bursts. Inside a run, the bursts are numbered from 0 to N and indexed by a burst Unix timestamp encoded in CET (UTC+1). Likewise, the GigaTracker data are grouped by SPS bursts and indexed by the same burst Unix timestamp encoded in UTC.

After the internal time alignment of the three GigaTracker stations, we searched for time coincidences with KTAG, which is placed immediately before the GigaTracker stations. First, we manually matched the "GigaTracker" bursts with the NA62 bursts using the timestamps. The correct association had to be checked by looking at the burst profiles. Indeed, depending on exact moment the GTK DAQ was started, the GigaTracker bursts can be shifted by ± 1 with respect to the NA62 bursts even if the timestamps concord.

We performed the manual matching for ten good NA62 runs, tabulated in Table 4.9. Out of the 10 runs, we were able to match a few bursts in the runs 1406 and 1433. The first positive matching using all the pixels of GTK_1 is shown in Figure 4.33. It became apparent that computing the time-over-threshold correction for every pixel would have been very hard under these

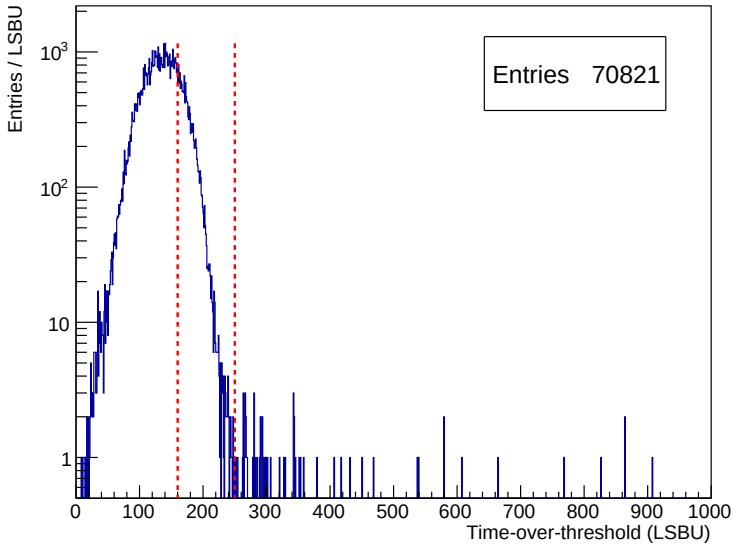

Figure 4.34: Time-over-threshold distribution of the hits, pixel (28,35) of GTK_3, dataset P1. The red lines marks the selection.

conditions. As a fall-back solution, we first computed the hit time resolution using only the GigaTracker stations (*standalone* method). Later, the collaboration corrected some of the bit flips that were corrupting the data and merged the STRAW trigger-less data and global NA62 data stream for the run 1520. We also computed the hit time resolution with this patched dataset (*trigger matched* method).

Standalone Method We chose the well illuminated pixel (28,35) on GTK_3 to act as a reference timing detector for the second station. In addition, to reduce the time walk effects, we selected hits with a time-over-threshold between 160 and 250 LSBU. The pixel (28,35) time-over-threshold distribution is displayed in Figure 4.34, the red lines defines the selected range.

Starting from this reference pixel, we looked at the hit time differences with 30 pixels on GTK_1. Using the ideas presented in the Section 3.2.4, we computed the time walk corrections, T_{corr}, independently for each pixel:

$$T_{\text{corr}}\,(\text{ToT}) = \text{cst.} + \text{slope} \times \text{ToT}\ . \tag{4.4}$$

A typical example is shown in Figure 4.35.

With the correction curves, we can compute the hit time resolution of each pixel. A representative distribution of the hit time difference is presented in Figure 4.36. We obtain, for the pixel (31,34),

$$\sigma_t < 681\ \text{ps}\ , \tag{4.5}$$

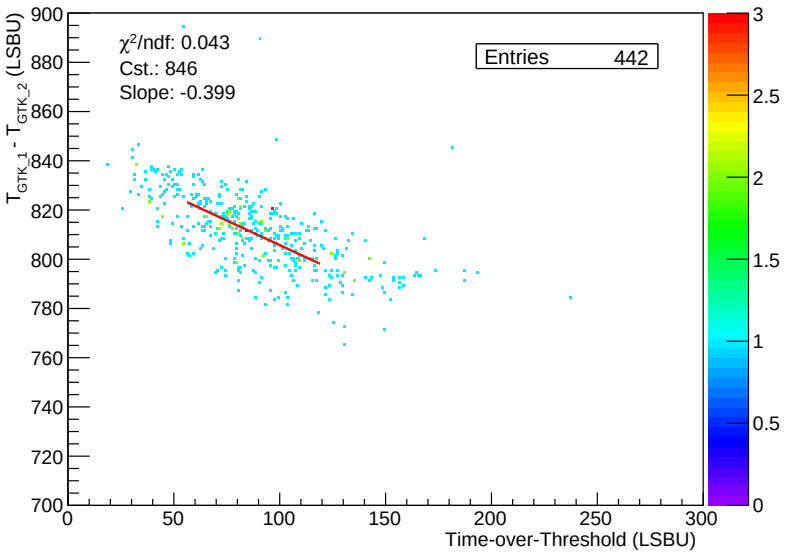

Figure 4.35: Time-over-threshold correction curve for the pixel (31,34) of GTK_1, dataset P1.

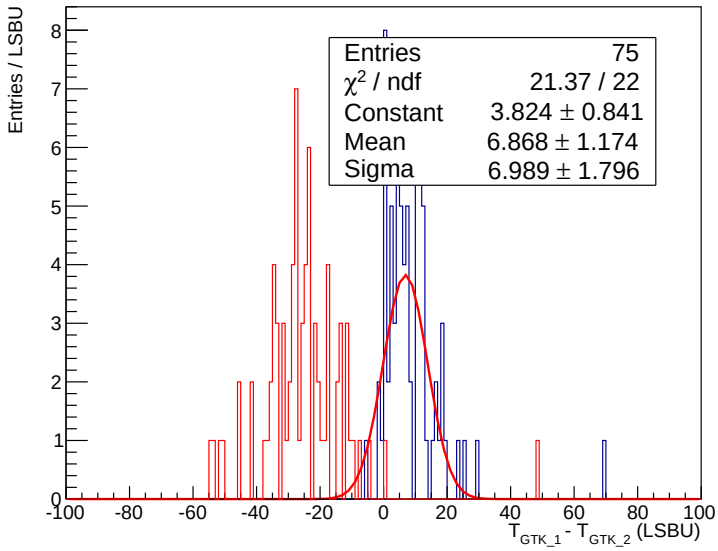

Figure 4.36: Distribution of the time differences between the pixel (28,35) of GTK_3 and the pixel (31,34) of GTK_1, dataset P1. The red and blue histograms are before and after the time walk correction respectively.

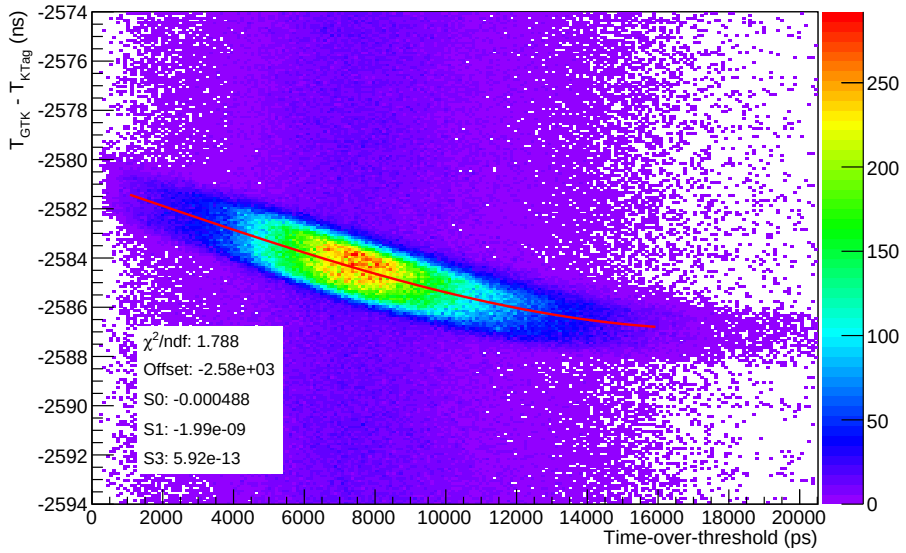

Figure 4.37: Global time-over-threshold correction curve for GTK_1 computed using the data from the run 1520. One has to be careful when comparing with the demonstrator (see Figure 3.25) as the present correction is not done pixel per pixel. The color scale indicates the number of entries per 97.7 ps × 97.7 ps bin.

where the time resolution of the reference pixel is not subtracted. It is apparent that we do not have enough statistics to perform a reliable pixel-per-pixel correction.

Trigger Matched Method Using the run 1520 patched data, we recomputed the hit time time resolution with KTAG as an external time reference. Once again, we looked at the hit time differences as a function of the hit time-over-threshold, the distribution is plotted in Figure 4.37. We fitted one correction curve, T_{corr}, for all the pixels:

$$T_{\text{corr}}\,(\text{ToT}) = \text{offset} + \text{S0} \times \text{ToT} + \text{S1} \times \text{ToT}^2 + \text{S2} \times \text{ToT}^3\ . \tag{4.6}$$

We will refine the results by applying an additional *row* correction. As we can see in Figure 4.38, since we used a global time walk correction instead of a pixel-per-pixel one, each row has a particular time offset. Using this additional correction, we can compute the global time resolution of GTK_1. As shown in Figure 4.39, we obtained a global hit time resolution,

$$\sigma_t < 337 \text{ ps}\ , \tag{4.7}$$

where the KTAG time resolution is not accounted for.

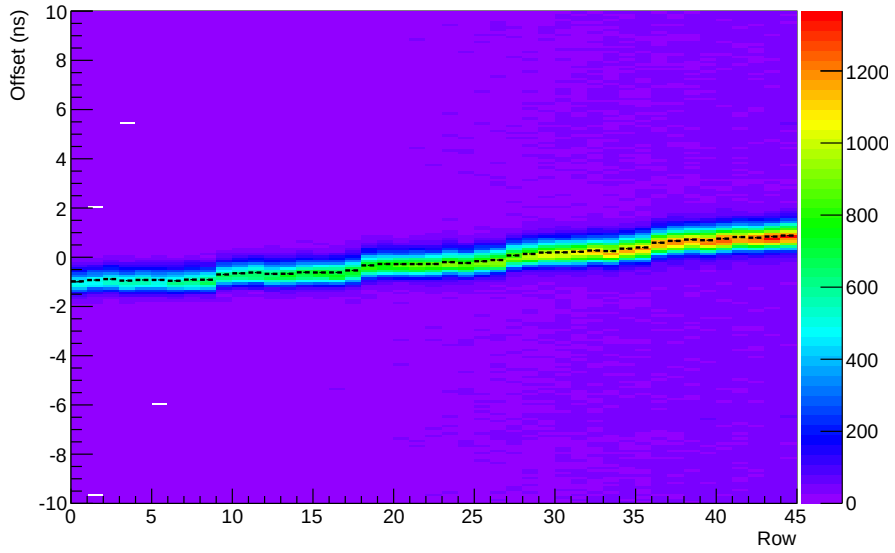

Figure 4.38: The black dashed segments indicates the row correction factor extracted from the graph.

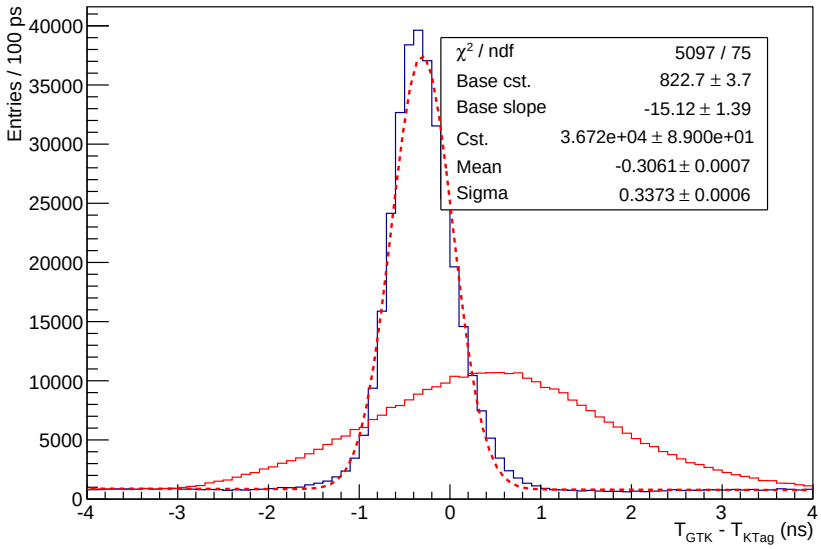

Figure 4.39: Global hit time resolution of GTK_1. The blue curve corresponds to the time walk- and raw- corrected time differences. The red curve is the raw distribution.

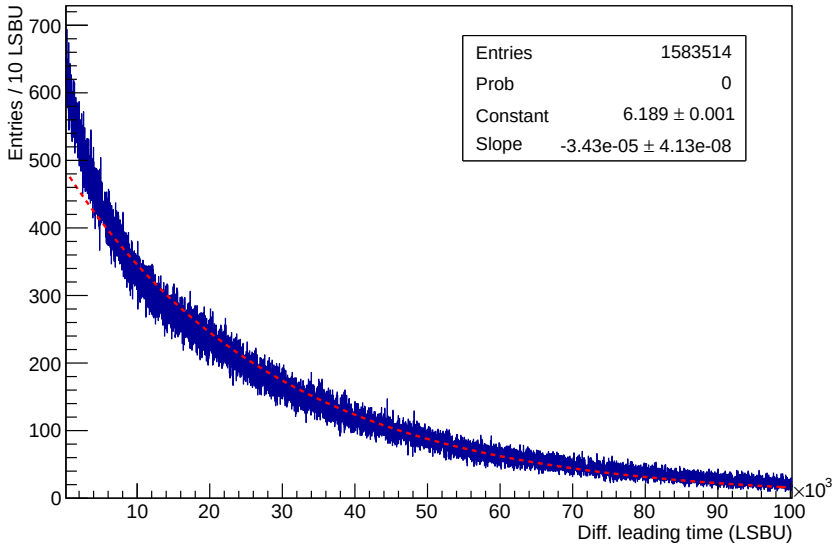

Figure 4.40: All the good pixels of GTK_3 are included, burst 1418346824. The dashed green line represents the fitted exponential; there is an excess of close consecutive hits. At least a part of this effect is caused by share sharing between adjacent pixels.

Hit Rates

The time difference, Δt, between two subsequent hits should follow the classic exponential distribution

$$P(\Delta t) = \lambda e^{\lambda \Delta t} \ , \quad \Delta t \geq 0 \ . \tag{4.8}$$

We obtained $\lambda = 3.43 \times 10^{-5}$ LSBU or ≈ 334 kHz by fitting an exponential to the time difference between consecutive hits on GTK_3 (see Figure 4.40). It agrees with the average hit rate calculated by dividing the total number of hits by the burst length:

$$1\,583\,514/5 \text{ s} = 316.7 \text{ kHz} \ . \tag{4.9}$$

If the station is well aligned, we can scale the total hit rate on the chip #0 to the total hit rate on the sensor by multiplying by 14.75, we find about 4.9 MHz at GTK_1 (third station) position. The multiplicative factor was computed using `NA62MC`. As we can see in Figure 4.40, there is an excess of close consecutive hits. If we zoom on the small time difference region (Figure 4.41) the excess of subsequent hit with $\Delta t < 60$ LSBU is clear. Since all the pixels of chip are included in this distribution, at least part of the excess is caused by the charge sharing effects between adjacent pixels.

To conclude, we made a crude estimate of the average dead time by looking at the time difference between consecutive hit in the same pixel (see Figure

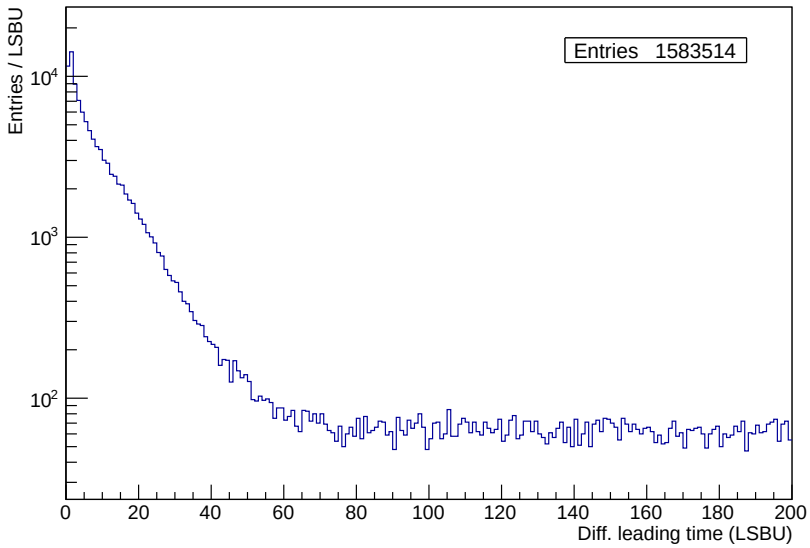

Figure 4.41: All the good pixels of GTK_3 are included, burst 1418346824. See also Figure 4.40.

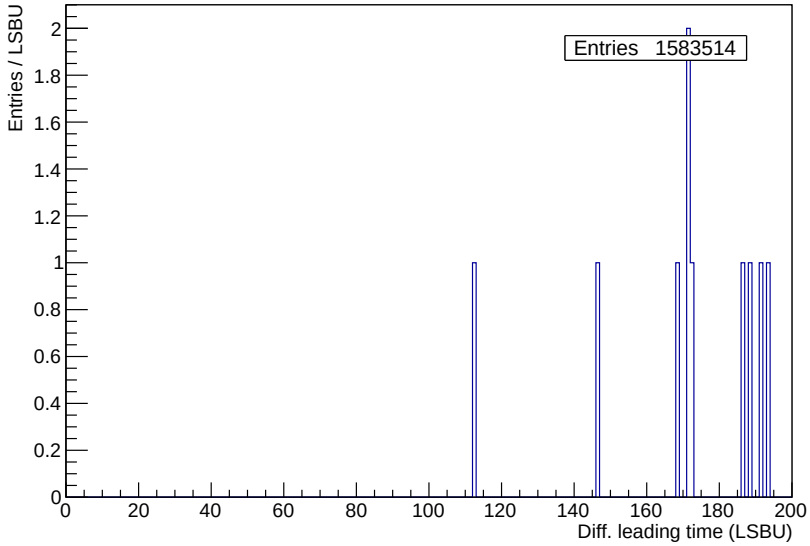

Figure 4.42: Time difference between consecutive hit in a pixel, GTK_3, burst 1418346824. The TDCpix hit arbiter logic forbid hits to close in time. The dead time corresponds to the analog pulse processing time which depends on the time-over-threshold.

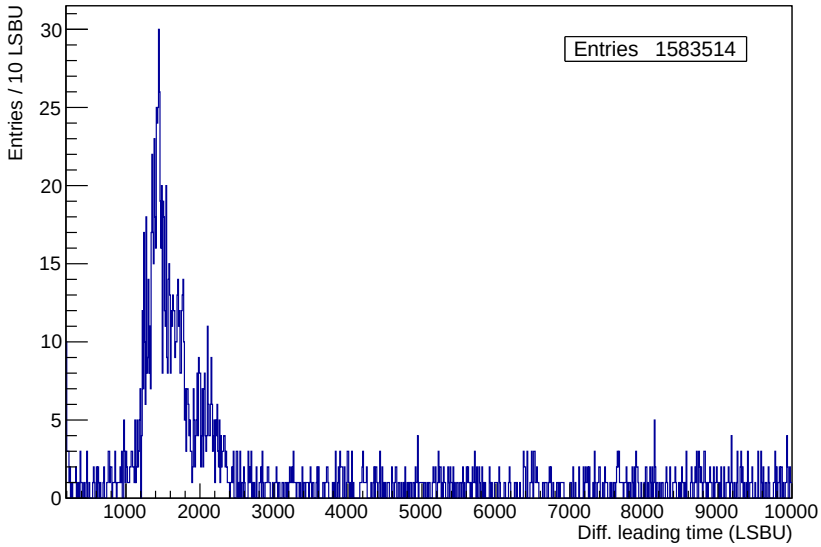

Figure 4.43: Time difference between consecutive hit in a pixel, GTK_3, burst 1418346824. A small cluster of abnormal hits is present around $\Delta T \approx 1500$ LSBU. This effect is not explained at the moment.

4.42). Using the parameters derived from the exponential fit presented in Figure 4.40 and supposing that the hit rate is constant over the whole chip we expect about 27 hits between 0 and 100 LSBU and the same amount between 100 and 200 LSBU. We can guess that the average dead time is around 150 LSBU. This number is in agreement with the time-over-threshold distribution shown in Figure 4.34. Indeed, the time-over-threshold corresponds more or less to time needed to process a hit in the front-end. If necessary, one can easily improve the estimation by increasing the statistics. Finally, we also noticed a small cluster of abnormal hits grouped around $\Delta T \approx 1500$ LSBU (see Figure 4.43). We do not have an explanation for this at the moment.

4.2.4 Summary

In 2014, the corner chip of all the three stations were readout. However, the second station vertical position was displaced by 20 mm which limited our ability to reconstruct tracks. The sensor bias voltage was limited to 170 V.

Despite this, the first results are promising; with the data collected we demonstrated that:

- Hit time resolution below is 320 ps at 170 V with a global time walk compensation (see Figure 4.39). Indeed, because of the limited statistics, the same time walk correction curve was used for a row of pixel.

- The average 5-pixels group dead time is around 150 LSBU (or 15 ns).
- The average hit rate on the corner chip was 334 kHz which is compatible with the beam condition during the run 1520.

Nevertheless, some subtle features remain to be understood. A small anomalous cluster of subsequent hits separated by 150 ns is visible in the data (see Figure 4.43). This still needs to be confirmed with the 2015 data. This effect is extremely tiny and does not affects the detector performances. In addition complex patterns are seen in the rate of illegal pixel address (see 4.25). This is not fully understood at the moment. Again, this effect is tiny and does not impact the detector performances.

4.3 NA62 Detector Performance

The 2014 pilot run was dedicated to the commissioning of the data acquisition and trigger systems and of the detectors. One of the of main limitations was the muon veto system; only the MUV3 detector was operational. In addition, the digital trigger was not ready, the experiment relied on a traditional NIM logic instead. The trigger rate was limited to about 10–20 kHz. The conditions were often unstable, causing data losses and corruptions. Moreover, neither the STRAW nor GigaTracker were included the global DAQ. Nevertheless, at the end of the 2014 data taking period some good runs, i.e. stable run conditions and most of the detectors included, were stored on disk. Among them, the run 1520 is especially useful as the GigaTracker and STRAW data streams were manually merged with the global NA62 stream.

This section summarises a first exploration of the global NA62 data. Using the run 1520, we studied the unexpected *beam component*: 75 GeV/c low angle tracks illuminating the downstream detectors. In addition, we selected $K^+ \to \pi^+\pi^+\pi^-$ like events among the signal. This channel can be used for GigaTracker alignment and for beam monitoring purposes.

4.3.1 Data Sources

The data source for this studies is the run 1520. Two triggers were running, Q1 $\times$!MUV3 downscaled by a factor 30 and Q1 downscaled by a factor 500. The Q1 condition means at least one coincidence between the two CHOD planes in the same quadrant. The !MUV3 condition means no coincidences between a pair of PMTs reading a MUV3 tile.

Out of the 1215 available bursts, 1055 were reconstructed without errors. No attempts have been made to recover the corrupted files. Each good run was mapped offline with the corresponding GigaTracker *trigger-less* run. We removed 350 bursts that contained no events or that were not compatible with the GigaTracker trigger-less rates. Indeed, as shown in Figure 4.44, the GigaTracker rates extracted from the NA62 data stream display unphysical varia-

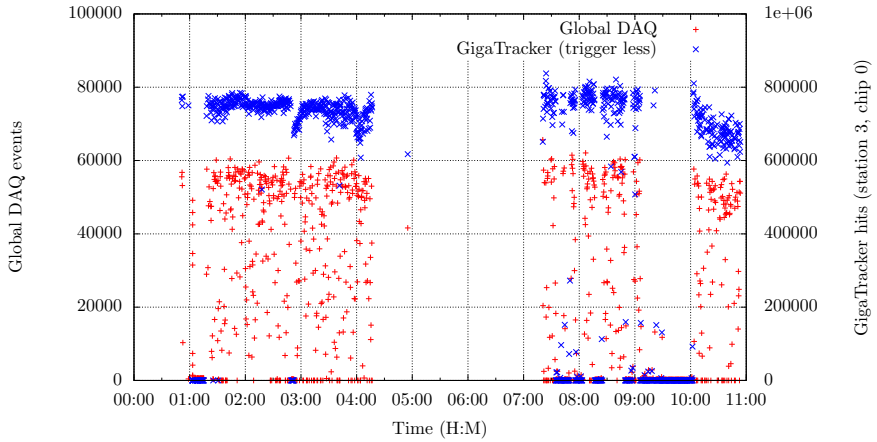

Figure 4.44: Matching of the NA62 global data stream with the GigaTracker trigger-less data, each point corresponds to a burst. The bursts having a too low number of events compared to the amount of hits recored by the GigaTracker were excluded from the study. Indeed, the NA62 data stream was affected by data corruptions.

tions. We were left with a list of 750 bursts and a total of 24 310 059 events. During the same period, 521 113 475 hits on the chip #5 of the third GigaTracker station were recorded. Noisy pixels were removed on a burst-by-burst basis as explained in Section 4.2.2. The GigaTracker sees all the tracks while only K^+ decays meeting the trigger conditions were stored on disk.

We generated and reconstructed the Monte Carlo samples with `NA62MC` rev. 550 (2015-06-12) and `NA62Reconstruction` rev. 557 (2015-06-21). The details are given in Table F.1 (Appendix F). The actual GigaTracker configuration during the run 1520 was implemented in the Monte Carlo. We reconstructed the data with `NA62Reconstruction` rev. 542 (2015-06-02) and a custom GigaTracker raw decoder. The decoder is the piece of software that unpacks the raw data and transforms them into a collection of well defined hits.

4.3.2 Single Track Selection

Early on, a significant number of reconstructed tracks having a momentum close to 75 GeV/c were spotted in the STRAW data. This was unexpected, most of the beam particles should travel through a gap without interacting with the subdetectors. This class of events was called the *beam component*, it is clearly visible in Figure 4.48. The component can be easily isolated and hence does not directly interfere with the NA62 physics goals. However, it occupies the trigger bandwidth and could speed up the aging of parts of the detector.

The primary goal of this short study was to check if the beam component

Table 4.10: GigaTracker geometry parameters used in this study. The station two was offset by +20 mm along the Y-axis and displaced by +15 mm along the Z-axis.

Station	Chip thickness (µm)		X axis offsets (mm)	
	Run 1520	Nominal	Run 1520	Nominal
1	450	100	-9	0
2	100	100	-6	0
3	450	100	-2	0

could be reproduced with `NA62MC`. In addition, we simulated the impact of the GigaTracker geometry and of the KTAG radiator gas on the magnitude of the effect. There are a couple of evident caveats to this work. First, the difference of the kaons and pions elastic interaction cross sections was not taken into account, they are similar but not identical, see for instance the Table 3.7 (Section 3.2.3). Second, the halo of muon surrounding the beam was not simulated.

Data Sets

By default, `NA62MC` propagates only the kaons that decays in the fiducial volume (from $z = 104$ m to $z = 180$ m). This effectively removes the kaons from the beam component at the Monte Carlo level. If we assume that pions behave similarly to the kaons, we can extrapolate the kaon contribution to the beam component from the pion one. We reconstructed a total of 997 940 kaon decays (N_K); see Table F.1 (Appendix F). We note $P_{!K} = 0.87$ and $P_{!\pi} = 0.98$ the probability that a 75 GeV/c kaon and pion, respectively, does not decay while crossing the fiducial volume. The number of pions (N_π) necessary to mimic the kaon contribution to the beam component is therefore

$$N_\pi = \frac{N_K P_{!K}}{P_{!\pi}} \ . \tag{4.10}$$

Using the formula above we find $N_\pi = 888\,048$. That is, if we propagate 888 048 pions in the detector with the Monte Carlo, they will act as the missing contribution of the 997 940 kaons.

GigaTracker and KTAG Geometry

The only components that are known to intercept the beam particle and could scatter them are the KTAG radiator gas and the GigaTracker detectors.

The GigaTracker stations installed in 2014 were thicker than the nominal design. Moreover, they were slightly offset from the beam axis. This was accounted for in the Monte Carlo simulation. Specifically, the cooling plate thickness in the beam acceptance was 370 µm instead of 130 µm, the readout chips of two stations were thicker and the second GigaTracker station was offset

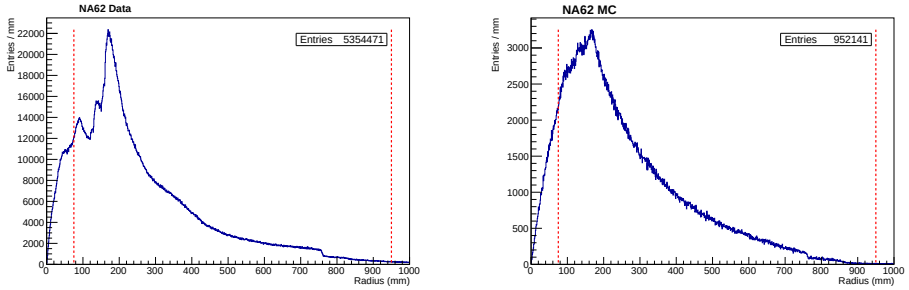

Figure 4.45: Radial distance between the STRAW track candidates and the nominal beam axis at the fit reference plane. The red lines indicate the selected region.

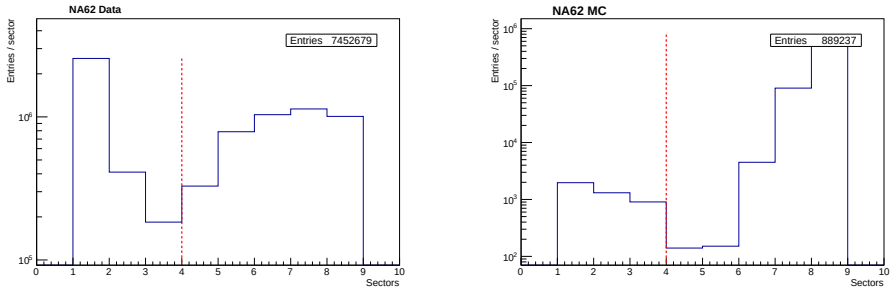

Figure 4.46: Candidates with > 4 activated KTAG sectors are considered to be kaons.

by +20 mm along the Y-axis and displaced by +15 mm along the Z-axis. The geometry parameters and offsets are grouped in Table 4.10. In 2014 the total silicon thickness of the third GigaTracker station, in the beam acceptance was 1020 µm instead of 530 µm.

The KTAG radiator gas pressures were, respectively, 1.736 bar and 3.670 bar for nitrogen and hydrogen. The nitrogen pressure was slightly adjusted to correspond to the run 1520 conditions.

Trigger and Selection

In the NA62 global data stream, we selected the events triggered by the Q1 × !MUV3 condition. This trigger was downscaled by a factor 30. For the Monte Carlo data, the same trigger was simulated, i.e. at least one coincidence between the two CHOD planes in the same quadrant and no coincidences between any pairs of PMTs reading a MUV3 tile.

We applied set of loose cuts: (a) the radial distance between the STRAW track candidate and the nominal beam axis must be between 7.5 and 95 cm

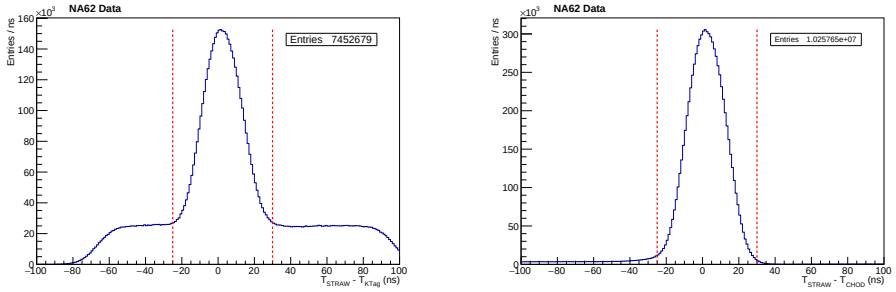

Figure 4.47: Time differences between the STRAW and the KTAG (left) and between the STRAW and the CHOD (right) candidates. The selection is marked by the red lines.

at the fit reference plane (see Figure 4.45), (b) a KTAG candidate with more than four KTAG sectors (see Figure 4.46) and (c), the STRAW track candidate time must be within 30 ns of at least one KTAG and one CHOD candidate (see Figure 4.47).

The events passing the selection are plotted in Figure 4.48 (data) and in Figure 4.49 (Monte Carlo). The detector illumination before the cuts is shown in Figure 4.50, the off-centred bright spot is caused by an inefficient MUV3 tile. To select the beam component, we applied an additional criterion: the STRAW track candidate momentum must be between 72 and 78 GeV/c. In the data, a significant amount of $K^+ \to \mu^+\nu_\mu$ type of events passes the selection. This feature is not reproduced by the Monte Carlo. It is at least partially explained by the fact that some of the MUV3 tiles were inefficient. The Z positions of the reconstructed decay vertices of the "beam component"-like events are shown the Figure 4.51. A cluster of events is clearly visible at third GigaTracker station Z position.

Finally, the RICH ring radius as a function of the STRAW track candidate momentum is plotted in Figure 4.52. The π and μ components of the beam are clearly visible. We can guess the presence of the unexpected kaon component.

Normalization and Results

We used the third GigaTracker station as a point of comparison between the data and the Monte Carlo. Indeed, in 2014, the GigaTracker was operated in trigger-less mode: all the hits were saved on disk. During the run 1520, only the chip #5 of the third station was read out. We replicated the run conditions with `NA62MC`, simulating the beam and the six main decay channels. The total number of generated events is reported in Table F.1 (Appendix F). Before the application of any trigger or selection we found 968 148 hits on the chip #5 (see Figure 4.53). For the run 1520 data, after the burst-by-burst matching of the global NA62 stream and the GigaTracker trigger-less data, we find 521 113 475 hits on the chip #5. The noisy pixels are filtered out.

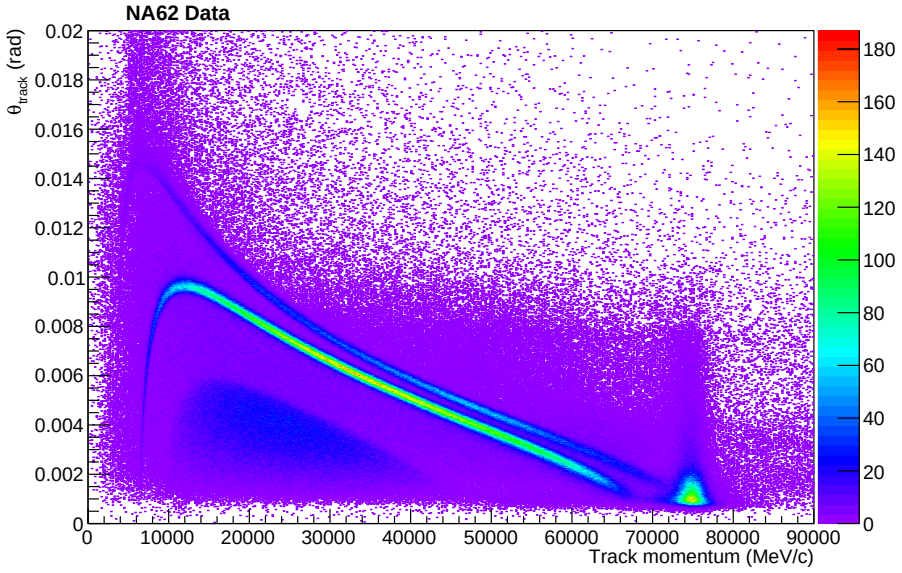

Figure 4.48: Single charged track selection. In addition to the beam component, the three main kaon decay modes are clearly visible, from the top to the bottom, $K^+ \to \mu^+\nu_\mu$, $K^+ \to \pi^+\pi^0$ and $K^+ \to \pi^+\pi^+\pi^-$. A significant fraction of $K^+ \to \mu^+\nu_\mu$ type of events passes the MUV3 cut. No constraint on the decay vertex was imposed. The cuts are detailed in the text.

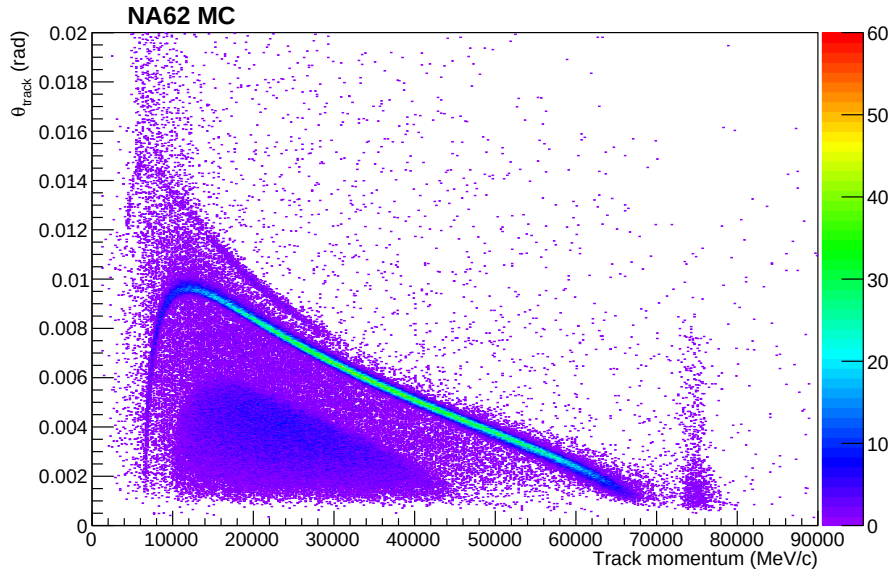

Figure 4.49: Single charged track selection. It is similar to the Figure 4.48 but for the Monte Carlo data. In addition to the beam component, the three main kaon decay modes are clearly visible, from the top to the bottom, $K^+ \to \mu^+\nu_\mu$, $K^+ \to \pi^+\pi^0$ and $K^+ \to \pi^+\pi^+\pi^-$. No constraint on the decay vertex was imposed.

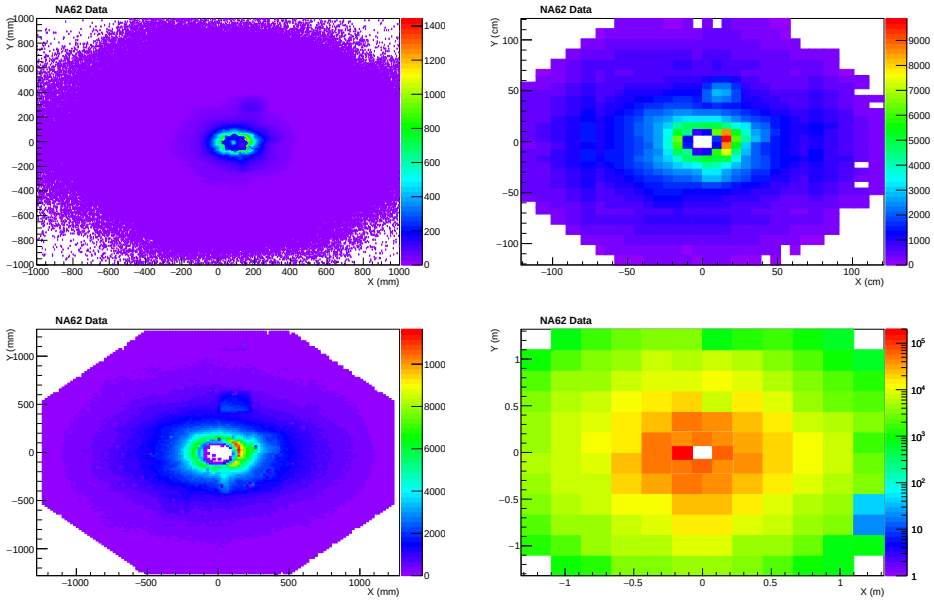

Figure 4.50: STRAW (top left), CHOD (top right) LKr (bottom left) subdetector illumination under the Q1 × !MUV3 condition. The beam component is visible on the right of the beam pipe gap. MUV3 (bottom right) illumination under the Q1 condition. A tile close to the center is clearly inefficient. The beam direction points out of the page.

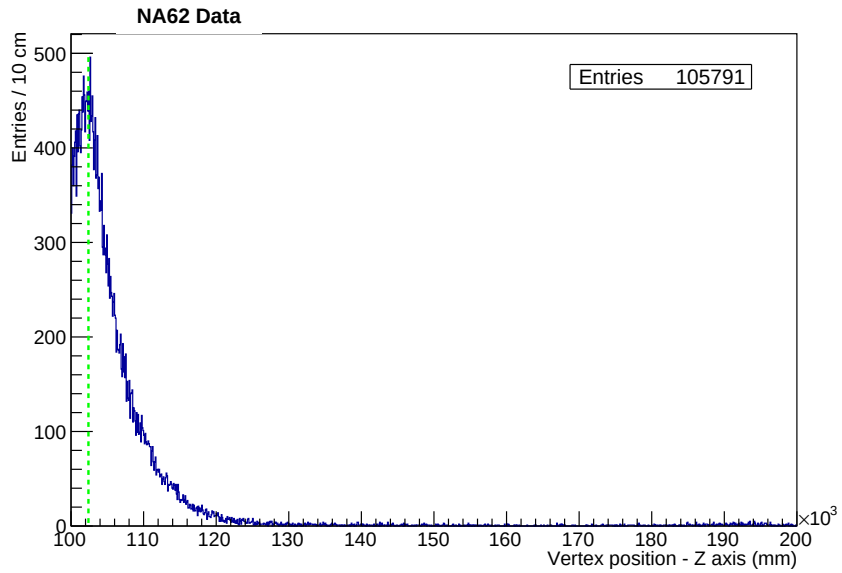

Figure 4.51: Reconstructed vertices of the beam component like events. The green line indicates the position of the last GigaTracker station.

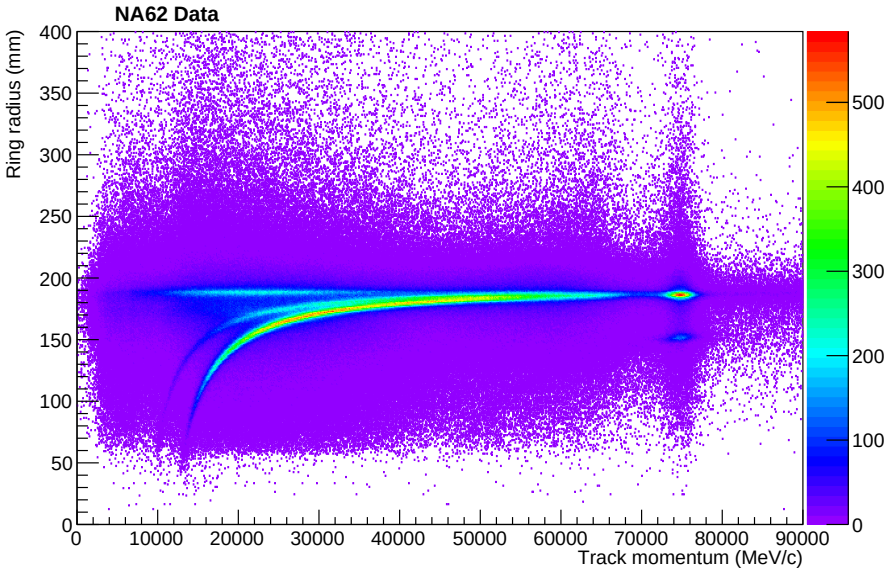

Figure 4.52: All the events passing the loose selection, no constraint on the decay vertex position or on the STRAW track candidate χ^2 are imposed. We see the electrons (top curve), muons (middle curve) and the pions (bottom curve) contributions. The beam component is also visible.

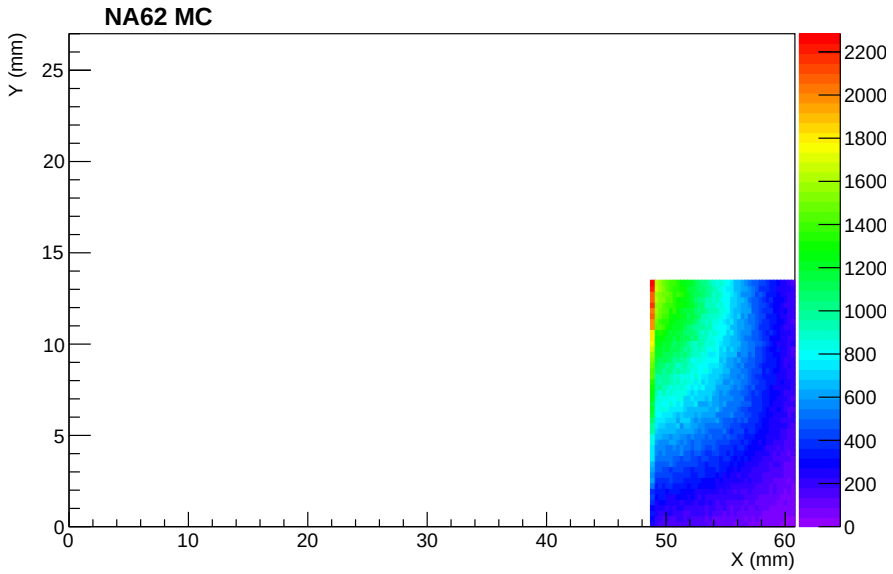

Figure 4.53: Illumination of the chip #5 of the third GigaTracker station. The beam direction points out of the page.

First, using the Monte Carlo data, 968 148 hits on GigaTracker lead to 1 234 beam component type events, the ratio of these two quantities is 1.3×10^{-3}. Second, using the NA62 data, 521 113 475 hits on GigaTracker correspond to 105 791 beam component type events. Compensating for the trigger downscaling factor, the ratio of these two numbers is 6.1×10^{-3}.

To sum up, the beam component is partially simulated by `NA62MC` but the default setting hide its effects. The current Monte Carlo simulation explains only about one fifth of the component. For the most part, it is due to scattering in the KTAG radiator gas and in the GigaTracker stations. In 2014, the effect was enhanced by a factor 1.6 because of the thicker GigaTracker stations.

The effect of the interaction of the beam with the magnets and collimator placed before the last GigaTracker station remains to be explored. Furthermore, the simulated GigaTracker magnets are perfect and use the design values for the field strengths, this hypothesis was never cross-checked with actual measurements.

Moreover, using the Monte Carlo only, we studied the effect on alternate configuration of the KTAG and GigaTracker on the magnitude of the beam component. The results are grouped in the Table 4.11, a large part of the events are caused by the last GigaTracker detector.

Table 4.11: Influence of the GigaTracker and KTAG on the beam component.

Scenario		Scaling
GigaTracker	KTAG	
Nomi.	N_2	1.0
Nomi.	H_2	0.74
Run 1520	N_2	1.60
None	N_2	0.35

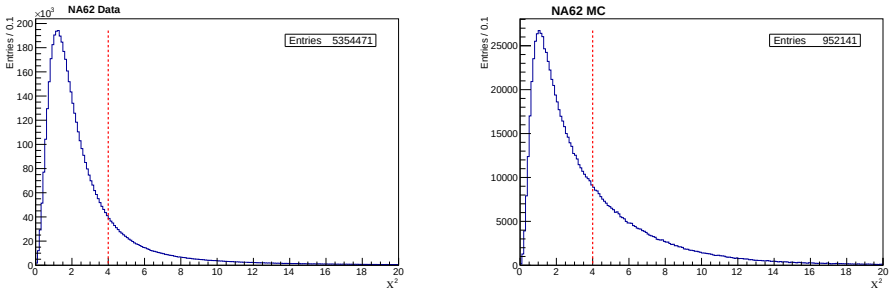

Figure 4.54: χ^2 of the STRAW track candidates. Only the tracks with $\chi^2 < 4$ were used to compute the mass spectrum.

4.3.3 A First $K^+ \to \pi^+\pi^+\pi^-$ Selection

To select the $K^+ \to \pi^+\pi^+\pi^-$ decays, we reused the previous cuts but this time asking for exactly three good STRAW track candidates. In addition, the χ^2 of the STRAW candidates must be < 4 (see Figure 4.54) and on the reconstructed vertex Z position must be between 105 and 170 m (see Figure 4.55). The decay vertex Z positions distribution displays a large cluster of events at low Z. This feature is not reproduced by the Monte Carlo and is still unexplained. Knowing the STRAW track candidate's momentum and assuming that they are indeed pions, we can reconstruct the kaon mass. The reconstructed mass spectrum is presented in Figure 4.56. The plot on the left shows events passing decay vertex Z position cut while the plot on the right focus on the low Z events ($Z < 105$ m). The reconstructed kaon mass distribution agrees relatively well with the Monte Carlo simulation given that the STRAW tracker was only partially commissioned in 2014. The large discrepancy for events with a low reconstructed Z remains to be understood.

4.3.4 Summary

We explored the data taken during the run 1520. This run is the only one where STRAW data were merged with the NA62 data stream. These preliminary studies are very crude as the detector and data acquisition system were only partially commissioned. Similarly, the Monte Carlo simulation was still in

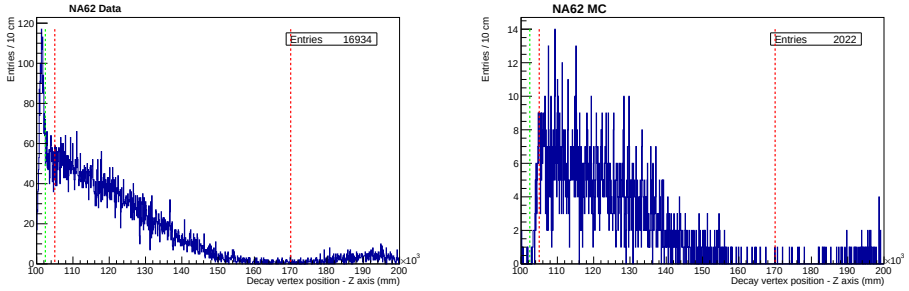

Figure 4.55: Reconstructed decay vertices of the three charged tracks decays. The red lines indicates the selection while the green line shows the position of the third GigaTracker station.

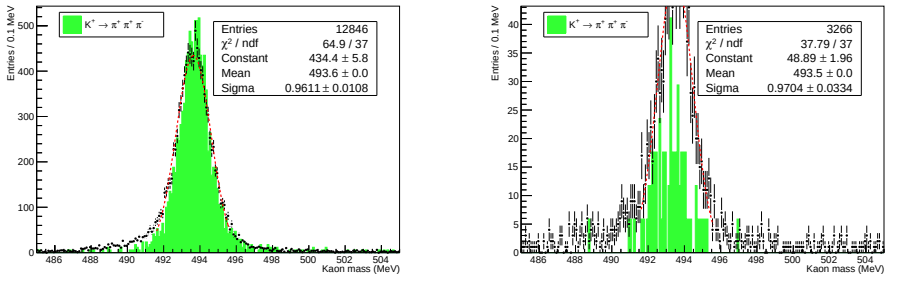

Figure 4.56: Reconstructed mass spectrum of the three charged tracks decays. The six main kaon decay channels are simulated. The plot on the left shows events passing decay vertex Z position cut while the plot on the right focus on the low Z events.

intense development.

The main takeaways are:

- An unexpected 75 GeV/c component is visible in the downstream detectors. About one fifth of the effect is explained by the Monte Carlo simulation. A large part of the beam component is simply due to scatterings in the last GigaTracker station (see Table 4.11).
- As a benchmark, we selected a sample of $K^+ \to \pi^+\pi^+\pi^-$ decay. This channel can be used to monitor the beam and therefore the GigaTracker. The first data-Monte Carlo comparison is encouraging (see Figure 4.56) even if it is still very simplistic.

Some features remain to be understood. To begin with, we don't have an explanation for the large excess of reconstructed $K^+ \to \pi^+\pi^+\pi^-$ decay vertices in the low-Z regions (see Figure 4.55). One should note that the muon vetoes were not fully operational, in addition, the STRAW track reconstruction algorithm we used was still in development.

The beam component is not fully reproduced by the simulation. This could at least be partially explained by the current status of the detector description in the Monte Carlo. For some elements of the beam line only the magnetic-field is modelled; in all the cases it is perfectly uniform over the whole magnet gap, which is unrealistic. Moreover, the beam pipe is not implemented.

4.4 Summary and Discussion

In 2010, a 45 pixels GigaTracker prototype was tested in beam. The campaign proved that the technology was adequate for the NA62 environment. Notably, a careful analysis demonstrated that hit time resolution below 150 ps could be achieved with a bias voltage of 300 V. The prototype turned to be a formidable learning tool. The detailed timing corrections methods were established using the 2010 datasets. We showed that good results can be achieved with linear correction per pixel. The correction factors strongly depend on the detector operating conditions. Furthermore, the detector efficiently was confirmed to be above 99 percent and the charge sharing effects showed no significant impacts.

In autumn 2014, for the first time, the full scale detector was tested in real conditions. Despite the fact that only a part of the detector was commissioned, the first results have been extremely encouraging. To begin with, GigaTracker gave key inputs to understand the secondary beam structure; the hit rate shows variations up to a factor of two during the burst "flat top". This structure proved to be a significant issue for the data acquisition system. Moreover, it was one of the first proof of the good behaviour of the detector.

Next, the hit time resolution have been determined. In a first stage, we used the FFT time alignment algorithm to manually find time correlations between the GigaTracker and the KTAG. Then, thanks to a collaboration effort, the

STRAW and GigaTracker data were manually merged with the global NA62 data stream for one good run. Using this limited dataset, we found a time resolution below 340 ps for a bias voltage of 170 V. Extrapolating the demonstrator results at a bias voltage of 170 V, in the ideal case, we can expect to reach 250 ps. This 35 percent difference is explained by the lack of statistics, we were limited to a time walk correction per row instead of a correction per pixel.

We were not able to study the tracking performance and the detection efficiency as it was impossible to reconstruct tracks with the 2014 dataset. Indeed, the second station vertical position was displaced by +20 mm with respect to the nominal value. As a result, most of the beam was not crossing the second detector, making the track reconstruction impossible.

Using the merged run we studied the beam component seen in the STRAW tracker. We showed that it was indeed simulated by the Monte Carlo after a proper configuration. As one could have expected, it is mostly caused by multiple scattering in the KTAG radiator gas and in the GigaTracker stations. In 2014, the effect was reinforced by a thicker GigaTracker detector. Nevertheless, the Monte Carlo simulation only explains one fifth of the effect. This still need to be carefully explored.

Finally, we concluded our study of the pilot run data with a simple $K^+ \to \pi^+\pi^+\pi^-$ selection. This decay is useful for the GigaTracker alignment and it allows to monitor the beam position by reconstructing the decay vertices. The reconstructed kaon mass distribution is in good agreement with the Monte Carlo prediction.

Conclusion and Outlook

The NA62 decay-in-flight technique relies on the accurate kinematic reconstruction of both the initial and the final state of the processes. This, coupled with the high intensity beam, puts strong constraints on the beam tracking, therefore, a new silicon pixel tracker dubbed the GigaTracker has been developed for NA62. The main challenges were the time resolution, the data throughput, the radiation hardness and the thermomechanical integration.

One of the key innovations of the GigaTracker is the readout ASIC. During the development phase, two designs were investigated. The TDCpix was selected for the final detector as the architecture was more mature when a choice had to be made. Nevertheless, the option based on the constant fraction discriminator is theoretically better for timing application as offline time walk compensation is not needed.

Another highlight of the detector is the silicon microchannel cooling plate. The device can convey large amounts of heat with a minimal amount of material while operating in vacuum. The application of the technique in HEP has been pioneered by NA62. Similar device will be used for the ATLAS and the LHCb tracker upgrade.

Outcomes

Time Resolution In this dissertation we have proven that a hit time resolution below 150 picoseconds could be achieved in real conditions [2]. This is an unmatched achievement for silicon pixel detectors. To reach such an accuracy the time walk compensation has been extensively explored.

There are multiple axis of attack to improve the situation. Using GigaTracker as an example, in ideal conditions the hit time resolution can be split into three parts: the electronics (40 ps), the straggling (60 ps) and the pixel geometry (70 ps). The contribution of the electronics will likely continue to diminish as the technology advances. Similarly, the pixel geometry can be tweaked to improve the electric field uniformity and the charge collection time. Going in that direction, silicon detectors with an intrinsic gain are currently developed [131]. The technique allows to combine thin sensors and large signals. Hit time resolution of the order of tens picoseconds are envisaged.

Sensor Radiation Hardness Furthermore, I have shown that the radiation hardness of the n-in-p sensors manufactured by FBK is adequate for the GigaTracker. The actual sensor lifetime will depend on the detector operating conditions but it should sustain at least 100 days of operation at nominal intensity and it will not be limited by the bulk depletion. The effect of the total ionizing dose (TID) on the TDCpix needs further evaluation.

Software Platform In addition to various hardware developments, I contributed to the experiment software platform. My main contribution has been the implementation and maintenance of a detailed Monte Carlo simulation of the GigaTracker. The model has been used to validate the detector mechanical supports design. I tackled the spatial alignment of the GigaTracker by proposing an algorithm which uses reconstructed $K^+ \to \pi^+\pi^+\pi^-$ decays and a model of the tracker's magnetic field to accurately reconstruct the detector positions. I also wrote the interface to the experiment's condition database and raw data unpacking tools for the GigaTracker.

Prospective Studies In parallel to the activities related to detector development I began to work towards the $K^+ \to \pi^+\nu\overline{\nu}$ analysis. Specifically, the Monte Carlo simulation was used to perform a prospective study of the background induced by the last GigaTracker station. I showed that the hit time-over-threshold can be used to reject a large fraction of problematic inelastic events.

This backgrounds remain challenging and should be evaluated with the data. For charge exchange processes, a first steps could be to reconstruct the $K_S \to \pi^\pm\pi^\mp$ decay originating from the last GigaTracker station. Similarly, one could take advantage of the thicker than nominal GigaTracker stations to study inelastic events and try to scale the results to the nominal thickness.

2014 Pilot Run Finally, I explored first NA62 data. The performances of full scale GigaTracker have been assessed; considering the operating conditions and the limited available statistics they were found in line with the expectations. I developed a simple selection for the $K^+ \to \pi^+\pi^+\pi^-$ decay, the results indicate that the NA62 detector is performing according to the predictions. However, an unexpected 75 GeV/c kaon component visible in the downstream detectors is only partially reproduced by the present Monte Carlo simulation.

Overall, the results obtained with the first partial NA62 datasets looks promising. The work carried out establishes a good platform to start more complete studies of the background rejection efficiency, and eventually, an analysis of the $K^+ \to \pi^+\nu\overline{\nu}$ decay.

Outlook

In 2016, after more than ten years of intense development, the NA62 experiment will enter in a more stable era. Particularly, the GigaTracker will be fully commissioned. That will considerably improve the events kinematic reconstruction. Another important improvement is the strengthening of global data acquisition and trigger system. It should be more stable at high beam intensities.

Nonetheless, key points remain to be addressed before reaching the $K^+ \to \pi^+\nu\overline{\nu}$ decay sensitivity. To begin with, the muon and photon rejection efficiencies have to be measured on data. This is essential to understand if the current experimental setup is up to the task. A reliable data driven estimation of the beam induced background is also critical. Likewise, the data acquisition and trigger chain needs to be reinforced to sustain reliably the nominal beam intensity while preserving the signal acceptance. Notably, efficient level one and two trigger algorithms have to be developed.

Past these immediate considerations, reaching a ten percent relative systematic uncertainty on the branching ratio requires a very detailed understanding of the whole experimental setup. Most of the challenges are probably still unknown.

Next to the $K^+ \to \pi^+\nu\overline{\nu}$ decay, the NA62 experiment opens the doors for many other searches from dark photon to heavy neutrinos and to axions. An unprecedented amount of K^+ decays will be recorded over the lifetime of NA62. It could be used to improve the limits on the branching ratios of lepton number violating kaon decays. Finally, thanks to the large amount of $K^+ \to \pi^+\pi^0$ decays, the experiment has the potential to study exotic π^0 decays.

A measurement of the decay branching ratio with a ten percent relative uncertainty is within reach in the coming years. Hopefully it will contribute to our understanding of the beyond the standard model physics. It would be especially powerful to have an accurate measurement of the complementary $K_L \to \pi^0\nu\overline{\nu}$ branching ratio. Indeed, a combination of both channels would provide precious information on the nature of the potential beyond the standard model physics. However, this measurement is much more complicated and will likely not happen in the near future. Yet, the recent progress in computing the ε'/ε ratio in the standard model framework could open a parallel way.

The experimental endeavour is also directed towards $K_L \to \pi^0\nu\overline{\nu}$. The KOTO experiment is currently taking data at J-PARC, the collaboration plan to reach the standard model sensitivity by 2020. Preliminary studies for adapting NA62 to neutral kaon decays in the long term have been done. Strong research and development efforts would be needed. For instance, one have to build photon detectors able to sustain a rate of one GHz of neutrons. Similarly, the very high intensity beam raises radio protection issues in the current NA62 environment.

Appendices

Contents

Appendix A

GigaTracker Angular and Momentum Resolution

The angular resolution of the detector is related to the pixel size and to the detector geometry. In first approximation we have

$$\sigma_\theta \approx \sqrt{\underbrace{\left(\frac{\sqrt{2}\sigma_{\text{pos}}}{d_{13}}\right)^2}_{5.4\ \mu\text{rad}} + \underbrace{\left(\frac{d_{12}}{d_{13}}\sigma_{\text{MS}}\right)^2}_{6.1\ \mu\text{rad}} + \underbrace{(\sigma_{\text{MS}})^2}_{11\ \mu\text{rad}}} = 13.4\ \mu\text{rad}\ , \tag{A.1}$$

where d_{12}, d_{23} and d_{13} are the distances between the first and the second station, the second and the third station and the first and the third station respectively. σ_{pos} is the hit position resolution related to the pixel size, $\sigma_{\text{pos}} = 300\ \mu\text{m}/\sqrt{12}$, and σ_{MS} is the multiple scattering contribution. Indeed, the track direction is given by the distance between the hits position on the first and third station (projected on the X- or Y-axis) divided by the distance between them (d_{13}). The second and third terms are the contributions of the multiple scatterings in the second and in the third stations, σ_{MS} can be computed using the Equation (2.11).

The same reasoning can be applied to compute the relative momentum resolution:

$$\frac{\sigma_p}{p} \approx \sqrt{\underbrace{\left(\frac{d_{23}}{d_{13}}\sigma_{\text{pos}}\right)^2}_{0.06\%} + \underbrace{\sigma_{\text{pos}}^2}_{0.14\%} + \underbrace{\left(\frac{d_{12}}{d_{13}}\sigma_{\text{pos}}\right)^2}_{0.08\%} + \underbrace{\left(\frac{d_{12}d_{23}}{d_{13}}\theta_{\text{MS}}\right)^2}_{0.10\%}} \Big/ d_v = 0.20\%\ , \tag{A.2}$$

where $d_v = 0.06$ m is the vertical displacement of the second station with respect of the first and third one. The three first terms are related to the pixel size of the first, second and third station respectively. Since they are identical, we simply use σ_{pos}. The last term is the contribution of the multiple scatterings

in the second station. The intercept theorem helps to derive the expression. In addition, the small-angle approximation was used for the last term.

Appendix B

Simple Pixel Simulation

We wrote simple programme to simulate the drift and the diffusion of the charge carriers generated by the passage of a charged particle in silicon. The weighting field (see Figure B.1) is computed using the analytical formulation of [132] with 280 µm wide readout electrode. The field effects at the extremities of electrode are exaggerated by this naive simulation. We assume that the electron-hole pairs are uniformly distributed along the particle path. The charge carriers are followed as they drift in the three dimensions due to the electric field; they are removed from the simulation when they reach the top or bottom interfaces. The side of the pixel are warped together, if a charge carrier crosses the left side it is tagged and reintroduced at the right side. This feature allows to study the charge sharing effects.

For high level injections the excess electrons and holes do not move independently, the electric field induced by the charge carriers tends to reduce the diffusion coefficient. This effect is accounted for by introducing an effective *ambipolar* diffusion coefficient [133]:

$$D_a = \frac{2k_B T}{e} \frac{\mu_e \mu_h}{\mu_e + \mu_h} \ , \tag{B.1}$$

that is independent of the carrier concentration. After a drift time τ, the radius of the charge column is

$$r^2(t) = 18 D_a t + r_0^2 \ , \tag{B.2}$$

where t is the time time elapsed since the charge injection and r_0 the initial radius.

The parameter used for the simulation are grouped in Table B.1. The current pulses that we obtained were found in good agreement with the one provided by the `Weightfield2` package [134].

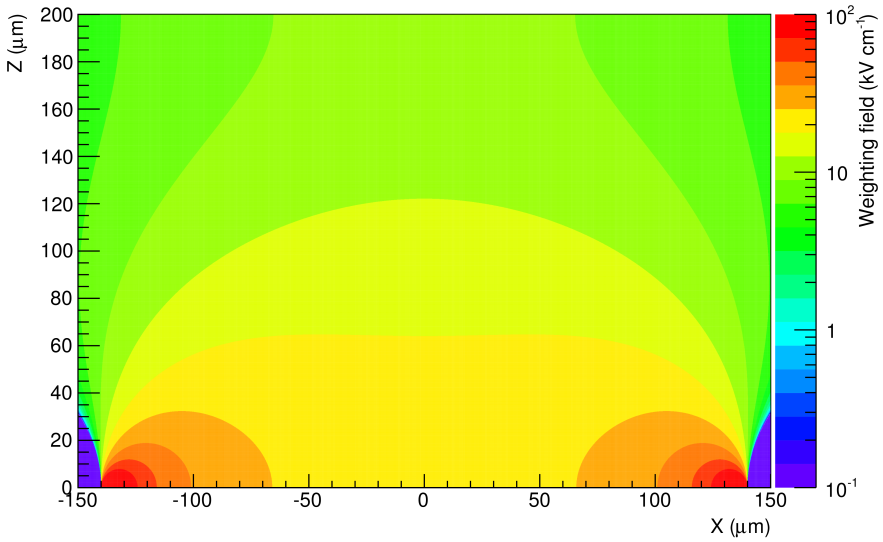

Figure B.1: Weighting field for 200 µm thick sensor with a 280 µm wide electrode at bias voltage of 300 V.

Table B.1: Pixel simulation parameters.

Parameter	Typical value	Description
V_{bias}	300 V	Sensor bias voltage
D	200 µm	Sensor thickness
L	300 µm	Pixel size
μ_e	1350 cm^2 V^{-1} s^{-1}	Electron mobility
μ_h	480 cm^2 V^{-1} s^{-1}	Hole mobility
v_e^{sat}	1.05×10^7 cm s^{-1}	Electron maximum drift velocity
v_h^{sat}	1.0×10^7 cm s^{-1}	Hole maximum drift velocity
Y	75	Electron-hole pairs per micrometer

Appendix C

Sensor Characterisation

This appendix summarises the results obtained from the FBK n-in-p sensor characterisation. The study is described in detail in the Section 3.2.1

C.1 Summary Tables

The measured depletion voltages and leakage currents at 200 V are detailed in Table C.1, Table C.2 and Table C.3.

Table C.1: Wafer 1 - Fluence ± 10 % - Bias voltage set at 200 V.

Diode	Fluence (1 MeV eq. n cm^{-2})	I_{leak} (µA)	V_{dep} (V)
2	1×10^{14}	-16.224 ± 0.026	-93.58 ± 0.43
3	1×10^{14}	-16.211 ± 0.026	-89.39 ± 0.66
4	2×10^{14}	-28.519 ± 0.039	-108.23 ± 0.36
5	2×10^{14}	-31.132 ± 0.041	-138.91 ± 0.37
6	5×10^{13}	-13.675 ± 0.024	-53.67 ± 0.28
7	1×10^{14}	-17.414 ± 0.027	-85.04 ± 0.45
8	1×10^{14}	-19.343 ± 0.029	-102.76 ± 0.94
9	2×10^{14}	-38.611 ± 0.049	-155.37 ± 0.35
10	2×10^{14}	-32.351 ± 0.042	-147.97 ± 0.46
11	2×10^{14}	-33.937 ± 0.044	-130.83 ± 0.41
12	3×10^{14}	-46.972 ± 0.057	-185.17 ± 0.39

Table C.2: Wafer 8 - Fluence ± 10 % - Bias voltage set at 200 V.

Diode	Fluence (1 MeV eq. n cm^{-2})	I_{leak} (µA)	V_{dep} (V)
1	5.0×10^{13}	-11.842 ± 0.022	-42.83 ± 1.80
2	1.0×10^{14}	-21.489 ± 0.031	-79.69 ± 0.54
3	1.0×10^{14}	-22.798 ± 0.033	-85.47 ± 0.76
4	2.0×10^{14}	-36.316 ± 0.046	-141.59 ± 0.54
6	1.0×10^{13}	-5.865 ± 0.016	-20.26 ± 0.15
7	5.0×10^{13}	-12.674 ± 0.023	-44.71 ± 0.44
8	8.4×10^{13}	-18.511 ± 0.029	-59.85 ± 0.41
9	1.8×10^{14}	-33.114 ± 0.043	-114.95 ± 0.58
10	2.0×10^{14}	-34.686 ± 0.045	-126.48 ± 0.35
11	2.7×10^{14}	-51.423 ± 0.061	-183.38 ± 0.33
12	3.0×10^{14}	-47.055 ± 0.057	-134.21 ± 0.43

Table C.3: Wafer 12 - Fluence ± 10 % - Bias voltage set at 200 V.

Diode	Fluence (1 MeV eq. n cm^{-2})	I_{leak} (µA)	V_{dep} (V)
1	3.8×10^{13}	-11.674 ± 0.022	-33.84 ± 0.48
2	8.4×10^{13}	-20.863 ± 0.031	-72.05 ± 0.31
3	8.4×10^{13}	-18.286 ± 0.028	-79.20 ± 0.54
4	1.8×10^{14}	-31.968 ± 0.042	-125.80 ± 0.35
5	1.8×10^{14}	-27.502 ± 0.038	-105.55 ± 0.30
6	8.4×10^{13}	-16.971 ± 0.027	-69.47 ± 0.38
7	1.8×10^{14}	-30.226 ± 0.040	-105.02 ± 0.29
8	2.7×10^{14}	-45.481 ± 0.055	-166.17 ± 0.32
9	4.7×10^{14}	-76.145 ± 0.086	-232.64 ± 0.27
11	1.8×10^{14}	-36.445 ± 0.046	-124.96 ± 0.25
12	2.7×10^{14}	-44.839 ± 0.055	-162.95 ± 0.32

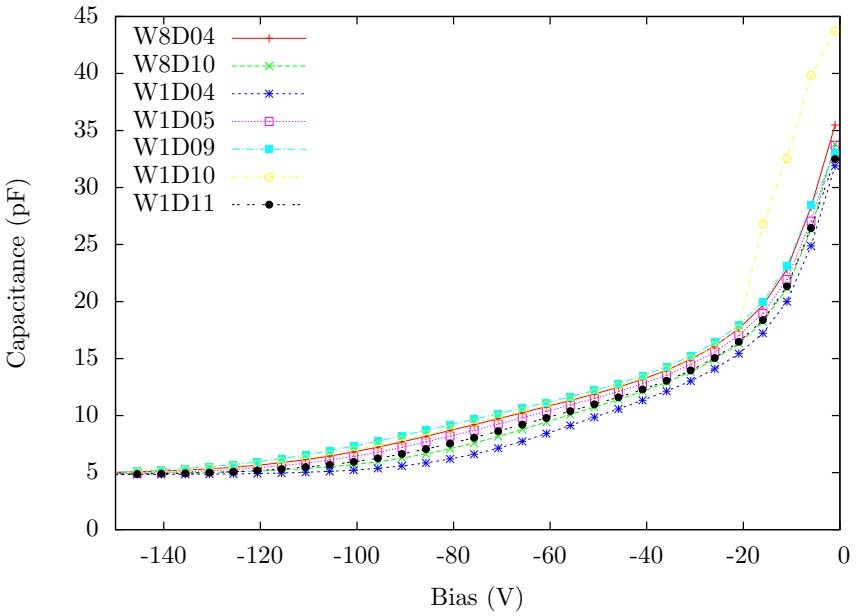

Figure C.1: C-V curves of all the diodes that received a fluence of 2×10^{14} 1 MeV eq. n cm^{-2}. All the measurements are in good agreement. The dispersion is explained by the diode's unique characteristics. In addition, the difference between the target fluence and the actually delivered fluence can varies up to ten percent.

C.2 C-V and I-V Curves

Two summary plots are presented for C-V and I-V measurements. First, the behaviour of devices subjected to a similar fluence is compared in Figure C.1 and Figure C.3. One has to keep in mind that all the diodes are unique and have therefore unique characteristics. Moreover, the fluence is affected by a ten percent relative uncertainty. Second, the effect of the fluence on the device is presented in Figure C.2 and Figure C.4. All the diodes where diced from the same wafer, the figures allow to appreciate the effect of the radiation damage.

The measured capacitance depends on the test signal frequency for irradiated devices. This effect is visible in Figure C.5 and Figure C.6.

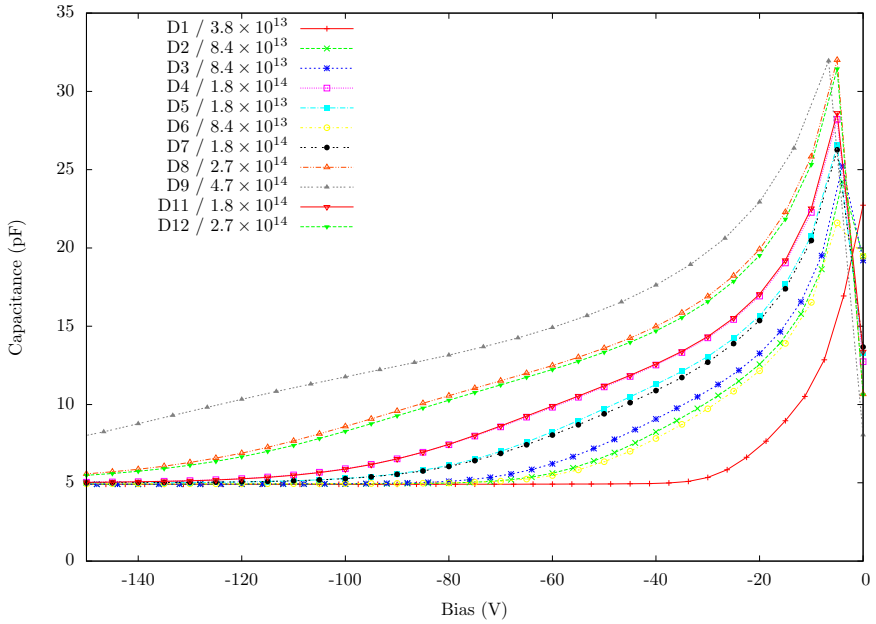

Figure C.2: C-V curves of all the diodes diced from Wafer 12.

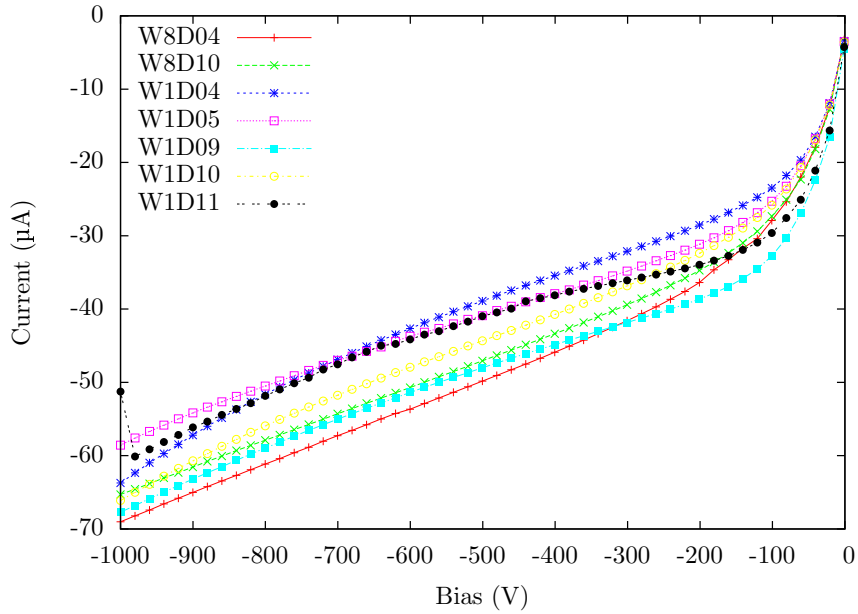

Figure C.3: I-V curves of all the diodes that received a fluence of Fluence 2×10^{14} 1 MeV eq. n cm^{-2}. All the measurements are in relative good agreement. The dispersion is explained by the diode's unique characteristics. In addition, the difference between the target fluence and the actually delivered fluence can varies up to ten percent.

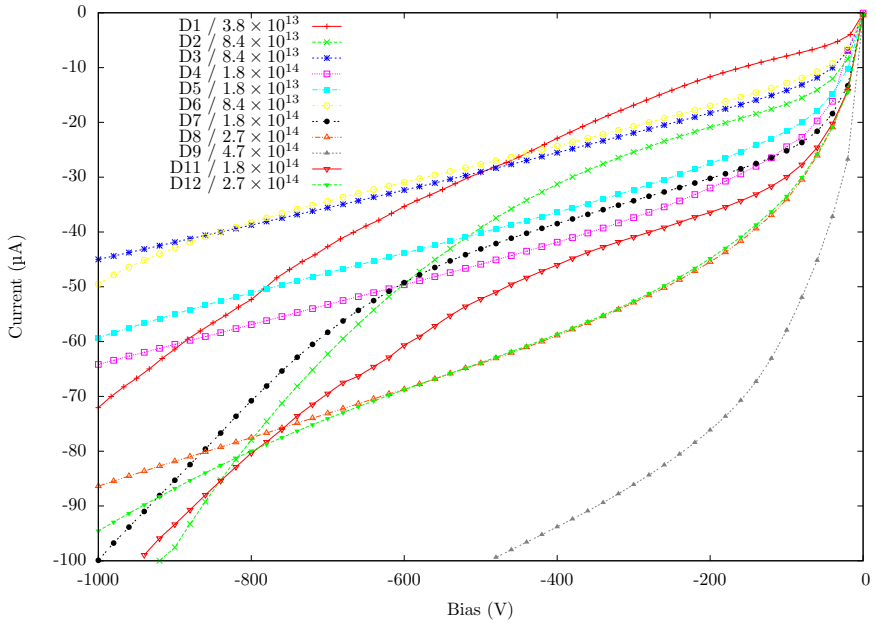

Figure C.4: I-V curves of all the diodes diced from Wafer 12.

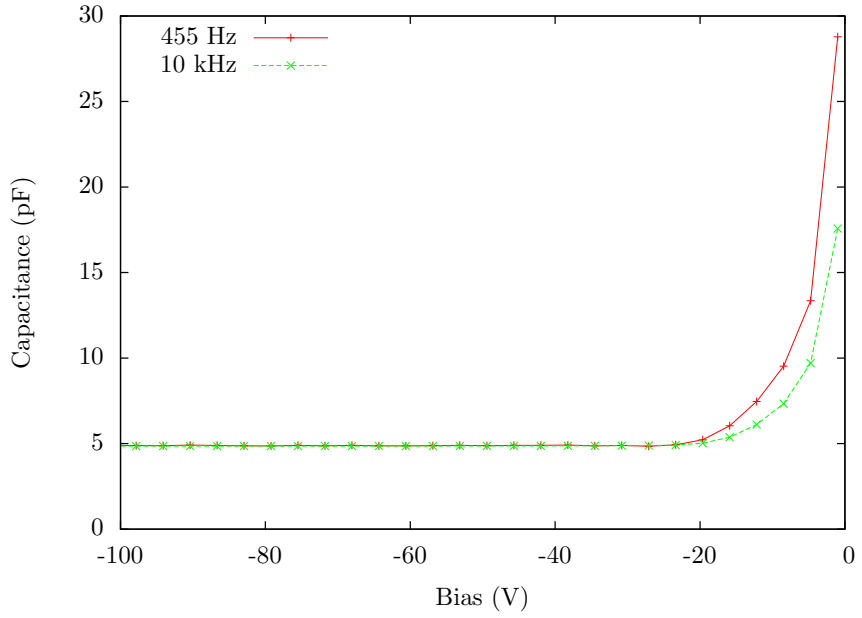

Figure C.5: Measured capacitance frequency dependence for a diode exposed to 1×10^{13} 1 MeV eq. n cm^{-2}.

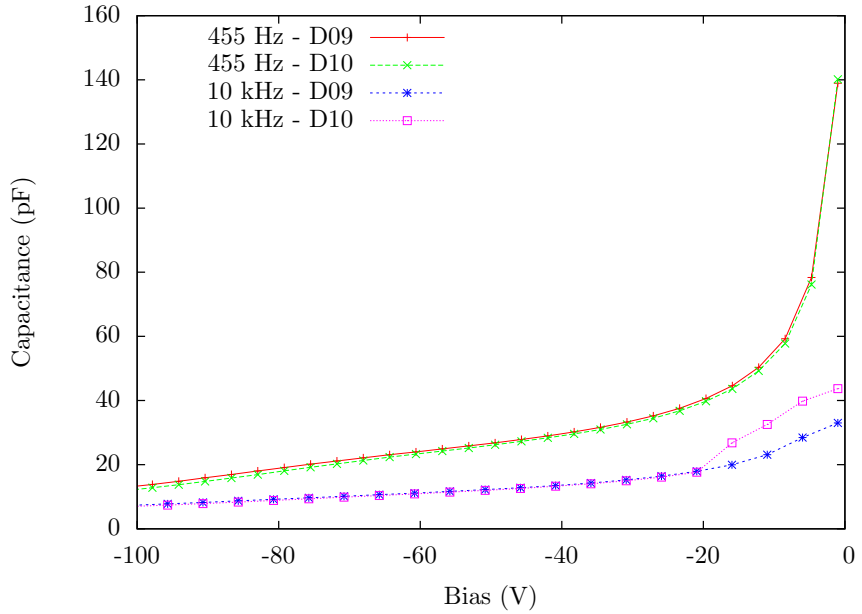

Figure C.6: Measured capacitance frequency dependence for devices exposed to 2×10^{14} 1 MeV eq. n cm^{-2}.

Appendix D

GigaTracker Digitalisation and Reconstruction

This appendix describes the procedure used to reconstruct tracks candidates from the simulated energy depositions in the sensors. First, the digitisation code simulates the readout electronics, it takes the `Geant4` output and transforms it to a format that is comparable to actual detector data format. Second, the reconstruction algorithm builds tracks candidates from triplets of clusters.

When a particle crosses a GigaTracker sensor, the `Geant4` simulation returns a series of energy deposits along the particle path with their position and time information. The energy deposits occurring in a same pixel during a configurable time window are summed, the default integration time is 5 ns. This corresponds to the readout peaking time. Moreover, the positions information are translated to a station and pixel ID. The energy realized in each pixel, E_{dep}, is converted to a charge using the simple formula

$$Q\ (\text{fC}) = q\frac{E_{\text{dep}}}{E_{\text{ion}}} = 1.6 \times 10^{-4}\ (\text{fC}) \times \frac{E_{\text{dep}}\ (\text{MeV}) \times 10^{6}}{3.6\ (\text{eV})}\ ,$$

where q is the elementary charge and E_{ion} is the mean energy necessary to create an electron-hole pair in silicon.

The charge, Q, is then used to compute the hit leading time, T_L, and trailing time, T_T. For that purpose two splines, $S_{\text{T}_1}(Q)$ and $S_{\text{ToT}}(Q)$, see Figure D.1 and D.2, were measured on the GigaTracker demonstrator with a laser setup. The curves are averaged over all the pixels of the prototype. Ideally, we should have a distinct set to curve for each pixel. Both curves are valid for a charge between 0.7 and 18 fC. The current digitisation rejects the hits if $Q < 0.7$ fC and assumes that the time-over-threshold saturates if $Q > 18$ fC, this does not reflect the performance of the final TDCpix.

The pulse leading time, T_1, is defined as

$$T_1 = S_{\text{T1}}(Q) - T_{\text{offset}}\ , \tag{D.1}$$

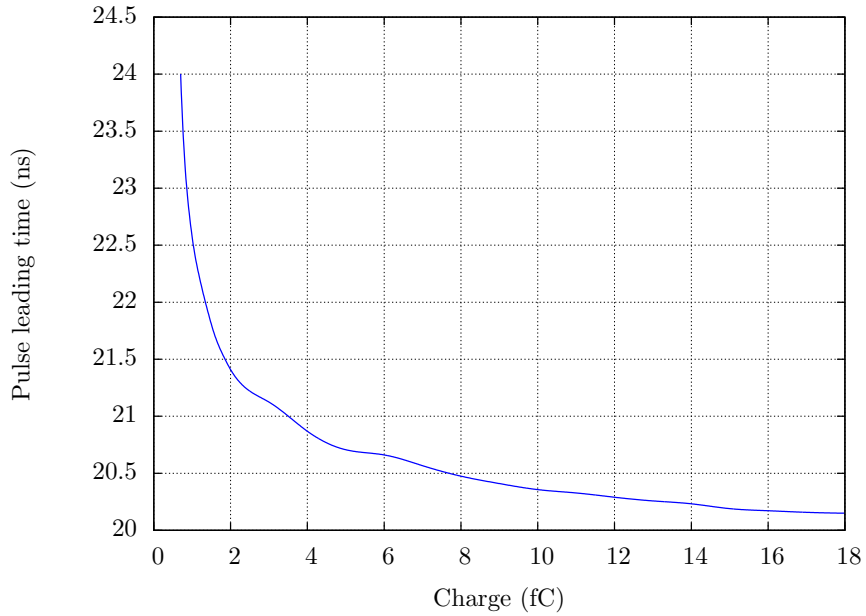

Figure D.1: $S_{\mathrm{T_1}}(Q)$. The curve was extracted from the GigaTracker demonstrator.

where T_{offset} is a configurable pixel time offset, in the current digitisation all the pixels have the same offset, 20.4 ns[1]. The pulse time-over-threshold, T_{ToT}, is

$$T_{\mathrm{ToT}} = S_{\mathrm{ToT}}(Q) \ . \tag{D.2}$$

The hit leading time is then computed as follows:

$$T_{\mathrm{L}} = T_{\mathrm{MC}} + T_1 + \mathcal{N}(0, \sigma_{\mathrm{hit}}) \ , \tag{D.3}$$

where T_{MC} is the time elapsed since the `Geant4` event was created plus the propagation time from the target to the `Geant4` responsibility region, given by the `TURTLE` [119] routine. $\mathcal{N}(0, \sigma_{\mathrm{hit}})$ is a Gaussian smearing applied to simulate the detector time resolution. The default value for σ_{hit} is 200 ps, the upper limit of the expected time resolution. Finally, the trailing time is calculated:

$$T_{\mathrm{T}} = T_{\mathrm{L}} + T_{\mathrm{ToT}}. \tag{D.4}$$

At this stage, the informations are passed to the reconstruction code, this part is common to the MC and real data. To measure the particles momentum, GigaTracker measures the displacement induced by a pair of opposite field identical magnets. The initial particle angle of incidence is preserved in very

[1]This number was extracted from the laser tests performed on the GigaTracker demonstrator.

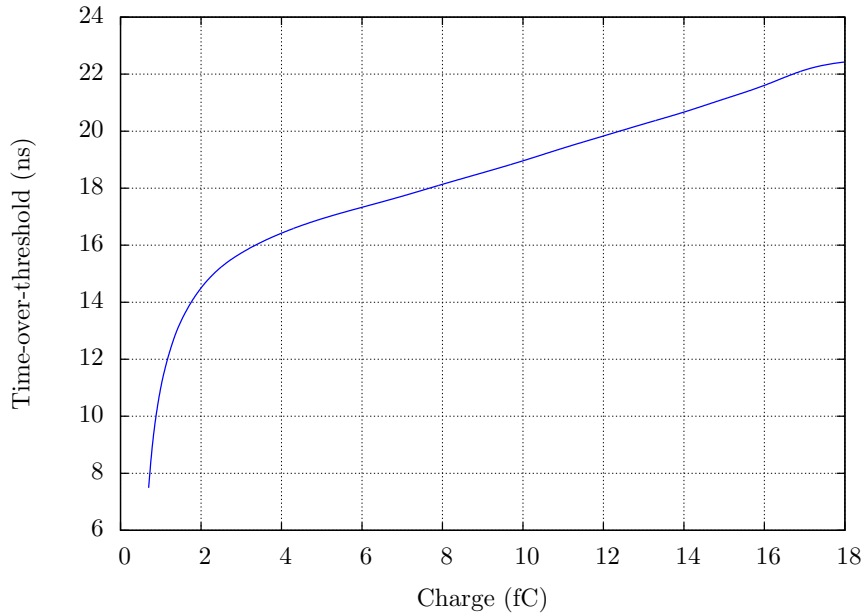

Figure D.2: $S_{\mathrm{ToT}}(Q)$. The curve was extracted from the GigaTracker demonstrator.

good approximation by the pair. A second pair brings back the beam in the original axis. See the Section 3.1.1 for a description of the detector layout.

Knowing this, one can write a system of linear equations describing the propagation of the particles in the detector: For the X axis

$$\begin{aligned} x_2 &= x_1 + d_{12}\frac{p_x}{p_z} \ , \\ x_3 &= x_1 + d_{13}\frac{p_x}{p_z} + \frac{\beta_{\mathrm{trim}}}{p} \ , \end{aligned} \tag{D.5}$$

and for the Y axis

$$\begin{aligned} y_2 &= y_1 + d_{12}\frac{p_y}{p_z} - \frac{\alpha_{\mathrm{bend}}}{p} \ , \\ y_3 &= y_1 + d_{13}\frac{p_y}{p_z} \ . \end{aligned} \tag{D.6}$$

where $\alpha_{\mathrm{bend}} = M_{\mathrm{bend}} \cdot d_{\mathrm{bend}} \cdot c$ and $\beta_{\mathrm{trim}} = M_{\mathrm{trim}} \cdot d_{\mathrm{trim}} \cdot c$. The clusters position is denoted (x_i, y_i) where $i = 1, 2, 3$ indicates the station. The parameters used for the kinematic reconstruction are listed in Table D.1. Knowing the cluster position and the magnets system parameters, we can compute the track 3-momentum (p_x, p_y and p_z) of the incoming particle using the relation D.5 and D.6. The 4-momentum of the track is then computed assuming that the track is a kaon

$$\mathbf{P}_{\mathrm{track}} = \begin{pmatrix} p_x \\ p_y \\ p_z \\ \sqrt{(p^2c^4 + m_k c^2)} \end{pmatrix} \ .$$

Parameter	Symbol	Value	Unit
GTK2 Y offset	Δy	0.06	m
Distance between GTK1 and GTK2	d_{12}	13.2	m
Distance between GTK1 and GTK3	d_{13}	22.8	m
Integrated *BEND* magnetic field	M_{bend}	4.1695	T m
Integrated *TRIM* magnetic field	M_{trim}	-0.3002	T m
Distance between the bending magnets doublets	d_{bend}	3.6	m
Distance between the trim magnet and GTK3	d_{trim}	0.625	m

Table D.1: Parameters used for the kinematic reconstruction. We always work in the NA62 coordinate system. See the Figure 3.1 for the exact configuration and placement of the magnets.

At this point we have a collection of track candidates, a discriminating variable capable of rejecting the tracks made with wrong combination of cluster triplets (*fake* tracks) needs to be constructed. For that purpose, three constraints are used, first, on the horizontal plane, the χ^2_X of the fit of a straight line to the x_i positions. A -0.750 mm offset is added to x_3 to account the TRIM5 magnet effect. The following uncertainties are passed to the linear least square method

$$\begin{aligned} \sigma_x &= \tfrac{0.3 \text{ mm}}{\sqrt{12}} = 0.0866 \text{ mm} , \\ \sigma_y &= \tfrac{0.3 \text{ mm}}{\sqrt{12}} = 0.0866 \text{ mm} , \\ \sigma_t &= 220 \text{ ps} . \end{aligned} \tag{D.7}$$

Second, on the vertical plane

$$\chi^2_Y = \left(\frac{y_2 - y_1}{\sigma_{12}} \right)^2 + \left(\frac{y_3 - y_2}{\sigma_{23}} \right)^2 , \tag{D.8}$$

where

$$\sigma_{12} = 1.42 \text{ mm} , \sigma_{23} = 1.20 \text{ mm} . \tag{D.9}$$

And, finally, the time of flight of the particle

$$\chi^2_T = \left(\frac{t_2 - t_1 - T_{12}}{\sigma_T} \right)^2 + \left(\frac{t_3 - t_2 - T_{23}}{\sigma_T} \right)^2 \tag{D.10}$$

where the t_i are the cluster timestamps,

$$\begin{aligned} T_{12} &= \beta \cdot c \cdot d_{12} , \\ T_{23} &= \beta \cdot c \cdot d_{23} , \end{aligned} \tag{D.11}$$

are the expected time of flight and

$$\sigma_T = 200 \text{ ps } \times \sqrt{2} , \tag{D.12}$$

the time resolution. For each track candidate, a global χ^2 is calculated

$$\chi^2 = \chi^2_X + \chi^2_Y + \chi^2_T . \tag{D.13}$$

Appendix E

GigaTracker Data Format and Unpacking

E.1 Demonstrator

To get the hit arrival time the fine time must be combined with the appropriate coarse counter. Let's call the fine counter F, the coarse counter updated on the clock leading edge C_L and the coarse counter updated on he clock trailing edge C_T. Looking at the Figure E.1, one see that if a hit arrives close to leading edge of the clock signal one need to use C_T. In the same way, if the signal is close to the trailing edge of the clock, one want to use $C_T - 1$. Finally, for the other cases one can safely use C_L. To summarise, there are three cases, depending on the value of the fine counter F:

1. If $1 < F < 30$, then the hit arrival time is given by $T = P_C \cdot C_L + P_F \cdot F$,
2. If $F < 2$, then we must use the coarse counter counting the trailing edges $T = P_C \cdot C_T + P_F \cdot F$,
3. Finally, if $F > 29$, then $T = P_C \cdot (C_T - 1) + P_F \cdot F$,

where P_C and P_F are the the bin size, respectively, of the coarse counters (3125 ps) and the fine counter ($\approx$ 97.7 ps). The coarse counters are reset before each spill.

E.2 Full Scale Detector

The TDCpix chip outputs a stream of binary packets that are collected by the off detector readout boards. In 2014, the boards were controlled by an off-the-shelf PC that wrote the packets on disk as stream of 32-bit words. A packet is composed of a 160 bits *header* followed by a *payload* consisting of two 48-bit

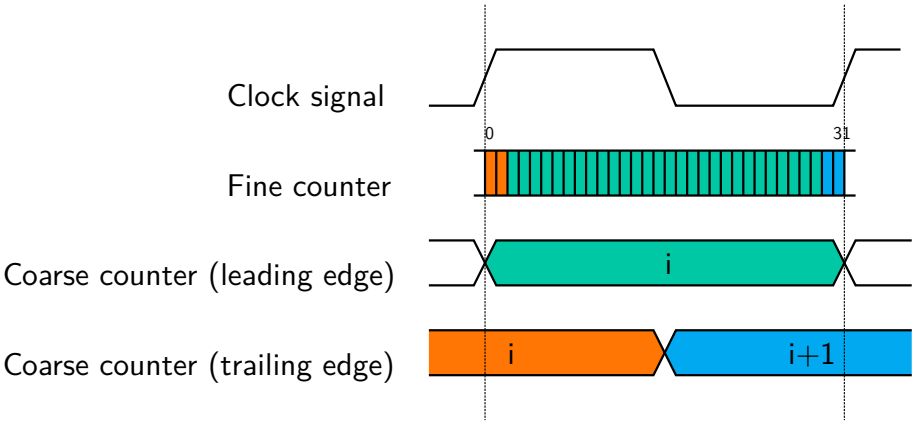

Figure E.1: The hit arrival time is given by the combination of the fine and the coarse counters. The two coarse counters allow to lift the ambiguity when a hit occurs close to the rising edge of the clock. They are incremented, respectively, on the leading and on the trailing edge transition of the clock.

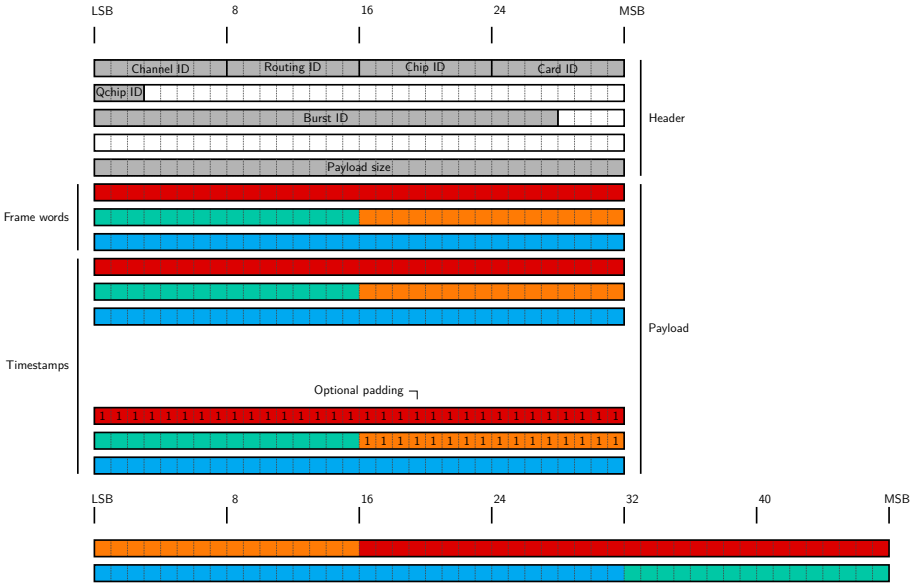

Figure E.2: GigaTracker *packet* 2014 format. The frame and timestamps words have to be unpacked before decoding, the color code indicates how to build the 48-bit words from the 32-bit words.

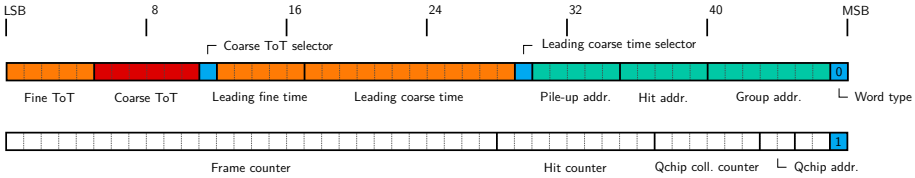

Figure E.3: *timestamp-* (top) and *frame-* (bottom) type 48-bit data word. The orange and red bit fields contain information about the timing while the green fields allow to reconstruct the osition of the hit. The orange fields are encoded in Gray, all the other are encoded in binary.

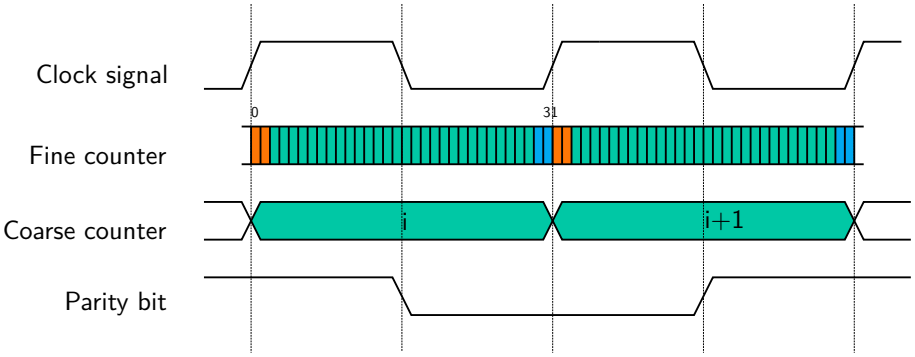

Figure E.4: If we set aside the frame counter, the hit arrival time is given by the combination of the fine and the coarse counter. Since the coarse counter is incremented on the leading edge of clock, there is an ambiguity on its value when a hit occurs very close to this edge. To choose the correct value, i or $i+1$, we have to check the value of the parity bit that is toggled on the trailing edge of the clock.

frame words and a variable number of 48-bit *timestamp words*. The packet data format is detailed in Figure E.2 and Figure E.3.

The last 32 bits of the header encodes the payload size in multiple of 32-bit words. To ensure that the payload always contains an even number of words padding can be present. The 32-bit words are written in little-endian format. Two disambiguation mechanisms allow to avoid race conditions when a hit arrives close to the clock rising edge.

Binary encodings of numbers are not unique, the TDCpix chip uses *Gray code* (also known as *reflected binary code*) and *natural binary code*. In the following, binary is used as a short for natural binary code. Before explaining the decoding procedure let's define `bin()` and `gray()` as the functions which transforms Gray encoded value to "natural" encoded value and vice versa.

The **hit leading time** is reconstructed from three counters, the `leading fine time`, encoded in Gray on 5 bits; the `leading coarse time`, encoded in Gray on 12 bits and the `frame counter`, encoded in binary on 28 bits.

It is convenient to define an intermediate variable, `leading coarse time binary`, which is equal to `bin(leading coarse time)`. If the value of `leading fine time` counter is greater than 20, i.e. close to the leading edge of the clock, a disambiguation mechanism has to be applied; The cutoff value was determined experimentally. The idea is illustrated in Figure E.4. Since the coarse counter is encoded in Gray the binary representations of i and $i+1$ are guaranteed to differ by only one bit. Therefore, the counter changes its parity with each count. If the `leading coarse time selector` differs from the parity of the `leading coarse time`, one needs to decrement the `leading coarse time binary` by one unit; if the `leading coarse time binary` is equal to 0, its value must be updated to 4095 (rollover).

Because of the queuing mechanism implemented in the TDCpix, hits belonging of the previous frame can be embedded in the frame. A second disambiguation system allows to correct for this. If the LSB of frame counter is not equal to the MSB of coarse counter, one needs to decrement by one unit the frame counter. Finally, the hit leading time is computed as follow

$$\begin{aligned} \texttt{leading time} = & \\ & \texttt{leading coarse time binary} \times 32 \\ & + \texttt{bin(leading fine time)} \\ & + \texttt{frame counter} \times 2048 \times 32 \ . \end{aligned} \tag{E.1}$$

where only the 11 LSB of the `leading coarse time binary` must be used.

The **time-over-threshold** is reconstructed in a similar way. Again three counters are needed, the `fine ToT`, encoded in Gray on 5 bits; the `coarse ToT`, encoding in binary on 6 bits and `leading coarse time`, encoded in Gray on 12 bits. Let's define two intermediate variables

$$\begin{aligned} \texttt{trailing coarse time binary} = & \\ & \texttt{coarse ToT} \\ & + \texttt{bin(leading coarse time)} \ , \\ \texttt{trailing coarse time} = & \\ & \texttt{gray(trailing coarse time binary)} \ . \end{aligned}$$

If the value of `coarse ToT` is equal to 63, the time-over-threshold dynamic range was exceeded and we need to raise a flag. Else, if the value of `bin(fine ToT)` is greater than 20 one have to rely on the disambiguation mechanism. The cutoff value was determined experimentally. Using the same ideas as above, if the `coarse ToT selector` differs from the parity of the `trailing coarse time`, one needs to decrement the `coarse ToT` by one unit; if the `coarse ToT` is equal to 0, its value is left as it is. Finally, the time-over-threshold is given by

$$\begin{aligned} \texttt{time over threshold} = & \\ & \texttt{coarse ToT binary} \times 32 + \texttt{bin(fine ToT)} \ . \end{aligned} \tag{E.2}$$

To conclude, the **pixel coordinates** are reconstructed from the `Qchip ID`, the `group address` and the `hit address`. The `Qchip ID` is extracted from the packet header, before computing the coordinates, its the value has to be mapped according to the following rules $0 \rightarrow 2$, $1 \rightarrow 0$, $2 \rightarrow 1$ and $3 \rightarrow 3$. The `hit address` is one-hot encoded on 5 bits, therefore, we have to apply the following rules $1 \rightarrow 0$, $2 \rightarrow 1$, $4 \rightarrow 2$, $8 \rightarrow 3$ and $16 \rightarrow 4$. A small fraction of hit address contains more than one "1" and are therefore illegal. This situation occurs when two pixel belonging to the same hit arbiter are hit very close in time. The hit arbiter didn't have the time to mask four other pixels after the first hit. After the two mapping, the column ID is given by

$$\texttt{column ID} = \texttt{Qchip ID} \times 10 + (9 - \texttt{group address}/9) \ , \tag{E.3}$$

and the row ID is computed as follow

$$\texttt{row ID} = (\texttt{group address} \mod 9) + \texttt{hit address} \times 9 \ . \tag{E.4}$$

Appendix F

Monte Carlo Production

An automated tool to produce Monte Carlo samples was developed. The user specifies the number of events and the desired decay channels, the program then splits the requested production in reasonably sized jobs and takes care of adjusting all the parameters. The tool relies on Apache `CouchDB`™ database to store the run card associated to each job. It turned out to be very useful to be able to find the exact parameters used to generate a particular `ROOT` file as it allows to diagnose problems related to a particular combination of parameters.

This tool was used to generate samples of the six main decay modes and of the beam component, the datasets are summarized in Table F.1. As the NA62 software framework was evolving quickly, a new production was initiated after every major upgrade.

Table F.1: Monte Carlo productions used for the early data-Monte Carlo comparisons. The number of events is related to the corresponding branching ratios. The beam components are normalized to the nominal kaon flux. Because of file corruptions, the generated samples of $K^+ \to \mu^+\nu_\mu$, $K^+ \to \pi^+\pi^0$ and $K^+ \to \pi^+\pi^+\pi^-$ are, respectively, 0.1 %, 0.5 % and 1.6 % too small.

Mode	$\mathcal{B}$ (%)	Events
$K^+ \to \mu^+\nu_\mu$	63.55	634500
$K^+ \to \pi^+\pi^0$	20.66	205600
$K^+ \to \pi^+\pi^+\pi^-$	5.59	56000
$K^+ \to \pi^0 e^+\nu_e$	5.07	50700
$K^+ \to \pi^0\mu^+\nu_\mu$	3.35	33530
$K^+ \to \pi^+\pi^0\pi^0$	1.76	17610
Beam	R	Events
Pion	532/53	10036130
Proton	171/53	3225899
Positron	0.151/53	2852

Appendix G

Kalman Filtering

This appendix details the Kalman filtering procedure we implemented to align the GigaTracker in space. A Kalman filter is clearly not needed for such a simple task, the model was developed while the author was studying the reconstruction algorithms for the GigaTracker. The code was trivially repurposed for the tracker spatial alignment, despite its apparent complexity the algorithm can be implemented very efficiently using standard linear algebra packages.

The filtering is done in two steps, an internal *state vector*

$$\mathbf{x} = \begin{pmatrix} x_2^{\text{off}} \\ y_2^{\text{off}} \\ x_3^{\text{off}} \\ y_3^{\text{off}} \\ x_{\text{ref}} \\ y_{\text{ref}} \\ \alpha/p_z \\ \beta/p_z \end{pmatrix} , \tag{G.1}$$

is updated at each step. The transitions dynamics are encoded in the *state transition matrix*

$$\Phi = \text{diag}\,(1,1,1,1,1,1,1,1) \ , \tag{G.2}$$

in this very simple model there is no dynamics, we included the magnetic fields in the track model. The initial *state vector covariance*

$$P_0 = \text{diag}\,(1,1,1,1,0,0,0,0) \tag{G.3}$$

encodes the fact that only x^{off} and y^{off} should be updated. The state vector is mapped into measurement predictions by the *measurement matrix*

$$M_1 = \begin{pmatrix} 1 & 0 & 0 & 0 & 1 & 0 & 0 & 0 \\ 0 & 0 & 1 & 0 & 1 & 0 & 1 & 0 \end{pmatrix} , \tag{G.4}$$

for the first step and

$$M_2 = \begin{pmatrix} 0 & 0 & 1 & 0 & 1 & 0 & 1 & 0 \\ 0 & 0 & 1 & 1 & 0 & 1 & 0 & 0 \end{pmatrix} , \tag{G.5}$$

for the second step. The error on the positions is introduced via the *measurement noise matrix*

$$V = \mathrm{diag}\left(\sigma_x^2, \sigma_y^2\right) \ . \tag{G.6}$$

We consider that there is no system noise in the model so the *system noise vector* $\mathbf{w}$ and the *system noise matrix* Γ are null. That is, we make the hypothesis that our model is perfect which is a significant simplification.

Starting from the matrix ϕ, the state vector $\mathbf{x}$ and the state vector covariance P, we compute two projected states:

$$\mathbf{x_p} = \phi_k \mathbf{x_k} + \underbrace{\Gamma_k w_k}_{0} \ , \tag{G.7}$$

$$P_p = \phi_k P_k \phi_k' + \underbrace{\Gamma_k}_{0} \ . \tag{G.8}$$

The index k indicates the step. The equation

$$\mathbf{y} = \mathbf{m_{k+1}} - M_{k+1}\mathbf{x_p} \ , \tag{G.9}$$

is used to calculate the vector $\mathbf{y}$ from the projected state vector and from the measurement vector $\mathbf{m}$ at the step $k+1$. It encodes the distance between the prediction and the observation. Two intermediate matrices are then computed, the estimated covariance matrix S and the *Kalman gain* K:

$$S = M_{k+1} P_p M_{k+1}' + V_{k+1} \ , \tag{G.10}$$

$$K = P_p M_{k+1}' S^{-1} \ . \tag{G.11}$$

The matrix K weighs the impact of the observation on the prediction. Finally, the updated state vector and state covariance matrix are given by

$$\mathbf{x_{k+1}} = \mathbf{x_p} + K\mathbf{y} \ , \tag{G.12}$$

and

$$P_{k+1} = \left(\mathcal{I} - K M_{k+1}\right) P_p \ . \tag{G.13}$$

Details can be found for instance in ref. [135] (p. 269 and following).

For our application, the procedure is repeated two times as we have only three steps. The offsets are extracted from the state vector after the last step.

Appendix H

Flip Chip Characterisation

The flip chip technique is extensively used in the semiconductor industry since the 1960s, however the thickness of the chip involved in the GigaTracker application is unusual. Moreover, ten chips have to be bonded to a single sensor. These two facts complicate the procedure since mechanical integrity and the planarity of the component must be guaranteed during the bonding process.

The assembly of the ten TDCpix chips and the sensor is realized by Fraunhofer IZM [136]. The main steps of the process are presented in Figure H.1. Without going into the details, the process takes place as follows: the module fabrication starts with the raw readout chip wafer and the sensor wafer (a). First, the chip wafer is thinned by mechanical grinding and mechanically and chemically polished (b). Second, a layer of UV light sensitive polyamide glue is deposited on the backside of the chip wafer and a glass carrier is attached (c). Third, under bump metallisation are applied on the sensor and chip wafers, in addition, solder bumps are deposited on the chip side (d). Forth, the chip and sensor wafer are diced with a diamond saw (e). Fifth the sensor and the chips are aligned (f). Sixth, the solder bumps are reflowed at 250 °C, completing the connection (g). Finally, the glass carrier is removed using an UV light laser. A thin layer of glue remains on the chips backside.

H.1 Test Campaign

To assess the yield of the process for 100 µm thick chips, Fraunhofer IZM bump-bonded a series of mock-up assemblies. Instead of real chip and sensor, two pieces of silicon with the same dimensions as the real chip and sensor were assembled, the true bump-bonding pads geometry was reproduced as well. When bounded, the two pieces form conductive daisy chain. A sketch of the device is shown in Figure H.2. The equivalent circuit is displayed in Figure H.3.

Both single assemblies (a dummy chip bonded to a small dummy sensor) and

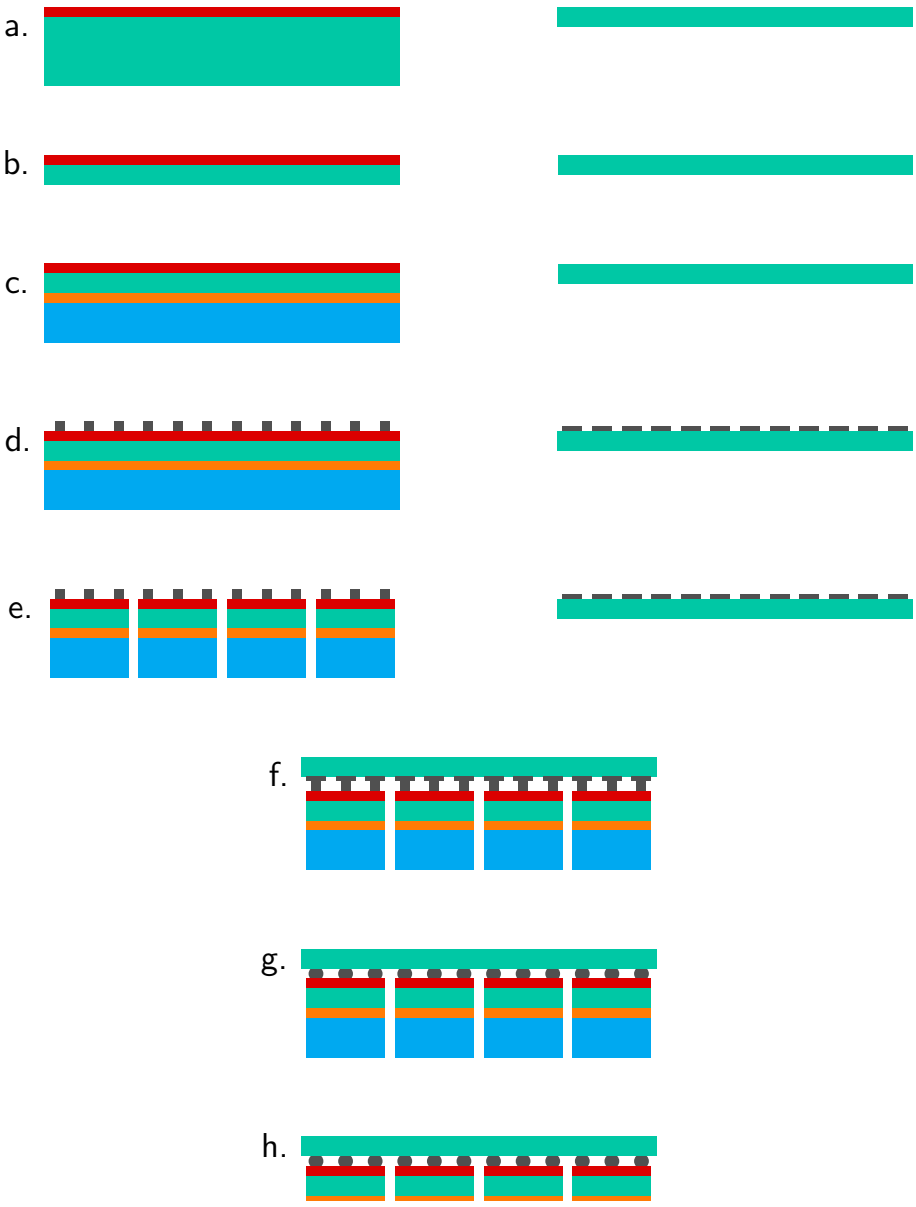

Figure H.1: Simplified sketch of the flip chip process. See the text for details.

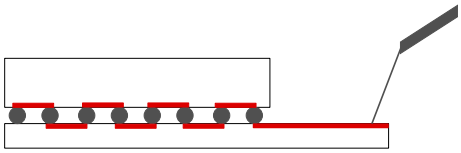

Figure H.2: Cartoon of the daisy chain, side view. One needle is depicted on the right.

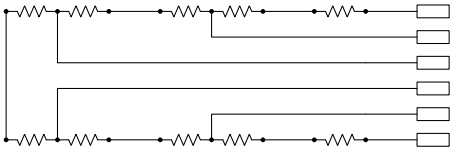

Figure H.3: Simplified electric scheme of the daisy chains. The rectangles represents the dummy chip pads.

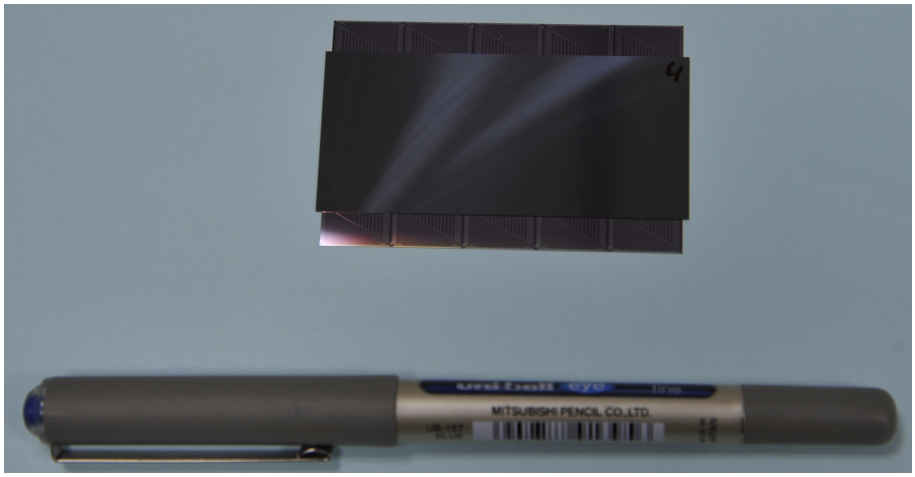

Figure H.4: Full assembly viewed from the top, the sensor covers most of the surface of the chips. The photograph gives an idea of the size of the GigaTracker sensor.

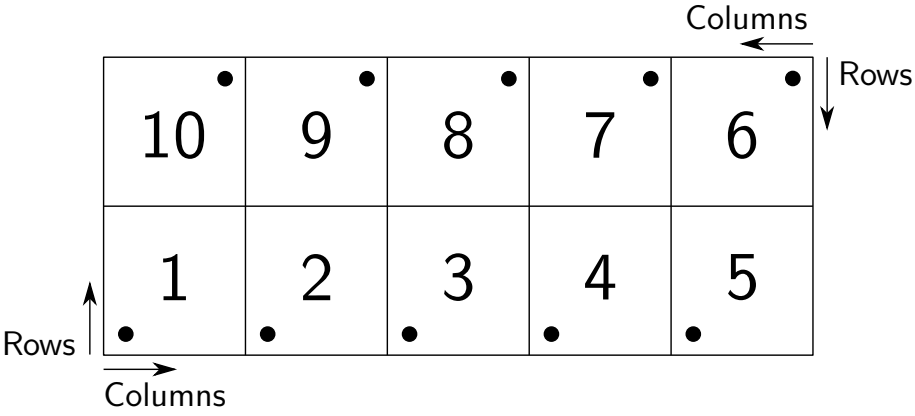

Figure H.5: Chip numbering scheme used for the dummy assemblies. The sensor side is pointing upwards.

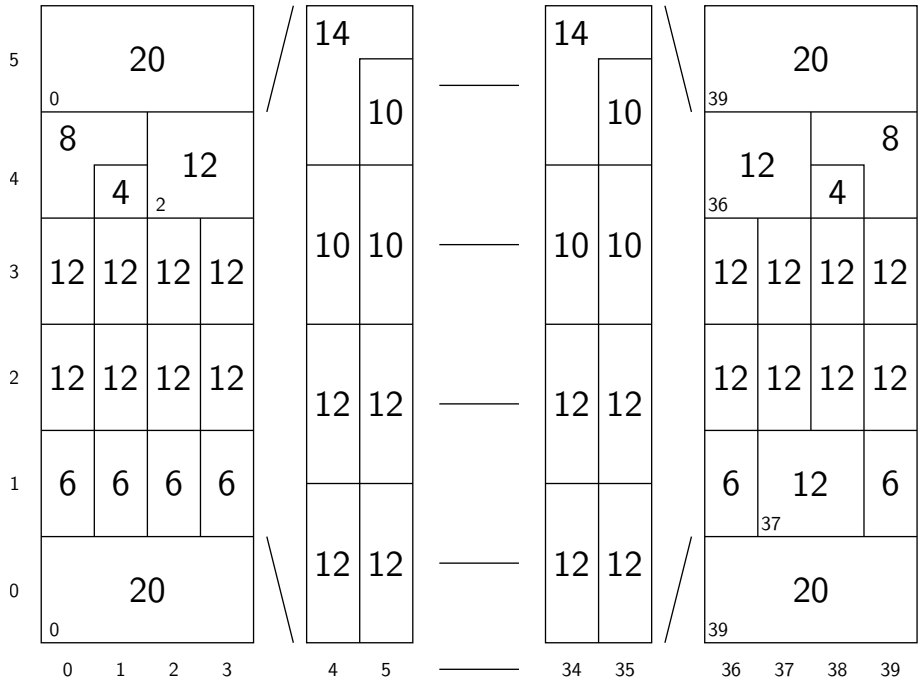

Figure H.6: The dummy assembly test chains are indexed by row and column number. Each box corresponds to a test chain, the number in the centre of the box indicates how many bump-bonds are connected to that chain. If the column in which the box belongs is ambiguous, it is indicated in the bottom left corner.

full assemblies (ten dummy chips bonded to a full scale dummy sensor) were fabricated, a photograph of a full module is presented in Figure H.4. Even on the full assemblies each chip was tested individually, so, unless explicitly stated otherwise, in the following sections we will always refer to single chips. A mapping between the chip IDs and their position on the sensor is presented in Figure H.5.

A total of 162 daisy chains were accessible through pads at the bottom of each chip: four were dedicated to the chip corners and 156 gave access to groups of six to twelve bump-bonds. The chains were indexed by row and column number, the mapping between the chip top surface (facing the sensor) and the row and the column is shown in Figure H.6. To assess the quality of the flip chip process we measured the resistance of each network individually using four points sensing. It was not possible to check each bump-bond individually.

All the measurements were performed with a standard wafer prober (Figure H.7) in the clean room of Fraunhofer IZM (SIIT) in Berlin. Two dummy assemblies (labelled 1 and 5) and three dummy single chips were tested. An overview of the measurements made on the chips of the assembly 5 is presented in Figure H.8, the black boxes indicates the broken chains. A zoom on two

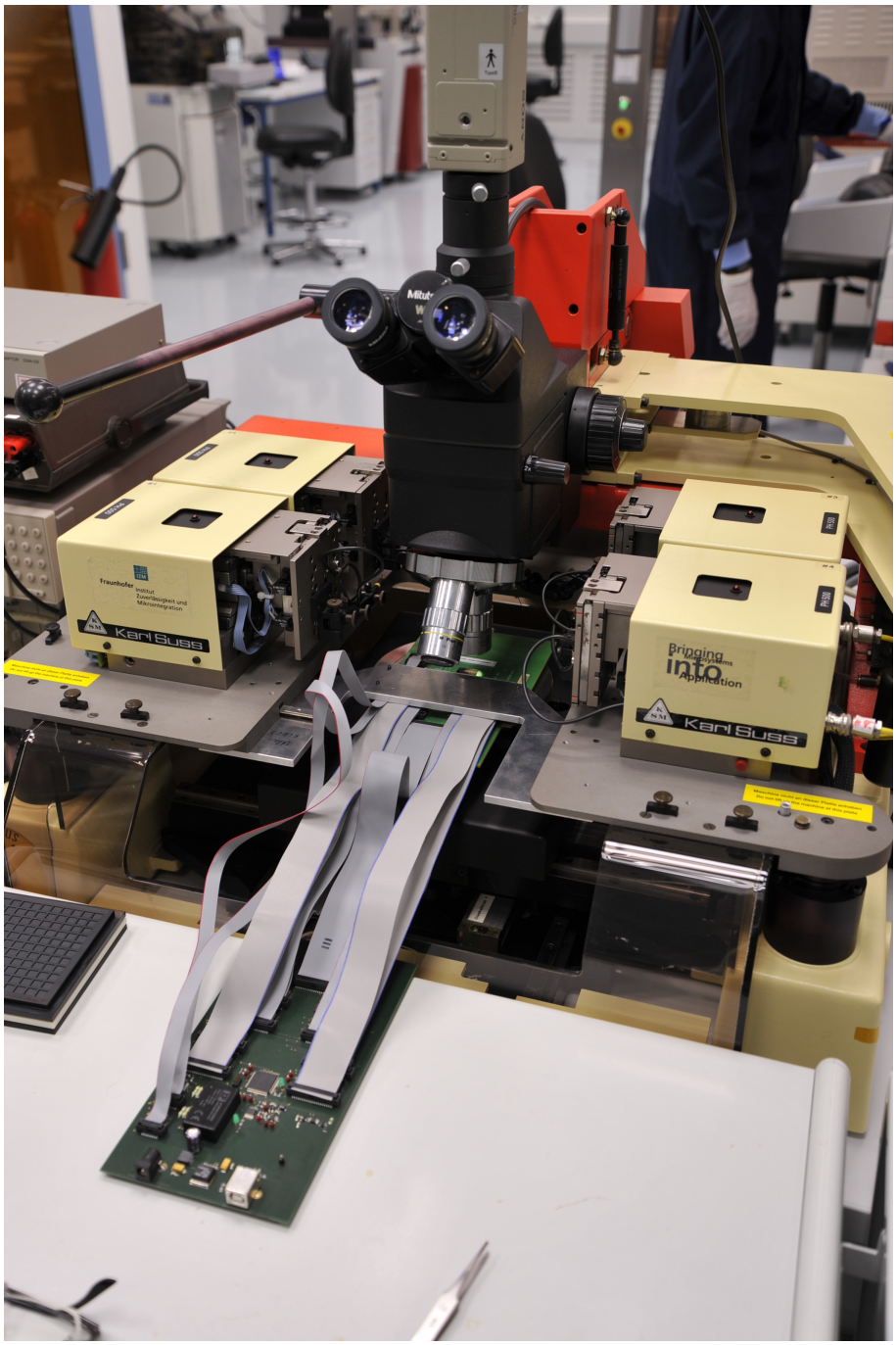

Figure H.7: Setup we used to measure the daisy chains resistance, the readout card is visible in the foreground.

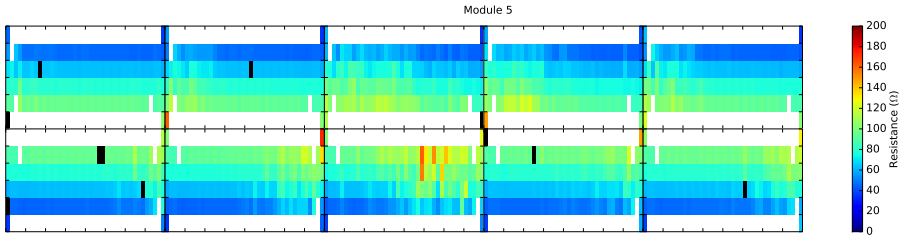

Figure H.8: Daisy chain resistance measurements on assembly 5. The black boxes corresponds to broken chains.

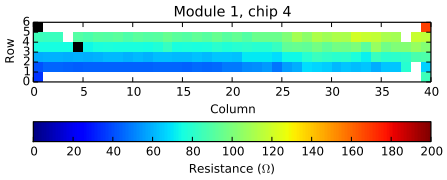

Figure H.9: Daisy chain resistance measurements on chip 4 of assembly 1.

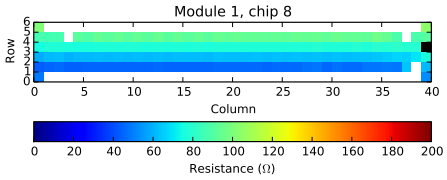

Figure H.10: Daisy chain resistance measurement on chip 8 of assembly 1.

of the ten chips of the assembly 1 is displayed in Figure H.9 and Figure H.10. The results obtained with the other eight chips are similar, a full view of the assembly 1 is shown in Figure H.11. At this stage, we can already conclude that the bump-bonding yield is 98.9 % for the assembly 1 and 99.3 % for the assembly 5.

H.2 Data Analysis

A top-bottom pattern is clearly visible in Figure H.9 and Figure H.10. The effect is simply understood if we remember that we measure the resistance of the whole chain, that is, of the bump-bonds, the connections and the traces. To confirm this, we looked at the typical resistance of the rows as a function of

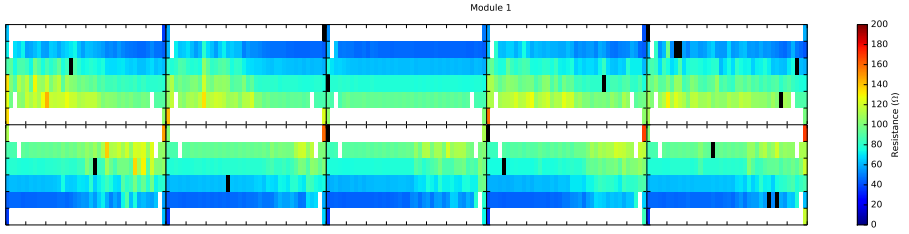

Figure H.11: Daisy chain resistance measurements for assembly 1. The black boxes corresponds to broken chains.

Table H.1: Average trace length, extracted from the circuit layout.

Row	Length (cm)
1	2.08 – 2.21
2	2.83 – 3.02
3	4.03 – 4.29
4	4.60 – 4.80

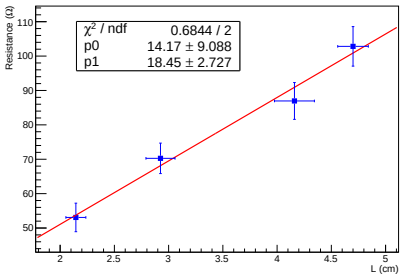

Figure H.12: Module 1.

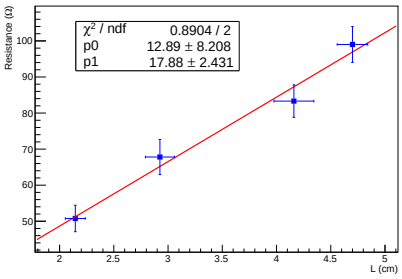

Figure H.13: Module 5.

the average trace length, tabulated in Table H.1. The resistance measurements of a whole column were averaged to obtain one figure per row. The results are plotted in Figure H.12 and Figure H.13, a linear trend is clearly visible.

Correcting for trace length and for the variation of the number of bump-bonds per chain, the top-bottom trend disappears but a left-right pattern appears (see Figure H.14 and Figure H.15). This feature was most likely caused by the non-planarity of the probe card needles with respect to the chips. Indeed, during the measurements we noticed that the probe station chuck and the tip of needles were not perfectly parallel. Systematically the needle prints were evident on the left part of chip while the no marks were visible on the right side. Unfortunately, this setting was not easily adjustable on the probe station thus we were forced to add mechanical spacers to correct as much as possible the planarity. Because of this, the needle contact pressures were not uniform, which lead to a variation of the contact resistance.

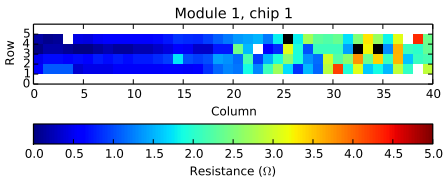

Figure H.14: Daisy chain resistance measurements on chip 1 of assembly 1.

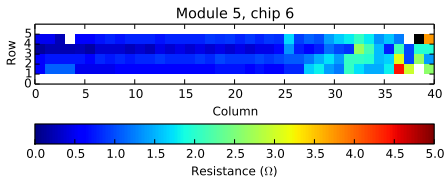

Figure H.15: Daisy chain resistance measurement on chip 6 of assembly 5.

H.3 Summary and Discussion

The test campaign demonstrated that IZM had envisaged an procedure precise enough to reliably bond ten individual 100 µm thick chips to a 200 µm thick sensor.

The bump-bonding yield of the two modules we characterized is 98.9% and 99.3% respectively. This is within the specifications.

Appendix I

TDCpix Characterisation

Ideally, each TDCpix chip should be tested before being bump-bonded to the sensor. Indeed, it is close to impossible to replace a defective readout chip once it is bump-bonded to the sensor.

The standard practice is to test the chips directly on the wafer, before dicing them. The test procedure should be automated in a large extant and run in an clean environment. The construction of an automated test bench started at CERN during the summer of 2014, unfortunately several issues delayed the program and we were not able to contribute to the tests themselves. The useful contributions to the setup are documented in this short section.

I.1 Preliminary Tests

Four high-speed current-mode logic (CML) buffers were not properly connected (see Figure I.1) in the first probe card batch. In addition, the existing standard mechanical support of the probe card was no providing enough mechanical clearance for some connectors, we had to design a new one. Despite this, we were able to test part of the setup and to power up two diced TDCpix chips.

Table I.1: First power-up of a TDCpix with the probe card. The supply voltage was set to 1.3 V.

Channel	Current draw (A)
Analog	0.178
PLL	0.144
SLVS	0.010
TDC	0.108
Temp	0
Digital	0.190

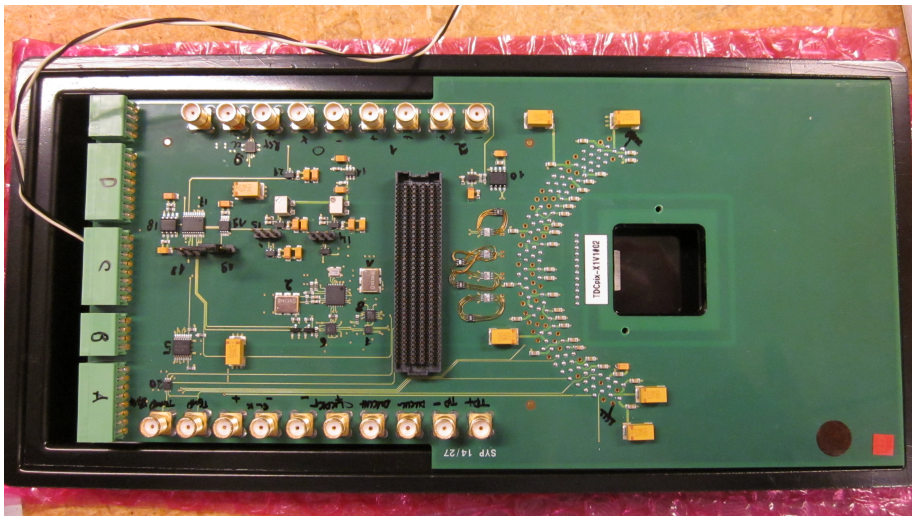

Figure I.1: Photograph of the TDCpix probe card. The four problematic high-speed CML buffers are situated in the middle of the picture, just right of the large black connector. To fix the PCB layout error the buffers were glued next to the corresponding prints on the PCB and manually connected with thin wires. This kind of arrangement is incompatible with high-speed signals therefore a revised version of the probe card had to be ordered.

After a significant learning period with the wafer prober, we were confident enough to make an attempt on a TDCpix chip. We were able to power up the chip and measure the current draws using the control program we wrote for the power supplies. However, it was impossible to configure the chip with the first probe card, therefore, the results does not bring much information. They are tabulated in Table I.1.

Aligning the probe card needles with the chip pads is an extremely tedious work. It was mostly done by eye with the help of a microscope. When the alignment is good, the chuck supporting the chip is raised towards the needles. The operator has to be very careful to not crunch the device under test while providing enough pressure to ensure a good ohmic contact.

The wafer prober can be equipped with an *edge sensor* that automatically stops the motors when the probe needles are in contact with the device under test. The original system was a simple mechanical contact embedded in the probe card and plugged in the prober. When the needles were too close of the device under test, the contact opened. Unfortunately, our probe card was not equipped with such a thing. Following an idea of the CERN ESE group [137], a small device that detects the contact of the probe needles with the chip was built and successfully tested. The electric scheme is presented in Figure I.2. Two needles of the probe card were re-purposed, one on the left side and one on the right side, they are symbolized by the switches *E1* and *E2*. Two MOSFETs simulate the mechanical switches expected by the wafer prober. The circuits

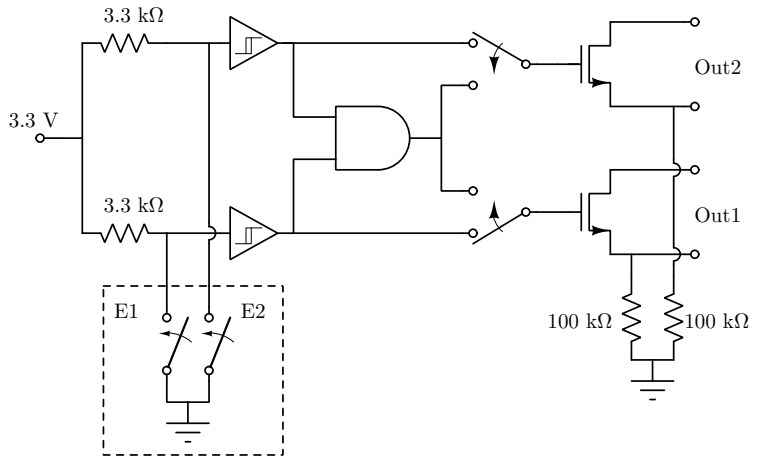

Figure I.2: Circuit diagram of the edge sensor.

Out1 and *Out2* are normally closed, depending on the edge sensor setting, when one or both needles are in contact with the chip the circuits *Out1* and *Out2* open and stop the motors.

Bibliography

[1] L. Susskind. "Dynamics of spontaneous symmetry breaking in the Weinberg-Salam theory". In: *Phys. Rev. D* 20.10 (1979), pp. 2619–2625. DOI: 10.1103/PhysRevD.20.2619.

[2] G. A. Rinella et al. "Test-beam results of a silicon pixel detector with time-over-threshold read-out having ultra-precise time resolution". In: *J. Instrum.* 10.12 (2015), P12016. DOI: 10.1088/1748-0221/10/12/P12016.

[3] J. H. Christenson et al. "Evidence for the 2π decay of the K_2^0 meson". In: *Phys. Rev. Lett.* 13.4 (1964), pp. 138–140. DOI: 10.1103/PhysRevLett.13.138.

[4] A. Alavi-Harati et al. "Observation of direct CP violation in $K_{S,L} \to \pi\pi$ decays". In: *Phys. Rev. Lett.* 83.1 (1999), pp. 22–27. DOI: 10.1103/PhysRevLett.83.22.

[5] V. Fanti et al. "A new measurement of direct CP violation in two pion decays of the neutral kaon". In: *Phys. Lett. B* 465 (1999), pp. 335–348. DOI: 10.1016/S0370-2693(99)01030-8.

[6] A. J. Buras et al. "Can we reach the Zeptouniverse with rare K and $B_{s,d}$ decays?" In: *J. High Energy Phys.* 2014.11 (2014), pp. 1–43. DOI: 10.1007/JHEP11(2014)121.

[7] A. J. Buras, M. E. Lautenbacher, and G. Ostermaier. "Waiting for the top quark mass, $K^+ \to \pi^+\nu\bar{\nu}$, B_s^0-$\overline{B_s^0}$ mixing, and CP asymmetries in B decays". In: *Phys. Rev. D* 50.5 (1994), pp. 3433–3446. DOI: 10.1103/PhysRevD.50.3433.

[8] A. J. Buras et al. "$K^+ \to \pi^+\nu\overline{\nu}$ and $K_L \to \pi^0\nu\overline{\nu}$ in the standard model: status and perspectives". In: *J. High Energy Phys.* 2015.11 (2015), pp. 1–34. DOI: 10.1007/JHEP11(2015)033.

[9] F. Mescia and C. Smith. "Improved estimates of rare K decay matrix elements from K_{l3} decays". In: *Phys. Rev. D* 76.3 (2007), p. 034017. DOI: 10.1103/PhysRevD.76.034017.

[10] A. V. Artamonov et al. "New measurement of the $K^+ \to \pi^+\nu\overline{\nu}$ branching ratio". In: *Phys. Rev. Lett.* 101.19 (2008), p. 191802. DOI: 10.1103/PhysRevLett.101.191802.

[11] J. K. Ahn et al. "Experimental study of the decay $K_L^0 \to \pi^0\nu\overline{\nu}$". In: *Phys. Rev. D* 81.7 (2010), p. 072004. DOI: 10.1103/PhysRevD.81.072004.

[12] T. Yamanaka. "The J-PARC KOTO experiment". In: *Progr. Theor. Exp. Phys.* 2012.1 (2012). DOI: 10.1093/ptep/pts057.

[13] The NA62 Collaboration. *NA62 technical design*. NA62-10-07. 2010. URL: https://na62.web.cern.ch/na62/Documents/TechnicalDesign.html.

[14] A. Francescon et al. "Application of micro-channel cooling to the local thermal management of detectors electronics for particle physics". In: *Microelectr. J.* 44.7 (2013), pp. 612–618. DOI: 10.1016/j.mejo.2013.03.012.

[15] A. Kluge et al. "The TDCpix readout ASIC: A 75 ps resolution timing front-end for the NA62 Gigatracker hybrid pixel detector". In: *Nucl. Instrum. Methods Phys. Res., Sect. A* 732 (2013). Vienna Conference on Instrumentation 2013, pp. 511–514. DOI: 10.1016/j.nima.2013.06.089.

[16] E. Cortina Gil and B. Velghe. "Characterisation of the GigaTracker n-in-p type sensors". NA62-16-XX, in preparation.

[17] T. Spadaro. "Lepton-flavor violation studies: Present status and future perspectives from NA62". 2013 International Workshop on Baryon and Lepton Number Violation, Heidelberg. 2013.

[18] O. I. Dahl et al. "Strange-Particle production in $\pi^- p$ interactions from 1.5 to 4.2 BeV/c. II. Two-body final states". In: *Phys. Rev.* 183.5 (1969), pp. 1520–1520. DOI: 10.1103/PhysRev.183.1520.4.

[19] M. K. Gaillard and B. W. Lee. "Rare decay modes of the K mesons in gauge theories". In: *Phys. Rev. D* 10.3 (1974), pp. 897–916. DOI: 10.1103/PhysRevD.10.897.

[20] J. Ellis et al. "Implications of recent measurements of B meson mixing and ϵ'/ϵ_K". In: *Nucl. Phys. B* 304 (1988), pp. 205–235. DOI: 10.1016/0550-3213(88)90625-6.

[21] G. Buchalla and A. J. Buras. "$K \to \pi\nu\overline{\nu}$ and high precision determinations of the CKM matrix". In: *Phys. Rev. D* 54 (11 1996), pp. 6782–6789. DOI: 10.1103/PhysRevD.54.6782.

[22] J. Brod et al. "Two-loop electroweak corrections for the $K \to \pi\nu\nu$ decays". In: *Phys. Rev. D* 83 (2011), p. 034030. DOI: 10.1103/PhysRevD.83.034030.

[23] U. Camerini et al. "Experimental search for semileptonic neutrino neutral currents". In: *Phys. Rev. Lett.* 23.6 (1969), pp. 326–329. DOI: 10.1103/PhysRevLett.23.326.

[24] J. H. Klems, R. H. Hildebrand, and R. Stiening. "Limits on the $K^+ \to \pi^+ + \nu + \overline{\nu}$ and $K^+ \to \pi^+ + n\gamma$ decay rates". In: *Phys. Rev. D* 4.1 (1971), pp. 66–80. DOI: 10.1103/PhysRevD.4.66.

[25] G. D. Cable et al. "Search for rare K^+ decays. II. $K^+ \to \pi^+\nu\overline{\nu}$". In: *Phys. Rev. D* 8.11 (1973), pp. 3807–3812. DOI: 10.1103/PhysRevD.8.3807.

[26] Y. Asano et al. "Search for a rare decay mode $K^+ \to \pi^+\nu\overline{\nu}$ and axion". In: *Phys. Lett. B* 107.1–2 (1981), pp. 159–162. DOI: 10.1016/0370-2693(81)91172-2.

[27] M. S. Atiya et al. "Search for the decay $K^+ \to \pi^+\nu\overline{\nu}$". In: *Phys. Rev. Lett.* 64.1 (1990), pp. 21–24. DOI: 10.1103/PhysRevLett.64.21.

[28] M. S. Atiya et al. "Search for the decay $K^+ \to \pi^+\nu\overline{\nu}$". In: *Phys. Rev. Lett.* 70.17 (1993), pp. 2521–2524. DOI: 10.1103/PhysRevLett.70.2521.

[29] S. Adler et al. "Search for the decay $K^+ \to \pi^+\nu\overline{\nu}$". In: *Phys. Rev. Lett.* 76.9 (1996), pp. 1421–1424. DOI: 10.1103/PhysRevLett.76.1421.

[30] S. Adler et al. "Evidence for the Decay $K^+ \to \ ^+\nu\overline{\nu}$". In: *Phys. Rev. Lett.* 79.12 (1997), pp. 2204–2207. DOI: 10.1103/PhysRevLett.79.2204.

[31] S. Adler et al. "Further evidence for the decay $K^+ \to \pi^+\nu\overline{\nu}$". In: *Phys. Rev. Lett.* 88.4 (2002), p. 041803. DOI: 10.1103/PhysRevLett.88.041803.

[32] V. V. Anisimovsky et al. "Improved measurement of the $K^+ \to \pi^+\nu\overline{\nu}$ branching ratio". In: *Phys. Rev. Lett.* 93.3 (2004), p. 031801. DOI: 10.1103/PhysRevLett.93.031801.

[33] T.-P. Cheng and L.-F. Li. *Gauge theory of elementary particle physics.* Oxford University Press, 1988.

[34] M. E. Peskin and D. V. Schroeder. *An Introduction to quantum field theory.* Westview Press, 1995.

[35] N. Cabibbo. "Unitary symmetry and leptonic decays". In: *Phys. Rev. Lett.* 10.12 (1963), pp. 531–533. DOI: 10.1103/PhysRevLett.10.531.

[36] S. L. Glashow, J. Iliopoulos, and L. Maiani. "Weak interactions with lepton-hadron symmetry". In: *Phys. Rev. D* 2.7 (1970), pp. 1285–1292. DOI: 10.1103/PhysRevD.2.1285.

[37] M. Kobayashi and T. Maskawa. "CP-violation in the renormalizable theory of weak interaction". In: *Prog. Theor. Phys.* 49.2 (1973), pp. 652–657. DOI: 10.1143/PTP.49.652.

[38] K. Olive and Particle Data Group. "Review of particle physics". In: *Chin. Phys. C* 38.9 (2014), p. 090001. DOI: 10.1088/1674-1137/38/9/090001.

[39] J.-M. Gérard. "An upper bound on the kaon B-parameter and $\mathrm{Re}(\epsilon_K)$". In: *J. High Energy Phys.* 2011.2 (2011), pp. 1–10. DOI: 10.1007/JHEP02(2011)075.

[40] S. Bertolini, M. Fabbrichesi, and J. O. Eeg. "Theory of the CP-violating parameter ε'/ε". In: *Rev. Mod. Phys.* 72.1 (2000), pp. 65–93. DOI: 10.1103/RevModPhys.72.65.

[41] A. J. Buras and J.-M. Gérard. "Upper bounds on ε'/ε parameters $B_6^{(1/2)}$ and $B_8^{(3/2)}$ from large N QCD and other news". In: *J. High Energy Phys.* 2015.12 (2015), pp. 1–20. DOI: 10.1007/JHEP12(2015)008.

[42] A. J. Buras and J.-M. Gerard. "Final state interactions in $K \to \pi\pi$ decays: $\Delta I = 1/2$ rule vs. ε'/ε". In: *ArXiv e-prints* (2016). arXiv: 1603.05686 [hep-ph].

[43] L. Wolfenstein. "Parametrization of the Kobayashi-Maskawa matrix". In: *Phys. Rev. Lett.* 51.21 (1983), pp. 1945–1947. DOI: 10.1103/PhysRevLett.51.1945.

[44] Charles, J. et al. "CP violation and the CKM matrix: assessing the impact of the asymmetric B factories". In: *Eur. Phys. J. C* 41.1 (2005), pp. 1–131. DOI: 10.1140/epjc/s2005-02169-1.

[45] V. M. Abazov et al. "Measurement of the anomalous like-sign dimuon charge asymmetry with 9 fb^{-1} of $p\overline{p}$ collisions". In: *Phys. Rev. D* 84.5 (2011), p. 052007. DOI: 10.1103/PhysRevD.84.052007.

[46] G. Borissov and B. Hoeneisen. "Understanding the like-sign dimuon charge asymmetry in $p\overline{p}$ collisions". In: *Phys. Rev. D* 87.7 (2013), p. 074020. DOI: 10.1103/PhysRevD.87.074020.

[47] R. Aaij et al. *Angular analysis of the $B^0 \to K^{*0}\mu^+\mu^-$ decay*. Tech. rep. Submitted to JHEP. 2015. URL: https://cds.cern.ch/record/2115087.

[48] V. Khachatryan et al. "Angular analysis of the decay $B^0 \to K^{*0}\mu^+\mu^-$ from pp collisions at $\sqrt{s} = 8$ TeV". In: *Phys. Lett. B* 753 (2016), pp. 424–448. DOI: 10.1016/j.physletb.2015.12.020.

[49] G. W. Bennett et al. "Measurement of the positive muon anomalous magnetic moment to 0.7 ppm". In: *Phys. Rev. Lett.* 89.10 (2002), p. 101804. DOI: 10.1103/PhysRevLett.89.101804.

[50] A. J. Buras, S. Uhlig, and F. Schwab. "Waiting for precise measurements of $K^+ \to \pi^+\nu\overline{\nu}$ and $K_L \to \pi^0\nu\overline{\nu}$". In: *Rev. Mod. Phys.* 80.3 (2008), pp. 965–1007. DOI: 10.1103/RevModPhys.80.965.

[51] G. Buchalla and A. J. Buras. "QCD corrections to the sdZ vertex for arbitrary top quark mass". In: *Nucl. Phys. B* 398.2 (1993), pp. 285–300. DOI: 10.1016/0550-3213(93)90110-B.

[52] A. J. Buras et al. "Charm quark contribution to $K^+ \to \pi^+\nu\overline{\nu}$ at next-to-next-to-leading order". In: *J. High Energy Phys.* 2006.11 (2006), p. 002. DOI: 10.1088/1126-6708/2006/11/002.

[53] J. Brod and M. Gorbahn. "Electroweak corrections to the charm quark contribution to $K^+ \to \pi^+\nu\overline{\nu}$". In: *Phys. Rev. D* 78.3 (2008), p. 034006. DOI: 10.1103/PhysRevD.78.034006.

[54] G. Isidori, F. Mescia, and C. Smith. "Light-quark loops in $K \to \pi\nu\overline{\nu}$". In: *Nucl. Phys. B* 718.1–2 (2005), pp. 319–338. DOI: 10.1016/j.nuclphysb.2005.04.008.

[55] A. J. Buras et al. "Rare decay $K^+ \to \pi^+\nu\overline{\nu}$ at the next-to-next-to-leading order in QCD". In: *Phys. Rev. Lett.* 95.26 (2005), p. 261805. DOI: 10.1103/PhysRevLett.95.261805.

[56] P. Langacker. "The physics of heavy Z' gauge bosons". In: *Rev. Mod. Phys.* 81.3 (2009), pp. 1199–1228. DOI: 10.1103/RevModPhys.81.1199.

[57] A. J. Buras, D. Buttazzo, and R. Knegjens. "$K \to \pi\nu\overline{\nu}$ and ε/ε' in simplified new physics models". In: *J. High Energy Phys.* 2015.11 (2015), pp. 1–33. DOI: 10.1007/JHEP11(2015)166.

[58] N. Arkani-Hamed et al. "Phenomenology of electroweak symmetry breaking from theory space". In: *J. High Energy Phys.* 2002.08 (2002), p. 020. DOI: 10.1088/1126-6708/2002/08/020.

[59] H.-C. Cheng and I. Low. "Little hierarchy, little higgses, and a little symmetry". In: *J. High Energy Phys.* 2004.08 (2004), p. 061. DOI: 10.1088/1126-6708/2004/08/061.

[60] M. Blanke, A. J. Buras, and S. Recksiegel. "Quark flavour observables in the Littlest Higgs model with T-parity after LHC Run 1". In: *ArXiv e-prints* (2015). arXiv: 1507.06316 [hep-ph].

[61] A. Crivellin et al. "Phenomenological consequences of radiative flavor violation in the MSSM". In: *Phys. Rev. D* 84.3 (2011), p. 035030. DOI: 10.1103/PhysRevD.84.035030.

[62] L. Randall and R. Sundrum. "Large mass hierarchy from a small extra dimension". In: *Phys. Rev. Lett.* 83.17 (1999), pp. 3370–3373. DOI: 10.1103/PhysRevLett.83.3370.

[63] M. Bauer et al. "Flavor physics in the Randall-Sundrum model: II. Tree-level weak-interaction processes". In: *J. High Energy Phys.* 2010.9 (2010), pp. 1–108. DOI: 10.1007/JHEP09(2010)017.

[64] A. J. Buras and L. Silvestrini. "Upper bounds on $K \to \pi\nu\bar{\nu}$ and $K_L \to \pi^0 e^+ e^-$ from ε'/ε and $K_L \to \mu^+\mu^-$". In: *Nucl. Phys. B* 546.1–2 (1999), pp. 299–314. DOI: 10.1016/S0550-3213(99)00010-3.

[65] M. Atiya et al. "A detector to search for $K^+ \to \pi^+\nu\overline{\nu}$". In: *Nucl. Instrum. Methods Phys. Res., Sect. A* 321.1–2 (1992), pp. 129–151. DOI: 10.1016/0168-9002(92)90382-E.

[66] A. V. Artamonov et al. "Study of the decay $K^+ \to \pi^+\nu\overline{\nu}$ in the momentum region $140 < P_\pi < 199$ MeV/c". In: *Phys. Rev. D* 79.9 (2009), p. 092004. DOI: 10.1103/PhysRevD.79.092004.

[67] S. Adler et al. "Measurement of the $K^+ \to \pi^+\nu\overline{\nu}$ branching ratio". In: *Phys. Rev. D* 77.5 (2008), p. 052003. DOI: 10.1103/PhysRevD.77.052003.

[68] G. Barr et al. "Performance of an electromagnetic liquid krypton calorimeter based on a ribbon electrode tower structure". In: *Nucl. Instrum. Methods Phys. Res., Sect. A* 370.2 –3 (1996), pp. 413–424. DOI: 10.1016/0168-9002(95)00800-4.

[69] M. Mota and J. Christiansen. "A high-resolution time interpolator based on a delay locked loop and an RC delay line". In: *IEEE J. Solid-State Circuits* 34.10 (1999), pp. 1360–1366. DOI: 10.1109/4.792603.

[70] A. Ceccucci et al. "The NA62 Liquid Krypton calorimeter readout module". In: *J. Instrum.* 6.12 (2011), p. C12017. DOI: 10.1088/1748-0221/6/12/C12017.

[71] H. Spieler. *Semiconductor detector systems*. Semiconductor Science and Technology. Oxford: Oxford Univ. Press, 2005.

[72] L. Rossi et al. *Pixel detectors: From fundamentals to applications*. Springer, 2006.

[73] C. Kittel. *Introduction to solid state physics*. John Wiley & Sons, Inc, 2004.

[74] S. M. Sze and K. K. Ng. *Physics of semiconductor devices*. John Wiley & Sons, Inc., 2006.

[75] T. Abe et al. "Belle II technical design report". In: *ArXiv e-prints* (2010). arXiv: 1011.0352 [physics.ins-det].

[76] D. Schroder. "The concept of generation and recombination lifetimes in semiconductors". In: *IEEE Trans. Electron Dev.* 29.8 (1982), pp. 1336–1338. DOI: 10.1109/T-ED.1982.20879.

[77] M. Tyagi and R. V. Overstraeten. "Minority carrier recombination in heavily-doped silicon". In: *Solid-State Electron.* 26.6 (1983), pp. 577–597. DOI: 10.1016/0038-1101(83)90174-0.

[78] C. Leroy and P.-G. Rancoita. *Principles of radiation interaction in matter and detection*. Third. World Scientific Publishing Company, 2011.

[79] H. Bichsel. "Straggling in thin silicon detectors". In: *Rev. Mod. Phys.* 60.3 (1988), pp. 663–699. DOI: 10.1103/RevModPhys.60.663.

[80] B. Rossi. *High-energy particles*. Englewood Cliffs, NJ: Prentice Hall, Inc., 1952.

[81] M. Fiorini and G. Aglieri Rinella. *Signal generation in Silicon, analytical and simulation studies*. GigaTracker working group meeting. CERN, 4 December 2010.

[82] C. A. Klein. "Bandgap dependence and related features of radiation ionization energies in semiconductors". In: *J. Appl. Phys.* 39.4 (1968), pp. 2029–2038. DOI: 10.1063/1.1656484.

[83] W. Shockley. "Currents to conductors induced by a moving point charge". In: *J. Appl. Phys.* 9.10 (1938), pp. 635–636. DOI: 10.1063/1.1710367.

[84] S. Ramo. "Currents induced by electron motion". In: *Proceedings of the IRE* 27.9 (1939), pp. 584–585. DOI: 10.1109/JRPROC.1939.228757.

[85] E. Gatti, G. Padovini, and V. Radeka. "Signal evaluation in multi-electrode radiation detectors by means of a time dependent weighting vector". In: *Nucl. Instrum. Methods Phys. Res., Sect. A* 193.3 (1982), pp. 651–653. DOI: 10.1016/0029-554X(82)90265-8.

[86] C. Canali et al. “Electron and hole drift velocity measurements in silicon and their empirical relation to electric field and temperature”. In: *IEEE Trans. Electron Dev.* 22.11 (1975), pp. 1045–1047. DOI: 10.1109/T-ED.1975.18267.

[87] G. Anelli et al. “Optimum segmentation and thickness of silicon pixel detectors for signal to noise ratio and timing resolution”. In: *IEEE Nuclear Science Symposium Conference Record*. Vol. 2. 2006, pp. 671–680. DOI: 10.1109/NSSMIC.2006.355947.

[88] F. Lemeilleur, G. Lindström, and S. Watts. *Research and development on silicon for future experiments*. http://rd48.web.cern.ch/RD48/. Accessed: 2015-05-05.

[89] C. Gianluigi and M. Moll. *Radiation hard semiconductor devices for very high luminosity colliders*. https://rd50.web.cern.ch/rd50/. Accessed: 2015-05-05.

[90] M. Moll. “Radiation damage in silicon particle detectors: microscopic defects and macroscopic properties”. PhD thesis. Hamburg Univ., 1999. URL: https://cds.cern.ch/record/425274.

[91] G. Lindström et al. “Developments for radiation hard silicon detectors by defect engineering—results by the CERN RD48 (ROSE) Collaboration”. In: *Nucl. Instrum. Methods Phys. Res., Sect. A* 465.1 (2001), pp. 60–69. DOI: 10.1016/S0168-9002(01)00347-3.

[92] C. Leroy and P.-G. Rancoita. “Particle interaction and displacement damage in silicon devices operated in radiation environments”. In: *Rep. Prog. Phys.* 70.4 (2007), p. 493. DOI: 10.1088/0034-4885/70/4/R01.

[93] H. Kraner. “Radiation damage in silicon detectors”. In: *Nucl. Instrum. Methods Phys. Res., Sect. A* 225.3 (1984), pp. 615–618. DOI: 10.1016/0167-5087(84)90114-5.

[94] G. P. Summers et al. “Correlation of particle-induced displacement damage in silicon”. In: *IEEE Trans. Nucl. Sci.* 34.6 (1987), pp. 1133–1139. DOI: 10.1109/TNS.1987.4337442.

[95] C. Dale et al. “High energy electron induced displacement damage in silicon”. In: *IEEE Trans. Nucl. Sci.* 35.6 (1988), pp. 1208–1214. DOI: 10.1109/23.25441.

[96] R. Wunstorf. “Systematische untersuchungen zur strahlenresistenz von silizium-detektoren für die verwendung in hochenergiephysik-experiment en”. PhD thesis. Hamburg Univ., 1992. URL: http://cds.cern.ch/record/243081.

[97] *Standard practice for characterizing neutron fluence spectra in terms of an equivalent monoenergetic neutron fluence for radiation-hardness testing of electronics*. West Conshohocken, PA: ASTM International, 2014. DOI: 10.1520/E0722-14.

[98] A. Vasilescu and G. Lindstroem. *Displacement damage in silicon, on-line compilation*. http://rd50.web.cern.ch/RD50/NIEL/default.html. Accessed: 2015-04-30.

[99] G. Summers et al. "Damage correlations in semiconductors exposed to gamma, electron and proton radiations". In: *IEEE Trans. Nucl. Sci.* 40.6 (1993), pp. 1372–1379. DOI: 10.1109/23.273529.

[100] M. Huhtinen and P. Aarnio. "Pion induced displacement damage in silicon devices". In: *Nucl. Instrum. Methods Phys. Res., Sect. A* 335.3 (1993), pp. 580–582. DOI: 10.1016/0168-9002(93)91246-J.

[101] I. Jun et al. "Proton nonionizing energy loss (NIEL) for device applications". In: *IEEE Trans. Nucl. Sci.* 50.6 (2003), pp. 1924–1928. DOI: 10.1109/TNS.2003.820760.

[102] M. Huhtinen. "Simulation of non-ionising energy loss and defect formation in silicon". In: *Nucl. Instrum. Methods Phys. Res., Sect. A* 491.1–2 (2002), pp. 194–215. DOI: 10.1016/S0168-9002(02)01227-5.

[103] G. Kramberger et al. "Effective trapping time of electrons and holes in different silicon materials irradiated with neutrons, protons and pions". In: *Nucl. Instrum. Methods Phys. Res., Sect. A* 481.1–3 (2002), pp. 297–305. DOI: 10.1016/S0168-9002(01)01263-3.

[104] M. Moll, E. Fretwurst, and G. Lindström. "Leakage current of hadron irradiated silicon detectors – material dependence". In: *Nucl. Instrum. Methods Phys. Res., Sect. A* 426.1 (1999), pp. 87–93. DOI: 10.1016/S0168-9002(98)01475-2.

[105] M. Fiorini. *Energy straggling contribution to the GigaTracker time resolution.* GigaTracker working group meeting. CERN, 14 December 2010.

[106] M. Noy et al. "Characterisation of the NA62 GigaTracker end of column demonstrator hybrid pixel detector". In: *J. Instrum.* 6.11 (2011), p. C11025. DOI: 10.1088/1748-0221/6/11/C11025.

[107] L. Gatignon. *Magnets kit for the experimental areas of the CERN PS/SPS complex.* Tech. rep. CERN-OPEN-2004-003. Geneva: CERN, 1991. URL: http://cds.cern.ch/record/711814.

[108] J. Kemmer and G. Lutz. "New structures for position sensitive semiconductor detectors". In: *Nucl. Instrum. Methods Phys. Res., Sect. A* 273.2–3 (1988), pp. 588–598. DOI: 10.1016/0168-9002(88)90061-7.

[109] P. Holl et al. "A double-sided silicon strip detector with capacitive readout and a new method of integrated bias coupling". In: *IEEE Trans. Nucl. Sci.* 36.1 (1989), pp. 251–255. DOI: 10.1109/23.34444.

[110] R. Richter et al. "Strip detector design for ATLAS and HERA-B using two-dimensional device simulation". In: *Nucl. Instrum. Methods Phys. Res., Sect. A* 377.2–3 (1996), pp. 412–421. DOI: 10.1016/0168-9002(96)00257-4.

[111] G. Nuessle. "Development of a novel micro channel cooling system for the NA62 GTK detector". PhD thesis. Univ. cath. Louvain, 2015. URL: http://hdl.handle.net/2078.1/171150.

[112] B. Taylor. "TTC distribution for LHC detectors". In: *IEEE Trans. Nucl. Sci.* 45.3 (1998), pp. 821–828. DOI: 10.1109/23.682644.

[113] E. Cortina Gil, S. Podolsk, and B. Velghe. "Offline database integration: Getting started". NA62-13-05. 2013. URL: https://na62.web.cern.ch/na62/restricted/NotesDoc/na62-13-05.pdf.

[114] Y. Allkofer et al. "Design and performance of the silicon sensors for the CMS barrel pixel detector". In: *Nucl. Instrum. Methods Phys. Res., Sect. A* 584.1 (2008), pp. 25–41. DOI: 10.1016/j.nima.2007.08.151.

[115] M. Fiorini et al. "Test of silicon sensors for a high rate pixel detector for the NA62 experiment". NA62-08-01. 2008.

[116] S. Onori et al. "Alanine dosimetry of proton therapy beams". In: *Med. Phys.* 24.3 (1997), pp. 447–453. DOI: 10.1118/1.597911.

[117] Z. Li and H. Kraner. "Studies of frequency dependent C-V characteristics of neutron irradiated p^+-n silicon detectors". In: *IEEE Trans. Nucl. Sci.* 38.2 (1991), pp. 244–250. DOI: 10.1109/23.289304.

[118] J. Allison et al. "Geant4 developments and applications". In: *IEEE Trans. Nucl. Sci.* 53.1 (2006), pp. 270–278. DOI: 10.1109/TNS.2006.869826.

[119] K. L. Brown and F. C. Iselin. *DECAY TURTLE (Trace Unlimted Rays Through Lumped Elements): a computer program for simulating charged-particle beam transport systems, including decay calculations.* Geneva: CERN, 1974. DOI: 10.5170/CERN-1974-002.

[120] A. Sergi. *NA62 software framework.* URL: http://sergiant.web.cern.ch/sergiant/NA62FW/html/.

[121] D. S. Ayres et al. "$\pi^{\pm}p$, $K^{\pm}p$, pp, and $\overline{p}p$ elastic scattering from 50 to 175 GeV/c". In: *Phys. Rev. D* 15.11 (1977), pp. 3105–3138. DOI: 10.1103/PhysRevD.15.3105.

[122] V. Ammosov et al. "Average charged particle multiplicity and topological cross sections in 50 GeVc and 69 GeVc pp interactions: Collaboration France-Soviet Union". In: *Phys. Lett. B* 42.4 (1972), pp. 519–521. DOI: 10.1016/0370-2693(72)90121-9.

[123] G. Akopdjanov et al. "Charged particle multiplicity distributions for 32 GeV/c $K^{\pm}p$ and pp interactions and for 50 GeV/c $\pi^{\pm}p$ interactions". In: *Nucl. Phys. B* 75.3 (1974), pp. 401–412. DOI: 10.1016/0550-3213(74)90083-2.

[124] M. G. D. Gilchriese. "A Systematic study of K^+ and K^- charge exchange at 8.36 GeV/c and 12.8 GeV/c". PhD thesis. SLAC, 1977. URL: http://lss.fnal.gov/archive/other/slac-0202.pdf.

[125] M. Frigo and S. Johnson. "The design and implementation of FFTW3". In: *Proc. IEEE* 93.2 (2005), pp. 216–231. DOI: 10.1109/JPROC.2004.840301.

[126] J. Jakubek. "Precise energy calibration of pixel detector working in time-over-threshold mode". In: *Nucl. Instrum. Methods Phys. Res., Sect. A* 633, Supplement 1 (2011). 11th International Workshop on Radiation Imaging Detectors (IWORID), S262–S266. DOI: 10.1016/j.nima.2010.06.183.

[127] L. Bonnet et al. "GasToF: Ultra-fast ToF forward detector for exclusive processes at the LHC". In: *Acta Phys. Polon.* B38 (2007), pp. 477–482.

[128] *Minutes of the 118th meeting of the SPSC, Tuesday 23 and Wednesday 24 June 2015*. Tech. rep. CERN-SPSC-2015-028. SPSC-118. Geneva: CERN, 2015. URL: http://cds.cern.ch/record/2032199.

[129] G. Arduini et al. *Measurement of the circumference and of the central frequencies at 26 and 450 GeV in the SPS*. Tech. rep. SL-MD-Note-257. Geneva: CERN, 1997. URL: http://cds.cern.ch/record/702414.

[130] R. Fantechi. Private communication. 2015.

[131] H. F.-W. Sadrozinski et al. "Ultra-fast silicon detectors". In: *Nucl. Instrum. Methods Phys. Res., Sect. A* 730 (2013), pp. 226–231. DOI: 10.1016/j.nima.2013.06.033.

[132] W. Riegler and G. A. Rinella. "Point charge potential and weighting field of a pixel or pad in a plane condenser". In: *Nucl. Instrum. Methods Phys. Res., Sect. A* 767 (2014), pp. 267–270. DOI: 10.1016/j.nima.2014.08.044.

[133] A. Taroni and G. Zanarini. "Plasma effects and charge collection time in solid state detectors". In: *Nucl. Instrum. Methods Phys. Res.* 67.2 (1969), pp. 277–282. DOI: 10.1016/0029-554X(69)90459-5.

[134] N. Cartiglia et al. "Weightfield2 package". Initially developed at HEPHY - Institute of High Energy Physics, Wien, Austria. URL: http://personalpages.to.infn.it/~cartigli/Weightfield2/Main.html.

[135] A. H. Jazwinski. *Stochastic processes and filtering theory*. Mathematics in Science and Engineering. New York, NY: Academic Press, 1970.

[136] T. Fritzsch et al. "Flip chip assembly of thinned chips for hybrid pixel detector applications". In: *J. Instrum.* 9.05 (2014), p. C05039. DOI: 10.1088/1748-0221/9/05/C05039.

[137] M. Noy. Private communication. 2014.